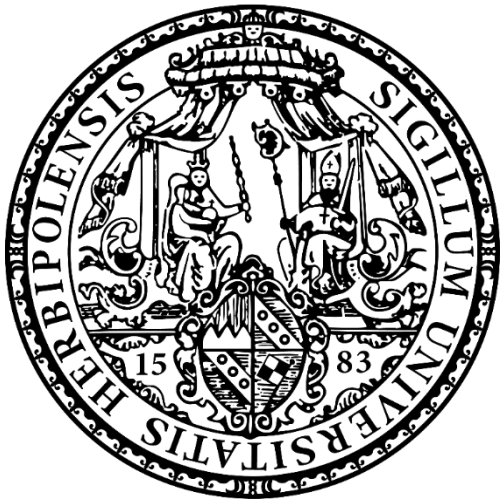


# Application of electron cryomicroscopy for structural and functional studies on the mechanosensitive channels of small conductance

Kryoelektronenmikroskopie zur strukturellen und funktionellen Untersuchung der mechanosensitiven Kanäle kleiner Leitfähigkeit

**Doctoral Thesis**

for a doctoral degree at the Graduate School of Life Sciences,
Julius-Maximilians-Universität Würzburg,
Section Biomedicine

Submitted by

**Vanessa Judith Flegler**

born in Würzburg

Würzburg 2021

**Submitted on:** ……

Office stamp

## Members of the Thesis Committee

| | |
|---|---|
| Chairperson: | Prof. Dr. Markus Sauer |
| Primary Supervisor: | Prof. Dr. Bettina Böttcher |
| Supervisor (Second): | Prof. Dr. Christian Stigloher |
| Supervisor (Third): | Prof. Dr. Rainer Hedrich |

Date of Public Defence: ……..……

Date of Receipt of Certificates: …….

To my family, past and present.

# AFFIDAVIT

I hereby confirm that my thesis entitled ”Application of electron cryomicroscopy for structural and functional studies on the mechanosensitive channels of small conductance” is the result of my own work. I did not receive any help or support from commercial consultants. All sources and / or materials applied are listed and specified in the thesis.

Furthermore, I confirm that this thesis has not yet been submitted as part of another examination process neither in identical nor in similar form.

Place, Date Signature

# EIDESSTATTLICHE ERKLÄRUNG

Hiermit erkläre ich an Eides statt, die Dissertation „Kryoelektronenmikroskopie zur strukturellen und funktionellen Untersuchung der mechanosensitiven Kanäle kleiner Leitfähigkeit” eigenständig, d.h. insbesondere selbständig und ohne Hilfe eines kommerziellen Promotionsberaters, angefertigt und keine anderen als die von mir angegebenen Quellen und Hilfsmittel verwendet zu haben.

Ich erkläre außerdem, dass die Dissertation weder in gleicher noch in ähnlicher Form bereits in einem anderen Prüfungsverfahren vorgelegen hat.

Ort, Datum Unterschrift

# PUBLICATIONS

**Part of this work has been published:**

Flegler VJ, Rasmussen A, Rao S, Wu N, Zenobi R, Sansom MSP, Hedrich R, Rasmussen T, Böttcher B. The MscS-like channel YnaI has a gating mechanism based on flexible pore helices. *Proc Natl Acad Sci U S A*. 2020 Nov 17;117(46):28754-28762

Flegler VJ, Rasmussen A, Borbil K, Boten L, Chen HA, Deinlein H, Halang J, Hellmanzik K, Löffler J, Schmidt V, Makbul C, Kraft C, Hedrich R, Rasmussen T, Böttcher B. Mechanosensitive channel gating by delipidation. *Proc Natl Acad Sci U S A*. 2021 Aug 17;118(33):e2107095118

Excerpted text passages and adapted or modified figures are indicated as such. Excerpted text was adapted to British English. The numbering of figures and tables, and references to literature were adapted to fit the style and structure of this work.

**Further publications:**

Flegler VJ, Rasmussen T, Böttcher B. More Than Just Closed and Open: Unraveling a Mechanosensor. *Trends Biochem Sci*. 2021 Aug;46(8):623-625

Haider MS, Lübtow MM, Endres S, Forster S, Flegler VJ, Böttcher B, Aseyev V, Pöppler AC, Luxenhofer R. Think Beyond the Core: Impact of the Hydrophilic Corona on Drug Solubilization Using Polymer Micelles. *ACS Appl Mater Interfaces*. 2020 Jun 3;12(22):24531-24543

Hahn L, Maier M, Stahlhut P, Beudert M, Flegler V, Forster S, Altmann A, Töppke F, Fischer K, Seiffert S, Böttcher B, Lühmann T, Luxenhofer R. Inverse Thermogelation of Aqueous Triblock Copolymer Solutions into Macroporous Shear-Thinning 3D Printable Inks. *ACS Appl Mater Interfaces*. 2020 Mar 18;12(11):12445-12456

Rasmussen T, Flegler VJ, Rasmussen A, Böttcher B. Structure of the Mechanosensitive Channel MscS Embedded in the Membrane Bilayer. *J Mol Biol*. 2019 Aug 9;431(17):3081-3090

Song B, Lenhart J, Flegler VJ, Makbul C, Rasmussen T, Böttcher B. Capabilities of the Falcon III detector for single-particle structure determination. *Ultramicroscopy*. 2019 Aug;203:145-154

Arlt C, Flegler V, Ihling CH, Schäfer M, Thondorf I, Sinz A. An Integrated Mass Spectrometry Based Approach to Probe the Structure of the Full-Length Wild-Type Tetrameric p53 Tumor Suppressor. *Angew Chem Int Ed Engl*. 2017 Jan 2;56(1):275-279

**Published data:**

| **Description** | **EMDB accession code** | **PDB accession code** |
|---|---|---|
| YnaI in Amphipols | 11558 | |
| Closed YnaI (DIBMALPs) | 11557 | 6ZYD |
| Closed YnaI 2 (DIBMALPs) | 11559 | |
| Intermediate YnaI (DBMALPs) | 11561 | |
| Open-like YnaI (DIBMALPs) | 11560 | 6ZYE |
| YnaI-G149A/G152A | 11556 | |
| Closed MscS (DDM) | 12997 | 7ONL |
| Open (delipidated) MscS (DDM) | 13003 | 7OO0 |
| Closed (re-lipidated) MscS (DDM) | 13006 | 7OO6 |
| Open MscS (LMNG) | 12996 | 7ONJ |
| YbiO in Amphipols | 11629 | 7A46 |

**Congress contributions:**

Poster presentation at the 12th international GSLS student symposium EUREKA! 2017, October 11-12, 2017, in Würzburg, Germany: Structural Studies on the Mechanosensitive Channels of small Conductance

Poster presentation at the 14th international GSLS student symposium EUREKA! 2019, October 9-10, 2019, in Würzburg, Germany: Structural Studies on the Mechanosensitive Channels of small Conductance

Poster presentation at the 12th international GSLS student symposium EUREKA! 2020, October 8-9, 2020, online: Structural Studies on the Mechanosensitive Channels of small Conductance

Invited talk at SMALP Conference February 2021, February 26, 2021, online: The mechanosensitive channel YnaI has a gating mechanism based on flexible pore helices

# ABSTRACT

Bacteria thrive and survive in many different environments, and as a result, they have developed robust mechanisms to adapt rapidly to alterations in their surroundings. The protection against osmotic forces is provided by mechanosensitive channels: their primary function is to maintain the integrity of the cell upon a hypoosmotic shock. The mechanosensitive channel of small conductance (MscS) is not only the smallest common structural unit of a diverse family that allows for a tailored response in osmoregulation; it is also the most intensively studied homologue. Mechanosensitive channels directly sense elevated membrane tension levels generated by increased pressure within the cell and open transiently. *Escherichia coli* has six paralogues that differ in their gating properties and the number of additional transmembrane (TM) helices. These TM helices, termed sensor paddles, are essential for sensing, as they directly contact the surrounding membrane; however, the role of the additional TM helices is still unclear. Furthermore, lipids occupy hydrophobic pockets far away from the membrane plane. A recent gating model for MscS states that increased membrane tension triggers the expulsion of lipids out of those pockets, modulating different conformational states of MscS. This model focuses on bound lipids, but it is still unclear to what extent the direct interaction with the membrane influences sensing and how relevant it is for the larger paralogues.

In the herein described work, structural studies on two larger paralogues, the medium-sized channel YnaI and the large channel YbiO were realised using electron cryomicroscopy (cryo-EM). Lipids were identified in YnaI in the pockets in a similar position and orientation as in MscS, suggesting a conserved sensing mechanism. Moreover, the copolymer diisobutylene/maleic acid (DIBMA) allowed the extraction of artificially activated YnaI from plasma membranes, leading to an open-like form of this channel. This novel conformation indicated that the pore helices bend at a GGxGG motif during gating, which is unique among the *Escherichia coli* paralogues, concomitant with a structural reorganisation of the sensor paddles. Thus, despite a high similarity of their closed states, the gating mechanisms of MscS and YnaI are surprisingly different. Furthermore, the comparison of MscS, YnaI, and YbiO accentuates variations and similarities between the differently sized family members, implying fine-tuning of channel properties in the pore regions and the cytosolic lateral entry sides into the channel.

Structural analyses of MscS reconstituted into different systems showed the advantages and disadvantages of certain polymers and detergents. The novel DIBMA copolymer and the more conventional amphiphilic polymers, so-called Amphipols, perturb contacting transmembrane helices or lead to their denaturation. Due to this observation, the obtained structures of YnaI must also be cautiously considered. The structures obtained in detergents resulted in unaffected channels; however, the applicability of detergents for MscS-like channels is limited by the increased required sample concentration.

The role of lipids for gating MscS in the absence of a membrane was examined by deliberately removing coordinated lipid molecules from MscS using different amounts and kinds of detergent. The effects on the channel were inspected by cryo-EM. These experiments showed that closed MscS adopts the open conformation when it is enough delipidated by incubation with the detergent n-dodecyl-β-D-maltoside, and adding lipids to the open channel reverses this process. The results agree with the state-of-the-art model that the amount of lipid molecules in the pockets and grooves is responsible for the conformational state of MscS. Furthermore, incubation with the detergent lauryl maltose neopentyl glycol, which has stabilising and delipidating characteristics, resulted in a high-resolution structure of open MscS exhibiting an intricate network of ligands. Based on this structure, an updated gating model is proposed, which states that upon opening, lipids from the pockets migrate into the cytosolic membrane leaflet, while lipids from the periplasmic leaflet enter the grooves that arise between the sensor paddles.

# ZUSAMMENFASSUNG

Bakterien gedeihen und überleben in vielen unterschiedlichen Umgebungen. Daher haben sie robuste Mechanismen entwickelt, um sich rasch an Veränderungen in ihrer Umgebung anzupassen. Den Schutz vor osmotischen Kräften gewährleisten mechanosensitive Kanäle: Ihre Hauptfunktion besteht darin, die Unversehrtheit der Zelle bei einem hypoosmotischen Schock zu erhalten. Der mechanosensitive Kanal geringer Leitfähigkeit (*mechanosensitive channel of small conductance*, MscS) stellt nicht nur die kleinste gemeinsame Struktureinheit einer Familie von Kanälen dar, die eine maßgeschneiderte Antwort auf hypoosmotischen Stress ermöglicht; er ist auch das intensivste untersuchte Familienmitglied. Mechanosensitive Kanäle registrieren erhöhte Membranspannungen, die durch steigenden Druck innerhalb der Zelle entstehen, und öffnen vorübergehend. In *Escherichia coli* gibt es sechs paraloge Kanäle, die sich in ihren Öffnungs-Eigenschaften und der Anzahl zusätzlicher transmembranen Helices unterscheiden. Diese Helices, die als *sensor paddles* bezeichnet werden, sind für das Erfassen ansteigender Membranspannung unerlässlich, da sie direkt mit der umgebenden Membran in Kontakt stehen; die Rolle der zusätzlichen transmembranen Helices ist jedoch noch nicht geklärt. Außerdem sitzen Lipide in hydrophoben Taschen weit entfernt von der Membran. Ei kürzlich vorgeschlagenes Öffnungs-Modell für MscS besagt, dass eine erhöhte Membranspannung zum Ausstoß der Lipide aus diesen Taschen führt, wodurch verschiedene Konformationszustände von MscS moduliert werden. Dieses Modell konzentriert sich auf die Rolle der Lipide, aber es ist noch immer unklar, inwieweit die direkte Wechselwirkung mit der Membran das Wahrnehmen der Membranspannung beeinflusst und welche Bedeutung sie für die größeren paralogen Kanäle hat.

In der vorliegenden Arbeit wurden Strukturstudien an zwei größeren paralogen Kanälen, dem mittelgroßen Kanal YnaI und dem großen Kanal YbiO, mittels Kryoelektronenmikroskopie (Kryo-EM) durchgeführt. In YnaI wurden Lipide in den Taschen in ähnlicher Position und Ausrichtung wie in MscS gefunden, was auf einen konservierten Mechanismus zur Wahrnehmung der Membranspannung schließen lässt. Darüber hinaus ermöglichte das Copolymer Diisobutylen/Maleinsäure (DIBMA) die Isolation von artifiziell aktiviertem YnaI aus Plasmamembranen, was zur Struktur einer anscheinend offenen Form dieses Kanals führte. Diese neuartige Konformation deutet darauf hin, dass sich die Porenhelices während des Öffnens im Bereich eines GGxGG-Motiv biegen, das unter den paralogen Kanälen von *Escherichia coli* einzigartig ist und mit einer strukturellen Reorganisation der *sensor paddles*

einhergeht. Trotz der großen Ähnlichkeit ihrer geschlossenen Zustände sind die Öffnungs-Mechanismen von MscS und YnaI also überraschend unterschiedlich. Darüber hinaus zeigte der Vergleich von MscS, YnaI und YbiO Unterschiede und Gemeinsamkeiten zwischen den unterschiedlich großen Familienmitgliedern. Diese Erkenntnissse deuten auf eine Feinabstimmung der Kanaleigenschaften im Bereich der Pore und an den zytosolischen seitlichen Eingängen der Kanäle hin.

Strukturanalysen von MscS, in verschiedene Systeme rekonstituiert, zeigten die Vor- und Nachteile von ausgewählten Polymeren und Detergenzien. Das neuartige DIBMA-Copolymer und herkömmlichere amphiphile Polymere, die sogenannten Amphipole, stören die kontaktierenden transmembranen Helices oder führen zu deren Denaturierung. Im Zuge dieser Beobachtung müssen auch die erhaltenen Strukturen von YnaI vorsichtig betrachtet werden. Die in Detergenzien erhaltenen Strukturen zeigen unbeeinträchtigte Kanäle; die Anwendbarkeit von Detergenzien für MscS-ähnliche Kanäle wird jedoch durch die erhöhte erforderliche Proteinkonzentration eingeschränkt.

Die Rolle der Lipide für das Öffnen von MscS wurde in Abwesenheit einer Membran untersucht, indem koordinierte Lipidmoleküle mit verschiedenen Mengen und Arten von Detergenzien bewusst von MscS entfernt wurden. Die Auswirkungen auf den Kanal wurden mittels Kryo-EM untersucht. Dabei zeigte sich, dass die geschlossene Form von MscS in die offene Konformation übergeht, wenn es durch Inkubation mit dem Detergenz n-Dodecyl-β-D-Maltosid ausreichend delipidiert wird, und dass die Zugabe von Lipiden zum offenen Kanal diesen Prozess wieder umkehrt. Die Ergebnisse stimmen mit dem Öffnungs-Modell überein, das besagt, dass die Menge der Lipidmoleküle in den Taschen und Furchen für den Konformationszustand von MscS verantwortlich ist. Darüber hinaus führte die Inkubation mit dem Detergenz Laurylmaltose-neopentylglykol, das sowohl stabilisierende als auch delipidierende Eigenschaften hat, zu einer hochaufgelösten Struktur des offenen MscS, die ein ausgeprägtes Netzwerk von Liganden zeigt. Auf der Grundlage dieser Struktur wird ein aktualisiertes Öffnungs-Modell vorgeschlagen, das besagt, dass bei der Öffnung Lipide aus den Taschen in die zytosolische Lipidschicht der Membran wandern, während Lipide aus der periplasmatischen Lipidschicht in die Furchen gelangen, die zwischen den *sensor paddles* entstehen.

# TABLE OF CONTENTS

# 1 INTRODUCTION

Numerous well-known biological processes, including the sensations of touch and hearing, proprioception, and blood pressure regulation in animals, or gravitropic responses and reactions to pathogenic invasion in plants, share one common basis – they rely on mechanosensitive (MS) ion channels. In prokaryotes, MS channels fulfil the evolutionarily most ancient function, as they react to hypoosmotic stress manifested as turgor pressure within the cell. First reported in 1987 (Martinac et al., 1987), the bacterial MS channel family became a model system for studying the processes of mechanosensation and mechanotransduction (O. Bavi et al., 2016; Blount et al., 1999a; Koçer, 2015; Martinac, 2011; Martinac et al., 2013; Martinac and Cox, 2017; Phillips et al., 2009; Ridone et al., 2018; Spencer et al., 1999; Teng et al., 2015; Wiggins and Phillips, 2005; Zhang et al., 2016). However, despite their ubiquitous importance, the underlying mechanisms are not fully understood. With the expanding number of possibilities regarding the handling of membrane proteins and the emerged power of electron cryomicroscopy (cryo-EM) to study these, functional studies can progressively be addressed and complemented by structural studies.

## 1.1 Overview of MS channels

All organisms experience mechanical forces, which are ubiquitous and diverse. Structurally distinct MS channels (figure 1.1) are found across the kingdoms of bacteria, plants, animals, fungi, and archaea and are activated by mechanical stimuli. Members of different superfamilies of MS channels are often present in the same organism but can be restricted to certain locations or tissues (Peyronnet et al., 2014).

### 1.1.1 PIEZO channels

In eukaryotes, various mechanosensory, developmental, and regulatory roles are assigned to PIEZO1 and PIEZO2, including processes like touch, blood pressure regulation, and epithelial homeostasis (Murthy et al., 2017). Despite their importance, they were only identified in 2010 (Coste et al., 2010), and their discovery was awarded with this year's Nobel Prize in Physiology or Medicine. Because of their extraordinary size with ~2500 amino acids per subunit, and the lack of any homology to other ion channels, their structures remained a mystery for a few years. By use of cryo-EM, the three-bladed propeller architecture of the PIEZO channels was revealed (figure 1.1 A) (Ge et al., 2015; Guo and MacKinnon, 2017; Saotome et al., 2017; Zhao et al., 2018). The three blades, each comprising 36 TM helices, are arranged around a central module that includes the pore, an extracellular domain, and a carboxy-terminal (C-terminal) domain. The pore in the presented structures is closed, and the blades are not planar but are curved within the putative membrane plane. Moreover, they are rigid enough to bend the lipid bilayer, creating a membrane dome (Guo and MacKinnon, 2017). It was hypothesised that upon tension, the dome flattens, and the blades straighten, providing the energy to open the channel.

### 1.1.2 OSCA and TMEM63 channels

The OSCA family represents a class of mechanosensitive channels in plants, and their homologues in animals are the TMEM63 channels (Murthy et al., 2018). OSCA channels mediate $Ca^{2+}$ increases upon osmotic stress, which is essential for osmosensing in *A. thaliana*, and mutations affect the stomatal and root growth responses to osmotic stress (Kefauver et al., 2020; Thor et al., 2020; Yuan et al., 2014). OSCA channels are important for protection against infections caused by fungi and bacteria and could evolve to potential candidates for breeding more resistant plants. Several structures of OSCA channels were elucidated and exposed the architecture of these proteins (Jojoa-Cruz et al., 2018; Liu et al., 2018; Maity et al., 2019; Zhang et al., 2018). These studies further aimed to decipher the structural foundations of OSCA mechanosensing. The dimeric channels have two pores and 11 TM helices per subunit (figure 1.1 B). Furthermore, they have a cytoplasmic domain, which forms the dimer interface. Among the structures of different members of the OSCA family, the main differences are found in this region (Liu et al., 2018).

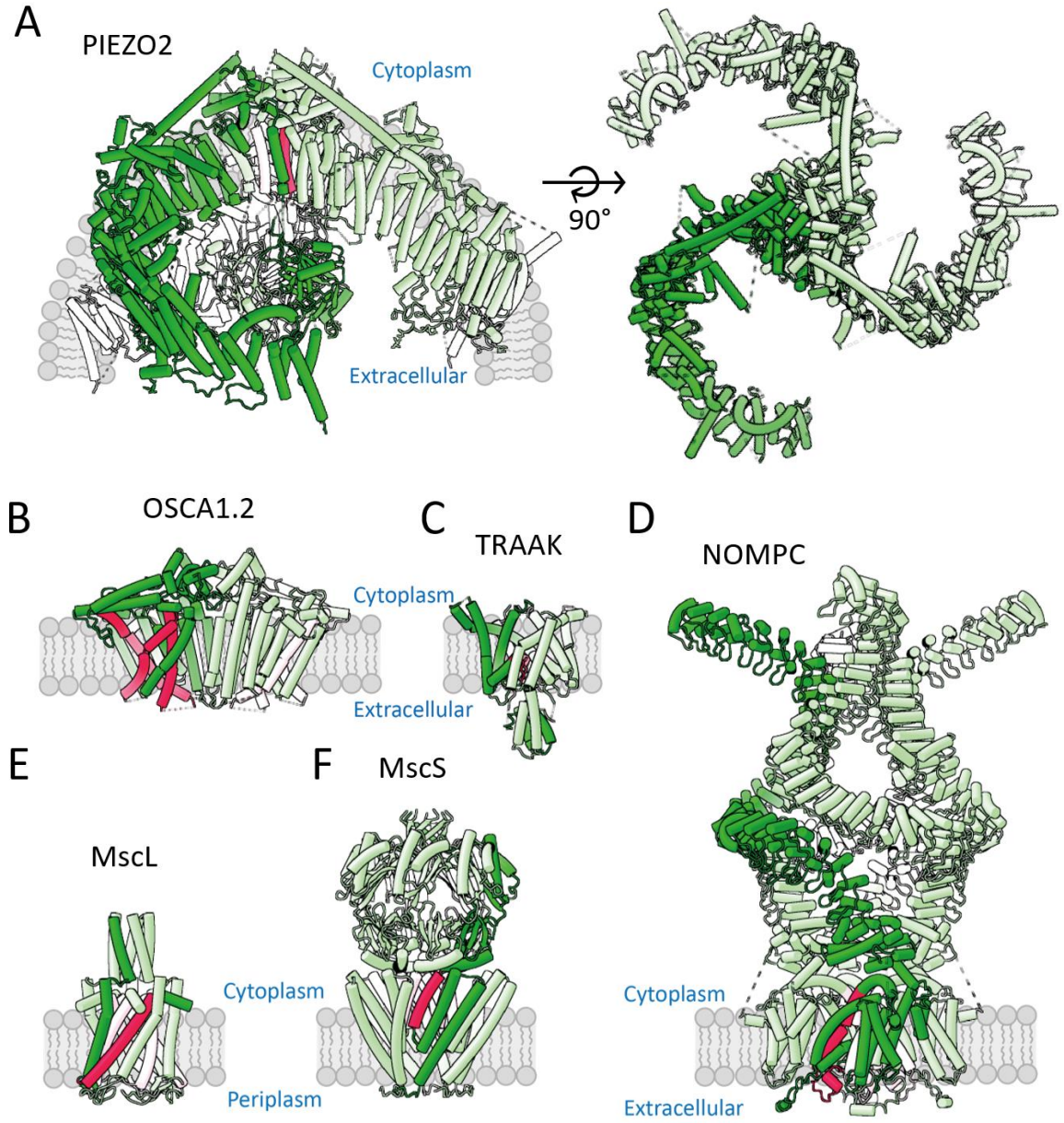


**Figure 1.1 | Structures of MS channels.** The same colour code is used for the different MS channels. One subunit is highlighted in dark green, and the remaining subunits are depicted in light green. The pore helix/ pore-lining sequence is shown in red for the highlighted subunit and in pale pink for the other subunits. The lipid bilayer is shown in grey. Only one member of each channel superfamily is shown, although structures of further members often exist, too. The structures are shown at the same scale. **(A)** In PIEZO2, each subunit contributes one helix to the pore, and the blades bend the lipid bilayer (PDB 6KG7 (Wang et al., 2019)). On the right, the channel is also depicted viewed from the cytosolic side, showing the arrangement of the three blades. **(B)** OSCA1.2 has two pores, and five TM helices contribute to each pore (PDB 6MGV (Jojoa-Cruz et al., 2018). **(C)** TRAAK also exhibits two pores, of which each is made up of two non-identical pore domains (PDB 3UM7 (Brohawn et al., 2012)). **(D)** In the TRP channel NOMPC, each subunit contributes one pore helix. A striking and unique feature of NOMPC is the spring-like cytoplasmic ankyrin repeats (PDB 5VKQ (Jin et al., 2017a)). **(E)** One helix of each subunit lines the pore in MscL (PDB 2OAR (Steinbacher et al., 2007)) and in **(F)** MscS (PDB 6RLD (Rasmussen et al., 2019a)). Figure inspired from Kefauver et al. (2020).

### 1.1.3 Two-pore potassium channels

TREK-1, TREK-2 and TRAAK are the only inherently mechanosensitive members of the two-pore potassium channel (K2P) family (Brohawn et al., 2014b). However, these $K^+$ selective channels are not only activated by mechanical forces but also by physicochemical stimuli (Brohawn, 2015). TRAAK and TREK channels are expressed in animals and plants and fine-tune electrical properties of the membrane (González et al., 2014). K2P channels are composed of two protomers, of which each contains one pore comprised of two non-identical pore domains (Brohawn et al., 2012; Lolicato et al., 2017). Additional to the transmembrane domain (TMD), an extracellular cap is present that creates a bifurcated pathway for the $K^+$ ions to the pore in TRAAK (figure 1.1 C). A striking feature is the presence of two lateral fenestrations in the TMD, which expose the ion-conducting pathway to the lipid bilayer (figure 1.2). A lipid molecule was suggested to block the pore in the closed form. This lipid is absent in the open conformation because rearrangement of the TM helices seals the lipid from the cavity (Brohawn, 2015).

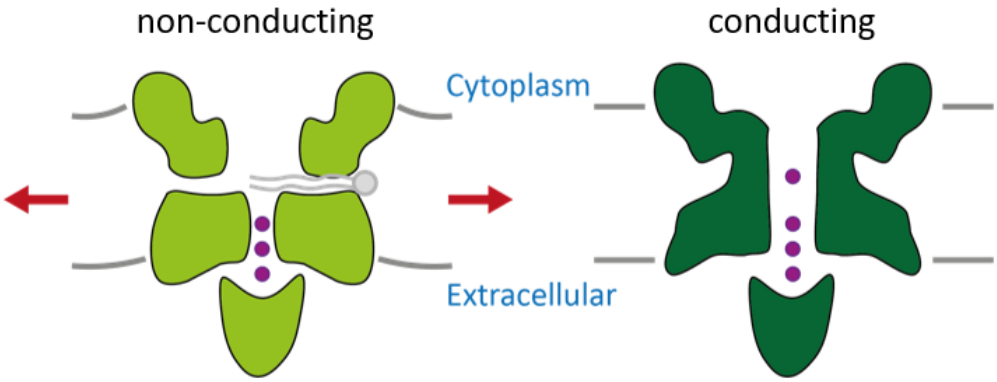


**Figure 1.2 | Model for TRAAK channel gating.** The K2P channel TRAAK is depicted in very simplified schemes in its non-conducting (light green) and conducting (dark green) conformation. In the non-conducting state, the tails of a lipid molecule (grey) enter the pore through fenestrations and block the ion-conducting pathway (purple dots). Due to structural rearrangements upon membrane tension (red arrows), no fenestrations are present in the conducting form of TRAAK, sealing the lipid and allowing ion conductance. Grey lines indicate the position of the membrane.

### 1.1.4 Transient receptor potential channels

Transient receptor potential (TRP) channels are present in the plasma membrane of different cells from different organisms (animals, plants, archaea) (Kefauver et al., 2020; Montell, 2005). They are involved in processes like thermosensation, chemosensation, photosensation, and mechanosensation, thereby including, among others, the perceptions of touch, pain, heat, and taste (Startek et al., 2019). The best-studied member of this large channel family is the thermosensitive capsaicin receptor TRPV1 (Caterina et al., 1997; Julius, 2013). However, while several TRP channel family members have been proposed to be mechanosensitive (Árnadóttir and Chalfie, 2010; Kefauver et al., 2020), so far, it was only shown that NOMPC from *Drosophila melanogaster* is inherently mechanosensitive (Cheng et al., 2010; Walker et al., 2000). All TRP channels share the basic tetrameric architecture observed in the first TRP structure of TRPV1, having six TM helices, flanked by the TRP- and C-terminal domain on one side of the sequence, and by a linker domain and several ankyrin repeats on the amino-terminal (N-terminal) side (Cao et al., 2013; Liao et al., 2013). NOMPC (figure 1.1 D) is structurally unique, as it has the largest number of ankyrin repeats among the known TRP channels. The ankyrin repeats associate the channel with microtubules, leading to the assumption that the ankyrin-repeat region acts as a spring that regulates the channel states (Zhang et al., 2015).

### 1.1.5 MscL and MscS

**Bacterial MS channels.** The maintenance of intracellular homeostasis is vital for all living cells (Levina et al., 1999). Bacteria grow and survive in many different environments because they have potent mechanisms to adapt quickly to sudden changes in their surroundings (Booth, 1985; Chung et al., 2006; Edwards et al., 2012; Hengge-Aronis, 2002). Key players of this exquisite stress response system are, among others, membrane proteins like channels and transporters that allow the passage of ions through an otherwise impermeable membrane. These membrane proteins enable them to preserve, e.g., a physiological pH, favourable cytoplasmic ion composition and turgor pressure. Among these, MS channels in the inner membrane gate as a consequence of a hypoosmotic shock: A sudden drop in the osmolarity of the surrounding medium results in a rapid influx of water into the cell, which increases the cell turgor. MS channels sense the resulting membrane tension and prevent a potential cell lysis by instantly

releasing internal osmolytes to restore the turgor level (Booth and Louis, 1999) (figure 1.3). They are tightly regulated and close immediately when the danger is alleviated (Edwards et al., 2005). Therefore, they are often designated as "safety valves" (figure 1.3 A).

Bacterial MS channels were discovered by applying the patch clamp technique to giant *Escherichia coli* (*E. coli*) spheroplasts (Berrier et al., 1989; Martinac et al., 1987). Two channels in the inner *E. coli* membrane (Blount et al., 1996) were distinguished, the mechanosensitive channel of large conductance (MscL) with a conductance of ~3 nS and the mechanosensitive channel of small conductance (MscS) with a conductance of ~1 nS (Rasmussen and Rasmussen, 2018; Sukharev et al., 1993). This discovery gave rise to the hypothesis that the presence of different kinds of MS channels enables a graded response, depending on the severity of the osmotic shock. When either of the two is knocked out in *E. coli*, the cells still survive, suggesting that one can compensate for the other. While there is no known paralogue of MscL in *E. coli*, five more MscS paralogues were identified (Edwards et al., 2012; Levina et al., 1999; Li et al., 2002; Schumann et al., 2010), which differ in their gating properties, sizes, and abundances in the cell membrane (figure 1.3 B) (Edwards et al., 2012; Li et al., 2007, 2002; Schumann et al., 2010).

**MscL.** The first crystal structure obtained from MscL from *Mycobacterium tuberculosis* revealed a homopentamer with two TM helices per subunit, one contributing to the pore and the other being more exposed to the surrounding membrane (Chang et al., 1998; Steinbacher et al., 2007). Another helix of each subunit forms the cytoplasmic domain of MscL, and a fourth helix is amphipathic and lies on the cytoplasmic leaflet (figure 1.1 E), which is important for tension sensing (Bavi et al., 2017; N. Bavi et al., 2016; Iscla et al., 2008). Within the pore, MscL possesses a hydrophobic seal at the cytosolic side that almost completely occludes the channel (Steinbacher et al., 2007). MscL is non-selective and, upon activation by high membrane tension, opens iris-like and creates a pore of ~30 Å in diameter (Perozo et al., 2002a; Sukharev et al., 1999; Wang et al., 2014). Because of its large pore, MscL has been investigated as a promising candidate for nanotechnological approaches (Rasmussen and Rasmussen, 2018). Engineered MscL variants, manipulated to regulate gating in the absence of pressure, allowed the controlled delivery of drugs or other bioactive compounds. Gating was enabled by light- and pH switches (Koçer et al., 2006, 2005), as well as by charge-induced activation (Doerner et al., 2012).

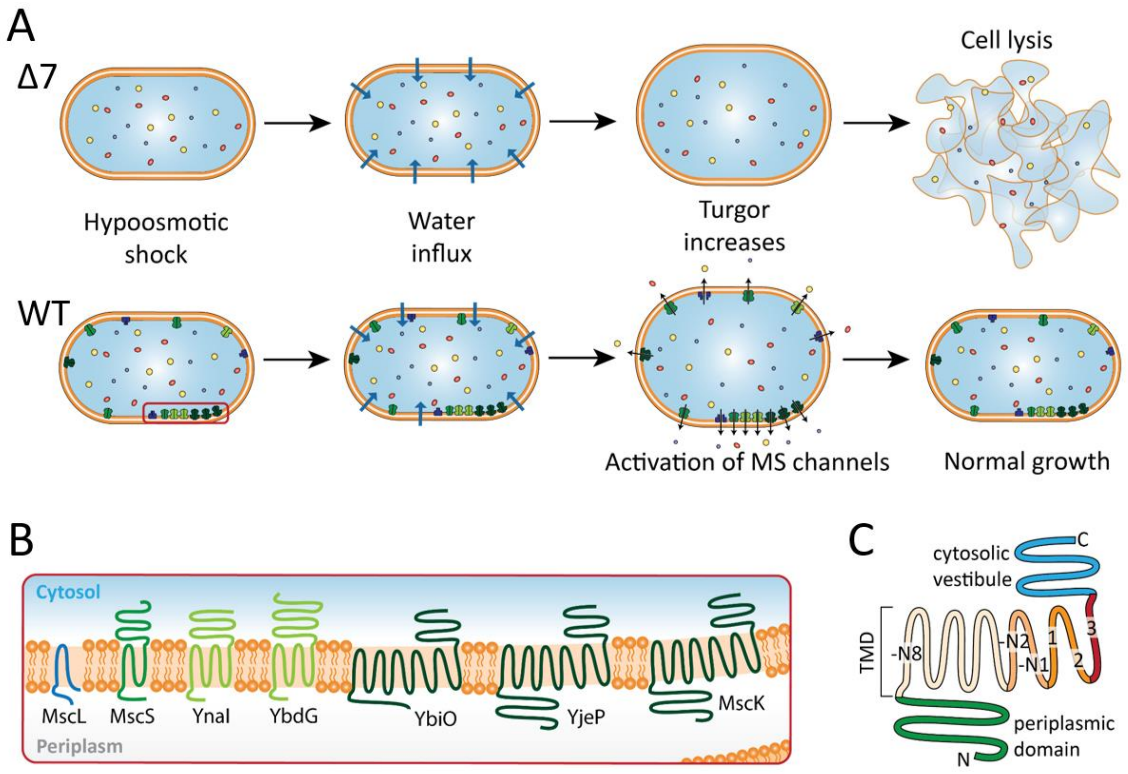


**Figure 1.3 | Functioning of MS channels in bacteria. (A)** MS channels are embedded in the inner membrane in wild-type (WT) *E. coli*. A hypoosmotic shock leads to the rapid entry of water (blue arrows) into the cell, and the pressure increases within the cell. This results in membrane tension that leads to the immediate activation of the MS channels. They release osmotically active substances to restore the turgor. Without functional MS channels (Δ7), the increased turgor will result in cell death. The designation Δ7 refers to an *E. coli* strain deficient in the seven genes for MS channels (Edwards et al., 2012) **(B)** The monomer topology of the MS channel family members is highlighted in the red box (A) is depicted. There are seven MS channels in *E. coli*, consisting of MscL (blue) and the MscS family (green shades). **(C)** The members of the MscS family have different domains: the cytosolic vestibule (blue), and different numbers of transmembrane spans, either three (MscS, orange), five (YnaI, YbdG, lighter orange) or eleven (YbiO, YjeP, MscK, very light orange). Following the MscS nomenclature, we name the additional helices TM-N1, TM-N2, … TM-N8 (-N for "minus N-terminal"). The larger paralogues also have an additional periplasmic domain (green). The N-terminus (N) and C-terminus (C) are marked.

**MscS.** Despite having a similar function, MscS differs structurally significantly from MscL. MscS assembles into a homoheptamer (Bass et al., 2002; Rasmussen and Rasmussen, 2018; Steinbacher et al., 2007) (figure 1.1 F) and is composed of two distinct domains: the TMD and the cytosolic vestibule (figure 1.3 C). Each subunit has three TM helices, of which the outer two are involved in sensing membrane tension, and the inner helix lines the pore and kinks outwards at the cytosolic side, connecting to the vestibule. MscS opens at lower membrane tensions and creates a pore of ~13 Å in diameter (Wang et al., 2008). The coordination of lipid

molecules plays a significant role in switching the conformational states of MscS (Zhang et al., 2021). MscS is portrayed in detail in chapter 1.2.

**MSL family.** Besides bacteria and archaea, MscS-like channels (MSLs) are present in plants. Responses to mechanical stimuli like touch, turgor pressure, or gravity are important for the development of plants and are linked to MS channels of different classes (Haswell, 2007). In *Arabidopsis thaliana* (*A. thaliana*), the channels MSL1-10 differ in their subcellular localisation and fulfil diverse functions: MSL1 in mitochondria and MSLs 2 and 3 in plastids are important for osmoregulation, while the remaining known MSLs occupy the plasma membrane (Wilson et al., 2013). Apart from their role in osmoregulation, more complex functions are suggested for the latter, e.g., controlling pollen hydration, germination, and tube growth (Hamilton et al., 2015), pathogen-triggered immunity (Z. Zhang et al., 2017), or even functions that are not related to pore formation and conductance (Veley et al., 2014). MSL10 from *Dionaea muscipula*, the Venus flytrap, is one of the channels highly specific to the trigger hair (Iosip et al., 2020).

## 1.2 The mechanosensitive channel of small conductance

### 1.2.1 Structure and function of MscS

**The overall architecture of closed MscS.** The archetypal *E. coli* MscS comprises 286 amino acids, and a first structure obtained by X-ray crystallography revealed the homoheptameric organisation of the complex with the sevenfold symmetry axis along the pore perpendicular to the membrane plane (Bass et al., 2002). The complex is divided into the cytosolic vestibule and the TMD (figure 1.4 A).

The vestibule encloses a chamber with varying diameters up to 40 Å (Bass et al., 2002; Steinbacher et al., 2007) and is comprised of a β domain, an αβ domain and a C-terminal β barrel. Multiple openings connect the vestibule to the cytosol: As the diameter of the narrow β barrel is only ~8 Å, the crystal structures hinted that access to the vestibule is via seven side portals – fenestrations at the interface of the β and αβ domains between adjacent subunits with diameters of ~8-14 Å. This pathway was also observed in molecular dynamics (MD) simulations (Sotomayor et al., 2006). A study comparing *E. coli* MscS with MscS from

*Thermoanaerobacter tengcongensis* (TtMscS), which has occluded side portals but a larger β barrel pore, also confirmed the suggestion that the entrance into the vestibule of *E. coli* MscS is the lateral portals (Zhang et al., 2012). Furthermore, it showed that the access into the vestibule is dependent on the organism: the entrance into the vestibule of TtMscS is via the β barrel, which is also responsible for its strong anion selectivity (Song et al., 2017; Zhang et al., 2012). These experiments also indicated that the weak anion selectivity of *E. coli* MscS shown previously in patch clamp experiments (Martinac et al., 1987; Sukharev, 2002) is determined in the vestibule (Zhang et al., 2012), which agrees with the observation that no pore residues are involved in ion selectivity (Edwards et al., 2008). Moreover, anion selectivity of *E. coli* MscS was linked to negatively charged residues near the portals, which interact with permeating cations (Cox et al., 2013). In addition to its role in gating and selectivity, the vestibule is essential for the stability and assembly of the homoheptamer (Rasmussen et al., 2007; Schumann et al., 2004).

The cytosolic vestibule is connected to the TMD via the helix TM3. Each subunit contributes one helix to the pore (helix TM3), divided by a kink at G113 (figure 1.4 F) into the amphipathic helix TM3b, which lies almost parallel to the membrane plane and connects to the vestibule, and the pore-forming helix TM3a. A distinct pattern of glycines and alanines in helix TM3a enables a close interaction of adjacent pore helices (figure 1.5 D) (Bass et al., 2002; Edwards et al., 2005). As the initially determined pore diameter was ~11 Å, this crystal structure was first deemed an open state because the experimental conductance of 1 nS would theoretically require a minimum pore diameter of only 8 Å (Bass et al., 2002; Sukharev, 2002). However, two hydrophobic sealing rings comprised of L105 and L109 are present at the cytosolic side of the pore (figure 1.4 A). MD simulations indicated that the pore is hydrophobic enough, and the sealing rings form a “vapour lock”, which keeps the channel closed (Anishkin et al., 2010; Anishkin and Sukharev, 2004; Rasmussen and Rasmussen, 2018). Consequently, the structure was reassessed to be closed, exhibiting a packing distance within the pore of only ~8 Å (Steinbacher et al., 2007). The helices TM3a are linked to a helix bundle (helices TM2 and TM1), which are designated as “sensor paddles”. The sensor paddles are tilted relative to the pore axis and thereby give the TMD an unusually tapered shape. Crystal structures were missing the ~20 ultimate N-terminal residues, and it was assumed that the pore of MscS is wholly embedded in the membrane plane (Sotomayor et al., 2006; Sotomayor and Schulten, 2004). However, quenching of tryptophan fluorescence of MscS mutants with brominated lipids (Rasmussen et al., 2019b) as well as the first cryo-EM structures of MscS in a membrane environment (Rasmussen et al., 2019a; Reddy et al., 2019) changed the view on the membrane

footprint of MscS, confirming that only the periplasmic half of the TMD is embedded in the bilayer. Moreover, only a part of the pore is in the plane of the cytosolic leaflet, while the other half of the pore is outside of the membrane plane (figure 1.4 A). The cryo-EM structures of MscS further revealed density N-terminally to helix TM1. One study suggested an amphipathic helix in this region that lies on the periplasmic leaflet and is important for mechanotransduction (Reddy et al., 2019), yet the formation of a helix is arguable. Nonetheless, a conserved W16 on the periplasmic side of helix TM1 is sensitive to mutagenesis concerning gating (Rasmussen et al., 2007), and because tryptophan residues often fulfil a role as anchoring residues (Killian and Von Heijne, 2000), this domain is termed anchor domain.

The five MscS paralogues were also shown to be heptamers (Edwards et al., 2012; Schumann et al., 2010) but exhibit either two (YnaI, YbdG) or eight (YbiO, YjeP, MscK) additional TM helices per subunit (Naismith and Booth, 2012) (figure 1.3 B, C). Moreover, the three large paralogues have an additional periplasmic domain, which is predicted to form a helical bundle arranged in a coiled-coil structure (Pivetti et al., 2003).

**Figure 1.4 | Structures of MscS. (A)** A cryo-EM structure of MscS in its closed conformation (PDB 6RLD (Rasmussen et al., 2019a)) is coloured by its domains: the cytosolic vestibule (blue), and the TMD, consisting of pore helices TM3a and TM3b (red/pink), sensor paddle helices TM1 and TM2 (orange/pale yellow), and periplasmic anchor domain (green). The side view is shown at the top, and the view along the symmetry axis from the periplasmic side is displayed at the bottom. The sealing ring residues L105 and L109 are depicted as spheres with Van der Waals radii. One subunit is coloured darker. The brown lines indicate the position of the membrane, and domains and pockets and portals are labelled. All other crystal- and cryo-EM structures of closed MscS resemble this architecture. The structures in (B)-(D) are depicted in the same orientation and colour code used for (A). **(B)** The crystal structure of MscS shows its open conformation from the side (top) and top (bottom) (PDB 5AJI (Pliotas et al., 2015)). Other open structures obtained for MscS are highly similar to this structure. **(C)** The cryo-EM structure of MscS in a sub-conducting state was captured in a lipid environment with short-chain lipids (PDB 6VYL (Zhang et al., 2021)). **(D)** The cryo-EM structure shows MscS in an inactivated state (PDB 6VYM (Zhang et al., 2021)). **(E)** The density map of closed MscS, shown in white, was gaussian-filtered for clarity (EMDB 4919 (Rasmussen et al., 2019a)) and is shown from the side (top) and top (bottom). Lipid densities and atomic lipid models are shown in yellow. The acyl chains and their corresponding densities (brown) in the pore, visible in the top view (bottom), are taken from another structure and map (PDB 6PWN and EMDB 20508 (Reddy et al., 2019)) and are fitted into the main map. **(F)** Relevant and explicitly mentioned residues are highlighted in the TMD of one monomer (white). The sealing ring residues L105 and L109 are coloured grey, the kink region at G113 observed in structures, and the hypothesised alternative kink region at G121 are depicted in orange, the residue A106, which leads to an open conformation when mutated to valine, is shown in red, residues involved in lipid coordination are blue, the anchoring W16 is depicted in green, and the residues G101 and A102, which eliminate adaptation upon mutation, are shown in pink.

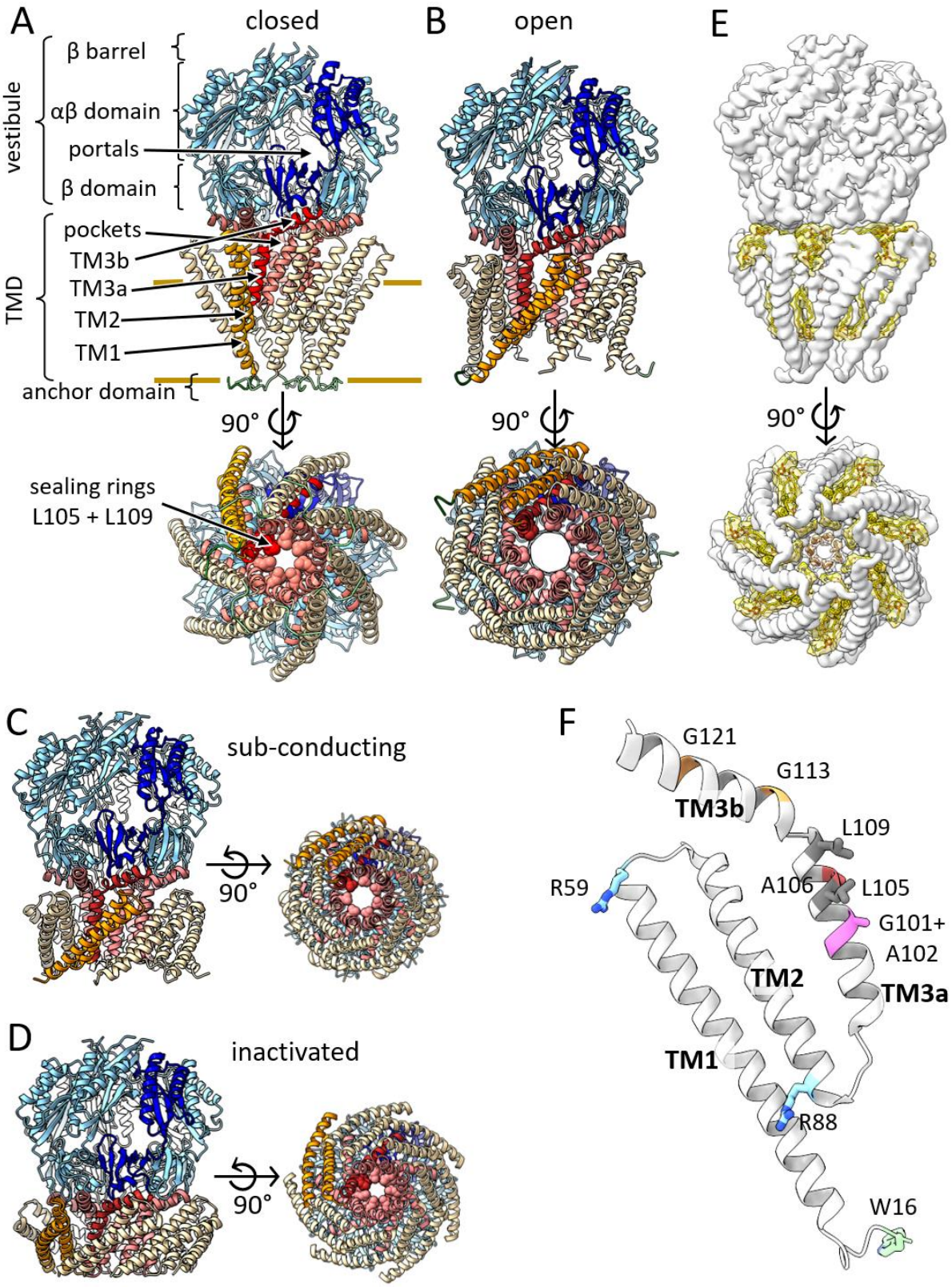
A
closed
B
open
E
β barrel
αβ domain
portals
β domain
vestibule
pockets
TM3b
TM3a
TM2
TM1
TMD
anchor domain
90°
sealing rings
L105 + L109
C
sub-conducting
D
inactivated
F
G121
G113
TM3b
L109
R59
A106
L105
G101+
A102
TM2
TM3a
TM1
R88
W16

**The open conformation of MscS.** The first structure of an open conformation of MscS was obtained from the A106V mutant of *E. coli* MscS (Wang et al., 2008). This residue is located between the two sealing residues in the pore, and the larger side chain of valine compared to alanine perturbs the tight interface between neighbouring helices and traps MscS in an open conformation. No changes are observed in the vestibule compared to the closed structure, but remarkable rearrangements occur in the TMD. The helices TM1 and TM2 rotate as a rigid body by ~45° clockwise and tilt by ~15° to the pore axis, which results in an overall flatter appearance of the TMD and a larger membrane cross-section at the periplasmic side (figure 1.4 B, figure 1.5 A, B). The helix TM3a rotates by ~15° clockwise around its helical axis and pivots around the kink residue G113. Helix TM3b merely changes compared to the closed state. Through rotation of the TM3a helix, the sealing residues L105 and L109 are withdrawn from the pore axis, which breaks the vapour lock. In addition to the rotation, the TM3a helix also shifts out of the centre. It moves more with its N-terminal end than with its C-terminal end, and as a result, the TM3 helices in the open state are parallel to each other and the pore axis and not diagonal to it like in the closed form (figure 1.5 C). The conserved glycine-alanine pattern makes the TM3a helices interact like a gear (figure 1.5 D), and perturbation of this critical interface leads to channels that are more difficult to gate (Blount and Iscla, 2020; Edwards et al., 2005). Additional to the point mutation in the pore, detergents influence the conformational state of MscS. Purifications of MscS not harbouring the A106V mutation with the detergent Fos-choline-14 (Bass et al., 2002) and Triton X-100 (Angiulli et al., 2020) produced a closed structure and, particularly interesting, the purification of MscS with the detergent n-dodecyl-β-D-maltopyranoside (DDM) resulted either in an open conformation (Lai et al., 2013; Pliotas et al., 2015, 2012) or a closed one (Lai et al., 2013; Rasmussen et al., 2019a; Reddy et al., 2019; Zhang et al., 2012). Further preparations also resulted in the closed or open conformations seen in the first crystal structures (Bass et al., 2002; Wang et al., 2008).

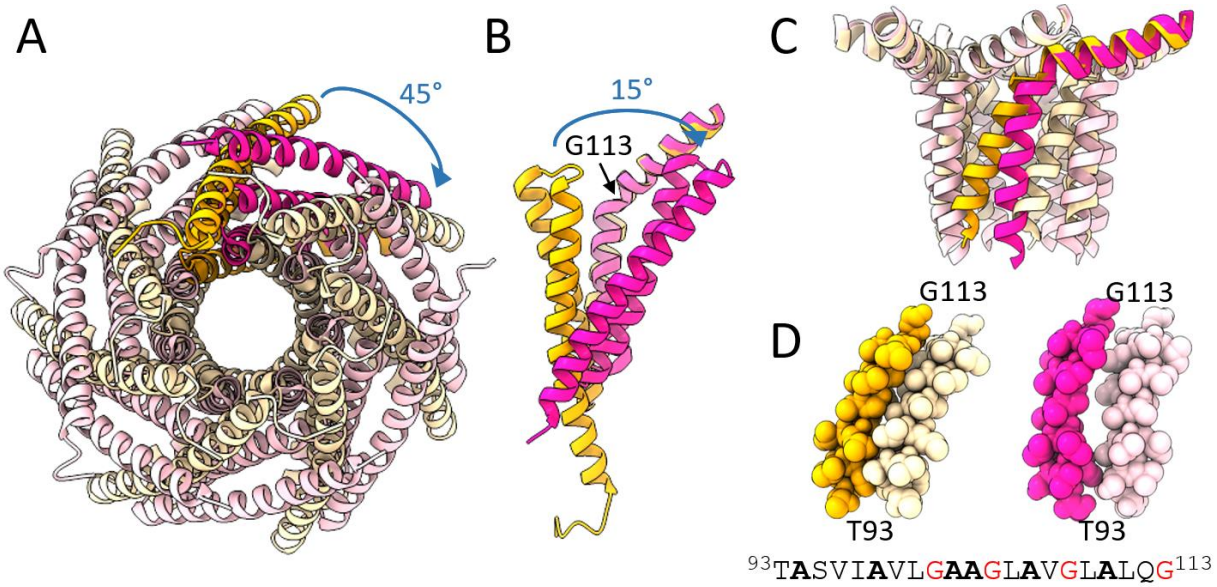


**Figure 1.5 | The opening transition of MscS.** MscS is shown in its closed (orange; PDB ID 6RLD (Rasmussen et al., 2019a)) and open (pink; PDB 5AJI (Pliotas et al., 2015)) conformation. One subunit is highlighted in darker colours. **(A)** The TMD is viewed from the periplasmic side, showing that the sensor paddles rotate as rigid bodies by ~45° clockwise (blue arrow), accompanied by a widening of the pore. **(B)** One subunit of each state is shown. The sensor paddles tilt by ~15° to the pore axis (blue arrow). The pore helices pivot around G113. **(C)** The pore helices TM3a in the closed state are diagonal with respect to the pore axis and are almost parallel to the pore axis in the open state. Hardly any change is observed in the TM3b helices. **(D)** The atoms of the TM3a helices of two adjacent subunits are shown as van der Waals radii. The tight helix-helix interface in the closed conformation is enabled by a "knobs-into-holes" conformation (Edwards et al., 2005), and gaps between the TM3a helices appear in the open state. The sequence of helix TM3a is given below, with alanines highlighted in bold black and glycines in red.

**Additional functional states and proposed gating mechanisms.** In electrophysiological experiments, open MscS channels will transition to a non-conducting state after sustained sub-saturating pressure to membrane patches. This behaviour is termed adaptation (Koprowski and Kubalski, 1998; Levina et al., 1999) and is the result of two processes: desensitisation and inactivation (Akitake et al., 2007). Desensitised channels can be directly reopened by applying a greater pressure stimulus (Akitake et al., 2007), while inactivated channels can only be activated again after a resting time of several minutes (Koprowski and Kubalski, 1998) in the absence of pressure. The molecular basis for adaptation was elusive for a long time and the subject of a controversial debate.

Extrapolated-motion dynamics simulations suggested that the TMD of the closed conformation would be more compact, and the alignment of paddle helices to pore helices acts like a dashpot that allows the differentiation between a slow and a fast hypoosmotic shock (dashpot model, figure 1.6) (Akitake et al., 2005). To allow for this compact architecture, the kink separating

the helices TM3a and TM3b would be at position G121 instead of G113. Electrophysiological experiments of channels with mutations in the two possible hinge regions supported this model (Akitake et al., 2007; Anishkin et al., 2008b, 2008a). The results suggested that the closed and desensitised conformations rely on the kink at G121, while the kink at G113, as observed in the crystal structures (Bass et al., 2002; Lai et al., 2013; Zhang et al., 2012), is a characteristic of the inactivated state. Independently, it was shown that mutations in the pore profoundly affect the ability of MscS to adapt; especially mutation of G113 impedes adaptation (Edwards et al., 2008). Nevertheless, the mutations G101D and A102P, located in the region unaffected by the kinking of the TM3 helix (figure 1.4 F), eliminate adaptation of MscS, which does not support the dashpot model. Furthermore, no structural data supports this model.

Another closed conformation of MscS was obtained by combining electron paramagnetic resonance (EPR) and spin labelling (Vásquez et al., 2008b, 2008a). This approach allows to judge whether spin-labelled positions are exposed to solvent or the membrane (Perozo et al., 2001, 1998), and the data was used to refine the closed crystal structure of MscS. The resulting structure was more compact than the closed crystal structure (Bass et al., 2002) but retained the kink at G113. MD simulations based on the EPR structure were carried out, and another gating model for MscS was deduced (Malcolm et al., 2015, 2011; Malcolm and Maurer, 2012). This model hypothesises that the intrinsic pressure of the lipid bilayer keeps MscS in a closed conformation, and application of extrinsic tension results in the relief of the intrinsic pressure and, thus, leads to channel opening, reminiscent of a Jack-in-the-box (Jack-in-the-box model, figure 1.6). In this model, the mutation A106V would prevent adaptation and consequently result in an open structure. According to this model, MscS should likely always be in an open conformation without a membranous environment, which does not apply to closed states of MscS observed in detergent micelles (Lai et al., 2013; Reddy et al., 2019).

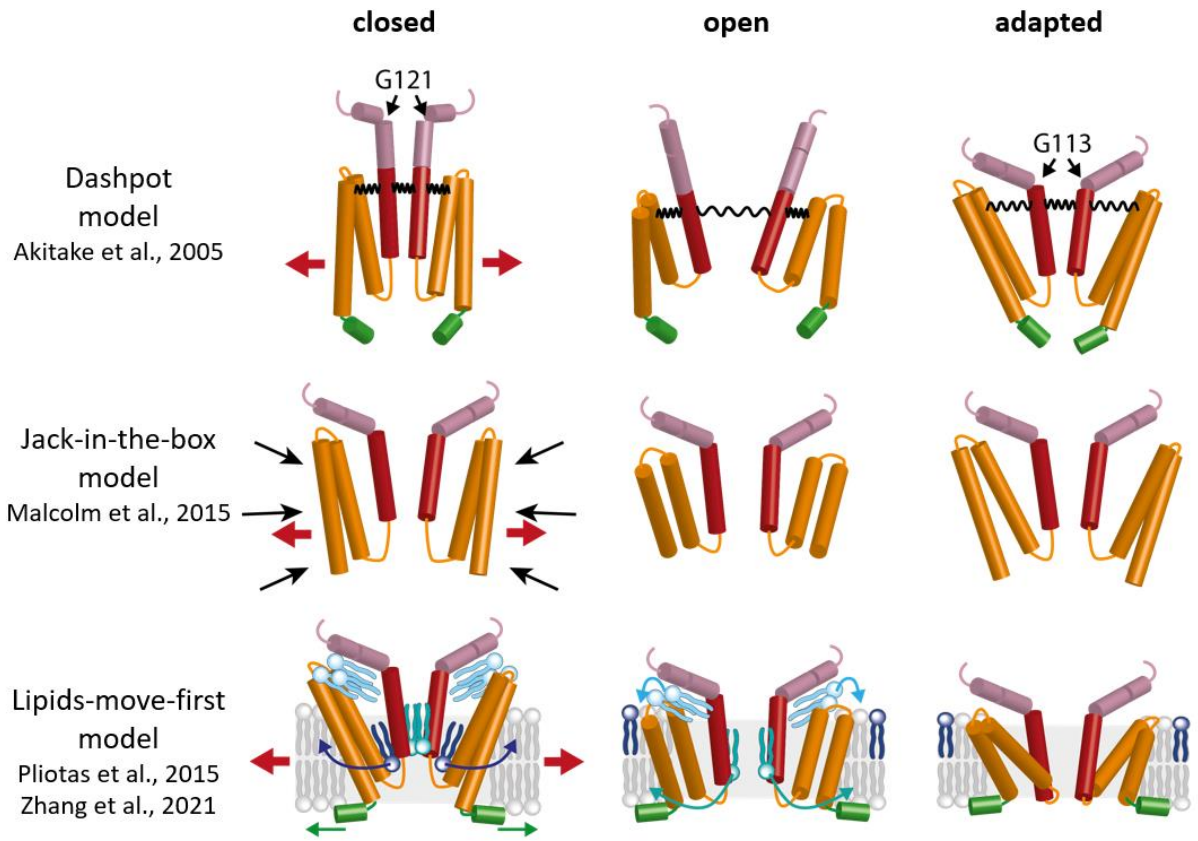


**Figure 1.6 | Gating models of MscS.** The models show the TMD of MscS. The helix TM3b is coloured in pink, helix TM3b in red, sensor paddle helices TM1 and TM2 in orange, and the anchor domain in green. For clarity, only two opposing subunits are represented. All models suggest a different closed conformation. The dashpot model and the Jack-in-the-box model present the closed from observed in the first crystal structure of MscS (Bass et al., 2002) as an adapted state. The dashpot model is based on extrapolated-motion dynamics simulations and suggests a dashpot mechanism between the sensor paddle- and pore helices (indicated as black springs), which allows the helices to collapse into the closed conformation. The Jack-in-the-box model was deduced from EPR and spin-labelling and subsequent MD simulations, suggesting that the intrinsic bilayer tension (black arrows) keeps MscS compressed in its closed conformation. Application of extrinsic tension leads to relief of the intrinsic tension and triggers gating. The lipids-move-first model, based on cryo-EM structures (Zhang et al., 2021), sees functional lipids as determinants for conformational switching. Upon tension, the gatekeeper lipid (blue) dissociates into the cytosolic leaflet. Pore lipids (turquoise) block the channel in the closed form, move to the periphery of the pore in the open state and finally leave the pore. The pocket lipids (light blue) leave the pockets progressively, driving MscS finally in an adapted state.

The competing gating models were challenged by pulsed electron-electron double resonance (PELDOR) studies. PELDOR allows to measure the distances between artificially introduced spin labels. The distances for DDM-solubilised MscS were in agreement with the open crystal structure (Pliotas et al., 2012), while the distances for MscS in membrane mimetics supported the closed crystal structure (Ward et al., 2014). Moreover, the first cryo-EM structures of MscS (Rasmussen et al., 2019a; Reddy et al., 2019) were obtained from MscS embedded in

nanodiscs, which provide a lipidic and therefore more native environment and, thus, a more native orientation of the pore helices. The cryo-EM structures depict the conformation observed in the first crystal structure (Bass et al., 2002), which stresses its legitimacy.
Additionally, with the availability of the first open crystal structure, it was hypothesised that adaptation is the consequence of mismatching the gear-like glycine and alanine residues between adjacent TM3a helices upon closing (figure 1.5 D) (Wang et al., 2008). Another possible mechanism for adaptation is based on lipid penetration of the pore (Zhang et al., 2016). However, a cryo-EM structure of an adapted state was recently obtained by Zhang et al. (Zhang et al., 2021) by developing a novel approach to imitate membrane tension within bilayer-providing nanodiscs. Lipid removal from the nanodiscs with β-cyclodextrin (βCD) creates a tension that enabled the observation of not only the open but also an adapted (inactivated) state (denoted as desensitised in Zhang et al.) by cryo-EM analysis (figure 1.4 D). This structure exhibits a substantial rearrangement of the paddle helices: The helices rotate clockwise (viewed from the periplasmic side) and the tilt angle of TM1 to the membrane normal increases to 67 ° compared to only 32 ° for the closed state, which results in a flat appearance of the TMD. This state is linked to depletion of associated lipids (lipids-move-first model, figure 1.6). The structure corresponds to the inactivated state, as a control with the mutant G113A, which prevents inactivation (Akitake et al., 2007; Edwards et al., 2008), did not adopt this novel conformation. The open conformation revealed a smeared-out density in the cryo-EM reconstruction, leading to a dynamic membrane domain interpretation in the open conformation. Furthermore, the use of short-chain lipids resulted in a sub-conducting state (figure 1.4 C), showing that hydrophobic mismatch alone is not sufficient to open MscS. Lipid extrusion plays the central role in this model, as it not only initiates gating but is also the basis for further conformational states.

### 1.2.2 Membrane-protein interactions

**Associated lipids in MscS.** The arrangement of the helices TM3a and TM3b and the sensor paddles creates pockets between adjacent subunits (figure 1.4 A). Aliphatic chains in these pockets were first identified in an open structure of MscS, and the presence of lipids was additionally indicated by native mass spectrometry and spectroscopic data (Pliotas et al., 2015; Rasmussen et al., 2019b). Cryo-EM structures revealed the membrane position and showed that the sensor paddles protrude into the cytosol (Rasmussen et al., 2019a; Reddy et al., 2019)

and interact with lipids beyond the membrane bilayer (figure 1.4 E). MD simulations further suggested that fewer lipids populate the complex in the open conformation (Pliotas et al., 2015), giving rise to the hypothesis that the extrusion of lipids from the pockets at increased tension triggers gating (lipids-move-first model, figure 1.6). Lipids can move through grooves between adjacent sensor paddles into the pockets because these grooves provide a sufficiently hydrophobic environment (Rasmussen et al., 2019a). Moreover, the first cryo-EM structure of MscS (Rasmussen et al., 2019a) in a closed conformation resolved three lipid molecules per subunit: two in the pockets, parallel to helix TM3b, and one in the grooves between two sensor paddles (figure 1.4 E). R59 (figure 1.4 F) coordinates one lipid in the pocket through a salt bridge, underpinned by the strong gain-of-function (GOF) phenotype of the mutant R59L (Rasmussen et al., 2019b). This phenotype agrees with the lipids-move-first model because this lipid should be easier to remove and thus facilitate gating by disrupting the salt bridge. Fluorescence quenching applied to tryptophan mutants of hydrophobic residues lining the proposed pockets showed strong quenching when incubated with brominated lipids (Pliotas et al., 2015). Particularly interesting is a lipid resolved at the periplasmic loop between the helices TM2 and TM3a, coordinated by R88 (figure 1.4 F). Because of its shape, it was termed “hook lipid” (Reddy et al., 2019) and later on, “gatekeeper lipid” (Zhang et al., 2021) because it was hypothesised to initiate the gating transition (lipids-move-first model, figure 1.6). The mutants R88W and R88S resulted in loss-of-function (LOF) phenotypes that are more difficult to activate (Edwards et al., 2008; Rasmussen et al., 2010), supporting that this lipid must be important for gating. However, its role in gating is a matter of discussion.

**The force-from-lipids principle.** Upon hypoosmotic shock, MS channels do not sense the increased turgor in the cell but the resulting membrane tension (Moe and Blount, 2005; Sokabe et al., 1991). Solubilised, purified and reconstituted channels retain their mechanosensitivity; hence, no additional proteins or cofactors are required for sensing, and the driving force for gating must be provided by the surrounding membrane (Sukharev, 2002; Sukharev et al., 1993). A biological membrane consists of two lipid leaflets, where the fatty acid tails face each other. One consequence of the self-assembly of lipid molecules into the bilayer is the pressure heterogeneity across the membrane, which is described by the anisotropic transbilayer pressure profile (figure 1.7 A) (Cantor, 1997; Chandler, 2005; Martinac et al., 2018). There is repulsion between the headgroups of two adjacent lipids and between the lipid tails and attraction between the glycerol groups. Hence, tension is highest at the onset of the lipid tails, and this region must be important for tension sensing (Cantor, 1997; Ridone et al., 2018). According to

the force-from-lipids principle, the anisotropic forces of the bilayer and their changes trigger the structural rearrangements for channel gating (Martinac et al., 1990). In a tensed membrane, the open conformation with a larger membrane cross-section is energetically more favourable. A simple area expansion can provide the energy for the conformational changes, given by $\Delta G = \vec{\sigma}\Delta A$, where $\vec{\sigma}$ is the membrane tension for channel opening and ΔA is the difference in the cross-sectional area between the open and closed state.

Nevertheless, other implementations of the force-from-lipids principle must be considered. Upon tension, the membrane stretches and becomes thinner. The extent of hydrophobic mismatch between the membrane-facing region of the MS channel and the bilayer can influence MS channel gating (figure 1.7 B) (Martinac et al., 2018; Martinac and Cox, 2017). A hydrophobic mismatch was shown to be important for gating MscL (Nomura et al., 2012; Perozo et al., 2002a), but not sufficient to fully open MscS under physiological conditions, as the reconstitution of MscS into a bilayer comprising short-chain lipids resulted in only a sub-conducting state (Zhang et al., 2021). Furthermore, a change in local membrane curvature can induce channel gating (Yoo and Cui, 2009). The cone-shaped TMD of MscS would not be well compatible with a flat membrane, and MD simulations suggested that it induces local membrane bending (Phillips et al., 2009; Pliotas et al., 2015; Sotomayor and Schulten, 2004). As the TMD of the open MscS conformation is less cone-shaped, a less pronounced membrane curvature – which would be the case in a tensed membrane – would favour this conformation (figure 1.7 C). The cryo-EM structures of MscS in nanodiscs (Rasmussen et al., 2019a; Reddy et al., 2019; Zhang et al., 2021), providing a membrane environment, did not show signs of membrane curvature, but this might as well be attributed to the limited size of the nanodiscs. Another alternative model focuses on amphipathic helices that sit parallel to the membrane plane on one bilayer leaflet and are a common structural feature of MS channels. Such helices have, for example, been discovered in members of the K2P family TRAAK and TREK (Brohawn et al., 2014a; Dong et al., 2015; Lolicato et al., 2014), in PIEZO channels (Saotome et al., 2017; Wang et al., 2019; Zhao et al., 2018), and the plant channel OSCA1.2 (Jojoa-Cruz et al., 2018; Liu et al., 2018; Maity et al., 2019; Zhang et al., 2018). One study suggested that the N-terminal anchor domain of MscS forms an amphipathic helix that lies on the periplasmic leaflet (Reddy et al., 2019), but so far, convincing evidence is missing. In MscL, the N-terminal domain is an amphipathic helix, too, and its role was investigated in great detail (N. Bavi et al., 2016; Iscla et al., 2008). It interacts tightly with lipids of the cytosolic leaflet, and these lipid interactions are maintained under tension. As a result, the movement of the lipids actively drags the N-terminal amphipathic helices apart, which transmits the force to the pore helices and

drive gating (figure 1.7 B) (Bavi et al., 2017). It should be noted that multiple implementations of the force-from-lipid principle can contribute to the tension sensing mechanism of one channel.

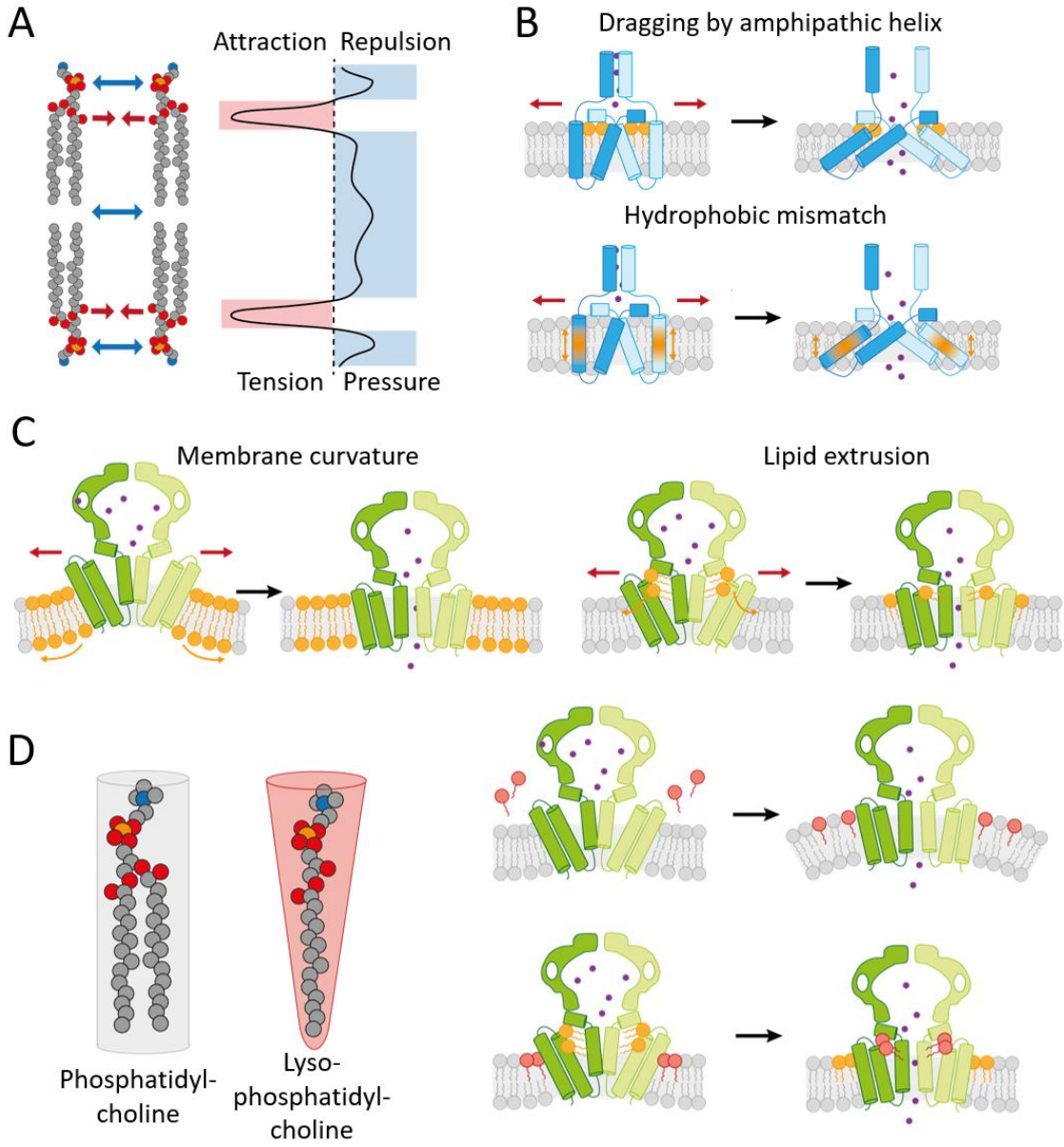


**Figure 1.7 | The force-from-lipids principle. (A)** Attraction and repulsion events between adjacent lipid molecules lead to an anisotropic transbilayer profile. The force-from-lipid principle states that changes in the bilayer and the resulting changes in this profile drive structural reorganisations of embedded proteins. **(B)-(D)** For clarity, only two subunits of MscL (light blue and dark blue) and for MscS (light green and dark green) are shown, respectively. The surrounding bilayer is depicted in grey. Regions crucial for the underlying mechanism are highlighted in orange. Red arrows represent the applied tension, and purple dots represent osmolytes. **(B)** The dragging model and hydrophobic mismatch model are involved in the gating of MscL. **(C)** Local membrane curvature and lipid extrusion from pockets play a role in MscS. **(D)** Lysophosphatidylcholine is cone-shaped (red) compared to cylindrical-shaped phosphatidylcholine (grey) (left). It can activate MscS either by enforcing membrane tension (upper right) or entering the pockets of MscS (lower right).

**MS channel activation by amphipaths.** Modulation of the transbilayer pressure profile can also be accomplished by doping the membrane with certain amphipathic molecules (Maingret et al., 2000; Martinac et al., 1990; Perozo et al., 2002b). One of the best-studied amphipaths is the cone-shaped, single-tailed lipid lysophosphatidylcholine (LPC) (figure 1.7 D). LPC can activate MscL and MscS (Perozo et al., 2002a, 2002b; Vásquez et al., 2008a), which was first contributed to its membrane curvature inducing properties (Yoo and Cui, 2009). This hypothesis was refuted later, indicating that LPC can directly create bilayer tension (Nomura et al., 2012; Pliotas et al., 2015). The lipid accessibility of the pockets in MscS provides an alternative activation mechanism of LPC: It was proposed that LPC molecules can migrate from preferably the cytosolic leaflet into the pockets and displace ordinary lipid molecules, destabilising the closed conformation because of its smaller hydrophobic volume (Pliotas et al., 2015). Whichever mechanism – the distortion of the surrounding membrane or specific interactions with the protein – is responsible for the activating effect of LPC on MS channels cannot be assessed from the current point of view.

### 1.2.3 Preliminary studies on YnaI

Additional to MscL and MscS, "mini conductance" activities were described in 1997 (Sukharev et al., 1997). YnaI was identified as one contributor to this novel conductance and functionally characterised in 2012. The generation of a "Δ7" strain (MJF641), lacking all seven genes for MS channels, enabled the individual electrophysiological characterisation and showed a unique single-channel conductance of ~0.1 nS. YnaI, a homoheptamer with 343 amino acids per subunit, can be stably expressed and purified with yields comparable to MscS (Edwards et al., 2012). The first glimpse at its structure was provided by a 13 Å cryo-EM map in 2015 (Böttcher et al., 2015) (figure 1.8 A). It revealed a conserved shape of the vestibule and a larger membrane domain than MscS, owing to its two additional TM helices per subunit (Naismith and Booth, 2012), which are probably also tilted like in MscS. Pockets between the paddle and pore helices similar to MscS were identified.

Fluorescence quenching showed that these pockets are, as in MscS, accessible to lipids (Böttcher et al., 2015), affirming that the two additional TM helices do not shield the pockets from lipids. The arrangement of the additional helices would imply that a local membrane curvature, which would better fit the tapered shape of the TMD, as well as the role of associated lipids, are conserved in YnaI and contribute to tension sensing as indicated for MscS (Böttcher

et al., 2015). A second cryo-EM structure only resolved the helices TM2 and TM3 (MscS nomenclature) of the TMD (figure 1.8 A), already hinting at a high degree of flexibility in this domain (Yu et al., 2018). Mutagenesis experiments and electrophysiology revealed that M158 in the pore helix, pointing toward the pore axis (figure 1.8 B), is responsible for potassium/sodium selectivity and that the presence of different anions highly affects the ion affinity and transmittance. M158 constitutes the narrowest region of the pore, and the mutation M158A results in a substantially higher conductance. In contrast, it was suggested that because of the overall negative surface potential inside the vestibule of YnaI, cations would be trapped there, and an anion selectivity should be the consequence (Hu et al., 2021).

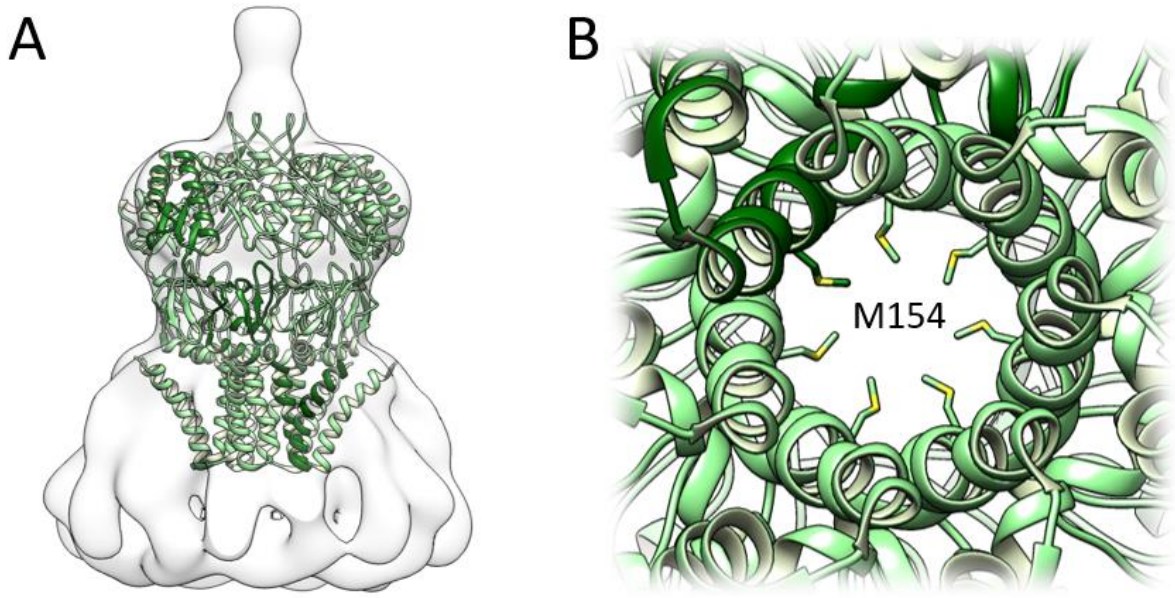


**Figure 1.8 | First structural studies on YnaI. (A)** The first model of YnaI (green, one subunit coloured darker), showing only the helices TM2 and TM3 of the TMD (PDB 5Y4O (Yu et al., 2018)) was fitted into the first cryo-EM map (white; EMDB 3035 (Böttcher et al., 2015)), showing a shape of the vestibule reminiscent to that of MscS. **(B)** M158 is shown in the pore of YnaI viewed from the periplasmic side.

## 1.3 Strategies for membrane protein purification

The structural and functional characterisation of MS channels requires the preceding isolation and purification of those. Therefore, the characteristics and peculiarities of membrane proteins must be taken into account. Up to one-third of the proteome in most genomes are predicted to be integral membrane proteins (Wallin and von Heijne, 1998), yet only a proportionally small fraction of all protein studies tackle their functional and structural characterisation. Reasons for this are technical challenges related to expression and purification and obtaining a stable, active protein. There are two structural classes of membrane proteins: β barrel membrane proteins and helical bundle membrane proteins (von Heijne, 1999). While the former often can be purified from inclusion bodies, this approach is rarely successful for the latter (Bannwarth and Schulz, 2003; Kiefer, 2003). Because of its usually low natural abundance, the desired membrane protein cannot be readily obtained in sufficient amounts and thus must be overexpressed. Subsequently, as membrane proteins are embedded in a complex lipid environment and are not soluble in aqueous solutions, they must be extracted from the membrane into a system that satisfies their hydrophobicity and renders them water-soluble and as well meets the needs of the subsequent studies (figure 1.9) (S. C. Lee et al., 2016).

**Figure 1.9 | Schematic overview of various single-particle approaches for membrane proteins.** A membrane protein (brown rods) in its native environment (grey lipids) can directly be extracted using SMA- or DIBMA copolymer (yellow). However, conventionally a membrane protein is extracted with classic detergents (red) that can subsequently be substituted by amphipols (black) or peptidisc peptides (blue). Alternatively, it can be reconstituted into a membrane-mimicking system with an artificial lipid composition (light brown), like membrane scaffold protein (MSP) (green) nanodiscs, the Salipro system using saposin (purple) or bicelles, which are small bilayer patches stabilised by special detergents (pink).

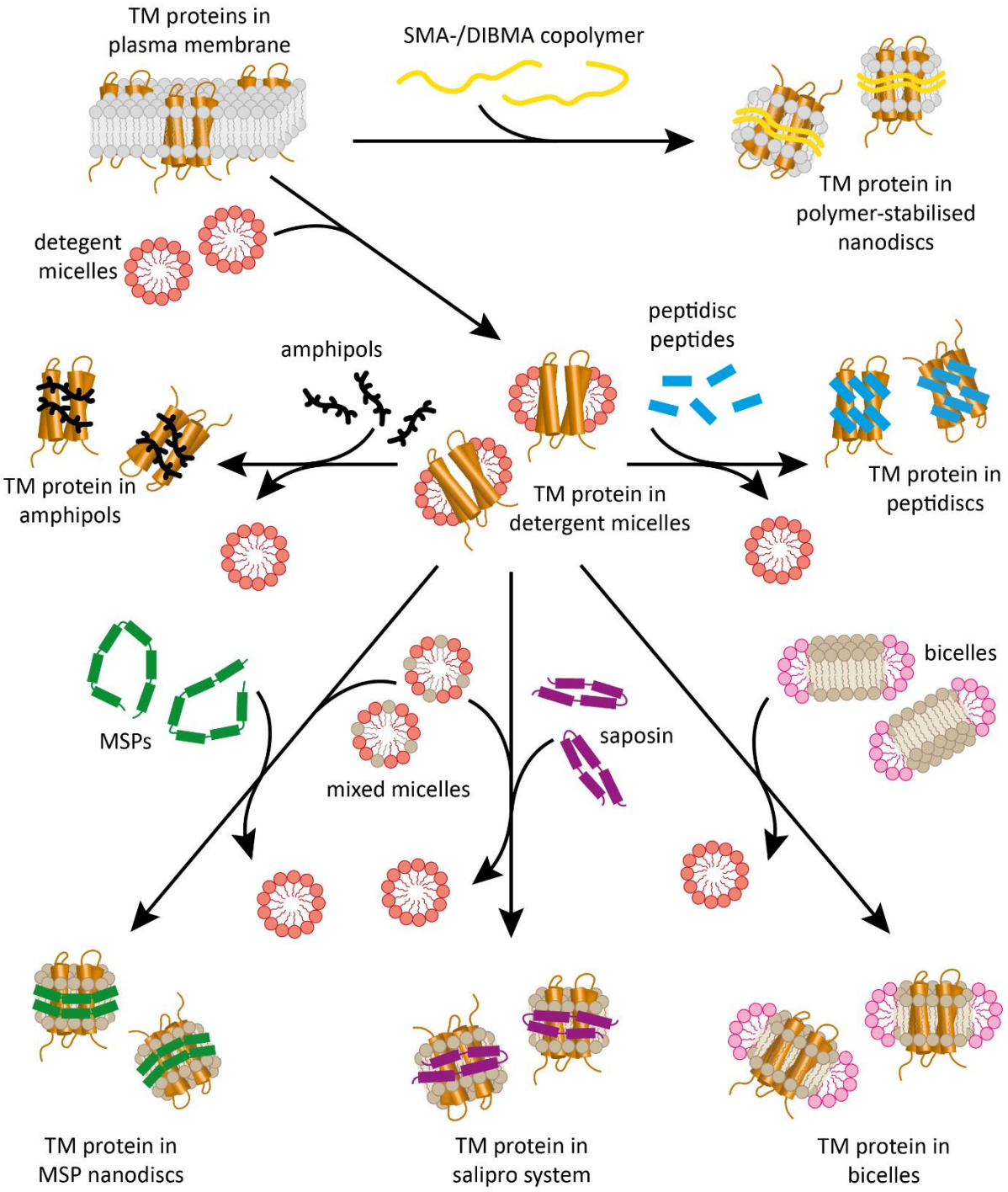
TM proteins in plasma membrane
SMA-/DIBMA copolymer
TM protein in polymer-stabilised nanodiscs
detegent micelles
peptidisc peptides
amphipols
TM protein in amphipols
TM protein in detergent micelles
TM protein in peptidiscs
MSPs
mixed micelles
saposin
bicelles
TM protein in MSP nanodiscs
TM protein in salipro system
TM protein in bicelles

### 1.3.1 Detergents

The conventional method to extract membrane proteins from their bilayer environment is the use of classic detergents. Detergents are amphipathic molecules that interact with the membrane protein via their hydrophobic part and provide water-solubility with their hydrophilic headgroup (figure 1.9) (Chipot et al., 2018; Seddon et al., 2004; Skrzypek et al., 2018). When used at or above their critical micellar concentration (CMC), the detergent molecules begin to self-organise in micelles and accumulate in the membrane. Consequently, the membrane breaks apart, generating protein-(lipid)-detergent complexes (Le Maire et al., 2000). Detergents can be classified based on their structure into ionic, non-ionic and zwitterionic detergents. Ionic detergents, like the anionic sodium-dodecyl sulfate (SDS), are typically harsh. They solubilise membrane proteins very effectively, but as they can additionally disrupt protein-protein interactions, they tend to destabilise membrane proteins. Non-ionic detergents are milder as they do not disrupt intra-protein interactions and are therefore preferred (Skrzypek et al., 2018). The most used detergent is DDM (figure 1.10), probably because it balances efficient solubilisation and preserves the native protein state very well (Stetsenko and Guskov, 2017). It is considered a mild detergent, stabilising a plethora of membrane proteins (Kotov et al., 2019), and its main disadvantage is that it forms a relatively large micelle (~70 kDa) (Slotboom et al., 2008), which can interfere with downstream applications. Another non-ionic detergent, lauryl maltose neopentyl glycol (LMNG), is gaining increasing attention for membrane protein studies (figure 1.10). Maltose neopentyl glycols have a stabilising effect on different membrane proteins, as their branched design is supposed to limit the conformational flexibility of the protein (Chae et al., 2010, 2008). The features of zwitterionic detergents lie between those of ionic and non-ionic detergents.

Though many membrane proteins have been studied using various detergents, it must be noted that micelles do not represent a lipid bilayer (Skrzypek et al., 2018). Membrane proteins are closely associated with their surrounding membrane, and their function is often dependent on their lipidic environment. Stripping the protein of these intimate interactions can be detrimental to protein stability and activity (Alemany et al., 2007; Gohon and Popot, 2003; Lee, 2005; Yang et al., 2014).

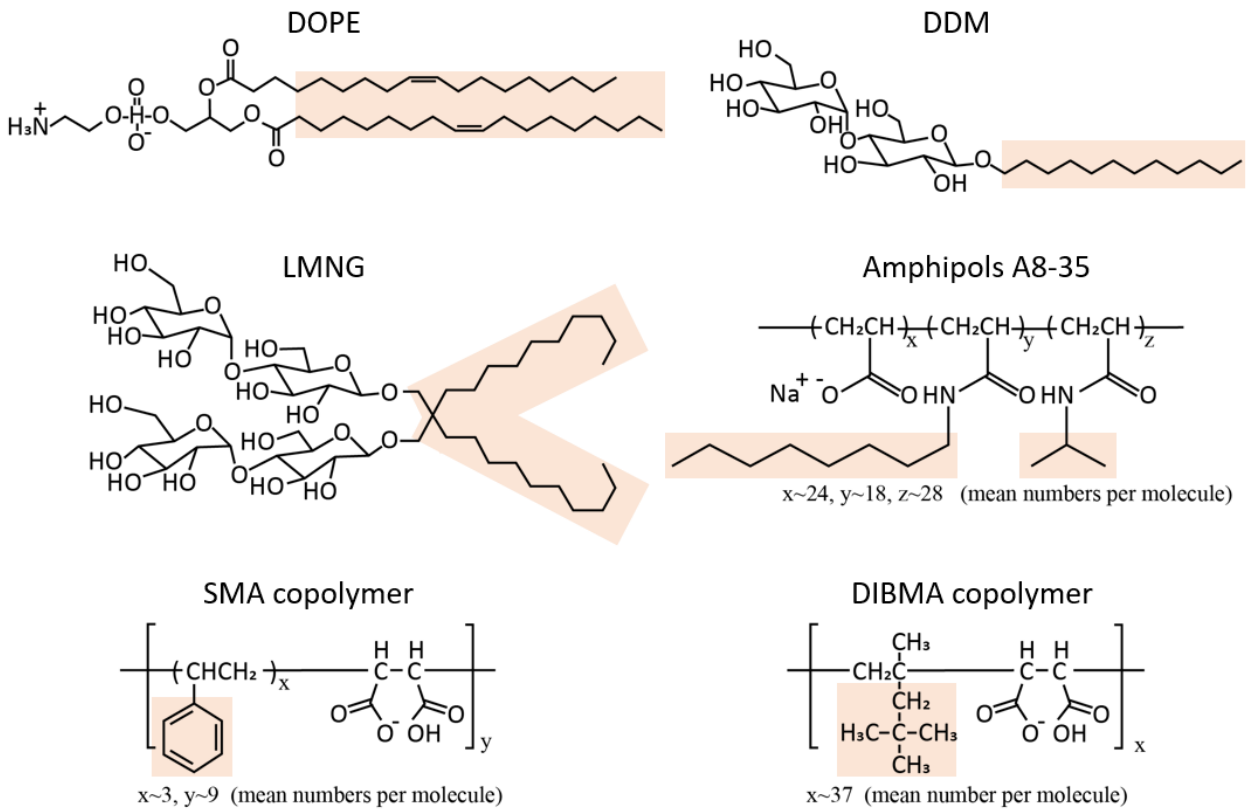


**Figure 1.10 | Overview of different detergents compared to a lipid structure.** Different detergents and polymers used for membrane protein purification, and a 1,2-dioleoyl-*sn*-glycero-3-phosphoethanolamine (DOPE) lipid molecule for comparison, are shown. Their hydrophobic moieties are highlighted in orange.

## 1.3.2 Membrane-mimicking systems

**Liposomes.** An alternative to keeping membrane proteins in detergent is to reinsert them into an artificial lipid environment after extraction. One widely used method is the reconstitution into liposomes, which is especially valuable for functional studies of membrane proteins (Chipot et al., 2018). This model system offers the benefits that, e.g., lipid composition can be accurately controlled, or their sizes can be tuned (Schwendener, 2014). Preferrable is the generation of unilamellar vesicles, which have a single phospholipid bilayer. During preparation, a small amount of solution is typically trapped within the liposome. This has the advantage that a specific substrate can be encapsulated in the liposome, and substrate translocation can be examined (Johnson and Lee, 2015). The most basic approach to reconstitute membrane proteins into liposomes (proteoliposomes) is to combine the detergent-stabilised proteins and the liposome dispersion and subsequently remove the detergent that stabilises the membrane protein. If the detergent concentration falls below the CMC, the protein

cannot be stabilised by detergent micelles anymore and is incorporated into the liposomes S. Detergent removal can be achieved by dilution, dialysis, gel filtration or adsorption to polystyrene beads (Bio-Beads) (Geertsma et al., 2008; Rigaud et al., 1995). Limitations of proteoliposomes are the heterogeneity of the sample, their tendency to aggregate, and their comparably large size for some further applications.

**Bicelles.** Detergent-solubilised lipid bilayer discs are formed when specific typically short-chain detergent (3-(cholamidopropyl)dimethylammonio-2-hydroxy-1-propane- sulfonate, CHAPSO) or -lipid molecules (dihexanoylphosphatidylcholine, DHPC) are combined with phospholipids (dimyristoylphosphatidylcholine, DMPC) (Sanders et al., 1994; Vestergaard et al., 2015). The phospholipids with the longer lipid tails assemble into a bilayer, and the short-chain detergent- or lipid molecules, which typically form micelles, stabilise the rim of the bilayer discs (Dürr et al., 2012; Sanders and Prosser, 1998). Membrane proteins inserted in these bicelles are surrounded by a membranous environment (figure 1.9), while the small particles size is compatible with many downstream applications. Bicelles proved especially useful for studying membranes and membrane proteins with nuclear magnetic resonance (NMR) since they can be magnetically aligned (Poget and Girvin, 2007; Sanders et al., 1994; Sanders and Sönnichsen, 2006). The composition and temperature are crucial for bicelles (Sanders and Prosser, 1998), and their morphology is heterogeneous (Vestergaard et al., 2015), which must be considered for further experiments.

**Protein-stabilised nanodiscs.** In contrast to bicelles, the lipid bilayer in nanodiscs is surrounded by typically two α-helical proteins, the membrane scaffold proteins (MSPs) (Bayburt et al., 2002, 1998; Bayburt and Sligar, 2010) (figure 1.9). The MSPs usually derive from the sequence of apolipoprotein-A1, and the resulting amphipathic α helices face the lipids with their hydrophobic side and provide excellent water-solubility with their hydrophilic surface facing the surrounding medium (Bayburt and Sligar, 2010). Several MSP variants were engineered, and the choice determines the final nanodisc size. Depending on the variant, nanodiscs with diameters between 6 and 17 nm can be generated (Grinkova et al., 2010; Hagn et al., 2013; Wang et al., 2015). The advantages of nanodiscs are the absence of detergent in the final sample, the longer lifetime compared to bicelles, their solubility and narrow dispersity, and the maintenance of the protein stability (Malhotra and Alder, 2014). These features made nanodiscs also very attractive for structural studies (Denisov and Sligar, 2016). The main drawbacks of nanodiscs are the relatively fixed sizes, the contribution of the MSPs to ultraviolet

(UV) absorption, and that the ratio of lipids, MSPs and detergent-solubilised membrane protein must be tightly controlled (Inagaki et al., 2013). Additionally, the positional variability of the protein within the nanodisc renders this system unsuitable for crystallisation. To avoid confusion with other disc-like particles, they will be termed "MSP nanodiscs" from here on.
The saposinlipoprotein (Salipro) system is similar to the MSP nanodiscs but uses the saposin A scaffold protein (Frauenfeld et al., 2016) (figure 1.9). Given the lipid-binding function of the saposin family (Ahn et al., 2006; Autzen et al., 2019; Bruhn, 2005; Popovic et al., 2012), it can provide a lipidic environment for the membrane protein while also making the Salipro particles water-soluble because of the amphipathic α helices of saposin (Autzen et al., 2019). Saposins are relatively small proteins (~10 kDa) and can thus adapt to different sizes and shapes of membrane proteins, which is an advantage over MSP nanodiscs. However, saposin also absorbs in the UV range, and the reconstitution still requires the optimisation of the ratio of lipids, MSPs and detergent-solubilised membrane protein.

### 1.3.3 Peptides and polymers

**Peptidiscs.** Similar to MSP nanodiscs, peptidiscs constitute a synthetic peptide mimicking the amphipathic helices of apolipoprotein-A1 that wraps around the membrane protein (Carlson et al., 2018) (figure 1.9). Reconstitution appears spontaneously when the detergent is removed: multiple copies of the peptide associate with the membrane protein, additionally retaining co-purified lipids (Carlson et al., 2019, 2018). As no external lipids are needed, the system requires little optimisation. Fast detergent removal in the presence of the peptidisc peptide can be accomplished using "on-column" or "on-bead" methods, which makes it a comparably rapid reconstitution method. Proteins with differently shaped and -sized membrane domains can be successfully incorporated into peptidiscs because several peptide molecules adapt to the shape and size of the membrane domain (Angiulli et al., 2020). Nevertheless, as the peptidisc peptides contain tryptophans and tyrosines, they also add to absorption in the UV range.

**Amphipols.** Amphipols are amphiphilic polymers with a hydrophilic backbone and numerous hydrophobic chains (Tribet et al., 1996) (figure 1.9, figure 1.10). The most studied and most used one is probably A8-35 (Gohon et al., 2006, 2004); however, they are all excellently water-soluble, and because of the multitude of hydrophobic groups, amphipols interact strongly with the membrane domain. This leads to one great advantage over detergents: because the affinity

of amphipols for the membrane domain is exceptionally high, they remain tightly bound to the protein even if no free polymer molecules are in solution (Popot, 2010). Hence, in contrast to detergents, no free monomers or micelles are in the solution that could interfere with subsequent downstream applications. Because amphipols are highly flexible, there are no size limitations of the membrane proteins. Therefore, the reconstitution into amphipols is rather simple: the detergent micelle of the solubilised membrane protein is replaced by amphipols through detergent removal, e.g., by Bio-Beads. The ratio of amphipols to protein must be optimised beforehand. One disadvantage of amphipols is their sensitivity to acidic pH or the presence of divalent cations, which can result in aggregation (Popot, 2010). Furthermore, amphipols seem to negatively influence membrane protein stability: Both the cryo-EM maps of transient receptor potential (TRP) cation channel V1 (TRPV1) and the TRP channel NOMPC exhibited a notable worse resolution in amphipols than in MSP nanodiscs (Gao et al., 2016; Jin et al., 2017b; Liao et al., 2013).

**Polymer-stabilised nanodiscs.** All the systems mentioned above have in common that they require previous solubilisation of the membrane proteins with classic detergents. As the lipids included in the MSP nanodiscs, bicelles and the Salipro system are chosen arbitrarily and added only during reconstitution, they do not represent the native lipid composition of the original environment of the protein. Endogenous lipids can be carried along during purification, but it is also possible that they are harshly removed when using detergents. Lipids frequently modulate and influence the functioning of membrane proteins (Dowhan et al., 2004; Dowhan and Bogdanov, 2002), and the choice of lipids can be crucial for protein activity or oligomerisation (Bogdanov et al., 2008; Henrich et al., 2017; Prabudiansyah et al., 2015; Proverbio et al., 2013). Lipids can also affect the activity of MscL and MscS, either by direct interactions with the channels or by alteration of membrane properties like curvature or stiffness (Nomura et al., 2012; Xue et al., 2020). Thus, it seems desirable to keep proteins in a close-to-native lipid environment. A novel alternative to solubilisation with classic detergents is the direct extraction of membrane proteins from the plasma membrane into polymer-stabilised nanodiscs (or polymer-lipid particles) with specific membrane-active amphipathic polymers (figure 1.9) to preserve the native lipid environment; hence, these polymers were alleged to generate so-called “native” nanodiscs. The formation of “lipid-polymer nanostructures” by application of poly(styrene-*co*-maleic acid) (SMA; figure 1.10) copolymer to membranes was already observed in 2001 (Tonge and Tighe, 2001). However, only eight years later, it was shown to extract membrane proteins from proteoliposomes into

nanoparticles, so-called SMALPs (SMA lipid particles) (Knowles et al., 2009). The particles were described as stable and monodisperse, and the extracted proteins retained their functions (Knowles et al., 2009; Long et al., 2013). SMA copolymer can extract proteins from several different cellular membranes (Gulati et al., 2014; Long et al., 2013). However, SMA copolymer has its limitations, as it is dependent on neutral or basic pHs and precipitates in the presence of an acidic pH or divalent cations, and, because of its aromatic styrene group, it interferes with spectroscopy techniques in the UV range (Dörr et al., 2016; S. C. Lee et al., 2016). Furthermore, the size of the formed discs is limiting for extraction of larger protein complexes or -oligomers (Swainsbury et al., 2017), although it was suggested that the disc size could be modulated by the ratio of protein, lipid and polymer (Craig et al., 2016; Cuevas Arenas et al., 2016; Vargas et al., 2015).

As an alternative to SMA, the poly(diisobutylene-*alt*-maleic acid) (DIBMA; figure 1.10) copolymer was introduced in 2017, and the deriving native nanodiscs are termed DIBMALPs (DIBMA lipid particles) accordingly (Oluwole et al., 2017). Because DIBMA copolymer is more aliphatic than SMA, it does not absorb UV light. Consequently, optical studies based on UV absorption, like protein quantification or UV circular dichroism, are not hampered by the UV absorption of the nanodiscs. Moreover, it is less sensitive to divalent cations, and at the same polymer-lipid ratio (e.g. 0.2), it forms larger (empty) discs compared to SMA (18 nm vs 13 nm, respectively), but membrane solubilisation is generally lower than for SMA (Grethen et al., 2017; Oluwole et al., 2017). DIBMA copolymer has mainly been used on artificial membranes, but solubilisation of native *E. coli* membranes indicated that DIBMA solubilises preferentially larger proteins (Grethen et al., 2017). Both SMALPs and DIBMALPs are compatible with many downstream applications. However, while several proteins in SMALPs produced cryo-EM structures with sub-nanometre resolutions (Johnson et al., 2020; Parmar et al., 2018; Qiu et al., 2018; Sun et al., 2018; Tascón et al., 2020; Yoder and Gouaux, 2020; Yu et al., 2021), the applicability of DIBMALPs for cryo-EM studies has not been demonstrated so far.

## 1.4 Electron microscopy

The structure and function of biological macromolecules are inevitably linked. Hence, structural biology has contributed substantially to our understanding of how proteins and macromolecular complexes work and fulfil their destined roles. The most effective techniques available for the structure elucidation of biological macromolecules are X-ray crystallography, NMR and electron microscopy (EM). Among these, x-ray crystallography has long been the most successful technique, as it is amendable to complexes of various sizes and can yield an atomic resolution, but a prerequisite is the crystallisation of the target sample. NMR can provide information about dynamics additional to the structure but is restricted to small proteins and complexes (<50 kDa), and proteins must be isotope-labelled. Both techniques require large amounts of a vastly pure protein sample. EM, in contrast, needs much less sample and can handle complexes of various sizes (Song et al., 2019) ranging between 43 kDa (Herzik et al., 2019) and 72 MDa (Zhang et al., 2010). By cryo-EM, vitrified biological molecules can be visualised in a close-to-native state, and the attainable resolution is no longer inferior to crystallographic resolutions, as exemplified by a 1.15 Å map of apoferritin (Yip et al., 2020).

### 1.4.1 General concepts of cryo-EM for structural biology

**Vitrification of biological specimens.** Biological macromolecules are compromised by the high vacuum needed in the beam path of an electron microscope and are highly susceptible to radiation damage. The deterioration of the specimens in an electron microscope by the high vacuum can be mitigated by dehydration or fixation methods. Among these, negative staining became popular, which replaces the water surrounding the specimen with a dried solution of a heavy metal salt (Brenner and Horne, 1959; van Bruggen et al., 1960). However, this can introduce artefacts and limits the attainable resolution to ~20 Å due to the properties of the stain, as only the stain – and therefore the exposed protein regions – are imaged (Cheng et al., 2006). Preserving the structural integrity of biological samples by keeping them in a hydrated environment was made possible by the discovery of vitreous ice (Dubochet et al., 1982). Vitrification at atmospheric pressure depends on a high cooling rate of $10^4$ K/s or greater, which is achieved by plunging the specimen, applied onto an EM grid, rapidly into a cryogen like liquid ethane or ethane/propane (Adrian et al., 1984; Bald, 1984; Dubochet et al., 1988; Tivol et al., 2008). Subsequently, frozen-hydrated molecules are embedded in vitreous, sufficiently

electron-transparent ice, which prevents dehydration of the molecules in the vacuum and the cooling protects them, to some degree, from radiation damage (Stark et al., 1996); thus preserving the native structure to its atomic level (Taylor and Glaeser, 1974) (figure 1.11).

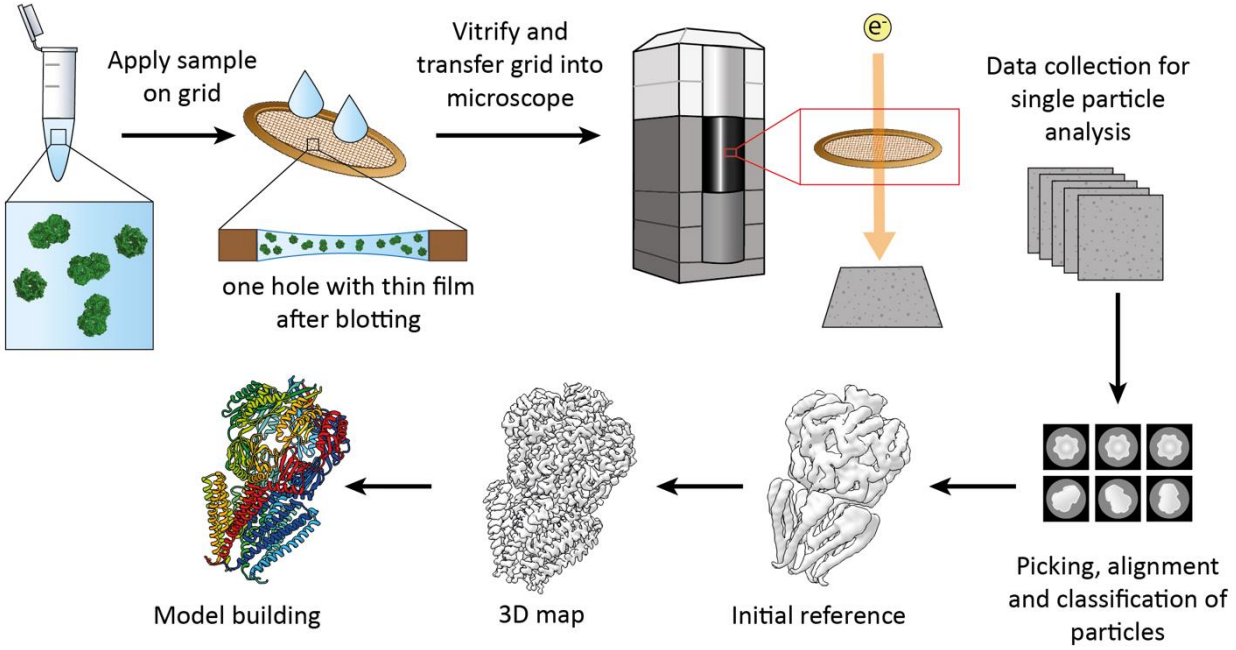


**Figure 1.11 | Simplified workflow for cryo-EM and subsequent single-particle analysis.** The sample is applied onto an EM grid, and after blotting, a thin film is formed within the single holes with monodispersed single particles. After vitrification, the macromolecules should ideally be captured in different orientations. The grid is transferred into a microscope, and an automated data collection is set up. One micrograph represents the 2D projection image of a 3D sample. Next, single 2D particle projections depicting various orientations are picked, aligned, and averaged to clean up the data set. Retained particles are refined against an initial reference, and the resulting 3D map can be used for (*de-novo*) model building if the attained resolution is sufficient. Maps and the model for this figure are prepared by using EMDB-4919 and PDB 6RLD (Rasmussen et al., 2019a).

**Cryo transmission electron microscopy.** Electrons emanating from an electron source are accelerated with voltages of typically 80-300 kV down the microscope column operated at high-vacuum and a low temperature (figure 1.12) (Fujiyoshi, 2013). Electromagnetic coils deflect the electron beam, and the condenser lens system spreads the beam on the specimen, while the condenser aperture regulates the illumination area and electron exposure. The beam is finally focused onto the specimen that sits between the two pole pieces of the objective lens. The electrons interact differently with the sample (Orlova and Saibil, 2011). For image formation of biological samples, the elastically scattered electrons are decisive, while inelastically scattered electrons mainly add noise and can be removed by energy filters (Wang

et al., 1997). Due to the scattering events of the electrons, the phase and amplitude of the electron waves change, resulting in amplitude contrast and phase contrast. Electrons that exit from the beam path – due to high scattering angles or backscattering – contribute to amplitude contrast, and typically, electrons are removed by the objective aperture to increase the amplitude contrast. Phase contrast is caused by the interference of the elastically scattered electrons and the unscattered electrons. Nevertheless, as the samples are relatively thin, biological macromolecules are only weak phase objects. In focus, phase contrast arises only from aberrations of the lens, so the objective lens is defocused to increase the contrast. The resulting image changes are described by the contrast transfer function (CTF). Image modulations by the CTF can be corrected during image processing. Image contrast can further be increased by applying a higher electron exposure, which on the other hand, increases radiation damage, and as exposure accumulates on the specimen, high-resolution information is lost (Glaeser, 2008; Grant and Grigorieff, 2015). The objective lens generates a real image of the object, and additional lenses further magnify the primary obtained image, and finally, the 2D projection image is recorded (figure 1.11).

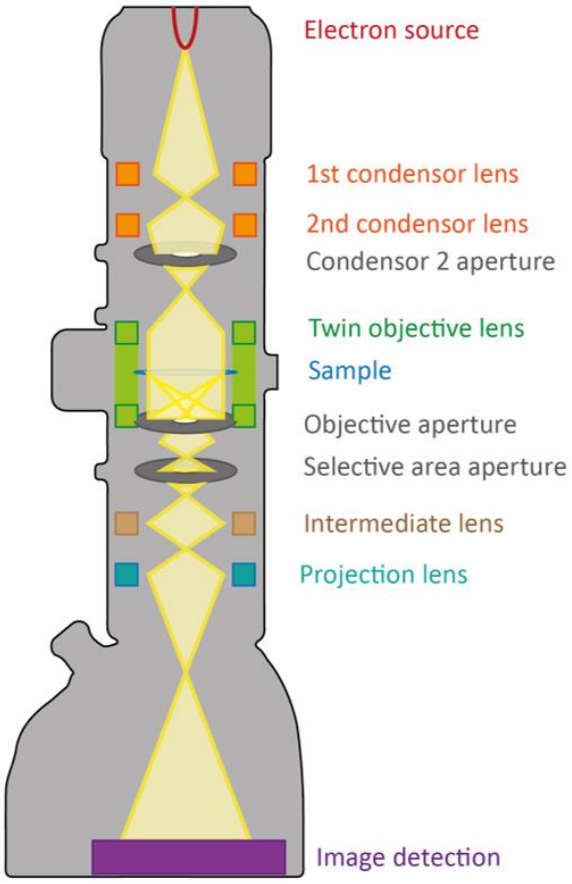


**Figure 1.12 | Simple schematic depiction of the TEM components.** The shown setup is exemplary, as different microscopes have different specifications. The Titan Krios (Thermo Fisher; formerly FEI), e.g., has a three-lens condenser system. The beam path is shown in yellow.

For decades, images have been recorded on film, which offered the advantages of direct electron detection, high image contrast, a large field of view, and a good detective quantum efficiency (DQE) at high spatial frequencies (Bai et al., 2013). The DQE is a measure for the detector performance: it describes how much noise is added to the output signal at each spatial frequency and is defined as the ratio of the signal-to-noise ratio (SNR) in the output image to the SNR in the input image (Ruskin et al., 2013). Different spatial frequencies account for differently sized details of the specimen, and an ideal detector would have a DQE of 1 for all spatial frequencies. Though the DQE of film is good at high spatial frequencies and therefore sufficient for high-resolution EM, its applicability is hampered by the need for subsequent digitisation of the images and the application of a higher defocus because the DQE at low spatial frequencies, and thus the image contrast, is low. Scintillator-based digital cameras – charge-coupled device (CCD) and conventional complementary metal-oxide-semiconductor (CMOS) cameras – convert incident electrons into photons before detection; in CMOS detectors, each photon further generates one secondary electron in the camera chip (Faruqi and Henderson, 2007). They offer the immediate availability of digital data, enabling high throughput and automated image acquisitions. Besides, they have a good DQE at low spatial frequencies, resulting in better image contrast. However, the poor DQE of these detectors for high spatial frequencies renders them unsuitable for high-resolution EM.

The development of CMOS-based direct electron detectors (DED) marked one milestone for the attainable resolution by cryo-EM (Faruqi and Henderson, 2007; Kühlbrandt, 2014; McMullan et al., 2016, 2009a, 2009b). In DEDs, the incident electrons are converted to secondary electrons that are detected in the camera chip. DEDs outperform other types of detectors concerning the DQE over all spatial frequencies. Moreover, DEDs have a fast frame readout rate, allowing them to fractionate the electron exposure for one image into many subframes. This feature made it possible to correct the image blurring caused by beam-induced particle movements and optimise the SNR of the final averaged movie for radiation-affected specimens by applying a relative weighting of single frames regarding accumulated exposure (Brilot et al., 2012; Campbell et al., 2012; Scheres, 2014).

**Single-particle analysis (SPA).** The core idea of SPA is averaging multiple copies of 2D projections of single macromolecules captured in various orientations to calculate a 3D reconstruction (figure 1.11). To correct an image for CTF effects, the CTF is estimated for the motion-corrected and dose-weighted micrograph. Subsequently, thousands of particles are

picked, extracted, aligned, and classified to improve the SNR. In recent image processing procedures, 2D classification serves to purge a data set to ensure that damaged particles or contaminations are excluded from further processing. Obtaining a 3D reconstruction from 2D projection images is dependent on the determination of the relative orientations of all particles. The central section theorem (Crowther et al., 1970) states that the Fourier transform of a 2D projection is a central slice through the 3D Fourier transform of the object and that Fourier transforms of any two projections will intersect along a "common line" (Van Heel, 1987). Hence, the original 3D structure can be obtained by calculating the inverse Fourier transform. Another approach for determining the orientation of images is based on the stochastic gradient descent (SGD) method (Zivanov et al., 2018). The obtained 3D structure serves as an initial model for subsequent refinements Single-particle images are refined against the reference, and by a projection-matching approach, the relative orientations of the particles can be refined. The Fourier shell correlation (FSC) helps to assess the resolution of a 3D map. Therefore, initially, the data set is randomly split into two sets, and corresponding spatial shells of the calculated Fourier transforms of the two resulting individual 3D reconstructions are compared. This method of processing is referred to as "gold-standard" FSC (S. Chen et al., 2013; Henderson et al., 2012; Scheres and Chen, 2012). The cross-correlation threshold is used to estimate the SNR of the resulting map. At a threshold of 0.143, the combined map from all particles compared to a noise-free model has an SNR of 1. The final image reconstruction represents a three-dimensional density map of the specimen, which can further be used for interpretations and model building.

### 1.4.2 Cryo-EM for the elucidation of membrane protein structures

**Sample preparation.** The first solved membrane protein structure was bacteriorhodopsin at 7 Å in 1975 (Henderson and Unwin, 1975; Unwin and Henderson, 1975), which was achieved by electron crystallography of the protein array embedded in glucose and at room temperature. Although stunning structures were revealed by (cryo-) electron crystallography (Gonen et al., 2004; Holm et al., 2006; Kühlbrandt et al., 1994; Murata et al., 2000; Nogales et al., 1998), obtaining 2D protein crystals can be challenging, and 2D crystals are often poorly ordered, which impairs high-resolution structure determination (De Zorzi et al., 2016). Single-particle cryo-EM offers several advantages for the structure elucidation of membrane proteins. A comparably small amount of protein is needed in sample preparation compared to x-ray

crystallography and NMR. Most membrane proteins are low abundant in cells and must be overexpressed, yet high protein yields are rarely obtained (Drew et al., 2003). Additionally, most of the larger biological macromolecules have a certain degree of intrinsic flexibility and conformational freedom, limiting SPA resolution but also may impede the growth of well-diffracting 3D protein crystals needed for X-ray crystallography. Membrane protein complexes are often too large for NMR; moreover, they must be isotope-labelled and remain stable during measurement (Nietlispach and Gautier, 2011). The latter is a minor issue in cryo-EM, as the sample can be expeditiously vitrified after purification and is captured in this state throughout the data collection. In the purification procedure, membrane proteins are typically extracted from the native membrane with detergents. Not-optimised detergent conditions can have deleterious effects on the membrane protein, and as detergents lower the surface tension of an aqueous solution, it could be a hurdle to obtain an appropriate ice thickness. Moreover, detergent micelles in the final sample can add to the background, which is primarily a problem for smaller membrane proteins (Vinothkumar, 2015). For these reasons, it often seems desirable to exchange the detergent. Suitable systems can substitute the detergent micelle and, in the case of bicelles, MSP-, salipro- and polymer-stabilised nanodiscs, provide a lipid bilayer environment while keeping the membrane proteins in a single-particle state. Membrane proteins can also be reconstituted into larger systems, like liposomes, and be investigated by cryo electron-tomography and subsequent subtomogram averaging (Bartesaghi and Subramaniam, 2009). This considers a more global effect of the lipid bilayer on the membrane proteins, but sub-nanometre resolution by subtomogram averaging is typically achieved for large symmetric particles like viruses (Ke et al., 2020; Schur et al., 2016, 2015).
However, it should be noted that the effects of detergents cannot be generalised, and structures of many membrane proteins have successfully been obtained in detergent (Fiedorczuk et al., 2016; Huynh et al., 2016; Meyerson et al., 2016; Sun et al., 2015; Wu et al., 2016). Interestingly, the ryanodine receptor 1 (RyR1) was prepared for cryo-EM in detergent (Yan et al., 2014), MSP nanodiscs (Efremov et al., 2014), or mixed micelles (Zalk et al., 2014). The three obtained structures revealed the same architecture, but the map of RyR1 prepared in the detergent CHAPS had a significantly better resolution. This underpins the fact that the system chosen for one membrane protein does not necessarily directly impact its overall structure, but minor differences can affect the attainable resolution.

**Computational approaches.** Many membrane proteins are dynamic by nature and can display multiple conformations in solution. Conformational (and often also compositional)

heterogeneity is present in most data sets – not only of membrane proteins. It is not only associated with intrinsic flexibility and functional properties of the macromolecule but also with the observation that complexes, which are stable in solution, can disintegrate or dissociate during specimen preparation (Alberts, 1998; Dunker et al., 2002; Stark and Chari, 2016). In practice, this increases the amount of data needed to obtain a given resolution, and the final map represents a superposition of various states (Henderson et al., 2011). Images of heterogenous regions of the structure are incorrectly aligned and averaged with other images representing the same region, resulting in the loss of the coherent signal and thus limiting the attainable resolution (Serna, 2019). While heterogeneity and integrity of the proteins can eventually also be observed in 2D class averages, maximum-likelihood-based 3D classification (Lyumkis et al., 2013; Scheres et al., 2006; Sigworth, 1998) has proven most powerful to unravel different conformational states present in one data set (Bartesaghi et al., 2015; Dürr et al., 2014; Loveland et al., 2017; Merk et al., 2016; Zalk et al., 2014; Zhao et al., 2015). Distinct classes – representing more homogenous subsets – can then be processed individually, providing superior information than one single map derived from coexisting conformational states. The possibility to implement this computational approach is also linked to the better image quality and the option for motion correction provided by DEDs because the ability to identify particle subpopulations depends on the SNR of the images.

Masking of individual subunits can be applied to 3D classifications, which is particularly useful if the flexible region is rather small (Scheres, 2016; Scheres et al., 2006, 2005). However, as the subvolume mask is not applied to the original 2D particles, this approach results in an inconsistency between the masked reference and the experimental data, and the masked-out data will add noise to the refinement (Ilca et al., 2015; Serna, 2019). Therefore, a signal subtraction procedure was developed to remove the experimental signal that is masked out in the refinement. Heterogeneity caused by subunits or individual domains that move separately from each other can be addressed by multibody refinements. In this approach, complexes are considered to be formed by independently moving rigid bodies. During processing, the signal of one rigid body is aligned to projections of a reference of only this body, and signal of all other rigid bodies is subtracted (Nakane et al., 2018; Nakane and Scheres, 2021). This approach also allows unique insights into the conformational variety of a complex. If a symmetric complex is rendered asymmetric because of individual subunits, the data set can be symmetry expanded. Each subunit of a complex is copied to the same location, resulting in n times more entries in the data file, with n being the number of symmetry-equivalent copies. The structure is finally obtained by masked 3D classification and refinement with no or only local angular

searches (Briggs et al., 2005; Kimanius et al., 2016; Serna, 2019). Finally, remaining heterogeneity can be detected by calculating a map with local resolution variations (Kucukelbir et al., 2014), which are also indicative of conformational heterogeneity.

## 1.5 Aims and scope of this thesis

*E. coli* has six genes for MscS-like channels. However, so far, only the smallest channel of this family, MscS, has been extensively studied structurally and functionally, although the presence of other MscS-like channels was already demonstrated almost 30 years ago (Cui et al., 1995; Levina et al., 1999). The paralogues differ in their number of TM helices. In MscS, these helices are essential for sensing the membrane tension; however, the gating paradigm of MscS is not ultimately understood.

Obtaining a high-resolution map of YnaI, which is sufficient for model building, as well as one of the large paralogues by use of cryo-EM and SPA shall enable a structural comparison between differently-sized members of the MscS-like family in *E. coli*. Furthermore, cryo-EM should be employed to gain functional insights into YnaI and evaluate a possible role for the additional TM helices. This work further aimed to unravel the determinants of the conformational state of MscS, and to investigate whether there might be a conserved mechanism for MscS-like channels. Lipid expulsion of the hydrophobic pockets was hypothesised to initiate the gating transition (Zhang et al., 2021), but the impact of the surrounding membrane is not fully clarified. Examination of MscS in the absence of a membrane shall therefore provide mechanistic insights into the role of lipids for gating.

# 2 MATERIALS AND METHODS

Many methods are taken from Flegler et al. (2020) and Flegler et al. (2021) and are adapted and complemented in the following sections. Experiments performed in collaborations with other groups are indicated as such.

Unless stated otherwise, all buffers and solutions were prepared with water from the ultrapure water system (TKA x-CAD, Thermo Scientific) at the Rudolf Virchow Center, and the pH was adjusted with NaOH or HCl, respectively. Buffers for size exclusion chromatography were filtered and degassed through a 0.22 µm membrane filter before use. Media were prepared with VE water from the in-house demineralised water connection at the Rudolf Virchow Center.

## 2.1 Molecular biology

### 2.1.1 Preparation of chemically competent *E. coli* cells

Treatment with $CaCl_2$ is known to make *Escherichia coli* (*E. coli*) cells highly competent for extracellular DNA uptake (Hanahan, 1983; Skrzypek et al., 2018). In this study, competent cells were made from two different strains: *E. coli* DH5α is used for plasmid amplification, and *E. coli* MJF641 ("Δ7") is used for overexpression of MS channels, as this strain lacks all seven genes of *E. coli* MS channels (table 2.1).

**Table 2.1 | Chemically competent cell strains used in this thesis.**

| Strain | Genotype/ specifications | Source |
|---|---|---|
| *Escherichia coli* DH5α | $F^-$ Φ80*lac*ZΔM15 Δ(*lac*ZYA-*arg*F) U169 *rec*A1 *end*A1 *hsd*R17($r_k^-$, $m_k^+$) *pho*A *sup*E44 *thi*-1 *gyr*A96 *rel*A1 $\lambda^-$ | Thermo Fisher Scientific |
| *Escherichia coli* MJF641 ("Δ7") | *ΔmscS, ΔmscK, ΔynaI, ΔybdG, ΔybiO, ΔyjeP, ΔmscL* | (Edwards et al., 2012) |

Cells were plated on a Luria Bertani (LB) agar and incubated at 37 °C overnight. Next, 5 ml LB medium (table 2.2) were inoculated with one colony and incubated overnight at 37 °C and 200 rpm. The complete overnight culture was transferred to 30 ml of LB medium and grown to an $OD_{600}$ of 0.4. Subsequently, cells were spun down at 4000 g and 4 °C, the cell pellet was resuspended in 30 ml 100 mM ice-cold $CaCl_2$ and incubated on ice for 4 h. Cells were centrifuged at 2000×g, 4 °C for 10 min and the pellet was resuspended in 3 ml 100 mM ice-cold and sterile $CaCl_2$. Ice-cold, sterile 50 % (v/v) glycerol was added to a final concentration of 10 % (v/v), and the suspension was incubated at 4 °C overnight. Test tubes and test tube racks were precooled. 200 µl aliquots were flash-frozen in liquid nitrogen and stored at -80 °C until further use.

**Table 2.2 | Media and their compositions.**

| Medium | Composition |
|---|---|
| LB medium (agar) | 10 g/l tryptone/peptone, 5 g/l yeast extract, 5 g/l NaCl, (10 g/l agar-agar) |
| SOC medium (agar) | 20 g/l tryptone/peptone, 5 g/l yeast extract, 0.5 g/l NaCl, 2.5 mM KCl, 10 mM $MgCl_2$, 20 mM glucose, (10 g/l agar-agar) |

### 2.1.2 Transformation of competent *E. coli* cells

For transformation, an aliquot of 200 µl of $CaCl_2$ competent *E. coli* cells was thawed slowly on ice, and 1 µl of plasmid DNA was added. The mixture was incubated on ice for 20 min before cells were heat-shocked at 42 °C for 2 min. After 5 more minutes on ice, 500 µl pre-warmed medium (37 °C; LB or SOC, table 2.2) was added to the cells and incubated at 37 °C, 200 rpm, for 45 min. Subsequently, cells were centrifuged, 400-500 µl of the supernatant were discarded, the cell pellet was resuspended in the remaining medium and immediately plated on selective agar plates (100 µg/ml ampicillin, LB or SOC, table 2.2). The plates were incubated at 37 °C overnight.

### 2.1.3 Site-directed mutagenesis

Specific changes to double-stranded deoxyribonucleic acid (DNA) can be introduced with site-directed mutagenesis (Shortle et al., 1981). A pair of primers with the targeted base changes in

the centre (table 2.3) were reverse complementary to each other. A second point mutation was introduced to create a restriction enzyme cleavage site for evaluation of the results. The primer melting temperature ($T_m$) of 68 °C was estimated using the NEB $T_m$ calculator ("NEB Tm Calculator,") (New England Biolabs, Ipswich/USA). The polymerase chain reaction (PCR) mixture and reaction protocol are given in table 2.4 and figure 2.1 (PCR cycler: Mastercycler EP gradient S (Eppendorf)).

The PCR product was incubated with 1 µl DpnI (20000 U/ml, New England Biolabs) per 50 µl PCR sample at 37 °C for at least 2 h to digest the original template. Afterwards, competent *E. coli* cells were transformed with 10 µl of the digested PCR product and DNA of colonies was analysed by sequencing (next section).

**Table 2.3 | List of oligonucleotides.**

| Construct name | Sequence (5'-3') | $T_m$ |
|---|---|---|
| YnaI_K108L_forward | CAG CAG ATT AAA CTG GGT CGT GAT ATC | 68 °C |
| YnaI_K108L_reverse | GAT ATC ACG ACC TTT TTT AAT CTG CTG | 68 °C |
| YnaI1_R2_forward | G AAC TCG CTG TTT TC | *Sequencing primer* |

**Table 2.4 | Setup for site-directed mutagenesis.**

| Component | Concentration | Pipetting scheme for 50 µl |
|---|---|---|
| Template | ~2-20 ng/µl | 1 µl |
| Primer forward | 0.5 µM | 2 µl |
| Primer reverse | 0.5 µM | 2 µl |
| 2x Mastermix | 1x | 25 µl |
| 5x GC Enhancer | 1x | 10 µl |
| Water | - | 10 µl |

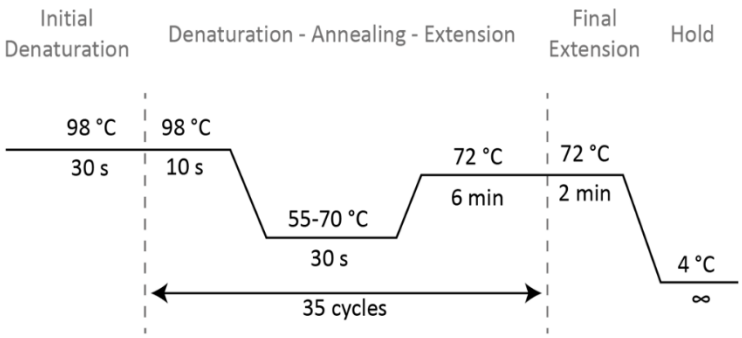


**Figure 2.1 | PCR cycling conditions.** Temperatures and times are given for each step. For the primer annealing step, a gradient with 3 °C increments was applied.

Additionally, two synthetic constructs with mutations in the pore were purchased from GeneArt (by Thermo Fisher Scientific). One construct bears the double-mutation G149A/G152A and the other the single mutation G152P. For the constructs, the synthetic genes were first inserted into the vector pMK-T, and further subcloned into pTrc using the restriction sites of NcoI and XhoI (figure 2.2) to ensure that the $His_6$ tag is on the C-terminal end of the protein. This provided the same backbone as for the wild type YnaI construct to allow comparative functional studies.

### 2.1.4 Isolation of plasmid DNA from Escherichia coli and DNA sequencing

To isolate plasmid DNA from *E. coli* DH5α cells, a 5 ml overnight culture was grown, and DNA was isolated using the Fast Gene Plasmid mini Kit (Nippon Genetics Europe GmbH, Düren/Germany) according to the manufacturer's protocol. The nucleotide sequence was determined by sequencing using the sequencing primer YnaI1_R2_forward (table 2.3, Microsynth Seqlab, Göttingen/Germany) and analysed with Snapgene Viewer 4.2.11 (free version; GSL Biotech SSL, San Diego/USA).

## 2.2 Microbiology

### 2.2.1 Cultivation and storage of cell cultures

**Overnight cultures.** Overnight cultures were used for plasmid preparations (*E. coli* DH5α), as precultures for overexpression of proteins, and as starting cultures for downshock experiments. In sterile 50-ml tubes, 10 ml LB medium were supplemented with 100 µg/ml ampicillin and were either inoculated with a colony from an agar plate or with glycerol cryo cultures. The incubation was carried out at 37 °C and 100 rpm overnight.

**Glycerol cryo cultures.** Glycerol cryo cultures were created for the long-term cultivation of *E. coli* cell cultures. 5 ml LB medium were supplemented with 50 µg/ml ampicillin and inoculated with a single colony from an agar plate. Cells were grown at 37 °C, 100 rpm, to an $OD_{600}$ of 0.6-0.7. Subsequently, 18 % (v/v) sterile glycerol was added and mixed by pipetting. 1-ml cultures were aliquoted in 2-ml cryo tubes, flash-frozen in liquid nitrogen and stored

at -80 °C. The created cryo cultures are listed in table 2.5. A simple plasmid map is depicted in figure 2.2.

**Table 2.5 | List of glycerol cryo cultures generated in this work.**

| Cell strain + plasmid | Vector size (bp) |
|---|---|
| *E. coli* MJF641 + pTrc-MscS-$H_6$ | 5009 |
| *E. coli* MJF641 + pTrc-YnaI-$H_6$ | 5180 |
| *E. coli* MJF641 + pTrc-YbdG-$H_6$ | 5396 |
| *E. coli* MJF641 + pTrc-YbiO-$H_6$ | 6372 |
| *E. coli* MJF641 + pTrc-YjeP-$H_6$ | 7498 |
| *E. coli* MJF641 + pTrc-MscK-$H_6$ | 7567 |

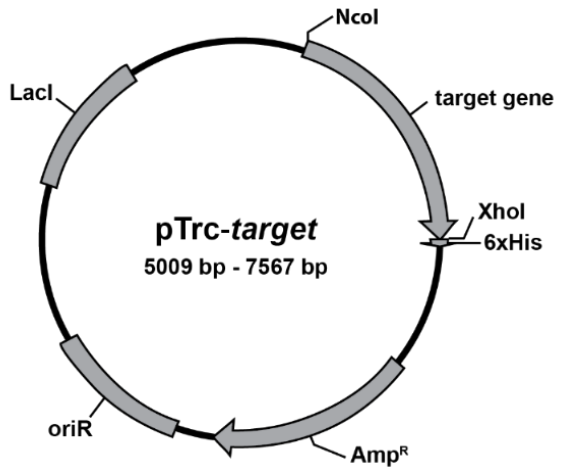


**Figure 2.2 | Simplified plasmid map.** The construct has a pTrc backbone and was used for expressing the desired proteins with a C-terminal $His_6$ tag ($LEH_6$; 6xHis). The vector contains an ampicillin resistance (AmpR), and the presence of a lac repressor (LacI) enables induction with IPTG. The origin of replication (oriR) and two selected restriction enzyme sites (NcoI and XhoI) are marked.

**Determination of cell growth.** Cell growth of *E. coli* cells was monitored photometrically. The measurements of the optical density at 650 nm were conducted with either a 4050 Ultrospec II (LKB Biochrom) or a Genesys 50 (Thermo Scientific) UV-visible spectrophotometer; the respective media were used as references. Growth curves were determined by diluting an exponentially growing pre-culture into LB medium and measurement of the $OD_{650nm}$ of the culture every 30 min, which was growing at 37°C and 250 rpm.

### 2.2.2 Overexpression of proteins in *Escherichia coli*

Proteins were produced recombinantly by overexpression in *E. coli* MJF641 cells. All proteins were expressed with a C-terminal $His_6$ tag to enable Nickel-nitrilotriacetic acid (Ni-NTA) affinity chromatography. An overnight culture supplemented with 100 µg/ml ampicillin was inoculated with either a single colony from an agar plate or the glycerol cryo culture of the desired cells. The next day, the overnight culture was transferred to a 100 ml preculture containing ampicillin and was incubated at 37 °C, 100 rpm, for 1.5 h. The main culture (1.5 l LB in a 5-l baffled flask) was inoculated with the preculture so that the starting $OD_{650}$ was between 0.05 and 0.1. They were incubated at 37 °C and 190 rpm until reaching an $OD_{650}$ of 0.7-0.8. Subsequently, the temperature was reduced to 30 °C for 30 min, and the culture was induced with 0.8 mM isopropyl β-D-thiogalactopyranoside (IPTG). The expression was carried out for 4 h. Cells were harvested by centrifugation at 4000 rpm (Avanti J-26 XP centrifuge with rotor JLA 8.1000 (both Beckman Coulter), 4 °C, for 20 min. The pellet was resuspended in phosphate-buffered saline (PBS) buffer (137 mM NaCl, 2.7 mM KCl, 10 mM $Na_2HPO_4$, 1.8 mM $KH_2PO_4$) with 20 ml buffer per 3-5 g cells (wet weight) and stored at -80 °C until use.

## 2.3 Biochemistry

### 2.3.1 Protein purification

A multi-step procedure was applied for the purification of the overexpressed proteins; in general, consisting of cell lysis, membrane solubilisation, affinity chromatography and size exclusion chromatography (SEC). Peculiarities of the different steps are mentioned explicitly in the respective sections. All buffers used for the different purification procedures are listed in table 2.6. An overview of the different detergents is given in table 2.7.

**Table 2.6 | Overview of buffers used for protein purifications.**

| Buffer | Designation | Composition |
|---|---|---|
| Solubilisation buffer A | Standard purification | 1 % (w/v) DDM, 50 mM Na-phosphate buffer pH 7.5, 300 mM NaCl, 10 % (v/v) glycerol, 25 (50[a]) mM imidazole, 0.2 mM PMSF |
| Solubilisation buffer B | Purification of open MscS | 1.5 % (w/v) DDM, 50 mM Na-phosphate buffer pH 7.5, 300 mM NaCl, 10 % (v/v) glycerol, 50 mM imidazole, 0.2 mM PMSF |
| Solubilisation buffer C | Purification in DIBMA | 50 mM Na-phosphate buffer pH 7.5, 300 mM NaCl, 10 % (v/v) glycerol, (5 % (w/v) DIBMA[b]) |
| Wash Buffer A | Standard purification | 0.05 % (w/v) DDM, 50 mM Na-phosphate buffer pH 7.5, 300 mM NaCl, 10 % (v/v) glycerol, 25 (50*) mM imidazole, 0.2 mM PMSF |
| Wash Buffer B | Purification of open MscS | 0.5 % (w/v) DDM, 50 mM Na-phosphate buffer pH 7.5, 300 mM NaCl, 10 % (v/v) glycerol, 25 (50*) mM imidazole, 0.2 mM PMSF |
| Wash Buffer C | Purification in DIBMA | 50 mM Na-phosphate buffer pH 7.5, 300 mM NaCl, 10 % (v/v) glycerol, 25 mM imidazole |
| Wash Buffer D | Replacement of DDM by LMNG | 0.03 % (w/v) LMNG, 50 mM Na-phosphate buffer pH 7.5, 300 mM NaCl, 10 % (v/v) glycerol, 25 (50*) mM imidazole, 0.2 mM PMSF |
| Elution buffer A | Standard purification | 0.05 % (w/v) DDM, 50 mM Na-phosphate buffer pH 7.5, 300 mM NaCl, 10 % (v/v) glycerol, 300 mM imidazole, 0.2 mM PMSF |
| Elution buffer B | Purification of open MscS | 0.5 % (w/v) DDM, 50 mM Na-phosphate buffer pH 7.5, 300 mM NaCl, 10 % (v/v) glycerol, 300 mM imidazole, 0.2 mM PMSF |

**Table 2.6 continues next page ►**

| | | |
|---|---|---|
| Elution buffer C | Purification in DIBMA | 50 mM Na-phosphate buffer pH 7.5, 300 mM NaCl, 10 % (v/v) glycerol, 300 mM imidazole |
| Elution buffer D | Replacement of DDM by LMNG | 0.03 % (w/v) LMNG, 50 mM Na-phosphate buffer pH 7.5, 300 mM NaCl, 10 % (v/v) glycerol, 300 mM imidazole, 0.2 mM PMSF |
| HPLC buffer AB | Standard purification / purification of open MscS | 0.03 % (w/v) DDM, 50 mM HEPES 150 mM NaCl, 5 mM EDTA |
| Modified HPLC buffer AB | Purification trial of larger paralogues | 0.075 % (w/v) DDM, 50 mM HEPES, 150 mM NaCl, 5 mM EDTA, 0.05 mg/ml Azolectin |
| HPLC buffer AC | Purification in DIBMA or amphipols | 50 mM HEPES, 150 mM NaCl, 5 mM EDTA |
| HPLC buffer D | Replacement of DDM by LMNG | 0.02 % (w/v) LMNG, 50 mM HEPES, 150 mM NaCl, 5 mM EDTA |

Buffers with the same identifier letter were used in one related purification procedure.
[a] 50 mM imidazole were only used for purifications of MscS.
[b] Solubilisation buffer C is prepared both with and without DIBMA
Na-phosphate buffer – $Na_2HPO_4$-$NaH_2PO_4$ buffer; PMSF – phenylmethylsulfonyl fluoride; LMNG – lauryl maltose neopentyl glycol; HEPES – 4-(2-hydroxyethyl)-1-piperazineethanesulfonic acid; EDTA – ethylenediaminetetraacetic acid; PMSF – phenylmethylsulfonyl fluoride

**Table 2.7 | Overview of detergents and polymers and their characteristics.**

| Detergent | Supplier | MW (Da) | CMC (mM) | CMC (%) |
|---|---|---|---|---|
| DDM | Glycon Biochemicals, Luckenwalde/Germany | 510.63 | 0.17 | 0.089 |
| LMNG | Anatrace, Maumee/USA | 1005.19 | 0.01 | 0.001 |
| DIBMA (Sokalan® CP 9) | BASF, Ludwigshafen/Germany | ~ 8400 | - | - |
| SMA (Xiran® SL 30010 P20) | Polyscope Polymers (now Orbiscope) Geleen/Netherlands | ~ 6500 | - | - |
| Amphipols A8-35 | Jena Bioscience, Jena/Germany | ~ 8000 | - | - |

**Cell lysis.** Frozen cells were thawed and supplemented with 100 µM PMSF and 5 mM ETDA and 2 mg/ml lysozyme and incubated on ice for 30-40 min, followed by one freeze-thaw cycle using liquid nitrogen. 10 mM $MgCl_2$ and 0.1 mg/ml DNase (Roche) were added, and after incubation on ice for 1 h, the lysate was cleared from cell debris by centrifugation for 30 min at 7200×g and 4 °C.

**Solubilisation.** The pellet was homogenised in 5 ml per 1 g original cell pellet in solubilisation buffer using a Dounce homogeniser with Teflon insert. After incubation on ice for 1 h, the supernatant was clarified by centrifugation at 7200×g and 4 °C for 30 min, and, if necessary, incubated with 10 mM $MgCl_2$ and 0.1 mg/ml DNase for further 10 min.

**Immobilised metal affinity chromatography (IMAC).** After solubilisation, the samples were filtered through a 0.22 µm or 0.44 µm syringe filter and were loaded onto a 0.5 ml prepacked Ni-NTA agarose (Sigma) Mobicol column (Biorad) equilibrated with wash buffer. They were washed with 40 ml wash buffer and eluted with elution buffer in four elution fractions (E0-E3) of 1 ml, with E1 being the fraction with the major protein content. The protein content of the single elution fractions was estimated by measuring the absorption at 280 nm (see section 2.3.2).

**Size exclusion chromatography.** Finally, the E1 IMAC elution fraction was filtered through a 0.1 µm centrifugal filter unit and further purified on a Superose 6 10/300 size exclusion column (GE Healthcare). For purification of MscS, also a Superdex 200 Increase column was used (GE Healthcare). Proteins were purified on the FPLC instruments Äkta Purifier (GE Healthcare) or NGC Chromatography System (Biorad).

**Reconstitution of MscS, YnaI, YbiO, and YjeP into Amphipols A8-35.** The IMAC elution fraction containing the DDM-solubilised protein was directly incubated with an eightfold excess (m/m) of Amphipols A8-35 (Jena Bioscience, Germany) from a 5 % (w/v) stock solution in water for 1 h at 4 °C. Subsequently, Bio-Beads SM2 (Biorad) were added at a concentration of 80 mg/ml and incubated with agitation at 4 °C overnight. The samples were further purified on a Superose 6 10/300 size exclusion column (GE Healthcare) in HPLC buffer AC.

**Detergent-free isolation of MscS, YnaI, and YjeP with SMA/DIBMA.** In this thesis, the term "detergent-free" is used to describe the absence of classic detergents. Cell lysis, DNase treatment and centrifugation were done as described above. The pellet was resuspended in 1.4 ml solubilisation buffer C per 1 g original cell pellet. Commercial styrene/maleic acid (SMA) or diisobutylene/maleic acid (DIBMA) are alkaline solutions and were dialysed beforehand for 1 d against 1 l solubilisation buffer C with the buffer being exchanged after 16 h using spectra/por dialysis tubing with 3.5 kDa MW cut-off (Spectrumlabs; *now Repligen*). The concentration of the copolymer after dialysis was determined by refractometry (uniREFRACTO 2 refractometer (LLG Labware), further diluted to a 5 % (w/v) solution, and added to the resuspended pellet at a final concentration of 2.5 % (w/v) (Oluwole et al., 2017). The samples were incubated at room temperature with gentle rotation for 20 h. After solubilisation, the samples were centrifuged at 7000×g and 4 °C for 30 min. The supernatant was filtered through a 0.44 µm syringe filter and loaded onto a prepacked Ni-NTA column, washed with 40 ml wash buffer C and eluted with elution buffer C. The protein-containing IMAC elution fraction E1 was further purified on a Superose 6 10/300 size exclusion column (GE Healthcare) in HPLC buffer AC.

**Extraction of LPC-treated YnaI from proteoliposomes.** LPC (table 2.9) can open MscS and MscL(Nomura et al., 2012; Perozo et al., 2002a, 2002b; Vásquez et al., 2008a). For the opening of YnaI, the DDM-purified protein was reconstituted into preformed DOPC/POPG (3:1) liposomes (see sections 2.3.3 and 2.3.4, table 2.9). 5 µM LPC (Nomura et al., 2012) was added to the proteoliposomes, and after incubation for 40 min at room temperature, 0.2 % (w/v) DIBMA was added, and the sample was incubated at room temperature for 20 h with gentle rotation. The sample was further purified as described in the previous paragraph.

**Delipidation and re-lipidation of MscS.** Lipids play an important role in determining the conformational states of MscS: removal of lipids from the pockets was proposed to lead to channel opening (Pliotas et al., 2015). To test whether and how MscS can be delipidated by increasing the solubilisation duration or the detergent concentration and kind of detergent, MscS was purified under different conditions as described above. It was first solubilised in solubilisation buffer A or B, containing 1 % (condition 0) or 1.5 % DDM (condition 1), respectively (table 2.6). The samples solubilised in 1.5 % DDM were further purified via a prepacked Ni-NTA column using wash buffer A (0.05 % DDM, condition 1) or B (0.5 % DDM, condition 2a) and eluted with elution buffer A (0.05 % DDM) or B (0.5 % DDM). For

purification of MscS in LMNG (condition 2b), MscS was solubilised in 1 % DDM, and the detergent was exchanged to LMNG on the Ni-NTA column with wash buffer D (0.03 % LMNG), eluted with elution buffer D (0.03 % LMNG). Subsequently, the samples were purified via SEC using HPLC buffer AB (0.03 % DDM, conditions 1, 2a) or D (0.02 % LMNG, condition 2b) and concentrated to ~ 5 mg/ml. A diagram of the workflow is given in figure 2.3. A cryo-EM and image analysis workflow (see sections 2.5.6 and 2.6.1) was applied to assess the conformational states of the different samples. For condition 3a, 0.1 mg/ml azolectin from a 10 mg/ml stock solution (in 0.5 % DDM) was added to the sample of condition 2a and incubated 30 min at room temperature before grids were prepared for cryo-EM.

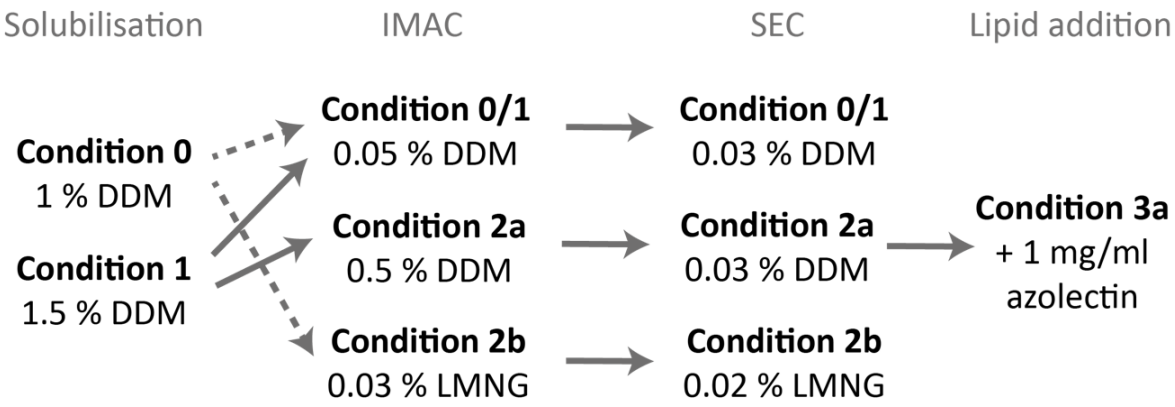


**Figure 2.3 | Workflow for delipidation/ re-lipidation of MscS.** MscS was solubilised under different conditions. Condition 0 refers to the standard purification (solubilisation in 1 % DDM, IMAC wash step with 0.05 % DDM, SEC in 0.03 % DDM). For condition 1, the DDM concentration in the solubilisation buffer was increased to 1.5 % DDM. For condition 2a, the DDM concentration was additionally increased in the IMAC wash step to 0.5 % DDM. The DDM concentration in the SEC buffer was maintained at 0.03 % DDM. For condition 3a, 1 mg/ml azolectin was added as mixed micelles. For condition 2b, MscS was solubilised in 1 % DDM and the detergent was exchanged to LMNG in the IMAC wash step.

**Solubilisation tests of YjeP with DIBMA.** Cells were lysed and treated as described and split into four equal parts after DNase treatment, resulting in four aliquots containing 1.1 g original cell pellet. The four aliquots were centrifuged at 7000×g and 4 °C for 30 min, and the cell debris pellets were further treated independently under different solubilisation conditions. DIBMA was prepared as described earlier, diluted to a 5 % stock solution, and the final volume of the sample was aimed to be [2x 1.4] ml per 1 g original cell pellet. As a control, one pellet was homogenised in 3 ml solubilisation buffer C supplemented with 1 mM DDM. The second pellet was first homogenised in 1.5 ml solubilisation buffer C containing 2 mM DDM before the addition of 1.5 ml DIBMA stock solution. For testing, whether less or more DIBMA is

beneficial for YjeP solubilisation, one pellet each was homogenised in a total volume of 3 ml, but the ratio of solubilisation buffer C and DIBMA stock solution was varied: For one trial, only one-third of DIBMA solution was used compared to standard, for the other three times the volume were used. Solubilisation was conducted overnight at 4 °C, and the next day, samples were centrifuged at 7000×g, 4 °C, for 30 min. Pellet (resuspended in $H_2O$) and supernatant of each sample were separated on an SDS-PAGE and analysed on a Western blot (see sections 2.5.3 and 2.6.1).

**Concentration and buffer exchange of protein samples.** HPLC elution fractions containing the desired protein complex were combined and concentrated using centrifugal filter units (Merck) with a cut-off molecular weight (MW) of 100 kDa for 500 µl protein sample. If a buffer exchange was necessary, the sample was concentrated to approximately 100 µl and filled up with target buffer. This procedure was repeated four to six times, and after the final centrifugation step, the sample concentration was determined.

### 2.3.2 Determination of protein concentration

Concentrations of purified proteins were determined photometrically with a 4050 Ultrospec II (LKB Biochrom) or a Genesys 50 (Thermo Scientific) UV-visible spectrophotometer. Absorption spectra were recorded at a wavelength range of 200-600 nm. Background subtraction at 320 nm was performed and the corrected absorbance at 280 nm ($A_{280,corr}$) was used in the Lambert-Beer equation [1] to calculate the protein concentration. Extinction coefficients were calculated with ProtParam (Expasy tools ("ExPASy - ProtParam tool,")) and are listed in table 2.8, among other characteristics.

$$c = \frac{A_{280_{corr}}}{\varepsilon_{280} * d} \qquad [1]$$

| | |
|---|---|
| $c$ | Concentration in mg/ml |
| $A_{280_{corr}}$ | Absorption at 280 nm corrected by absorption at 320 nm |
| $\varepsilon_{280}$ | Extinction coefficient at a wavelength of 280 nm in |
| $d$ | Path length |

**Table 2.8 | Selected parameters of proteins purified in this study.** The C-terminal His6 tag ($LEH_6$) is considered for every channel, as well as the cleavage of the N-terminal signal sequences in YbiO and YjeP.

| Protein name | Uniprot ID ("UniProtKB") | $MW_{subunit}$ (kDa) | $MW_{heptamer}$ (kDa) | $\varepsilon_{280}$ (mg/ml) |
|---|---|---|---|---|
| MscS | P0C0S1 | 31.82 | 222.74 | 1.019 |
| YnaI | P0AEB5 | 39.70 | 277.90 | 1.102 |
| YbdG | P0AAT4 | 47.54 | 332.78 | 1.373 |
| YbiO | P75783 | 80.91 | 566.37 | 1.327 |
| YjeP | P39285 | 122.80 | 859.60 | 1.012 |

## 2.3.3 Generation of small unilamellar liposomes

Unilamellar liposomes were generated from Azolectin (Sigma Aldrich), DOPC/POPG (3:1) lipid mixture produced from stock solutions in chloroform or from *E. coli* polar lipid extract (table 2.9) as described by Edwards et al. (1997). The lipid films were dried under an Argon stream, and the remaining chloroform was evaporated under vacuum before hydration buffer (150 mM NaCl, 50 mM HEPES pH 7.5, 5 mM EDTA) was added at a final concentration of 1 mg/ml lipid. After thoroughly shaking for 10 min and incubating at room temperature for 20 min, 5 freeze-thaw cycles were done (liquid nitrogen-cooled ethanol bath and 30 °C water bath). Multiple extrusion (Avanti Mini extruder) through a polycarbonate filter with a pore size of first 1 µM followed by extrusion through a filter with a pore size of 100 nm yielded predominantly small unilamellar liposomes.

**Table 2.9 | Overview of lipids used in this study.**

| Lipid and abbreviation | Full name, synonyms / composition | Supplier | MW (Da) |
|---|---|---|---|
| Phosphatidylethanolamine, PE | - 1,2-dioleoyl-*sn*-glycero-3-phosphoethanolamine (DOPE)<br>- 18:1 (Δ9-Cis) PE | Avanti | 744.034 |
| Phosphatidylcholine, PC | - 1,2-dioleoyl-*sn*-glycero-3-phosphocholine (DOPC)<br>- 18:1 (Δ9-Cis) PC | Avanti | 786.113 |

**Table 2.9 continues next page ►**

| | | | |
|---|---|---|---|
| Phosphatidylglycerol, PG | - 1-palmitoyl-2-oleoyl-*sn*-glycero-3-phospho-(1'-rac-glycerol) (POPG)<br>- 16:0-18:1 PG | Avanti | 770.989 |
| Cardiolipin, CL | - 1',3'-bis[1,2-dipalmitoleoyl-*sn*-glycero-3-phospho]-glycerol<br>- 16:1 CL<br>- Diacylglycerol (DAG) | Avanti | 1389.750 |
| Lysophosphatidylcholine, LPC | - 1-Acyl-*sn*-glycero-3-phosphocholin<br>- L-α-Lysolecithin | Sigma Aldrich | 503.334 |
| *E. coli* polar lipid extract | 67 % PE, 23.2 % PG,<br>9.8 % CL | Avanti | ~ 813 |
| Azolectin | Phospholipid mixture from soybean; mainly PC, cephalin and phosphatidylinsositol | Sigma Aldrich | ~ 1090 |

### 2.3.4 Reconstitution of MscS and YnaI into preformed liposomes

Proteins were reconstituted into the preformed liposomes via detergent removal by Bio-beads. According to Knol et al. (1996), this approach should lead to unidirectionally reconstituted proteins. The buffer of the Ni-NTA elution fraction of the DDM-solubilised protein was exchanged (50 mM HEPES pH 7.5, 150 mM NaCl, 5 mM EDTA, 0.03 % DDM), and DDM was added to the liposomes at a final concentration of 1 mM, followed by incubation at room temperature for 30 min. Proteins were added to the liposomes at a 1:1000 protein-to-lipid molar ratio MscS, YnaI and incubated at 28 °C for 1 h. Wet Bio-Beads SM2 (Biorad) were added at a concentration of 80 mg/ml and incubated at room temperature with gentle rotation. Further Bio-beads were added after 2 h and incubated overnight at 4 °C. The next day, Bio-beads were removed, and the proteoliposomes were stored at 4 °C.

For treatment with LPC, 5 µM LPC (final) were added to the proteoliposome dispersion and incubated for 40 min at RT. For subsequent cryo-EM application, the sample was vitrified immediately after the 40 min incubation time.

### 2.3.5 SDS polyacrylamide gel electrophoresis

Analysis of protein samples by their MW was achieved by discontinuous SDS polyacrylamide gel electrophoresis (SDS-PAGE) according to Laemmli(Laemmli, 1970). Buffers and solutions for SDS-PAGE are listed in table 2.10. Self-made 12 % gels (table 2.11) were cast using a mini gel system (Invitrogen). Samples were mixed with the appropriate volume of 5x Laemmli sample buffer, denatured for 5-10 min at 95 °C, and 15-25 µl were loaded onto a 12 % gel together with 5 µl prestained protein ladder (BlueEasy, NipponGenetics) as MW standard. Electrophoresis was executed in SDS running buffer at 100 V until samples entered the stacking gel, followed by 180 V until the loading dye reached the bottom of the gel. For detection of protein, gels were stained with colloidal Coomassie G250 solution (Roth) for at least 2 h and afterwards destained with water. Gels used for Western blotting were not stained.

**Table 2.10 | Buffers and solutions required for SDS-PAGE analysis and mini gel preparation.**

| Buffer/ solution | Composition |
|---|---|
| Separation gel buffer | 1.5 M Tris-HCl, pH 8.8 |
| Stacking gel buffer | 0.5 M Tris-HCl, pH 6.8 |
| 10x Laemmli running buffer | 3 % (w/v) Tris-HCl, 14.4 % (w/v) glycine, 1 % (w/v) SDS |
| 5x Laemmli loading buffer | 250 mM Tris-HCl (pH 6.8), 10 % (w/v) SDS, 5 % (v/v) β-mercaptoethanol, 50 % (v/v) glycerol, 0.05 mg/ml bromphenol blue |

**Table 2.11 | Pipetting scheme for four SDS mini gels.**

| Buffer/ stock solution | 12 % separating gel | 5 % stacking gel |
|---|---|---|
| Acrylamid/Bisacrylamid 40 % (v/v) | 12 ml | 2 ml |
| Water | 10.2 ml | 9.3 ml |
| Separation gel buffer | 7.5 ml | - |
| Stacking gel buffer | - | 3.8 ml |
| 10 % (w/v) SDS | 300 µl | 150 µl |
| 10 % (w/v) APS | 150 µl | 150 µl |
| TEMED | 15 µl | 15 µl |

APS – ammonium persulfate; TEMED – tetramethylethylenediamine

### 2.3.6 Western blot analysis

Western blotting (Towbin et al., 1979), followed by immunostaining, was implemented to detect certain proteins on a membrane. Required buffers and solutions are listed in table 2.12. The SDS gel, nitrocellulose membrane (Amersham™ Protran™ 0.45 µm NC, GE Healthcare) and filter papers were equilibrated in transfer buffer for 15 min. The components were assembled in a cassette in transfer buffer, and the cassette was placed in a wet transfer tank. The transfer was performed at a constant current of 400 mA and maximum voltage for 50 min (MscS), 60 min (YnaI and YbdG) or 80 min (YjeP), respectively. Afterwards, the membrane was optionally stained with Ponceau S solution to monitor transfer completeness and destained in water again. The membrane was blocked in 25 ml blocking buffer at room temperature for 1 h or at 4 °C overnight. Then, the membrane was washed three times in TBST buffer for 10 min. For immunodetection, a Penta-His-horseradish peroxidase (HRP) conjugated antibody (Qiagen, Germany) that binds to the C-terminal $His_6$ tag was employed, and 12.5 ml antibody solution were added to the membrane and incubated at room temperature for 1 h or at 4 °C overnight. The membrane was rewashed three times in Tris-buffered saline (TBS) with Tween (TBST) for 10 min before freshly prepared substrate solution was added immediately before visualisation with a Fusion FX imager (Vilber). For visualisation, enhanced chemiluminescence in auto mode was used.

**Table 2.12 | Buffers and solutions required for Western blotting.**

| Buffer/ solution | Composition |
|---|---|
| 1x transfer buffer | 24 mM Tris HCl pH 8.3, 194 mM glycine, 20 % (v/v) methanol |
| Ponceau S staining solution | 0.1 % (w/v) Ponceau S, 5 % (v/v) acetic acid |
| 1x TBST | 6.06 g/l Tris-HCl pH 7.6, 8.76 g/l NaCl, 0.1 % (v/v) Tween-20 |
| Blocking buffer | 3 % (w/v) milk powder (on-fat) in TBST |
| Antibody solution | 5 % (w/v) milk powder (non-fat) in TBST + 1:1000 Penta-His antibody |
| HRP substrate solution | 750 µl HRP substrate (Pierce ECL Western Blotting Substrate, Thermo Scientific) per membrane |

# 2.4 Physiological and analytical methods

## 2.4.1 Electrophysiological experiments

*The following paragraph is excerpted and extended from Flegler et al. (2020).**

The patch clamp technique allows recordings of single-channel currents in the picoampere (pA) range and provides an excellent method to characterise the behaviour of mechanosensitive channels. As *E. coli* cells are too small to be used for patch clamping, the cells are transformed to single filaments ("snakes") by applying cephalexin and finally to giant protoplasts by lysozyme and EDTA (figure 2.4). Protoplast generation was performed as reported previously (Blount et al., 1999b; Chesler and Szczot, 2018).

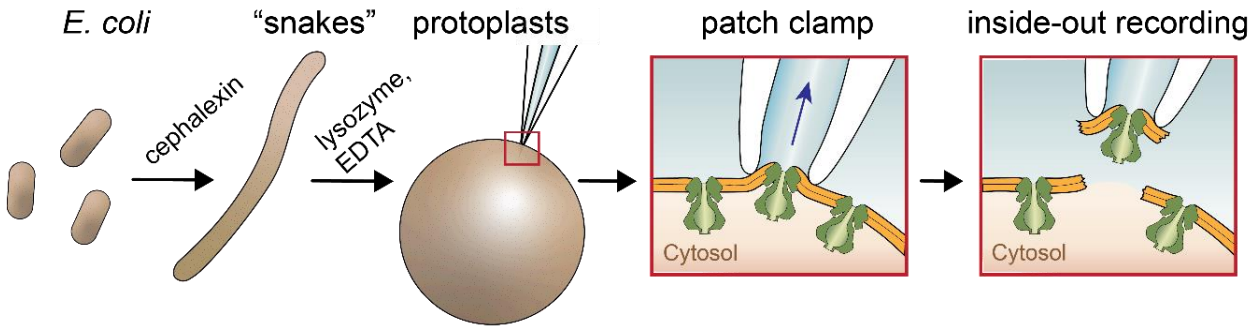


**Figure 2.4 | Patch clamping of *E. coli* protoplasts.** Induced *E. coli* cells were incubated with cephalexin to produce "snakes" that were further treated with lysozyme and EDTA to yield giant protoplasts. Tight contact is established between the pipette (white) and the plasma membrane (orange) by suction. Pulling the membrane leads to breaking the patch from the protoplast, enabling access to the cytosolic moiety of the channel ("inside-out" configuration).

Patch clamp recordings were conducted on membrane patches derived from giant protoplasts using the strain MJF429 (*ΔmscS, ΔmscK*) and for controls MJF641 (*ΔmscS, ΔmscK, ΔynaI, ΔybdG, ΔybiO, ΔyjeP, ΔmscL*) (table 2.13) transformed with plasmids (Edwards et al., 2012; Levina et al., 1999). The culture was induced with 1 mM IPTG for 90 min before protoplast generation.

**Table 2.13 | Cell strains used for protoplast generations.**

| Strain | Specifications | Source |
|---|---|---|
| *Escherichia coli* MJF429 | *ΔmscS, ΔmscK* | (Edwards et al., 2012) |
| *Escherichia coli* MJF641 ("Δ7") | *ΔmscS, ΔmscK, ΔynaI, ΔybdG, ΔybiO, ΔyjeP, ΔmscL* | (Edwards et al., 2012) |

Excised inside-out patches were analysed at an applied potential of +20 mV (YbiO) or +40 mV (YnaI) with pipette and bath solutions containing 200 mM KCl, 90 mM $MgCl_2$, 10 mM $CaCl_2$, and 5 mM HEPES buffer at pH 7.0. All data were acquired at 3-kHz filtration using a HEKA EPC-8 amplifier and Pulse software (HEKA Elektronik, Germany). The pressure threshold for activation of the YnaI or YbiO channels was referenced against the activation threshold of MscL ($P_{MscL}$:$P_{YnaI}$ or $P_{MscL}$:$P_{YbiO}$, respectively) to determine the pressure ratio for gating, as previously described (Blount et al., 1996). Measurements were conducted on at least six patches derived from a minimum of two independent protoplast preparations. Pressure ratios are given as mean ± standard deviation. Reference measurements with the WT channels resulted in $P_{MscL}$:$P_{YnaI}$ = 1.04±0.06 (n=6) for YnaI WT and of $P_{MscL}$:$P_{YbiO}$ = 1.16±0.19 (n=6) for YbiO WT and are in agreement with published values (Edwards et al., 2012).

* All electrophysiological experiments were carried out by Dr. Akiko Rasmussen from Prof. Dr. Rainer Hedrich's group (Botany I, Julius Maximilians University Würzburg).

## 2.4.2 Hypoosmotic downshock assay

The hypoosmotic downshock assay was used to study the survival rate of cells after a hypoosmotic shock and was performed as described earlier (Booth et al., 2007; Böttcher et al., 2015; Levina et al., 1999). The assay is indicative for LOF phenotypes, as these are much less able to protect *E. coli* from a hypoosmotic shock and lead to cell death. MJF641 (Δ7) cells were transformed with YnaI constructs (YnaI wildtype and mutants), and overnight cultures were grown, as well as for the Δ7 strain only. Additionally, the media for pre-cultures were prepared and incubated at 37 °C overnight. For both overnight and pre-cultures, control medium (table 2.14) was used.

**Table 2.14 | Media used for hypoosmotic downshock assay.**

| Medium | Composition/ setup |
|---|---|
| 2x LB medium | 20 g/l tryptone/peptone, 10 g/l yeast extract, 10 g/l NaCl |
| Control medium (0.3 M NaCl) | 10 ml 2x LB, 3 ml 2 M NaCl, 7 ml $H_2O$ |
| Shock medium | 10 ml 2x LB, 10 ml $H_2O$ |
| Control medium agar plates | 180 ml 2x LB, 60 ml 2 M NaCl, 120 ml $H_2O$, 5 g agar |
| Shock medium agar plates | 180 ml 2x LB, 180 ml $H_2O$, 5 g agar |

The next day, $OD_{650}$ was measured for the overnight cultures; pre-cultures were inoculated with the overnight cultures to give a starting $OD_{650}$ of 0.05 and were grown until an $OD_{650}$ of 0.4 was reached. The main cultures, which consisted of 18 ml of control medium supplemented with 0.3 mM IPTG preheated to 37 °C, were inoculated with ~2 ml of the pre-cultures and grown to an $OD_{650}$ of 0.3. 96-well-plates were prepared with control and shock medium according to the scheme in figure 2.5. Cells were then shocked by 20 times dilution into shock medium or as a control dilution into control medium. After an incubation of 10 min at 37°C, serial dilutions were conducted and plated on corresponding agar plates. From each dilution row, four repeats were plated. Plates were incubated at 37 °C overnight, and the survival ratio ($n_{shock}/n_{control}$) was determined by calculating colonies on the shock plates ($n_{shock}$) and culture plates ($n_{control}$). Mean values and standard deviations of the triplicate experiments are calculated for the ratio of shock to control.

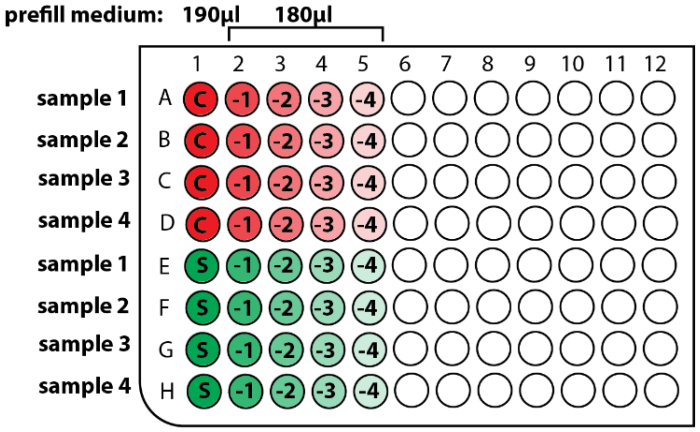


**Figure 2.5 | Pipetting setup for 96-well-plate hypoosmotic downshock assay.** For each sample, five wells were filled with control (C, red) and shock (S, green) medium as indicated. The arrangement in the 96-well-plate allows usage of a multipipette for serial dilutions (vertically) as well as for plating the dilution row (horizontally). The scheme was modified from Dr. Akiko Rasmussen.

### 2.4.3 Whole-cell Western blot analysis

The expression levels of YnaI mutants were tested by whole-cell Western blot analysis as described previously (Miller et al., 2003a, 2003b). MJF641 cells were transformed with YnaI constructs, purified to single colonies and 5 ml overnight cultures were grown. 30 ml LB medium for the pre-culture were prewarmed to 37 °C and inoculated with the overnight culture to give a starting $OD_{650}$ of 0.05. The preculture was grown to an $OD_{650}$ of 0.4, and meanwhile, 30 ml LB medium for the main cultures for each test (+IPTG) and control (-IPTG) were prewarmed to 37 °C. The main cultures were inoculated with the preculture such that the initial $OD_{650}$ was 0.05, and the $OD_{650}$ was monitored until an $OD_{650}$ of 0.4. Cells were then induced in exponential phase ($OD_{650}$ = 0.4) for 30 min with 0.3 mM IPTG. Subsequently, the $OD_{650}$ was measured ($OD_{650,harvest}$), and 1 ml of cells were harvested by centrifugation at 10000×g and room temperature for 1 min. For sample preparation for Western blotting, [2.2/$OD_{650,harvest}$*25] µl of the harvested cells were centrifuged at 10000×g for 1 min, and the pellet was resuspended in 20 µl of solubilisation buffer (20 % glycerol, 2 % SDS, 0.12 M Tris-HCl (pH 6.8), 0.5 g/l bromphenol blue, 2 % (v/v) β mercaptoethanol). Samples were heated at 100 °C for 10 min before loading onto an SDS gel. SDS-PAGE and Western blot were conducted as described in sections 2.3.5 and 2.3.6, respectively.

### 2.4.4 Thin layer chromatography

**Lipid extraction from protein samples.** Bound and attached lipids were extracted from protein samples prior to thin layer chromatography (TLC) following the method from Bligh and Dyer (1959) as described in Pliotas et al. (2015). In a glass test tube, chloroform, methanol and the protein sample in its respective buffer were added in a 1:2:0.8 volume ratio and mixed vigorously for 5 min. One volume part chloroform was added again, and mixing was continued for 1 min. Subsequently, one volume part (which is the same volume as chloroform) 1 M KCl was added, and after mixing for another minute, the tubes were centrifuged at 310×g for 5 min. The organic phase was transferred to a new test tube and dried under an argon stream. The lipid film was dissolved in 15-25 µl of chloroform to be spotted on a TLC plate.

**Thin layer chromatography of phospholipids.** A silica F254 TLC aluminium plate (20x20 $cm^2$, VWR (Darmstadt/Germany)) was heated on a hot plate at 70 °C for 10 min before use.

Lipid extracts in chloroform deriving from 250-500 µg of protein sample were spotted on the TLC plate together with lipid and detergent standards as references. A closed tank was lined with a 20x20 $cm^2$ filter paper, filled with chloroform, methanol and 1 M KCl in a 10:10:3 ratio as mobile phase (Pliotas et al., 2015). The spots were dried entirely before the plate was placed in the equilibrated tank until the mobile phase ascended two thirds to three-quarters of the plate. The plate was removed from the tank and, after drying, was stained with 0.05 % (w/v) primuline (Sigma-Aldrich, Munich/Germany) solution in acetone:water (8:2) and spots were visualised under a UV lamp (Skipski, 1975). To specifically detect phosphoethanol amine, the plate was sprayed with 0.1 % (w/v) ninhydrin (Alfa Aesar by Thermo Fisher Scientific, Kandel/Germany) in acetone:water (8:2) followed by heating at 120 °C until pink spots developed (Skipski et al., 1964).

### 2.4.5 High-mass MALDI mass spectrometry

*The following paragraph is unaltered excerpted from Flegler et al. (2020).* †

All mass spectrometric data were obtained in linear positive ion mode on a MALDI-TOF/TOF mass spectrometer (model 4800 Plus, AB Sciex, Concord/ON, Canada) equipped with a high-mass detector (HM2, CovalX AG, Zurich, Switzerland) (F. Chen et al., 2013). The HV1 and HV2 voltages of the HM2 detector were set to −3.5 kV and −20.0 kV, respectively. MALDI was initiated by a Nd:YAG laser pulse (355nm), and 500 shots per spectrum were accumulated. Sinapinic acid (TokyoChemical Industry, Eschborn) was used as the matrix for protein detection. Results are given as mean of 5 independent experiments with standard deviations.

† High-mass MALDI mass spectrometry was carried out by Na Wu from Prof. Dr. Renato Zenobi's group (Analytical Chemsitry, ETH Zürich).

## 2.5 Electron microscopy

### 2.5.1 Preparation of continuous carbon grids

For the generation of a thin carbon layer, graphite was thermally evaporated onto the freshly split side of a mica plate (2x2 cm, PLANO) in a DESK 4 sputter coater (Denton Vacuum). Prior to evaporation, the end of one graphite rod was sharpened, and the end of a second

graphite rod was ground on filter paper. The graphite rods are mounted in the coater so that the prepared ends of both graphite rods contact. In the coater, they are connected to voltage. When the chamber was sufficiently evacuated to a vacuum of approximately $6x10^{-7}$ Torr, the graphite rods were heated by application of a current of 15-20 mA for ~1 s until incandescence was observed. Care was taken that the graphite rods did not spark. The carbon layer was then floated onto copper grids: Therefore, a metal rack covered with filter paper was submerged in a glass beaker filled with water. 400 mesh copper grids (maxtaform, Agar Scientific) were cleaned by dipping into chloroform, dried, and placed on the filter paper. The coated mica sheet was gripped with forceps, and the carbon layer was carefully floated onto the water surface. Subsequently, the water level was lowered by initiating water drainage through a tube with a syringe until the carbon film covered the grids. The grids were dried on the filter paper overnight and baked for 10 min at 100 °C before use.

### 2.5.2 Negative-stain transmission electron microscopy

Negative-stain EM was primarily used for quality control of the samples and monitoring purifications. Carbon-coated 400-mesh copper-rhodium grids were glow-discharged (plasma cleaner PDC-002, Harrick) for 1-2 min at medium intensity before 6 µl of samples were added. If necessary, the samples were diluted in droplets of the respective buffer directly on parafilm before being incubated on the grid for 1 min. Then the grids were blotted, washed on three droplets of VE water and three droplets of 2 % uranyl acetate solution, with the last staining for 5-10 min. Excess liquid was removed by blotting in-between. Samples were imaged on an FEI Tecnai T12 electron microscope with a $LaB_6$ or tungsten filament at 120 kV using a single-tilt room temperature holder and recorded with an Eagle CCD camera at 4.4 Å/pix using SerialEM for low-dose imaging (Mastronarde, 2005). For the small data set of negatively stained YbiO, 60 micrographs were collected manually with a pixel size of 2.2 Å using Serial-EM. The micrographs were imported into *Relion* 3.1 and further processed without CTF estimation. Particles were picked automatically using the Laplacian-of-Gaussian blob picker with a minimum diameter of 250 Å and a maximum diameter of 300 Å, respectively. The data was purged in several rounds of 2D classification.

### 2.5.3 Electron cryomicroscopy

Quantifoil 400 mesh R 1.2/1.3 copper grids with circular holes were glow-discharged in air for 2 min at medium power (plasma cleaner PDC-002, Harrick). Subsequently, 3.5 µl sample were applied on the grids and plunge frozen in liquid ethane with a Vitrobot IV (FEI/ Thermo Fisher) and the following settings: wait time 0 s, drain time 0 s, blot time 3 to 7 s, blot force -5 to -25, chamber humidity 100 % and chamber temperature 4 °C. Alternatively, a manual plunging device, according to the design by Bellare et al. (1988), was used at room temperature with single-sided blotting of 8 s. The sample concentrations varied depending on the chosen reconstitution system: Samples of MscS and YnaI in Amphipols or DIBMA copolymer had ~0.4-0.5 mg/ml, while the MscS samples in detergent were concentrated to 4-7 mg/ml. YbiO in modified HPLC buffer AB (see table 2.6) was concentrated to ~5 mg/ml.
For checking of vitrified specimen, the samples were imaged using a Gatan 626 cryo-transfer holder in an FEI Tecnai T12 Spirit transmission electron microscope equipped with a $LaB_6$ or tungsten filament at 120 kV. Images were recorded with an Eagle CCD camera under low-dose conditions with a total exposure of ~30 $e^-/Å^2$ and a targeted underfocus of 2-3 µm. For image acquisition, SerialEM (Mastronarde, 2005) was used, and the micrographs were binned 2x, resulting in a pixel size of 4.4 Å/pix at specimen level. The grids were discarded after sample checking.
For data acquisition, vitrified grids were transferred to a Thermo Fisher Titan Krios G3 transmission electron microscope, and movies were acquired at 300 kV with a Falcon III camera at a nominal magnification of 75000, which corresponds to a calibrated pixel size of 1.0635 Å. For this, the cross-correlation between experimental EM maps and maps calculated from related crystal structures was maximized (Song et al., 2019). Data was collected with the EPU-acquisition software (Thermo Fisher) either in integrating or counting mode.

## 2.6 Image processing and model building

### 2.6.1 Single-particle image processing

Movies were motion-corrected and dose-weighted with *Motioncor2* (Zheng et al., 2017) and imported into *Relion* (versions 2.1, 3.0, or 3.1) for further data processing unless described

otherwise (Scheres, 2012). The contrast transfer functions (CTFs) were determined using *Ctffind4* (Rohou and Grigorieff, 2015). C7 symmetry was imposed in all 3D refinements. Nominal resolutions were determined in *Relion* during postprocessing after gold standard refinement for an FSC threshold of 0.143 and are corrected for the contribution of the mask.

For the processing of YnaI in Amphipols A8-35, motion-corrected micrographs were imported into cisTEM (Grant et al., 2018), CTFs were estimated, and particles were picked using a blob-based algorithm. Extracted particles were 2D-classified, and selected class averages showing side views were used to calculate an initial model with the ab-initio 3D reconstruction option embedded in cisTEM. The obtained initial model as well as the particles were exported to and further processed in *Relion* 2.1. Details are listed in table 3.1.

Particles for closed YnaI-DIBMALPs were initially picked with the Laplacian-of-Gaussian blob picker in *Relion* 3.0 (Scheres, 2012). After extraction with a boxsize of 300 px and a background diameter of 250 Å, the extracted particles were 2D classified. Three 2D class averages representing well-centred side views were used for template-based particle picking. Data was purged during several rounds of 2D classification. Particles in 2D classes showing contaminations, damaged or multiple particles, and top views were excluded from further processing, yet some classes exhibited off-centred particle averages. As a starting reference for a first iterative 3D refinement, the previously obtained map of YnaI in Amphipols was low-pass filtered to 30 Å. Particles were subjected to another 2D classification with a small search range and -step, and classes representing off-centred particles were discarded. Subsequently, further iterative rounds of 3D classifications and 3D refinements were started. For 3D masks used for 3D classifications, 3D refinements, and postprocessings, an initiation threshold between 0.012 and 0.015 was chosen. Additionally, the binary map was extended by 6-10 pixels, and a soft edge of 4-8 pixels was added. Finally, the best 3D class, showing the clearest density for the outer TM helices and containing most particles, was refined to 3.0 Å resolution. Further details for image processing of YnaI-DIBMALPs are given in chapter 3.1.3 and table 3.2.

For the data set of LPC-treated YnaI-DIBMALPs, particles were picked with *CrYOLO* (Wagner et al., 2019) and further processed in *Relion* 3.0. Particles were 2D-classified, already showing the presence of different conformational states. Selected particles based on side view classes were further 3D classified into three classes using a map of closed YnaI low-pass filtered to 30 Å as reference. One 3D class showed a map reminiscent of closed-like YnaI-DIBMALPs, and one class showed a different membrane domain. The particles in the classes representing the closed-like form were processed individually in consecutive rounds of 2D-

and 3D classifications, resulting in a map of the closed-like form at 3.8 Å resolution. Particles in the classes with the altered membrane domain were subjected to several 2D- and 3D classifications, resulting in two further maps: an open-like form (4.1 Å) and a structural intermediate between the closed and the open conformation (3.3 Å). Details are listed in table 3.3.

For data processing of MscS reconstituted in Amphipols A8-35 and MscS purified with DIBMA copolymer, particles were initially picked with *crYOLO* (Wagner et al., 2019) and processed in *Relion* 3.1 following the standard pipeline. In short, side-view 2D class averages from the extracted *crYOLO*-picked particles were chosen as references for autopicking. Subsequently, particles were extracted and purged in one or two rounds of 2D classification. An initial reference was generated in *Relion* based on particles from appropriate 2D classes and used for 3D refinement. Further rounds of 3D classifications and 3D refinements resulted in maps with resolutions of 4.1 Å (MscS-DIBMALPs) and 8.5 Å (MscS in Amphipols), respectively. Details are listed in table 3.4.

For all MscS data sets of the delipidation/ re-lipidation experiments, particles were picked with *CrYOLO* (Wagner et al., 2019) and further processed in *Relion* 3.1 (Scheres, 2012). After 2D classification, appropriate side view class averages were chosen for reference-based autopicking. Particles were purged in two rounds of 2D classification, discarding all projections along the C7 symmetry axis. An initial reference was generated in *Relion*. Per-particle CTF correction and beam tilt correction were conducted with the *CTFrefine* option embedded in *Relion*. In successive rounds of 3D refinements and 3D classifications, the maps were finally refined to 3.9 Å (condition 1), 3.1 Å (conditions 2a and 3a) and 2.3 Å (condition 2b). Further details are given in table 3.5.

For YbiO, 2372 particles were initially picked manually and 2D-classified. Selected classes served as templates for autopicking in *Relion*. The data was cleaned in two rounds of classification, and an initial model was generated in Relion based on particles from one class representing side views and one representing tilted views. A 3D refinement was conducted, subjected to 3D classification, and the best class was further refined to 3 Å. Details are listed in table 3.6.

### 2.6.2 Asymmetric image processing of closed-like YnaI-DIBMALPs

Asymmetric image processing was performed in *Relion* 3.0. The particles of the final map of closed-like YnaI-DIBMALPs obtained after consensus processing with C7 symmetry imposed were symmetry expanded (*relion_particle_symmetry_expand*) into 875000 asymmetric units. Thereby, each subunit was placed in the same position, and the symmetry expanded particles were subjected to a focussed 3D classification into five 3D classes with C1 symmetry, without alignment, imposing a regularisation parameter of T=4 and using a smooth mask on one subunit of the channel. Repetitively, the class with most particles was selected and classified into three 3D classes using regularisation parameters of T=15, T=20, T=8 and T=20. The regularisation parameter T is used to control overfitting, and larger values of T are required in masked classifications, as in 3D classifications, the resolution is estimated from the power spectrum of each reconstruction. However, in masked classifications, typically, only a small part is selected (Scheres, 2016). A map was calculated from the final 491770 asymmetric units (unmasked) with C1 symmetry (*relion_reconstruct*). The local resolution was calculated with *relion_postprocess*. A map of the most consistent particles was calculated with C7 symmetry imposed. The subset included particles of which all seven subunits grouped into the same class (8579 particles). These particles were locally refined (*relion_refine*) using C7 symmetry and a mask on the whole channel. The map was filtered for varying local resolutions with *relion_postprocess*.

### 2.6.3 Image processing of YnaI-proteoliposomes

For YnaI-containing proteoliposomes, a *CrYOLO* (Wagner et al., 2019) model was trained by manual picking of 193 particles (proteoliposomes without LPC) and 1011 particles (proteoliposomes with LPC), respectively, using *cryolo_boxmanager*. Automatic particle picking using the generated model resulted in 33856 particles (without LPC) and 140352 particles (with LPC). Upon extraction, particles were purged in several rounds of 2D classifications. The final number of particles ending up in classes that showed clear features of both the bilayer and the channel were 18480 particles (without LPC) and 15739 particles (with LPC).

### 2.6.4 Model building and refinement

De-novo model building for closed-like YnaI and YbiO was performed in *Coot* (Emsley et al., 2010) version 0.8.9.1. For closed-like YnaI, no density was visible for the eleven C-terminal residues, and no distinct side-chain densities were discernible for the two N-terminal transmembrane helices TM-N2 and TM-N1 as well as the loop connecting helix TM-N1 to helix TM-1. Hence, alpha helices with alanine residues were placed in these densities and are termed "UNK" (unknown) in the model. An atomic model of YbiO was built from residue 517 (located in helix TM2) to residue 723, and a fragment of helix TM2 was modelled as an alpha helix with "UNK" side chains. The ultimate C-terminal residues 724-741 were not modelled. *Phenix* (Adams et al., 2010) version 1.17.1 was used for real-space refinement imposing secondary structure restraints. The models were validated with *MolProbity* (Chen et al., 2010). For the model of open-like YnaI, the model of closed-like YnaI was placed in and adapted to the density of the open-like YnaI map. The loop connecting helix TM3a to helix TM2 as well as helix TM2 was placed in the gaussian filtered map for better visibility. The model was also real-space refined in *Phenix* and validated with *MolProbity* (Chen et al., 2010). Model building and real-space refinement for the different MscS conformations were performed in *Coot* (Emsley et al., 2010) version 0.9.2 and *Phenix* (Adams et al., 2010) version 1.19-4092. The structures of closed MscS in azolectin MSP nanodiscs (PDB 6RLD (Rasmussen et al., 2019a)) or open MscS in DDM (PDB 6AJI (Pliotas et al., 2015)) were used as starting models for modelling. The models were validated with *MolProbity* (Chen et al., 2010).
All images were created with *UCSF Chimera* versions 1.12 or 1.15 (Pettersen et al., 2004) or *UCSF ChimeraX* (Goddard et al., 2018; Pettersen et al., 2021).

## 2.7 Bioinformatical analyses

### 2.7.1 Prediction and simulations of pore hydration

*The following paragraph is unaltered excerpted from Flegler et al. (2020).* [$]
The pore size and hydrophobicity along the channel axis of each structure and through its cytosolic side-portals were determined using *CHAP* (Klesse et al., 2019). The likelihood of observing a hydrophobic barrier to permeation was predicted on the basis of the structures

alone according to a previously described model, derived from analysing ~200 ion channel structures (Rao et al., 2019). MD simulations were performed using *GROMACS* 2018 (Abraham et al., 2015), with each protein structure embedded in a POPC (1-palmitoyl-2-oleoyl-*sn*-glycero-3-phosphocholine) lipid bilayer membrane (Stansfeld et al., 2015), solvated on either side with the TIP4P/2005 water model (Abascal and Vega, 2005) and 0.15 M NaCl. The OPLS all-atom protein force field were used with united-atom lipids (Jorgensen et al., 1996). Temperature and pressure were maintained at 37 °C and 1 bar, respectively, using the velocity-rescaling thermostat (Bussi et al., 2007) and a semi-isotropic Parrinello and Rahman barostat (Parrinello and Rahman, 1981), with coupling constants of $\tau T = 0.1$ ps and $\tau P = 1$ ps. The integration time-step was 2 fs. Bonds were constrained through the LINCS algorithm (Hess et al., 1997), and positional restraints at a force constant of 1000 kJ $mol^{-1}$ $nm^{-2}$ were placed on backbone atoms of the protein to preserve its experimentally observed conformation whilst allowing for side chain flexibility. A Verlet cut-off scheme was applied, and long-range electrostatic interactions were calculated using the Particle Mesh Ewald method (Darden et al., 1993). Water free energy profiles were computed, by *CHAP*, on the final 20 ns of triplicate 30-ns equilibrium simulations, sampling at 500 ps intervals and applying a bandwidth of 0.14 nm for density estimation. Computational electrophysiology simulations were conducted, in triplicates of 200 ns, by applying an external uniform electric field in the membrane normal direction to generate a transmembrane potential difference of -200 mV or +200 mV, corresponding to negative or positive potential in the cytosolic side, respectively.

[$] All simulations were carried out by Shanlin Rao from Prof. Dr. Mark Sansom's group (Biochemistry, University of Oxford).

### 2.7.2 Alignments

Pairwise and multiple sequence alignments were generated with *Clustal O* version 1.2.4 (Madeira et al., 2019) or *COBALT* (Papadopoulos and Agarwala, 2007). For structural alignments, the *MatchMaker* and *Match -> Align* options embedded in *UCSF Chimera* version 1.15 were used. Sequence identity and sequence similarity were calculated based on the *Match -> Align* output file with the *Ident and Sim* server ("Ident and Sim").

### 2.7.3 Secondary structure prediction

For protein topology prediction based on the protein sequence, the *PSIPRED* server (Buchan and Jones, 2019) was used. In particular, *PSIPRED* 4.0 (Jones, 1999) was used for secondary structure prediction and *MEMSAT-SVM* (Nugent and Jones, 2009) for membrane helix prediction.

### 2.7.4 Interaction analyses

Salt bridges were analysed using the *Salt Bridges* function of *VMD* (Humphrey et al., 1996). Hydrogen bonds were identified using the function *Find HBonds* embedded in *UCSF Chimera* (Pettersen et al., 2004).

# 3 RESULTS

## 3.1 Structural and functional characterisation of YnaI

Although conductances apart from MscL and MscS were reported already 1997 (Sukharev et al., 1997), the first characterisation of YnaI was not described until 2012 (Edwards et al., 2012). YnaI was found to be stable in DDM, producing a pure product with a similar yield as MscS. However, the first structure of YnaI in 2015 showed that the complex prepared in DDM tended to aggregate on multiple points during concentrating, which was revealed by 2D class averages (Böttcher et al., 2015). As concentrating of YnaI in DDM seemed to be the critical step, several approaches were tried to find a suitable detergent-free system, enabling high-resolution structure determination of YnaI.

### 3.1.1 Purification and cryo-EM structure of YnaI in Amphipols A8-35

**3D reconstruction of YnaI in Amphipols A8-35 is limited by preferential orientation.** As YnaI was not incorporated into MSP nanodiscs, that proved successful for structure determination of MscS (Rasmussen et al., 2019a; Reddy et al., 2019) Amphipols A8-35 were tried for purification and structure determination of YnaI. Amphipols are amphipathic, short synthetic polymers that can substitute for detergents and are able to keep numerous different membrane proteins soluble in aqueous solutions (Tribet et al., 1996; Zoonens and Popot, 2014). Yu et al. (Yu et al., 2018) published a cryo-EM structure of *E. coli* YnaI in amphipols that showed a well resolved cytosolic vestibule and pore but did not resolve the sensor paddles. The purification of YnaI in Amphipols A8-35 showed a symmetric main peak with a maximum at 14 ml in the SEC chromatogram (P1) (figure 3.1 A), and the SDS-PAGE implied that the final YnaI sample is rather pure (figure 3.1 B). The additional band at ~40 kDa might be DnaJ, a bacterial HSP40 protein, that is a common contamination in protein purifications (Cuéllar et al., 2013; Winardhi et al., 2018). Although the theoretical MW of one YnaI monomer is 39.7 kDa, the band is visible at an apparent MW of ~35 kDa in the SDS-PAGE. It should be

noted that membrane proteins often show an anomalous migration in SDS-PAGEs, because a huge part of the membrane part is shielded by detergent (or polymer, respectively) molecules, which can impede SDS binding (Rath et al., 2009). The full-length of YnaI was confirmed by mass spectrometry (figure 3.1 D).

Monodisperse, homogenous particles were visible in both NS and cryo-EM micrographs (figure 3.1 C and E). A first 2D classification revealed that the majority of all picked particles are oriented in the ice with the symmetry axis perpendicular to the plane of the cryo-EM grid (figure 3.1 E). These views along the symmetry axis are referred to as "top views". Less than 2 % of the particles were present as side views that are necessary for 3D reconstruction. Data acquisition details and map parameters are listed in table 3.1. The top views clearly showed the sevenfold symmetry predicted for YnaI, while the side view 2D class averages displayed two distinct parts; one that is reminiscent of the cytosolic vestibule of MscS, and a TMD with several rod-shaped densities, corresponding to the TM helices. Compared to the 2D side view class averages of MscS, this moiety is less compact and reveals a huge indentation. A reconstruction with an overall resolution of 3.3 Å was obtained (figures 3.1 F, G) with a well resolved vestibule but a significantly less resolved TMD. Only helical densities for the TM helices 1 and 2 (according to the MscS nomenclature, see figure 1.3 C) are visible. The additional two helices are probably affected by the Amphipol belt; however, also the limited number of particles could play a role.

**Table 3.1 | Data acquisition and map parameters of YnaI in Amphipols A8-35.**

| | |
|---|---|
| **EMDB code** | **EMD-11558** |
| **Data collection** | |
| Microscope | Titan Krios G3 |
| Voltage (kV) | 300 |
| Camera | Falcon III EC |
| Data collection mode | linear |
| Electron exposure ($e^-/(Å^2)$) | 48 |
| Underfocus (µm) | 2.2 – 2.8 |
| Pixel size (Å) | 1.0635 |
| Number of movies | 3216 |
| **Map parameters** | |
| Final number of particles | 67740 |
| Symmetry imposed | C7 |
| Map resolution (Å) | 3.3 |
| Sharpening *B*-factor ($Å^2$) | -184 |
| Processing Software | *Relion* 2.1 |

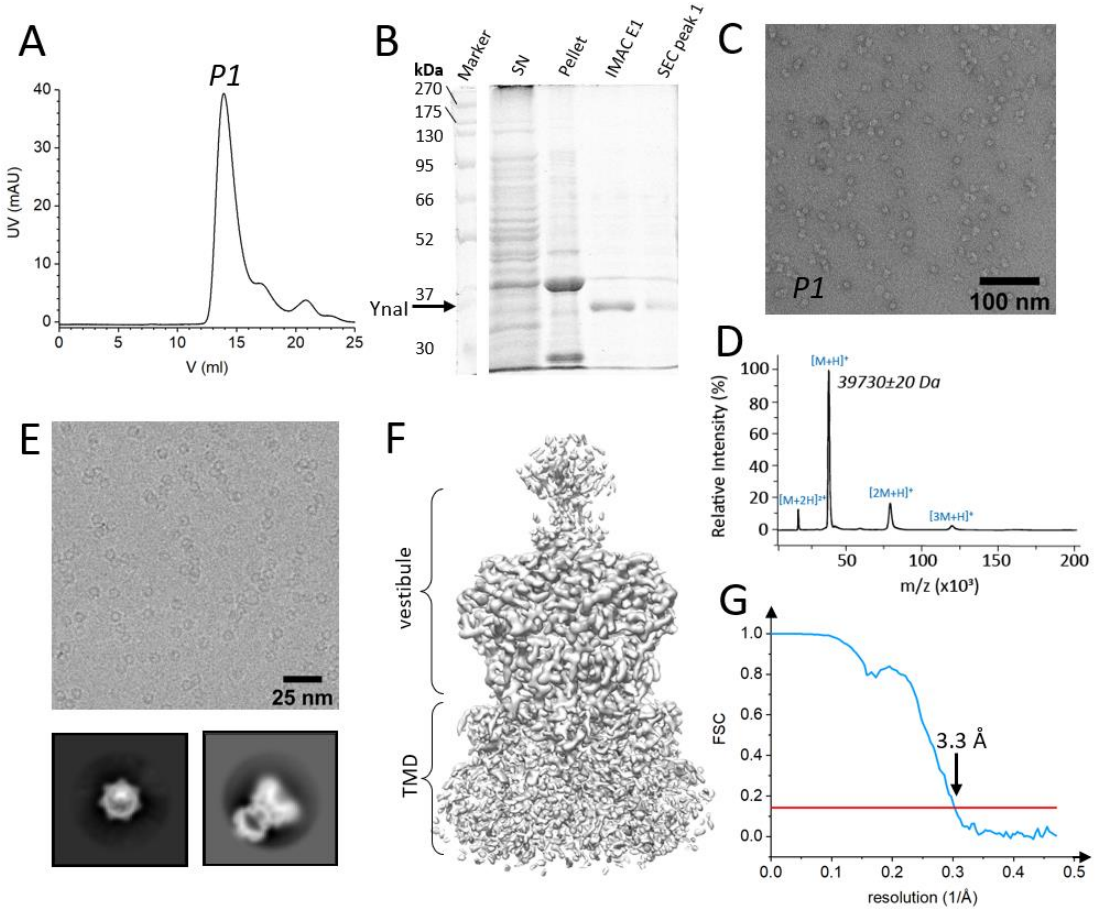


**Figure 3.1 | Purification and cryo-EM analysis of YnaI in Amphipols A8-35. (A)** The SEC chromatogram shows a symmetric main peak with its maximum at 14 ml (P1). **(B)** The purification was monitored by SDS-PAGE and the supernatant (SN) and pellet after solubilisation were applied on the gel, as well as the Ni-NTA elution fraction E1 (IMAC E1) before reconstitution into Amphipols A8-35, and the SEC elution fraction of the maximum of P1 after reconstitution into Amphipols A8-35. The position of YnaI is indicated by an arrow. **(C)** Part of an NS micrograph from SEC P1 (maximum) shows well distributed single particles. **(D)** The high-mass MALDI mass spectrum shows a mass of 39730±20 Da for YnaI (theoretical mass 39701 Da; initial methionine removed and additional $His_6$ tag ($LEH_6$) added), confirming the full-length of YnaI. **(E)** Part of a micrograph from the cryo-EM data collection and representative 2D class averages reveal the dominance of top view particles (> 98 %). The edge of the box corresponds to 25 nm. **(F)** The cryo-EM map at 3.3 Å resolution shows a well resolved cytosolic domain and a significantly worse resolved TMD. **(G)** Corresponding FSC curve with the threshold of 0.143 marked in red.

## 3.1.2 Detergent-free isolation of YnaI

**SMA copolymer cannot extract YnaI from *E. coli* membranes.** Styrene-maleic acid copolymer (SMA) was already shown in 2009 to extract membrane proteins from their lipid environment and to produce homogenous particles with diameters ranging from 9 to 11 nm (Knowles et al., 2009). Since then, it has been successfully applied to purify many proteins

(Dörr et al., 2014; Knowles et al., 2009; Morrison et al., 2016; Swainsbury et al., 2017), which were further subjected to cryo-EM analysis, many resulting in maps with sub-nanometre resolutions (Johnson et al., 2020; Parmar et al., 2018; Qiu et al., 2018; Sun et al., 2018; Tascón et al., 2020; Yoder and Gouaux, 2020; Yu et al., 2021). As an established system, it was tested whether SMA can solubilise YnaI from plasma membranes and reduce the preferred particle orientation in cryo-EM samples. SMA was added to the cell debris pellet after lysis and incubated overnight at room temperature (S. C. Lee et al., 2016). Photometric analysis of the IMAC elution fractions showed no signal at 280 nm indicative of protein content. This is supported by the associated SDS-PAGE (figure 3.2) because no band is visible for the IMAC elution fraction E1. However, the bands for the supernatant and the pellet around 35-40 kDa are not clearly distinguishable. One possibility is that YnaI is highly aggregated or not solubilised at all and therefore detected only in the pellet. Another option is that one of the bands in the lane of the supernatant is YnaI, but it is stuck to the column during IMAC. Nickel affinity purification of SMALPs is in general practicable (Pollock et al., 2018), yet it is still possible that the protein aggregates on the column and remains tightly bound. Either way, SMA cannot effectively solubilise YnaI and yield single particles, which is possibly caused by the limited nanodisc size achievable with SMA (Knowles et al., 2009).

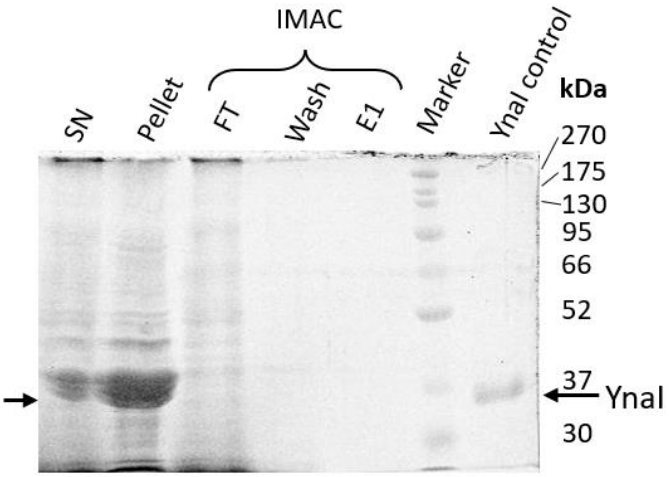


**Figure 3.2 | SDS-PAGE analysis of the purification of YnaI with SMA copolymer.** The supernatant (SN) and the pellet after solubilisation show that probably most of the protein is present in the pellet. No detectable protein signal is visible in the E1 elution fraction from the Ni-NTA column. The control is derived from YnaI solubilised in DDM. The black arrows indicate the position of YnaI.

**YnaI is extracted from *E. coli* membranes by DIBMA copolymer.** As an alternative to the SMA copolymer, the DIBMA copolymer was shown in 2017 (Oluwole et al., 2017) to extract membrane proteins from plasma membranes and assemble them into native nanodiscs. Like SMA, DIBMA was directly added to the cell debris pellet after lysis, and the polymer and cell debris pellet were incubated overnight at room temperature as similarly described by Grethen et al. for isolated membranes, showing that solubilisation at 4 °C or for shorter time periods

did not yield solubilised protein (Grethen et al., 2017). The photometric inspection of the IMAC elution fractions revealed that the protein yield is ~0.15 mg per 1 g cell pellet (wet weight). This is significantly less compared to the solubilisation of YnaI in DDM (~0.4 mg protein per 1 g cell pellet). SDS-PAGE analysis of the purification (figure 3.3 B) revealed that a notable amount of protein was still in the pellet after solubilisation, confirming partial protein solubilisation with the DIBMA copolymer. The IMAC E1 elution fraction showed a protein band at around 37 kDa on the SDS-PAGE, corresponding to YnaI. The protein was already vastly pure, but the IMAC was followed by a SEC (figure 3.3 A) to separate possible higher oligomers and aggregates. On the SEC chromatogram, the highest peak has its maximum at 8 ml elution volume (P1) and is followed by a shoulder (~12 ml, P2). Both peaks derive from YnaI as shown by SDS-PAGE, but negatively stained micrographs show that only aggregated particles are present in the first peak (figure 3.3 C), whereas there are both single particles and aggregates in the second peak (figure 3.3 D), probably owing to the large overlap of the peaks. Therefore, only fractions of P2 were pooled, concentrated to 0.4 mg/ml and prepared for cryo-EM data collection.

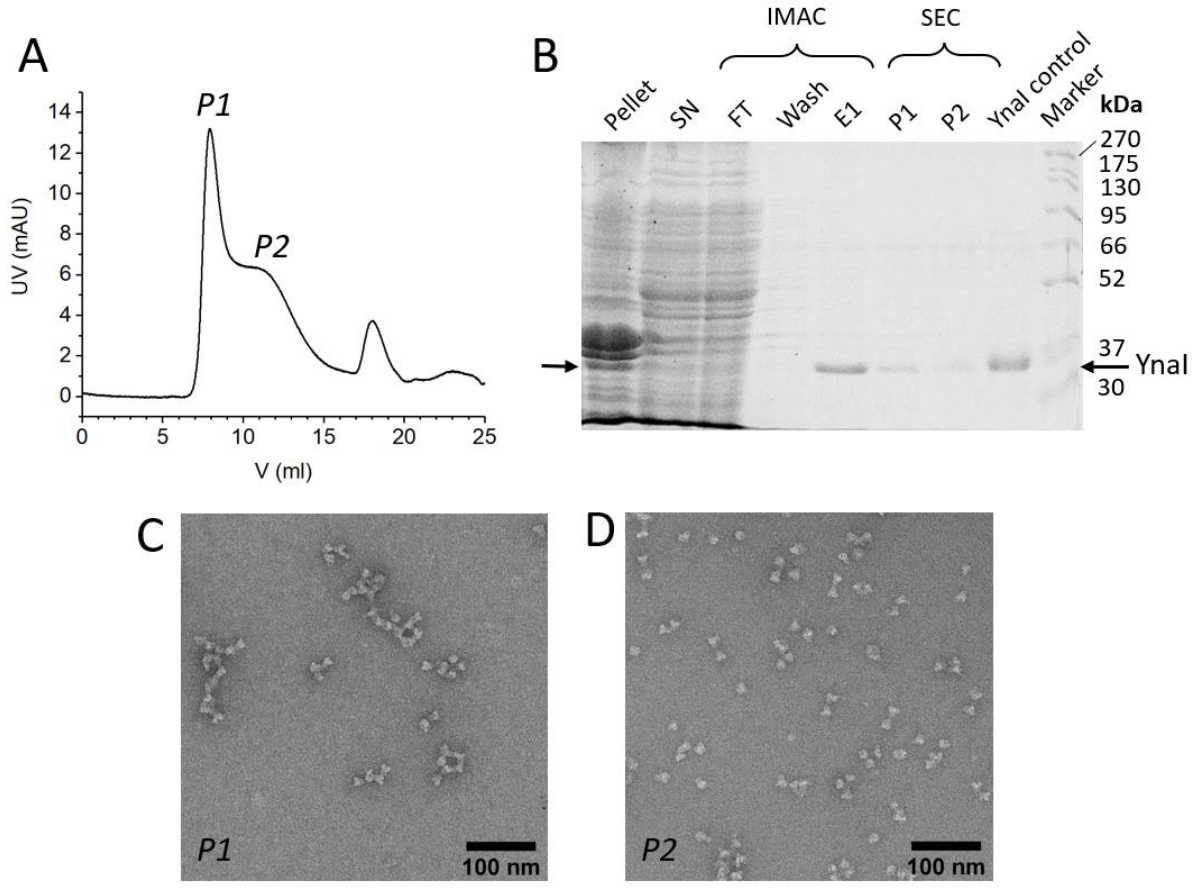

◄ **Figure 3.3 | Purification and analysis of YnaI-DIBMALPs. (A)** The SEC chromatogram shows two peaks that are not well separated, with maxima at 8 ml (P1) and ~12 ml (P2). **(B)** SDS-PAGE analysis was used to monitor the purification of YnaI-DIBMALPs. In the supernatant (SN) after solubilisation, there is much less YnaI detectable as in the pellet. The elution fraction E1 from the Ni-NTA column and the two SEC elution fractions of the maxima of P1 and P2 indicate pure protein. As a control, YnaI solubilised in DDM is shown. Micrographs of negatively stained YnaI-DIBMALPS of the SEC elution fraction of the maximum of **(C)** P1 shows aggregates and **(D)** P2 the presence of both single particles and dimers-/trimers-of-heptamers.

### 3.1.3 Structure of YnaI in its closed form in DIBMA-stabilised nanodiscs

**Preferential orientation is reduced in the YnaI-DIBMALPs data set.** Micrographs of vitrified YnaI-DIBMA lipid particles (YnaI-DIBMALPs) (figure 3.4 A) indicated no large aggregates in the data set, but mainly single particles and smaller aggregates consisting of only few particles. From more than 1.84 million initially picked particles, 64 % were grouped into 2D classes with clearly apparent secondary structure features during initial 2D classification. From these, 67 % resembled top views that were excluded from further processing. The 2D class averages equal those of YnaI in amphipols, exhibiting clear secondary structure features but a sharper membrane part. Besides the side views, also tilted views were present in this data set (figure 3.4 B) due to the reduced preferential orientation. Finally, a map with an overall resolution of 3.0 Å was calculated from 327161 particles (figure 3.4 C, D).

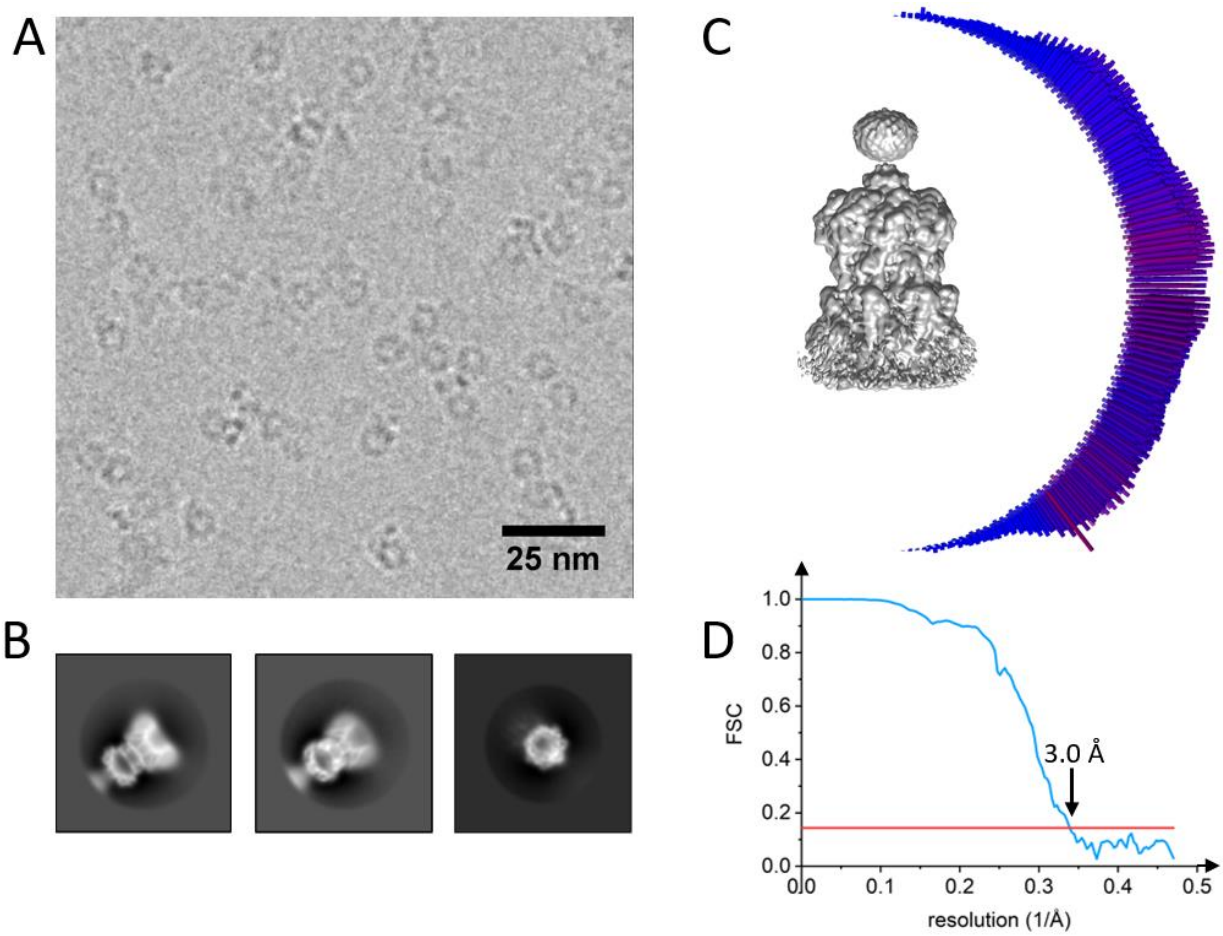


**Figure 3.4 | YnaI-DIBMALPs single-particle analysis. (A)** A representative part of a micrograph of vitrified YnaI-DIBMALPs used for data analysis is shown. **(B)** Typical 2D class averages. The edge of the box corresponds to 31.9 nm. Top views (right) were excluded from the reconstruction. **(C)** Surface representation of the final map without *B*-factor sharpening. The plot shows the angular distribution of the particle orientations. **(D)** Fourier Shell Correlation (FSC) curve of the map. The threshold of 0.143 is represented by the red horizontal line. Figure adapted from Flegler et al. (2020).

**Table 3.2 | Data acquisition and map parameters (A) and model parameters (B) of closed-like YnaI-DIBMALPs.**

**A**

| | |
|---|---|
| **EMDB code** | **EMD-11557** |
| **Data collection** | |
| Microscope | Titan Krios G3 |
| Voltage (kV) | 300 |
| Camera | Falcon III |
| Data collection mode | linear |
| Electron exposure ($e^-/(Å^2)$) | 81 |
| Underfocus (µm) | 1.4 – 2.3 |
| Pixel size (Å) | 1.0635 |
| Number of movies collected | 3958 |

**Table 3.2 continues next page ►**

| | |
|---|---|
| **Map parameters** | |
| Final number of particles | 327161 |
| Symmetry imposed | C7 |
| Map resolution (Å) | 3.0 |
| Sharpening *B*-factor (Å$^2$) | -109 |
| Processing Software | *Relion* 3.0 |

**B**

| | |
|---|---|
| **PDB code** | **6ZYD** |
| **Model composition** | |
| Non-hydrogen atoms | 34503 |
| Protein residues | 2268 |
| Ligands | 7 |
| **Validation** | |
| MolProbity Score | 1.57 |
| Clashscore | 5.07 |
| Poor rotamers (%) | 0.00 |
| *R. m. s. deviations* | |
| Bond lengths (Å) | 0.012 |
| Bond angles (°) | 1.164 |
| *Ramachandran plot* | |
| Favoured (%) | 95.65 |
| Allowed (%) | 4.35 |
| Outliers (%) | 0.00 |

**YnaI in DIBMA-stabilised nanodiscs is in a closed-like conformation.** The map is reminiscent of closed MscS and resembles the previous maps of YnaI in amphipols obtained in this study and an earlier published one (Yu et al., 2018). However, the map of YnaI-DIBMALPs revealed additional densities in the outer membrane part (figure 3.5). These densities must correspond to the two additional TM helices that are predicted for YnaI, and following the MscS nomenclature, they were named TM-N1 ("minus N-terminal") and TM-N2 (see figure 1.3 C). The quality of the map becomes noticeably worse towards this outer membrane part, and the additional helices could be better visualized in a gaussian-filtered map (figure 3.5). Helix backbones were placed in the densities for these two helices, but the map quality in this region did not suffice for side-chain model building (see figure 3.9 ). However, while the density for helix TM-N1 is clearly visible as such, the density of the outermost helix TM-N2 is very weak, and thus there is some uncertainty in the correctness of the model in this region. A later published cryo-EM map of YnaI in LMNG confirms the position of helix TM-N1 but shows differences in the morphology and position of helix TM-N2 (Hu et al., 2021).

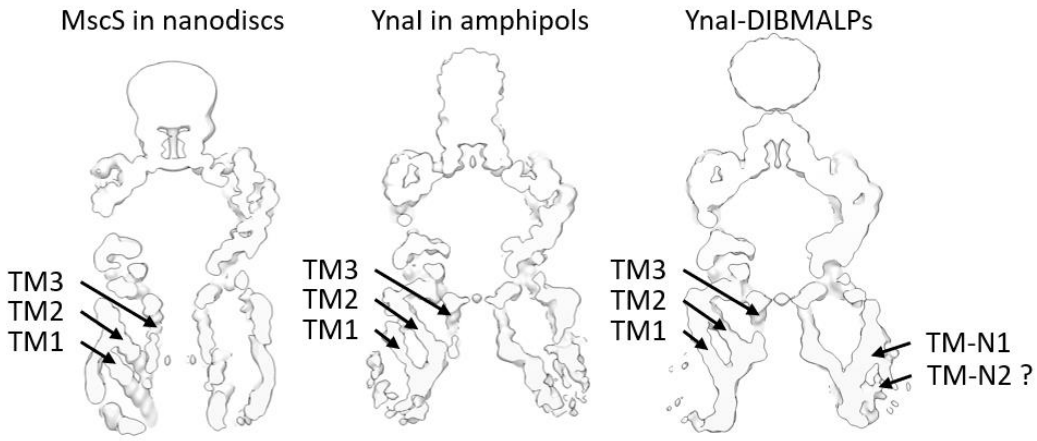


**Figure 3.5 | Comparison of the densities of MscS in MSP nanodiscs, YnaI in amphipols and YnaI-DIBMALPs.** Central slices are shown for the three aligned EM maps, and the densities corresponding to the transmembrane helices TM1, TM2, TM3, TM-N1 and TM-N2 are indicated for each. The map of YnaI-DIBMLPs shows a density of the helix TM-N1, but the helix TM-N2 can only be suggested. YnaI in Amphipols shows no distinct densities in the same region. All maps are shown at the same contour level and were gaussian-filtered for clarity (*Volume Filter* option embedded in *UCSF Chimera* (Pettersen et al., 2004); width 1.5; applied on *B*-factor sharpened maps). For MscS, a previously published EM map was used (EMDB-4919) (Rasmussen et al., 2019a).

The full-length YnaI comprises 343 amino acids. As the overall architecture of YnaI resembles that of the closed state of MscS, this YnaI conformation is referred to as "closed-like" (figure 3.6). YnaI assembles into a homoheptamer with overall dimensions of 125 Å (length along symmetry axis) and 95 Å (diameter) and is thus marginally shorter but slightly wider than MscS (135 Å and 90 Å, respectively).

The C-terminal β barrel of YnaI is shorter than in MscS, but it should be noted that the eleven C-terminal residues were not modelled in YnaI, while only six residues are missing in MscS (Rasmussen et al., 2019a). The lateral portals are remarkably smaller in YnaI, but the remaining part of the cytosolic vestibule, comprising the αβ and β domains and portals, are highly similar. This resemblance is also reflected by the root mean square deviation (r.m.s.d.) between the two models: superimposition of YnaI with MscS in a closed conformation (PDB 6RLD (Rasmussen et al., 2019a)) resulted in an overall r.m.s.d. of 1.8 Å for the α carbons for one subunit of each model aligned. This r.m.s.d. highlights the similarity between the two structures, despite having only a sequence identity of 10.7 % and a sequence similarity of 71.7 %.

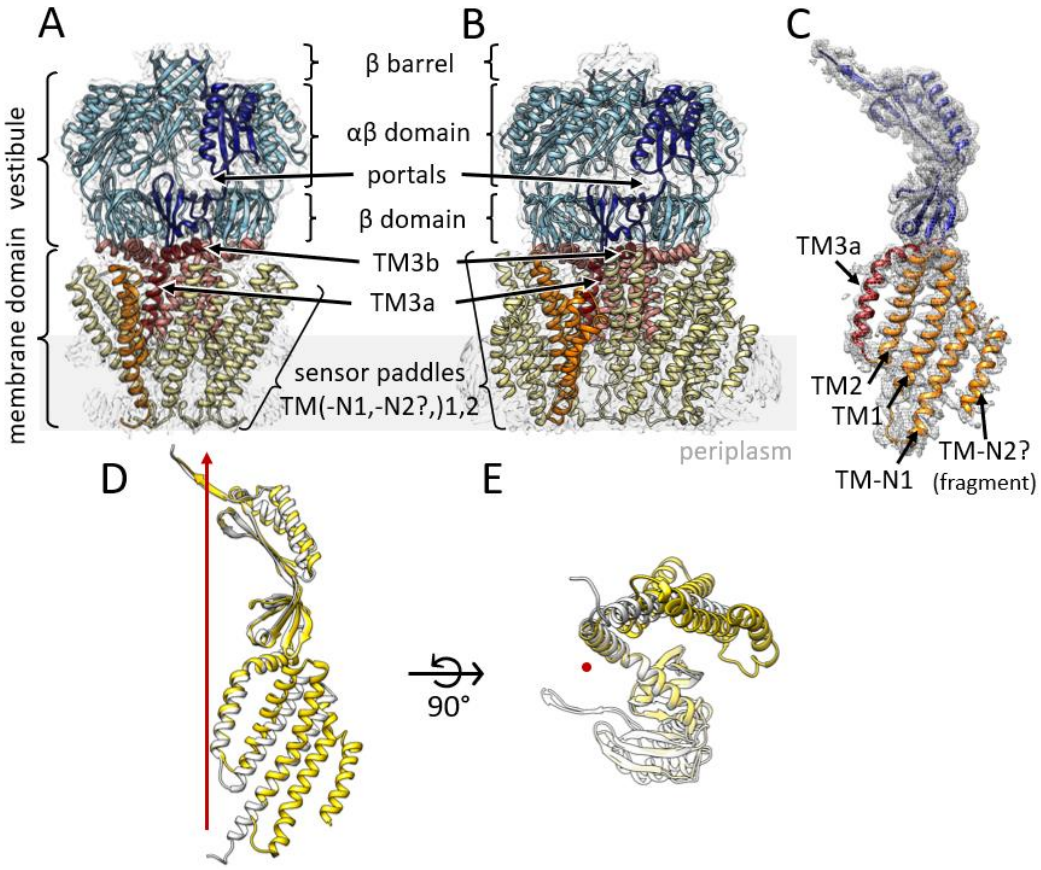


**Figure 3.6 | Cryo-EM structure of YnaI compared to MscS.** Side views of the atomic models of **(A)** MscS (PDB-6RLD and EMDB-4919 (Rasmussen et al., 2019a)) and **(B)** YnaI in their corresponding EM densities. The domains are coloured identically to highlight the similarity of the architecture of both channels: the cytosolic vestibule (blue), pore helices TM3 (red; separated by a kink into TM3a and TM3b), and tilted sensor paddles (yellow, orange). One subunit each is highlighted in dark colours. The membrane plane is indicated as a grey rectangle. **(C)** One subunit of YnaI is shown in its EM density (depicted as grey mesh). The map quality becomes gradually worse towards the outer TM helices. **(D)** Overlay of single subunits of YnaI (yellow) and MscS (white) viewed from the side and **(E)** along the symmetry axis (red arrow/dot) from the periplasmic side. The paddle of YnaI is extended by two additional TM helices compared to MscS, while only minor changes are visible in the vestibule. Part of the figure adapted from Flegler et al. (2020).

**The heptameric assembly is stabilised through interactions in the vestibule.** Most interactions present in the YnaI heptamer are intramolecular ones. To analyse how the heptamer may be stabilised, interactions between adjacent subunits were examined. Hydrogen bonds and salt bridges between adjacent subunits were exclusively observed in the vestibule. Three pairs of intermolecular salt bridges were found, that are R190 and D189, and R202 and D176 in the β domain and R236 and D210 in the αβ domain (see figure 3.30).

Excluding intramolecular hydrogen bonds from the analysis, the majority of hydrogen bonds was found in the β domain and the β barrel, where they connect adjacent β sheets. The β sheet

of one β domain extends to the neighbouring β domain via antiparallel β strands (figure 3.7 A). Involved residues are between S225 and N228 of one strand and P213 and Y215 of another strand. This observation is in agreement with a recently published YnaI structure (Hu et al., 2021). Furthermore, excessive hydrogen bonding is observed in the β barrel. For MscS, it has been shown that the β barrel is necessary for a stable assembly of the protein complex: mutants with the C-terminal residues deleted led to active channels that showed, however, changes in assembly or stability(Schumann et al., 2004). In YnaI, five inter-strand hydrogen bonds were identified between the residues P327 and D334 of each subunit that stabilise the intertwined parallel β strands of the barrel (figure 3.7 B).

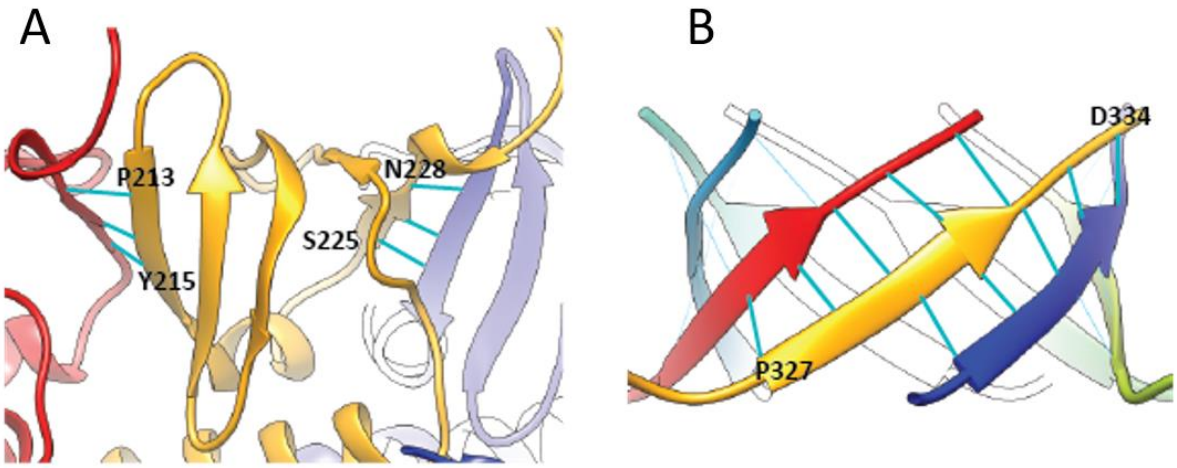


**Figure 3.7 | Intermolecular H bonds in YnaI. (A)** Hydrogen bonding in the β domain stabilises antiparallel β strands between two adjacent subunits. **(B)** Stabilisation of the C-terminal β barrel by intermolecular hydrogen bonds. Subunits are coloured uniquely, and hydrogen bonds are indicated as light blue lines. Residues that specify the region are shown.

**The TM helices 3, 2 and 1 of YnaI show minor differences to the analogous helices of MscS.** The TM3 helices are kinked at Asp162, corresponding to Gly113 in MscS, and dividing TM3 into TM3b and the pore helix TM3a. The kink angle between TM3a and TM3b is 125° for both MscS and YnaI, and TM3b is 20° tilted with respect to the plane of the membrane. With lengths of 20 and 19 amino acids, respectively, the TM3a helices of YnaI and MscS are comparably long, and both have two hydrophobic sealing rings within the cytosolic end of the pore, consisting of L105 and L109 for MscS and of L154 and M158 for YnaI. M158 in YnaI was proposed to be responsible for $Na^+$/K+ ion selectivity (Yu et al., 2018). The pore helices are N-terminally preceded by the sensor paddle helices TM1 and TM2. The characteristic tilt of the sensor paddle TM1 and TM2 of ~30° relative to the symmetry axis is maintained in YnaI, but the paddle in YnaI is rotated less around the symmetry axis than the paddle in MscS,

resulting in an almost linear arrangement of the three helices TM1, TM2 and TM3a (figure 3.6 E). Moreover, the membrane plane is visible in the map of YnaI. Only the periplasmic half of the membrane domain is embedded in the membrane, and the TM1 and TM2 helices protrude into the cytosol by 15 Å (figure 3.6 B, 3.8 A). The TM2 helices in both proteins are similarly long with a length of ~40 Å, but the TM1 helix of YnaI has a length of 47 Å and thus is significantly shorter than the TM1 helix in MscS with 59 Å. N-terminally to TM1, MscS has an anchor domain that is almost parallel to the membrane plane and interacts with the periplasmic membrane leaflet (Rasmussen et al., 2019a). YnaI instead exhibits a loop that connects to the additional helix bundle, helices TM-N1 and TM-N2.

**The outer paddle bundle is shifted against the inner paddle bundle.** The additional two TM helices TM-N1 and TM-N2 form a helix bundle that lies parallel to the inner helix bundle TM1 and TM2 but are shifted by ~15 Å towards the periplasmic side. With a length of ~45 Å, this bundle is completely buried in the membrane and does not protrude into the cytosol like the TM1-TM2 helix bundle. As it is shifted against the inner helix bundle, the pore of YnaI is partly lifted out of the plane of the membrane on the cytosolic side, resulting in an indentation in the membrane on the periplasmic side (figure 3.8 A) that is larger than in MscS. The staggered arrangement of the inner and outer sensor paddle gives the membrane domain of YnaI a dome-like architecture that encloses the indentation at the periplasmic side. The outer and inner helix bundles of the same subunit are tightly packed against each other, indicated by the close arrangement of TM-N1 and TM1 as well as by density bridges observed between these two helices (figure 3.8 B).

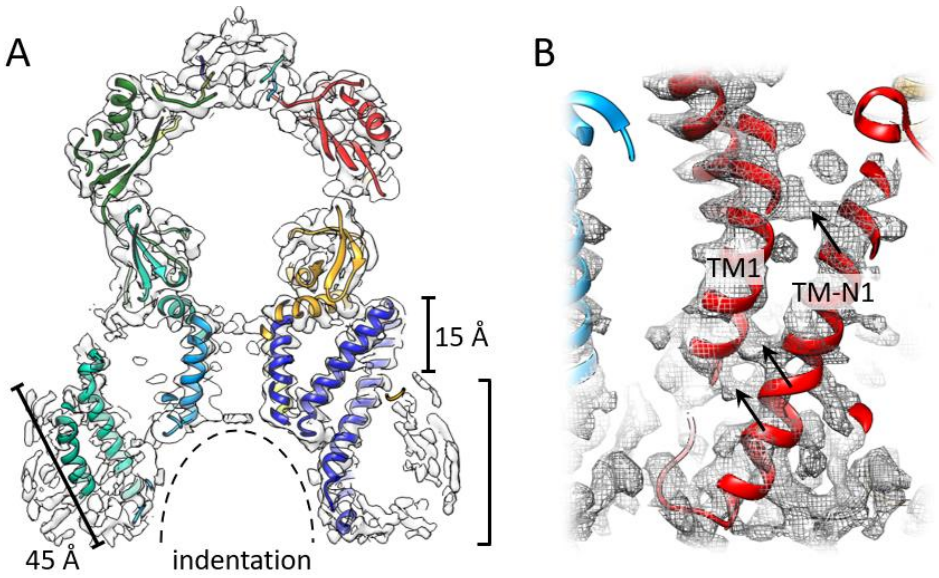


**Figure 3.8 | The inner and outer paddle bundles are staggered. (A)** A central slice of YnaI (coloured by its subunits) is shown in its EM density (white). The shifted organisation of the inner and outer helix bundle give rise to an indentation at the periplasmic side (dashed line). The inner helix bundle (visible in dark blue subunit) protrudes from the membrane (square bracket) by 15 Å. The length of the outer helix bundle (visible in turquoise subunit) is 45 Å. **(B)** The helices TM1 of the inner paddle bundle and TM-N1 of the outer paddle bundle of the same subunit (red ribbon; density depicted as grey mesh) are very close, which is underpinned by density bridges (arrows) observed between these two helices. Part of the figure adapted from Flegler et al. (2020).

The density quality in the membrane domain becomes worse towards the N-terminal helices, which did allow tracing of the helix backbone of the TM-N1, but no reliable assignment of the side chains. Moreover, the presence of helix TM-N2 could only be suggested based on the filtered map, and the density does not show helical features. A better resolved structure in the region of the helix TM-N2 shows a different position of this helix (Hu et al., 2021). Thus, the position of TM-N2 in the DIBMA structure mgith be not correctly modelled or the different experimental condition causes a different positioning of TM-N2. The behaviour of the TMD is also reflected in the *B*-factors of the model (figure 3.9 A), showing that the *B*-factors rise abruptly in the pore helix. This trend is also underpinned by the asymmetric classification of YnaI (figure 3.9 B, C). Upon symmetry expansion, the subunits of the complexes are classified individually, and only for a subset of complexes, all seven subunits ended up in the best-resolved class. The final map of these channels with C7 symmetry imposed again also shows the diminished resolution for the outer helices (figure 3.9 D). These findings imply that the extended sensor paddle becomes increasingly more flexible towards helix TM-N2 or, additionally, is damaged.

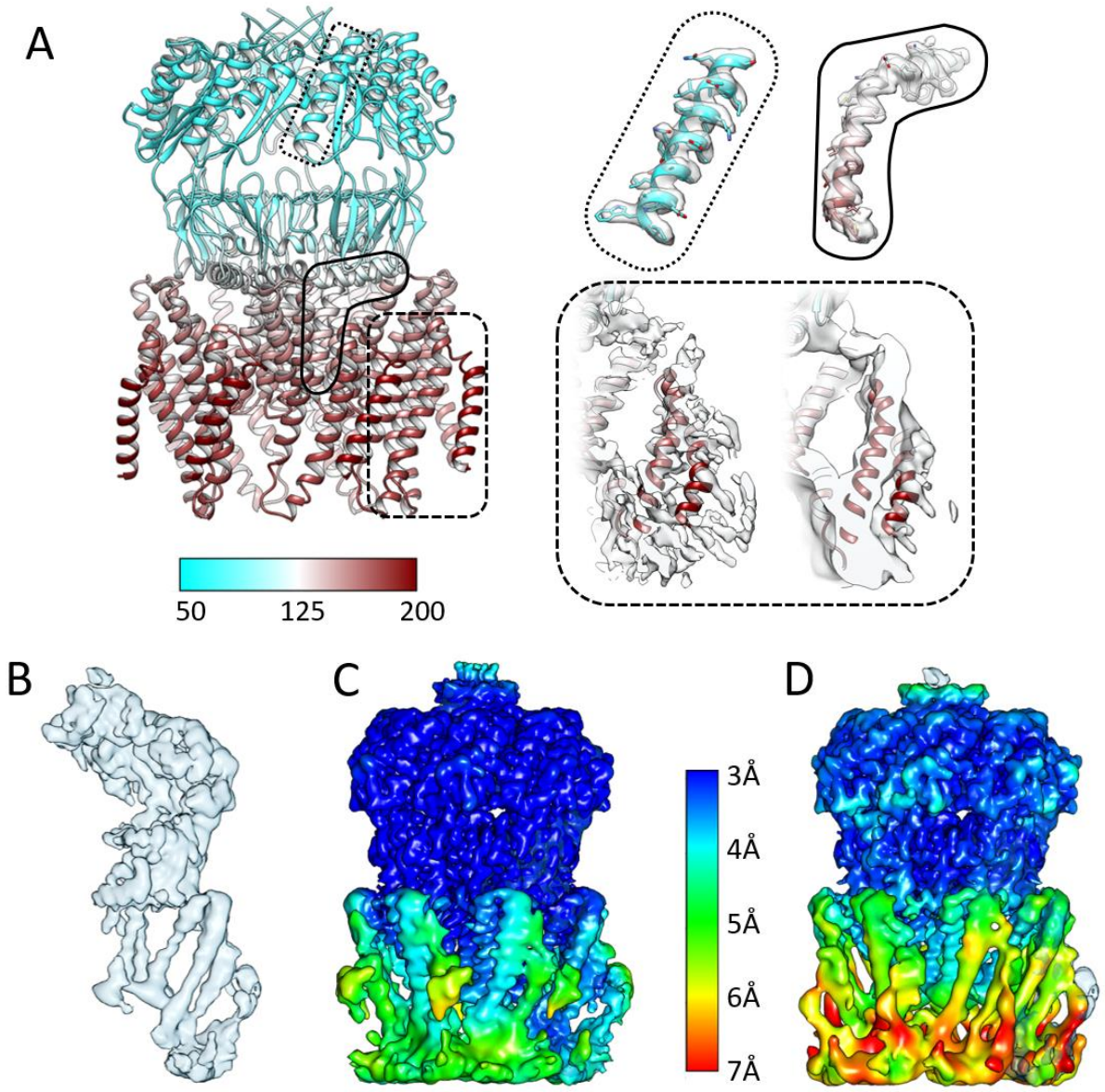


**Figure 3.9 | Local and asymmetric analysis of closed-like YnaI. (A)** The model of YnaI (left) is coloured by its local *B*-factors (determined with *Phenix* ADP-refine for the model with a sharpened map). Close-ups of different structural regions that are indicated by the boxes are shown on the right together with the respective map. *B*-factors are low in the cytosolic vestibule (dots), become abruptly higher at the TM3 helix (solid line). The outer paddle helices TM-N1 and TM-N2 (dashes) are shown in their respective map before (left) and after (right) application of a gaussian filter. **(B)** For the asymmetric classification of one subunit of YnaI, particles at the end of standard processing with C7 symmetry were symmetry expanded. With a mask for only one subunit and its immediate surroundings, the particles were classified without alignment imposing C1 symmetry. The particles that grouped in the best-resolved class were further classified until stable classes were obtained. **(C)** The final particles were used for calculating a map of the whole complex using C1 symmetry and no mask. The map is coloured by local resolution determined with *Relion*. **(D)** The most consistent particles were refined with C7 symmetry imposed: Only channels, of which all seven subunits grouped into the final class, were included. The map is filtered for local resolution and coloured according to its local resolution. The colour key is the same for (C) and (D). Figure adapted from Flegler et al. (2020).

**The transmembrane domain is propeller-shaped.** Viewed from the periplasmic side, the outer helix bundle comprising TM-N1 and the putative TM-N2 is clockwise rotated around the symmetry axis to a higher degree than the inner helix bundle formed by TM1 and TM2 (~ 30°; figure 3.10), which explains why it is only marginally wider in diameter than MscS despite having two additional helices per subunit. This is also a noteworthy difference compared to the eukaryotic mechanosensitive channel AtMSL1, which shows a similar overall architecture as *E. coli* YnaI, but has its TM helices arranged in an almost straight line (Deng et al., 2020; Li et al., 2020). The more recent structure of YnaI in the detergent LMNG confirmed the staggered arrangement of the inner and outer helix bundle, as well as the location of helix TM-N1, but reveals positional and orientational differences for helix TM-N2 and the loop connecting this helix to helix TM-N1 (Hu et al., 2021). These differences already indicates that the outermost helix TM-N2 likely is affected by the DIBMA copolymer because this helix is in direct contact with the polymer.

With the organisation of the helices, the transmembrane domain of closed-like YnaI resembles the shape of a seven-bladed propeller and reveals empty spaces between the single blades. Consequently, no inter-subunit interactions are observed between the paddle helices of adjacent subunits.

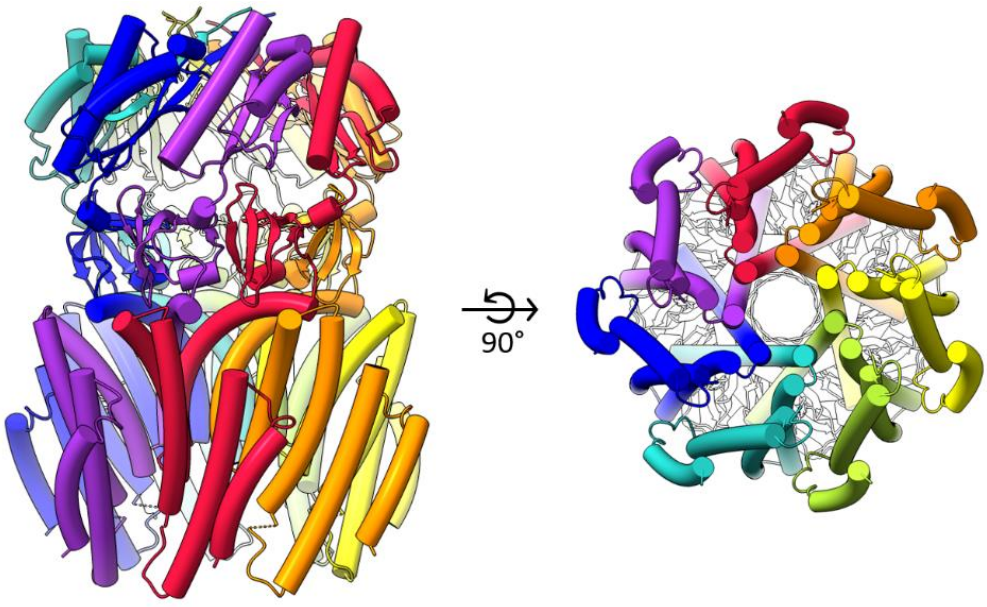


**Figure 3.10 | Arrangement of the α helices in YnaI.** Atomic model of YnaI viewed from the side (left) and along the pore axis from the periplasmic side (right). The helices are depicted as tubes, and subunits are coloured uniquely. The structural organisation of the TM helices is reminiscent of a seven-bladed propeller, and empty spaces are present between the single blades.

### 3.1.4 Coordination of lipids in the pockets of YnaI

**Lipids in the pockets change the pressure threshold required for opening.** The structural organisation of the membrane domain creates pockets between the kinked TM3 and paddle helices. The spatial separation of the paddles of different subunits gives rise to grooves between them, allowing lipids from the membrane bilayer to migrate into these pockets. After model building of the protein complex, unassigned densities exposed not only the position of the membrane bilayer (figure 3.11 A, B) but also showed that lipid shaped densities are present in the pockets (figure 3.11 A, C). One lipid molecule per subunit was modelled in the lipid shaped density. As the resolution did not allow a reliable assignment, a PE molecule was chosen to be modelled as this is the most abundant lipid in *E. coli* (Raetz and Dowhan, 1990). Besides, this assignment was supported by TLC (figure 3.11 G). The phosphate headgroup of the resolved lipid is in close proximity to K108, which is located in the loop connecting the TM1 and TM2 helices and is likely to form a salt bridge via its $\varepsilon$-amino group (figure 3.11 D). To probe the involvement of this lysine in the lipid coordination, it was mutated to an uncharged leucine (K108L). In electrophysiological experiments the $P_{MscL}$:$P_{YnaI}$ ratio for the K08L mutant increased from 1.04 ± 0.06 to 1.24 ± 0.09 (both n = 6; Student's unpaired t-test: P = 0.0018), exhibiting normal staircase-like activities (figure 3.11 E). This means that less pressure is required to open the mutant channel, highlighting that the coordination of a lipid molecule by K108 is important for sensing.

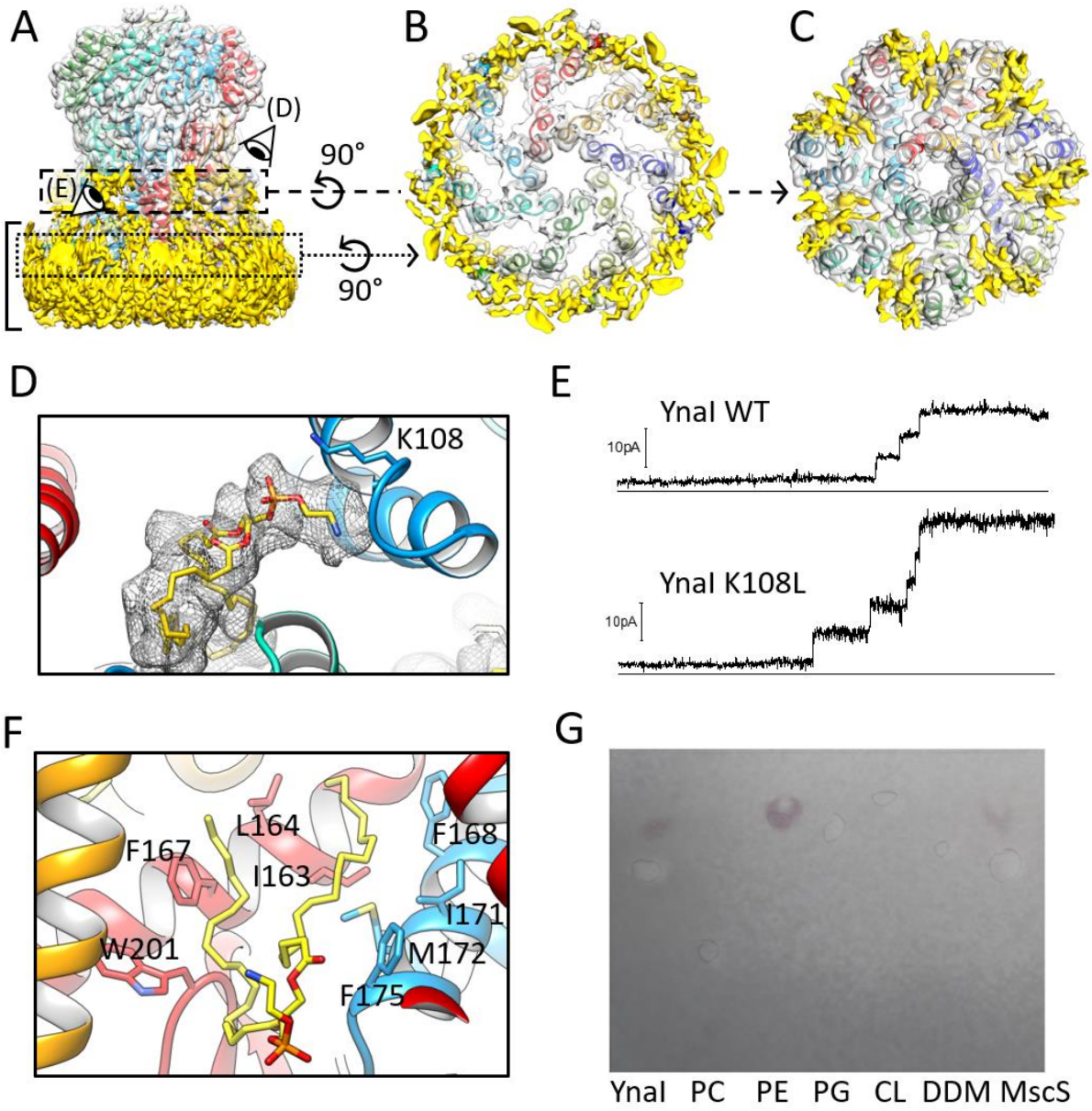


**Figure 3.11 | Interaction of YnaI with lipids. (A)** The side view of closed-like YnaI shows the atomic model (subunits are coloured uniquely) in its respective map (white), and unassigned densities are coloured yellow at the same contour level. The bracket indicates the position of the membrane. **(B)** shows the slice highlighted in the dotted box in A viewed along the symmetry axis from the periplasmic side. The space between the paddles of adjacent subunits is empty, and the outer paddle helices TM-N1 and TM-N2 are buried mainly in the membrane-/polymer belt. **(C)** shows the slice highlighted in the dashed box in A viewed along the symmetry axis from the periplasmic side. Elongated densities project towards the symmetry axis. **(D)** The view into a pocket from the cytosolic side as depicted in A shows a PE lipid molecule (yellow) in its density (grey mesh). The phosphate headgroup of the lipid is near K108. **(E)** Patch clamping traces of YnaI WT (top) and the mutant K108L (bottom) indicate that K108L shows normal staircase-like openings and a conductivity similar to WT YnaI but requires a lower tension for opening. **(F)** In the close-up of a pocket from the periplasmic side, the PE lipid molecule is shown in yellow. Selected hydrophobic residues that are mainly in the TM3b helices of adjacent subunits are shown and labelled. **(G)** TLC analysis of the lipid extract from 275 µg YnaI solubilised and purified in DDM under standard conditions implies that PE is predominantly associated with the

◄ protein complex, as also observed for MscS (lipid extract from 305 µg protein). The picture is an overlay of the analysis of the TLC plate under UV light (bright spots framed with pencil) and after treatment with ninhydrin (purple spots). 15 µg from all lipid- and DDM standards were applied on the plate. The discrepancy in the migration observed for PE for YnaI and MscS and the PE control is probably caused by a non-ideal solvent front. Part of the figure adapted from Flegler et al. (2020).

**The pockets are populated by numerous hydrophobic amino acid residues.** The lipid tails of one PE molecule face towards the sevenfold symmetry axis. Within the range of 4-6 Å of the lipid tails, F168, I171, M172 and F175 are found on one TM3b helix, and I163, L164 and F167 on an adjacent TM3b helix. W201 protrudes from a loop in the β domain into the pocket and is also near a lipid tail (figure 3.11 F). These residues contribute to the hydrophobicity of the pockets and favour the coordination of the lipid molecules. This finding is in agreement with previous tryptophan fluorescence quenching experiments that showed, e.g. that F168W is highly accessible to lipids (Böttcher et al., 2015). W201 did also show small quenching by brominated lipids, but G152W, which is located in the TM3a helix and had shown high accessibility to lipids, too, is not found within the immediate proximity of the lipid tails. It should be noted that due to the limited density quality in the pockets, only one lipid per subunit was modelled. However, the additional density in this region (figure 3.11 C) indicates the presence of at least another lipid per pocket, similarly as seen for MscS, where two lipids were resolved (Rasmussen et al., 2019a). So, it is nonetheless probable that G152 is near a lipid.

**Phosphatidylethanolamine is the predominantly co-purified lipid.** One-dimensional TLC was applied to analyse the lipids that co-purify with YnaI. Therefore, YnaI was solubilised and purified in DDM under standard conditions and lipids from 275 µg protein sample were extracted and applied on a TLC plate together with lipid standards. Only PE and DDM were detected in the YnaI lipid extract (figure 3.11 G). The inner membrane of *E. coli* grown at 37 °C is composed of approximately 75 % PE, 19 % PG and 6 % CL (Morein et al., 1996). However, trace lipids like phosphatidylserine (PS) and phosphatidic acid (PA) that are also present in *E. coli* membranes (Oliver et al., 2014) have not been tested, or their possible significance for the coordination in YnaI could get lost due to the overexpression of the protein. It should be stressed that for TLC analysis, YnaI was solubilised and purified in detergent and not with DIBMA. Nonetheless, the PE observed in the TLC must be co-purified and thus, originate from the plasma membrane, which also holds true for DIBMA-solubilised YnaI because no lipids were added during purification. Contrary, Hu et al. (2021) recently observed enrichment of PS and CL in their YnaI preparation, also solubilised in detergent.

### 3.1.5 Structure of YnaI in an open-like conformation

**LPC-treated YnaI can be extracted from proteoliposomes using DIBMA.** The open conformation of MscS has been addressed either by a point mutation in the pore (Wang et al., 2008) or the choice of detergent (Lai et al., 2013). With DIBMA being able to extract YnaI from membranes, it was tested whether YnaI could be activated in a membrane prior to extraction. The lysolipid LPC has been shown to open MscL and MscS in patch clamp experiments (Perozo et al., 2002a, 2002b; Vásquez et al., 2008a). Therefore, DDM-purified YnaI was reconstituted into DOPC:POPG (3:1) proteoliposomes and subsequently treated with LPC. Though PC is not a native *E. coli* lipid, this composition was chosen because it led to less aggregation of MscS channels in earlier reconstitution experiments (Vásquez et al., 2008b). 5 µM LPC (Nomura et al., 2012) were added to YnaI proteoliposomes (figure 3.12 C), and the channels were isolated using DIBMA copolymer. The experimental approach is depicted in figure 3.12 A and was monitored with SDS-PAGE analysis (figure 3.12 B), showing that the majority of YnaI was successfully eluted from the IMAC column and is still full-length. Both the negative stain and cryo-EM micrographs show monodispersed and homogenous particles but predominantly as top views (figure 3.12 D, E). This is different from the increased number of side views in the previous YnaI-DIBMALPs data set and hints that the observed reduced preferential orientation is a consequence of aggregation.

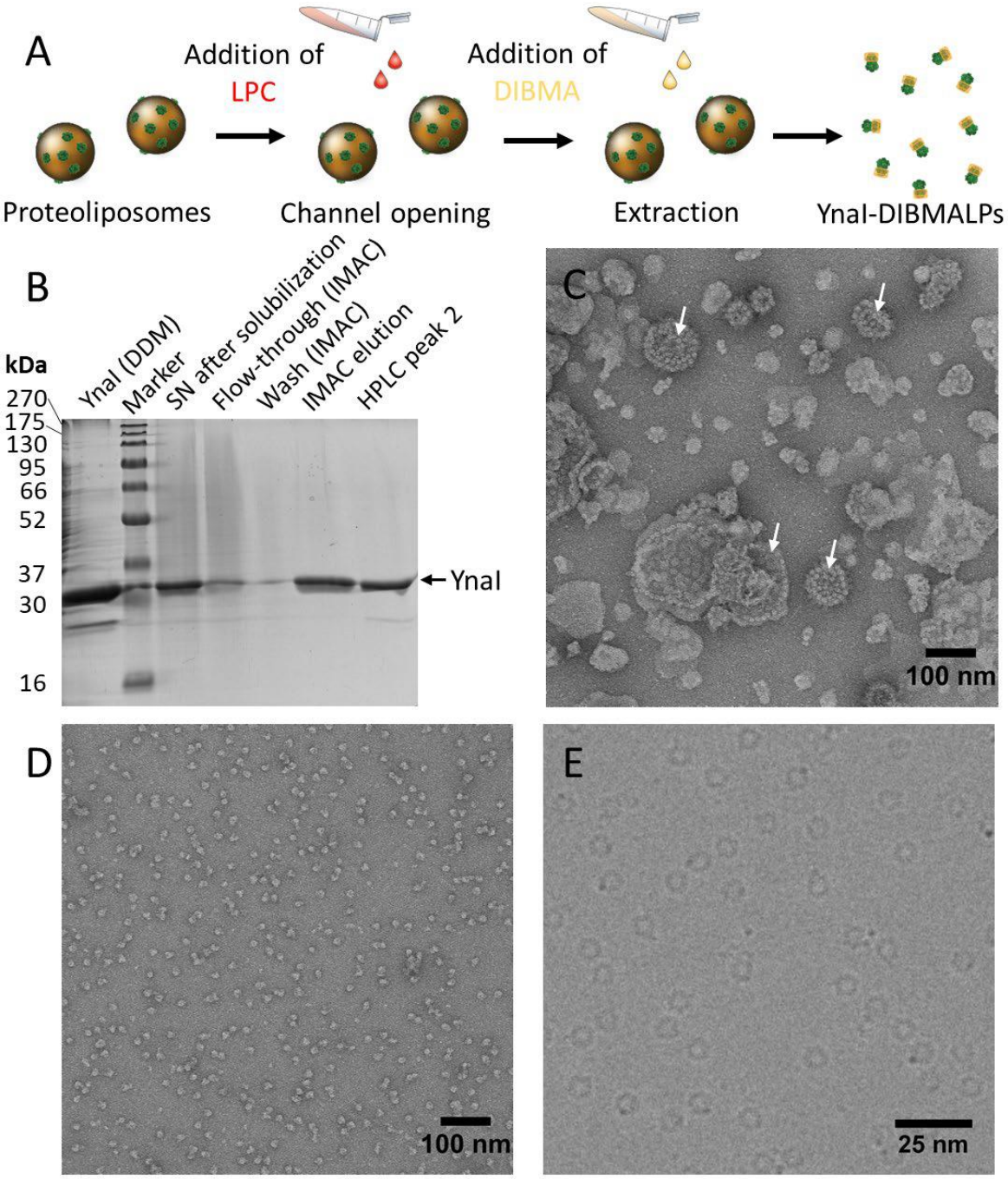


**Figure 3.12 | Extraction of LPC-treated YnaI from proteoliposomes. (A)** Experimental design for activating YnaI with LPC prior to extraction from membrane vesicles with DIBMA copolymer. **(B)** Sample preparation was monitored by SDS PAGE: DDM-purified YnaI was purified via IMAC (YnaI (DDM)), and after a buffer exchange reconstituted into preformed liposomes. LPC was added to the proteoliposomes before the addition of DIBMA. The supernatant (SN; after solubilisation in DIBMA and subsequent centrifugation) and samples from the following purification confirm that YnaI is still full-length after the complete procedure. **(C)** The negatively stained micrograph shows that YnaI is reconstituted into liposomes (white arrows). **(D)** Negatively stained micrograph of LPC-activated YnaI-DIBMALPs. **(E)** A representative part of a micrograph of vitrified particles from the cryo-EM data collection. Figure adapted from Flegler et al. (2020).

**Three different conformations of YnaI are present in the data set.** A data set consisting of 4161 movies was collected and analysed. During image processing, 2D class averages already showed two differently shaped membrane domains of YnaI (figure 3.13): One looks like the closed-like channel that was isolated directly from native E. coli membranes and accounted for about 13 % of all side view projections. The other arrangement showed significant differences in the membrane part: its width perpendicular to the membrane is reduced as well as the indentation that is plainly visible on the periplasmic entry side of the closed channel. Further 3D classification resulted in three different conformations that were individually processed (figure 3.14, figure 3.15). The data collection and map parameters are listed in table 3.3.

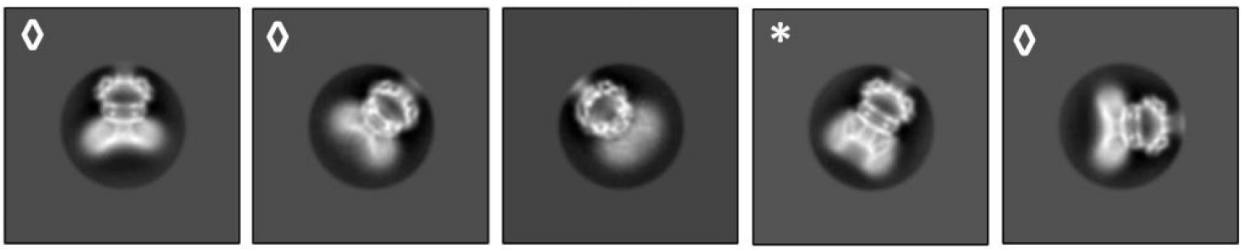


**Figure 3.13 | Selected 2D class averages present in the data set of LPC-treated YnaI.** 13 % of the side views equal those of the data set of closed-like YnaI (*), whereas 44 % of the particles present in side-view orientation (◊) exhibit a less pronounced indentation in the membrane moiety and a smaller dimension perpendicular to the membrane plane. The side of the box equals 31.9 nm. Figure adapted from Flegler et al. (2020).

**Table 3.3 | Data acquisition and map parameters (A) of LPC-treated YnaI-DIBMALPs and model parameters (B) of open-like YnaI.**

| | YnaI (closed-like) | YnaI (intermediate) | YnaI (open-like) |
|---|---|---|---|
| **A** | | | |
| **EMDB code** | **EMD-11559** | **EMD-11561** | **EMD-11560** |
| **Data collection** | | | |
| Microscope | | Titan Krios G3 | |
| Voltage (kV) | | 300 | |
| Camera | | Falcon III | |
| Data collection mode | | counting | |
| Electron exposure ($e^-/(Å^2)$) | | 70 | |
| Underfocus (µm) | | 1.0 – 2.0 | |
| Pixel size (Å) | | 1.0635 | |
| Number of movies collected | | 4161 | |

**Table 3.3 continues next page ►**

| | | | |
|---|---|---|---|
| **Map parameters** | | | |
| Final number of particles | 20016 | 9309 | 3646 |
| Symmetry imposed | C7 | C7 | C7 |
| Map resolution (Å) | 3.8 | 3.3 | 4.1 |
| Sharpening *B*-factor (Å$^2$) | -138 | -134 | -127 |
| Processing Software | | *Relion* 3.0 | |

**B**

| | |
|---|---|
| **PDB code** | **6ZYE** |
| **Model composition** | |
| Non-hydrogen atoms | 24556 |
| Protein residues | 1568 |
| Ligands | 0 |
| **Validation** | |
| MolProbity Score | 1.31 |
| Clashscore | 4.93 |
| Poor rotamers (%) | 1.04 |
| R. m. s. deviations | |
| Bond lengths (Å) | 0.008 |
| Bond angles (°) | 0.898 |
| Ramachandran plot | |
| Favoured (%) | 97.81 |
| Allowed (%) | 2.19 |
| Outliers (%) | 0.00 |

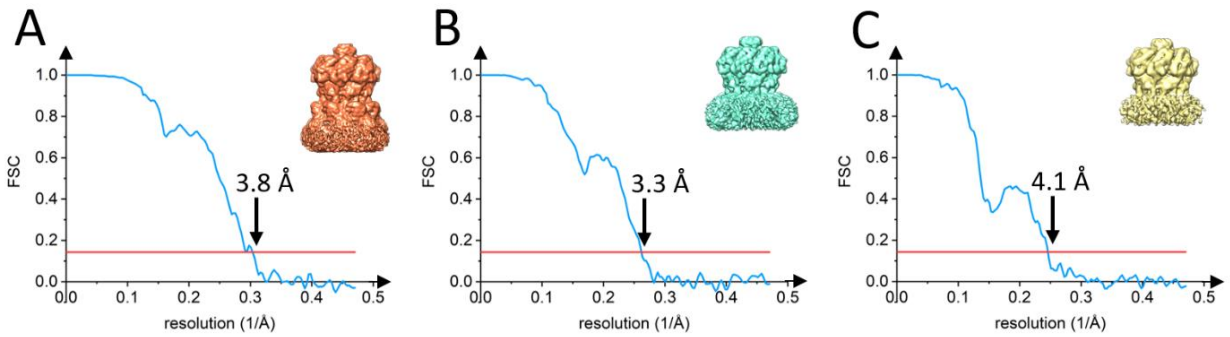


**Figure 3.14 | Maps obtained from the LPC-treated YnaI data set.** FSC curves for the closed-like **(A)**, the intermediate **(B)** and the open-like channels **(C)**. The threshold of 0.143 is represented by the red horizontal line. The final maps are shown in the top right corner of each FSC plot. Figure adapted from Flegler et al. (2020).

**One conformation represents the closed-like YnaI.** One of the three conformations resulted in a map of 3.8 Å resolution and resembled that of the closed-like channel isolated in DIBMA-stabilised nanodiscs but does not resolve the outer paddle helices TM-N1 and TM-N2 (figure 3.14 A, 3.15 A (red)). The other two conformations show no changes in the cytosolic vestibule but differences in the membrane domain (figure 3.15 A). Compared to the closed-like conformation, a notably lower number of particles is in the final maps of the two novel conformations. The membrane domains of these two conformations are barely resolved, and for better visualisation, a gaussian filter was applied. One possibility for this observation might be that the two novel conformations exhibit increased flexibility in the TMD or that they are affected by the contacting polymer or the LPC.

**One conformation is in an open-like form.** One of the two novel conformations led to a map of 4.1 Å resolution and showed three significant variations compared to the closed-like channel (figure 3.14 C, 3.15 A (yellow)). (i) The pore is widened, and the minimal diameter between the TM3a helix centres increases from 14 Å to 18 Å. For this reason, this state is referred to as "open-like". (ii) Concomitant with an outward bending of the periplasmic half of the TM3a helices, the pore is shortened from 30 Å to 20 Å. This is also accompanied by a reduction of the depth of the periplasmic indentation from 25 Å to 10 Å. (iii) The TMD is completely buried in the membrane, as no density related to the TMD is visible on the cytosolic side of the membrane. This results in an overall flatter appearance of the membrane domain, and the pore is pulled into the plane of the membrane upon these structural rearrangements.

**One conformation is structurally an intermediate between the closed-like and open-like forms.** The third conformation present in the data set (map with 3.3 Å) shows elements of both the closed-like and the open-like states and is therefore called "intermediate" (figure 3.14 B, 3.15 A (blue)): The pore is not widened, and the TM3a helices are less bent away from the symmetry axis than observed for the open-like conformation. The depth of the periplasmic indentation is 15 Å and lies between those of the closed-like and open-like conformations. As observed for the open-like state, the TMD is buried in the membrane. These findings indicate that the movement of pore and paddle helices is not tightly coupled.

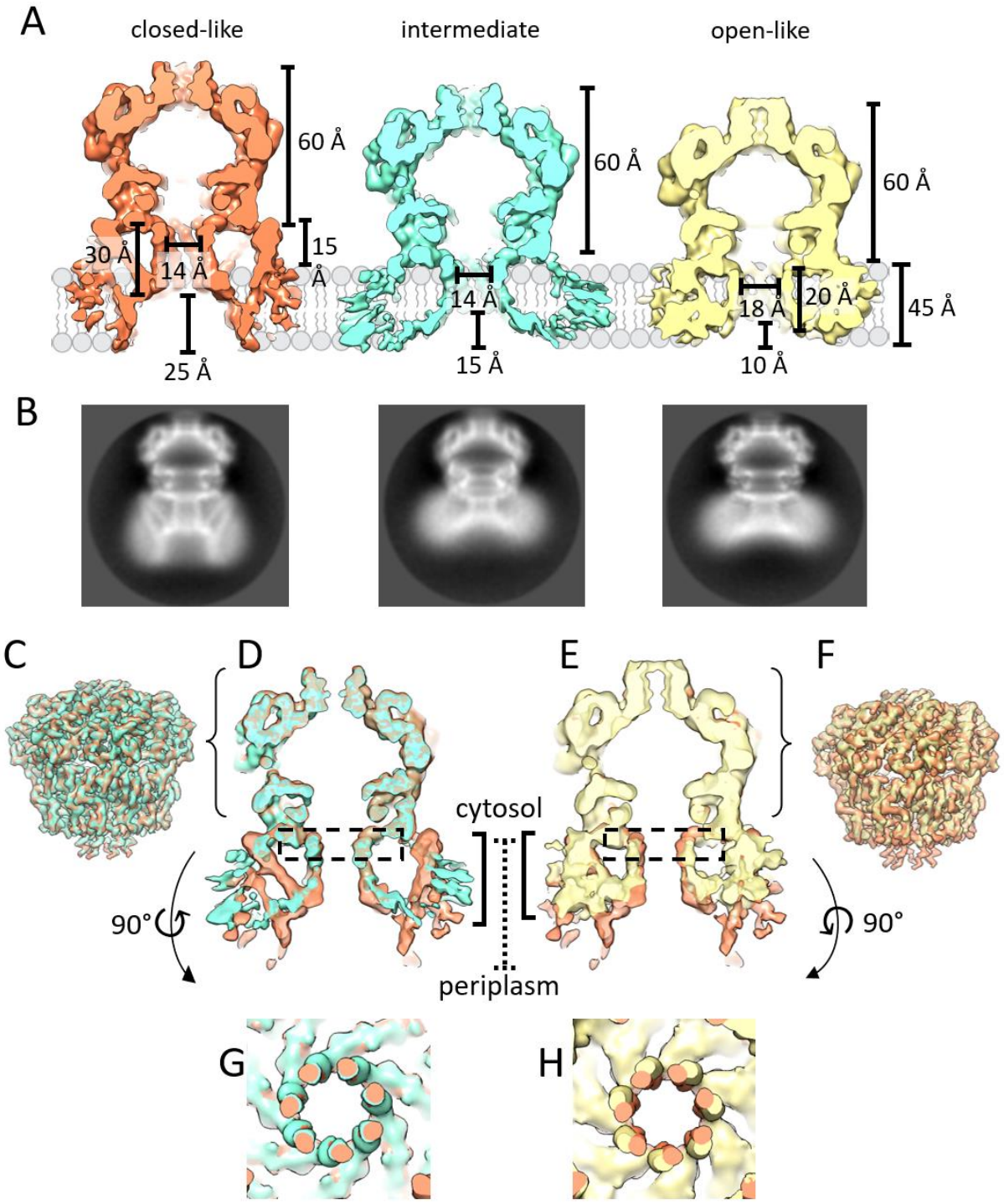


**Figure 3.15 | YnaI is captured in a closed-like, intermediate and open-like conformation in the data set of the LPC-treated sample. (A)** The dimensions of structural features in the closed-like (red), intermediate (blue) and open-like (yellow) conformations of YnaI are marked. While no significant differences are visible in the cytosolic vestibule, differences in the membrane domain suggest that major changes happen in the membrane domain upon gating in this part of the complex: In the closed-like conformation, the inner paddle helices TM1 and TM2 protrude into the cytosol. In the open form, the TMD seems to be completely buried in the membrane, which is accompanied by a reduced indentation on the periplasmic side. **(B)** 2D class averagesclass of the different conformations are shown below each map; the circle diameter is 160 Å. **(C)-(H)** Comparison of the intermediate (C, D, G)

◄ and open conformation (E, F, H) to the closed-like. **(C), (F)** The overlays of the maps at a low contour level reveal no differences in the cytosolic vestibule. **(D), (E)** The width of the membrane domains of the intermediate (D) and open-like (E) conformations are diminished compared to the closed-like conformation (width of the membrane domain indicated as brackets for the intermediate and open-like conformations and as a dotted line for the closed-like conformation). **(G), (H)** Slices of the pore helices highlighted in dashed boxes in D and E viewed along the symmetry axis from the periplasmic side. The pore helices of the intermediate conformation (G, blue) exhibit the same diameter as the closed-like conformation (red), while the pore helices of the open-like conformation (H, yellow) are slightly more spaced than in the closed-like conformation. The maps shown in A, D, E, G and H are gaussian-filtered for better visibility. Figure adapted from Flegler et al. (2020).

The intermediate state might originate from two different points in the conformational cycle: Either it could represent a transition intermediate or an adaptive state. The existence of at least one intermediate state has been reported for MscS based on patch clamp experiments (Shapovalov and Lester, 2004). Recently, the structure of a sub-conducting and an adapted conformation of MscS that the channel adopts after having fully opened under sustained tension was presented (Zhang et al., 2021). Though, the presented sub-conducting state of MscS shows different structural rearrangements of the membrane part as the observed intermediate state obtained for YnaI. Adaptation, the loss of conductivity under pressure, was shown in patch clamp experiments for MscS (Koprowski and Kubalski, 1998; Levina et al., 1999; Sukharev et al., 1997). However, it has not been tested for YnaI before, so electrophysiological experiments were performed under standard conditions and under a prolonged pressure stimulus (figure 3.16). Single-channel openings are observed as the pressure is applied, and under continued pressure, no spontaneous closings occur that would indicate adaptation. Therefore, the obtained intermediate map most likely represents a transition intermediate between the closed-like and the open-like state. This leads to the assumption that the bending of the TM3a helices occurs gradually and precedes pore widening.

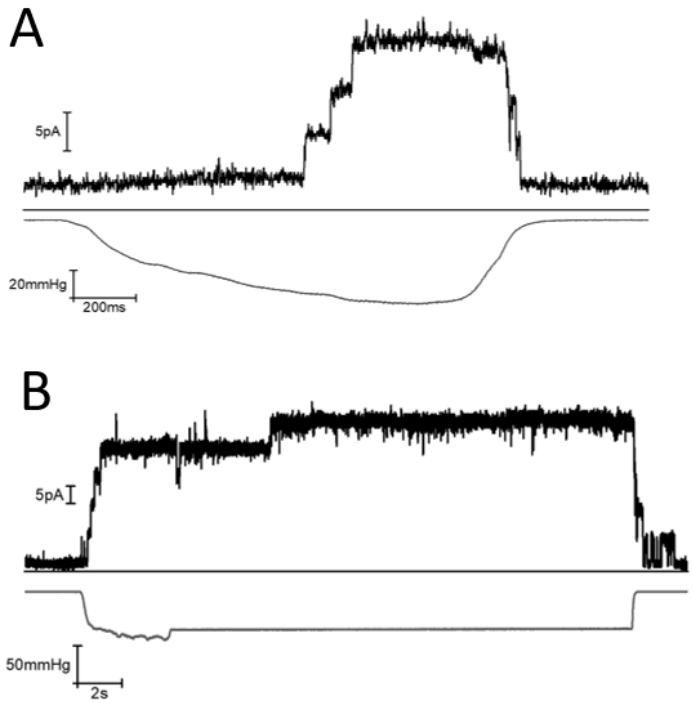


**Figure 3.16 | Electrophysiological characterisation of YnaI. (A)** A representative patch clamp trace of WT YnaI is shown together with the applied pressure. Staircase-like, single-channel openings are visible in the top trace. **(B)** The patch clamp trace of WT YnaI under a prolonged pressure stimulus shows no spontaneous closings that would indicate adaptation. A voltage of +40 mV was applied. Figure adapted from Flegler et al. (2020).

**Bending of the TM3a helices is enabled by a GGxGG motif.** The 4.1 Å map of the open-like conformation allowed model building of the vestibule and the pore helices, which shows that the glycine-rich TM3a helices bend away from the pore axis at the region of $^{149}$GGIGG$^{153}$ in the sequence (figure 3.17). This indicates that the gating mechanism of YnaI differs enormously from MscS. MD simulations (3 × 200 ns) predicted a hydrated pore for open-like YnaI, and a small number of ions were observed to pass the TM gate in computational electrophysiology simulations, which is congruent with a conductance of ~10 pS (V = -200 mV) and ~40 pS (V = +200 mV) with a $Cl^-$ selectivity. The observed reduced conductance compared to the value that was determined experimentally (100 pS (Edwards et al., 2012)) hints that the obtained open-like conformation is indeed only ”open-like” and does not represent the ultimately open conformation.

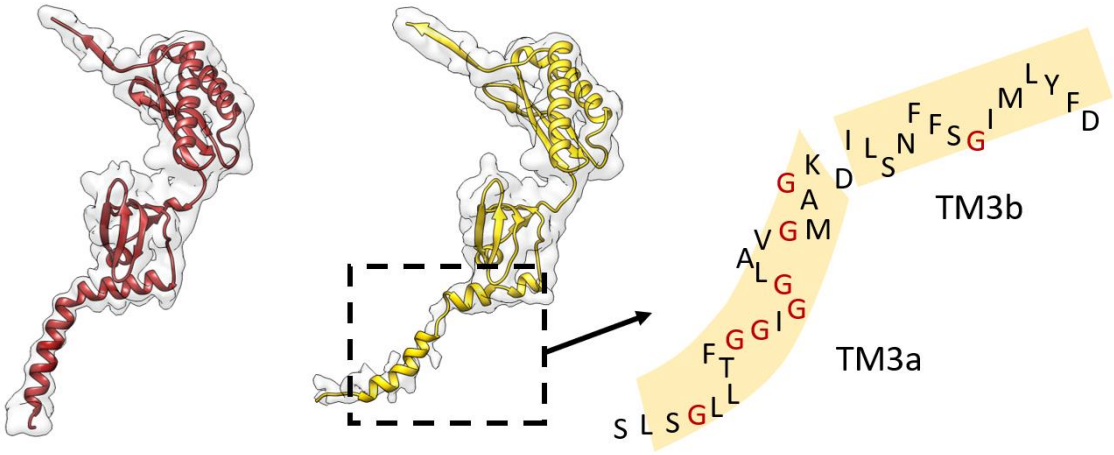


**Figure 3.17 | Widening of the pore in YnaI. (A)** One subunit of YnaI in its closed-like (red) and open-like (yellow) conformation is shown in their corresponding densities (grey). For the illustration of the open-like channel, the model of the closed-like form was fitted into the density of the open-like channel and real-space refined in *Phenix*. The sequence of the TM3a and TM3b helices is shown schematically on the right; glycines are highlighted in red. Bending of the TM3a helix (dashed box) upon opening is observed in a glycine-rich stretch ($^{149}$GGIGG$^{153}$). Figure adapted and modified from Flegler et al. (2020).

The bending of the pore helices was further probed by two different mutations of the $^{149}$GGIGG$^{153}$ sequence. The double mutation G149A/G152A changes the sequence to $^{149}$AGIAG$^{153,}$ which is similar to the glycine pattern in MscS ($^{100}$LGAAG$^{104}$). This mutation should make the TM3a helix more rigid, lowering the propensity of bending in this region and thereby stabilising the closed conformation. Another mutant, G149P, should support bending of the TM3a helix in this region, stabilising the open-like conformation. The mutants were characterised by several independent experiments.

Whole-cell Western blot analysis showed that the G149A/G152A mutant has a similar, even slightly higher expression as WT YnaI, which agrees with the observed inconspicuous growth curves (figure 3.18 A, C). A cryo-EM map shows that the TM3a helix is not distorted by the mutation (figure 3.18 D). Hypoosmotic downshock assays confirmed that the G149A/G152A mutation leads to a LOF phenotype: The survival ratio (shock/control) of the double mutant is only 0.43 compared to 1.44 for WT YnaI (figure 3.18 B), so this mutant is much less able to protect *E. coli* from dying after suffering a hypoosmotic downshock. In electrophysiological experiments, YnaI opens only in 19 % of all pressure trials (compared to 87 % for WT YnaI). However, when it is opening, it exhibits normal conductance and opens at the same pressure threshold as WT YnaI (1.00 ± 0.05 [n = 6] vs. $P_L$:$P_{YnaI\text{-}WT}$ = 1.04 ± 0.06 [n = 6]) (figure 3.18 E). The G149P mutant showed very low expression in whole-cell Western blot analysis (figure 3.18 A) and a severe growth phenotype (figure 3.18 C), which prevented purification and

structure determination. The growth curve of the G149P mutant agrees with the expected GOF phenotype, which can result in slower growth rates due to leakage and disturbance of cell homeostasis. Such a severe growth phenotype is also observed for strong GOF mutants of MscS like L109S (Miller et al., 2003a) and R59L (Rasmussen et al., 2019b). In downshock assays, a GOF mutant should be able to protect *E. coli* from a hypoosmotic shock similarly to WT. However, G149P also shows a diminished survival ratio of 0.81 compared to WT YnaI (1.44) (figure 3.18 B). This behaviour can be explained by the severely reduced expression level because it means that significantly fewer channels are present in the cells, which has also been observed for the MscS GOF mutant L109S (Miller et al., 2003a). In electrophysiological experiments, G149P shows a short dwell time (figure 3.18 E). Because of the short dwell time, two simultaneously open channels could not be observed, which is a prerequisite for determining a pressure threshold (Blount et al., 1996). The pressure ratio for one open YnaI implies that it is slightly easier to open than WT YnaI, which concurs with the fact that GOF mutants have a lower pressure threshold for opening or staying open. Though even for the YnaI G149P mutant, a higher tension is required for opening than MscS, and the electrophysiological experiments alone do not explain its severe growth phenotype. Conclusively, the mutagenesis experiments underpin the importance of the GGxGG motif in gating.

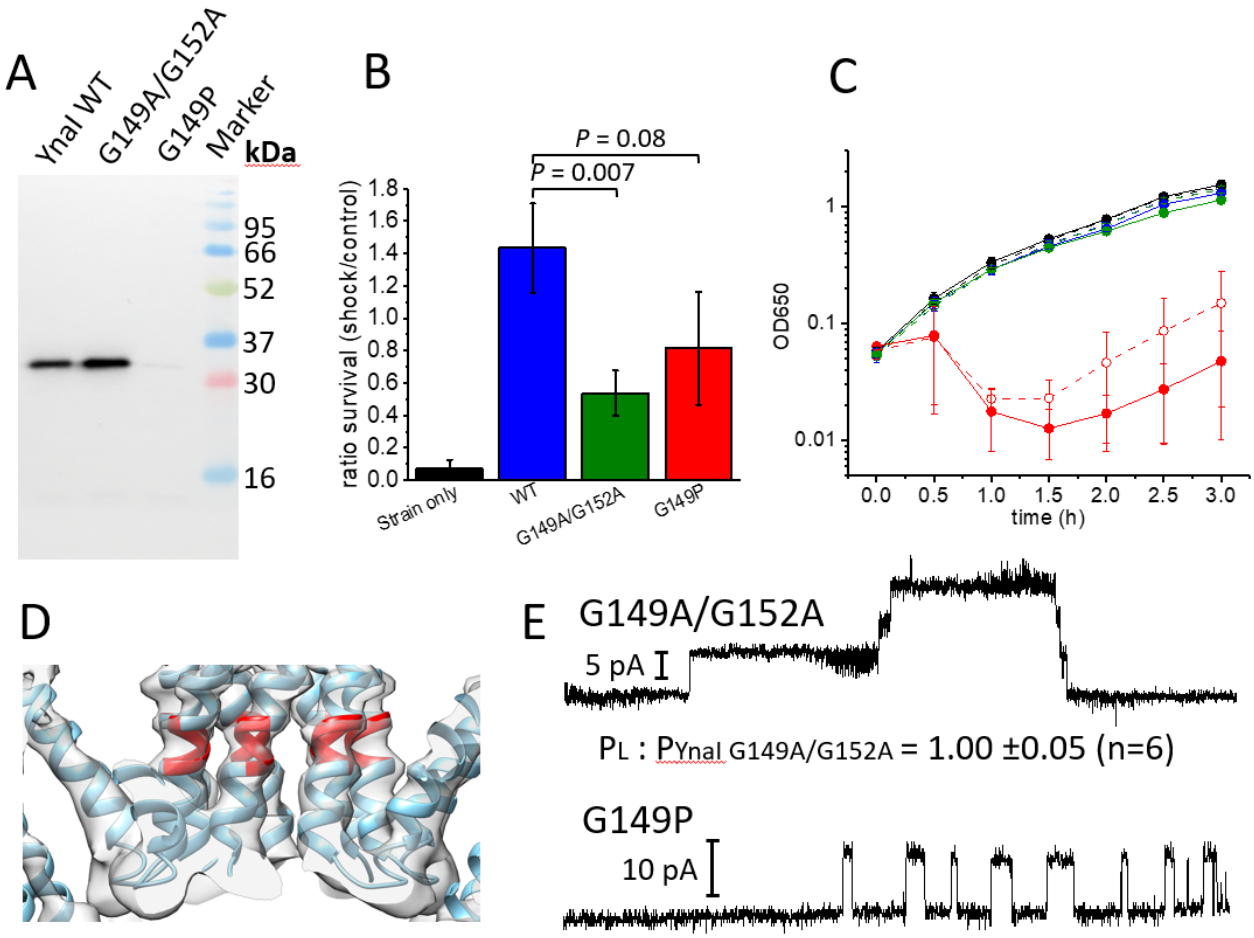


**Figure 3.18 | Characterisation of the GGxGG motif mutants in YnaI. (A)** The whole-cell Western blot analysis of the expression levels of the mutants shows that WT YnaI and the G149A/G152A mutant are expressed equally well, while the G149P mutant exhibits a strongly reduced expression level. Cells were induced for 30 min with 0.3 mM IPTG. **(B)** For the osmotic downshock assays, cells were diluted into a medium that had 0.3 M less NaCl (shock) or into an identical medium (control). Survival is shown as the ratio of counted colonies for the shock relative to control. Mean values are shown with standard deviations for three independent experiments, and *P* values for the Student's unpaired t-test are indicated. **(C)** Growth curves are shown for the strain MJF641 only (black), WT YnaI (blue), G149A/G152A (green) and G149P (red) without (open symbols/dashed lines) or with (filled symbols/solid lines) induction by 1 mM IPTG. Mean values are shown with standard deviations for three independent experiments. **(D)** A cryo-EM map of YnaI G149A/G152A at 4.2 Å resolution (grey) is shown together with the model of WT YnaI in its closed-like conformation (blue ribbon). In the slice, the pore helices TM3a and the paddle helices TM2 are visible, with the GGxGG motif is highlighted in red. **(E)** Electrophysiological traces for G149A/G152A (top) and G149P (bottom). A trace of WT YnaI for comparison is shown in figure 3.16. Figure adapted from Flegler et al. (2020).

### 3.1.6 Investigation of the local membrane environment of YnaI

**YnaI- and MscS containing proteoliposomes differ in size.** MD simulations of closed and open MscS did not only show lipid-filled pockets but a locally curved membrane around the channel (Pliotas et al., 2015; Sotomayor and Schulten, 2004), which was suggested previously based on the conical shape of the membrane domain (Phillips et al., 2009). As the tapered shape of the membrane domain is maintained in YnaI, it would also suggest a local membrane curvature. YnaI containing proteoliposomes (figure 3.19 A, right) exhibited overall larger diameters than MscS containing proteoliposomes (figure 3.19 A, left), despite originating from the same batch of preformed liposomes. Interestingly, proteoliposomes prepared from *E. coli* polar lipid mixture where overall bigger than those consisting of DOPC:POPE (3:1), but the proteoliposomes containing YnaI where still bigger than the MscS containing ones. Changing the protein:lipid molar ratio did not result in less or more occupied proteoliposomes, but in the number of occupied or empty liposomes, suggesting that insertion of one channel into a liposome favours the insertion of further channels. The different sizes of the MscS- and YnaI containing proteoliposomes hint that the membrane around the channels might be locally bend, because the different sized channels do not simply adapt to the global curvature of the preformed liposome, which should result in similarly sized proteoliposmes.

**The membrane around YnaI is only slightly locally curved.** YnaI containing proteoliposomes were further subjected to data collection and subsequent processing. At first sight, 2D class averages show the channels embedded in the clearly visible lipid bilayer and the global curvature of the liposome (figure 3.19 B). The particles deriving from LPC-treated proteoliposomes showed no discernible differences. For these, a flatter channel was expected, as observed for the open-like channel that was obtained earlier by SPA from the LPC-treated data set. However, flatter membrane domains (marked with *) were observed for both data sets; thus, it seems more likely that this is due to the location of the channel in the proteoliposome or the tilt angle of the projection respectively. A closer look at one of the 2D class averages from the data set of the proteoliposomes without LPC shows that the membrane is slightly locally bent at the position where it is attached to the channel (figure 3.19 C).
The observation that open-like channels were not observed in the proteoliposome-data set is surprising because the conditions were equal to those used earlier: 5 µM LPC was added to 1 mg/ml proteoliposomes containing YnaI in a molar ratio of 1:1000.

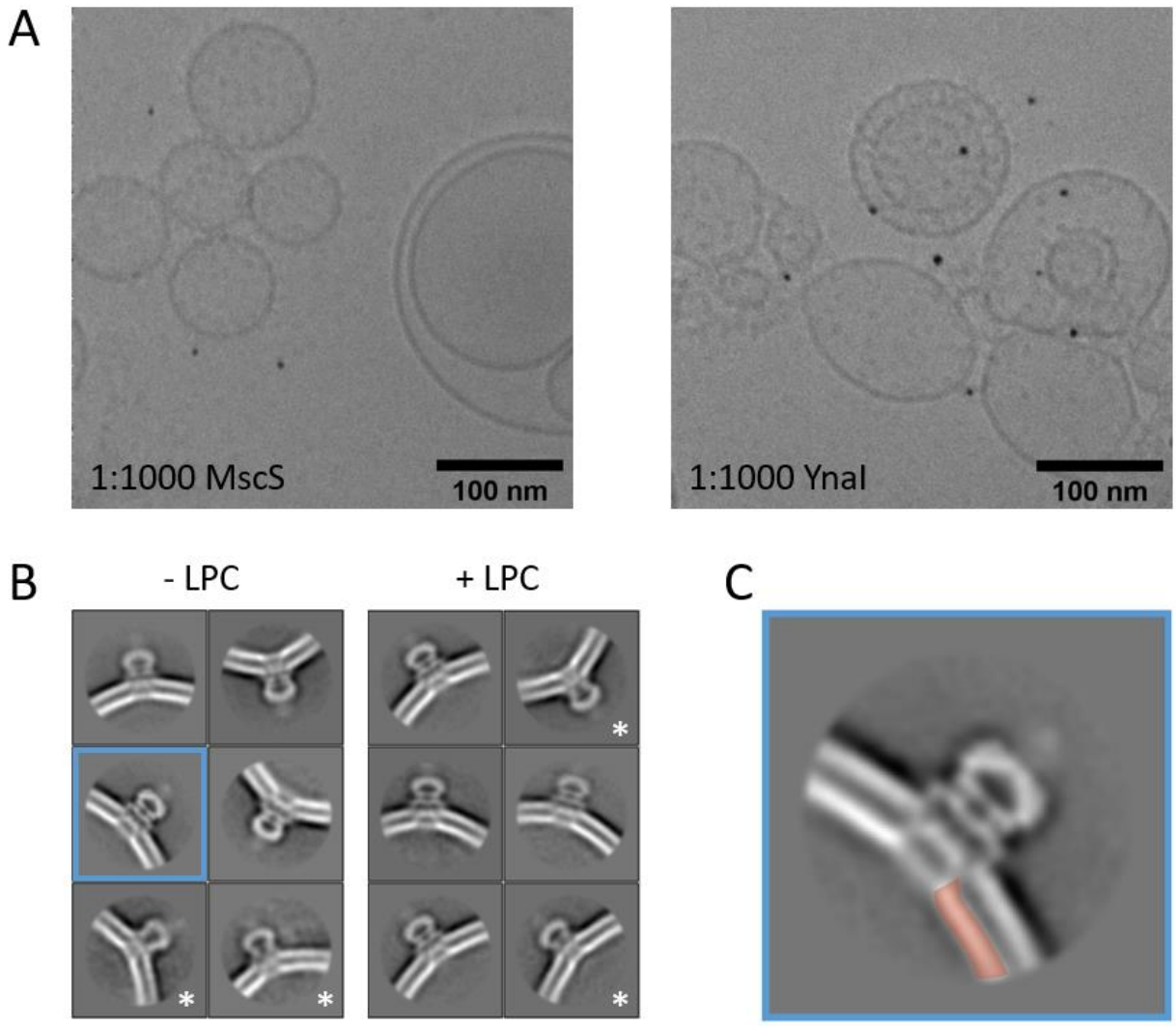


**Figure 3.19 | Examination of the membrane of YnaI containing proteoliposomes. (A)** The comparison of DOPC:POPE (3:1) proteoliposomes shows that those containing MscS (left) are overall smaller than those containing YnaI (right). In addition, empty liposomes are present, which can be seen on the right half of the MscS proteoliposome sample. **(B)** Single-particle processing of patches derived from proteoliposomes yielded 2D class averages clearly showing the bilayer and the embedded channel in side-view orientation. No detectable differences are present between the class averages from the data set with and without LPC. Class averages that show channels with an apparently flatter membrane domain are marked (*). **(C)** The close-up of the 2D class highlighted in the blue box in (B) shows that the membrane is locally bent where it is attached to the channel. This is, however, only visible for one leaflet (highlighted in red). The side of the boxes in (B) and (C) equals 31.9 nm.

## 3.2 Different purification strategies applied to MscS

Additional to doping the membrane with LPC, or the A106V point mutation in the pore, the purification protocol and the reconstitution method, respectively, affect the conformational state of MscS. MscS purified in the detergents Fos-choline-14 (Bass et al., 2002) and DDM (Lai et al., 2013; Zhang et al., 2012), as well as reconstitution of MscS in MSP nanodiscs (Rasmussen et al., 2019a; Reddy et al., 2019) and into peptidiscs (Angiulli et al., 2020), resulted in the closed conformation. However, it is documented that the purification of MscS with DDM also produced the open conformation (Lai et al., 2013; Pliotas et al., 2015, 2012). To unravel the determinant of the conformational state, MscS was purified using different detergents and reconstitution systems, and its conformation was determined by cryo-EM.

### 3.2.1 MscS in Amphipols A8-35 and in DIBMA-stabilised nanodiscs

Both YnaI in Amphipols A8-35 and in DIBMA-stabilised nanodiscs were found in a closed-like conformation. Therefore, it should be tested whether these two systems also capture MscS in its closed form. The samples were prepared equivalent to YnaI, and cryo-EM data collections were acquired. The micrographs (figure 3.20 A and C, left) of the two data sets show both single particles and smaller aggregates. The class averages representing top views (figure 3.20 A and C, upper right) clearly show the sevenfold symmetry of MscS. Because of the flatter membrane domain observed in the side view class averages of both data sets (figure 3.20 A and C, lower right), MscS was first considered to be in an open conformation. Further processing of the data resulted in final maps with an overall resolution of 8.5 Å for MscS in Amphipols (13396 particles) and 4.1 Å for MscS-DIBMALPs (13052 particles), respectively (figure 3.20 B and D). These maps revealed the typical architecture of the cytosolic vestibule but exhibited major variations in the TMD: While the pore helices TM3a are resolved, and their positions match those of the closed conformation (figure 3.20 B and D), the paddle helices TM1 and TM2 are not resolved at all. Moreover, for both maps, no density is visible in TMD that corresponds to helices. This suggests that the unresolved paddle helices are not caused by the limited particle number but are more likely denatured. Data acquisition and map parameters are given in table 3.4.

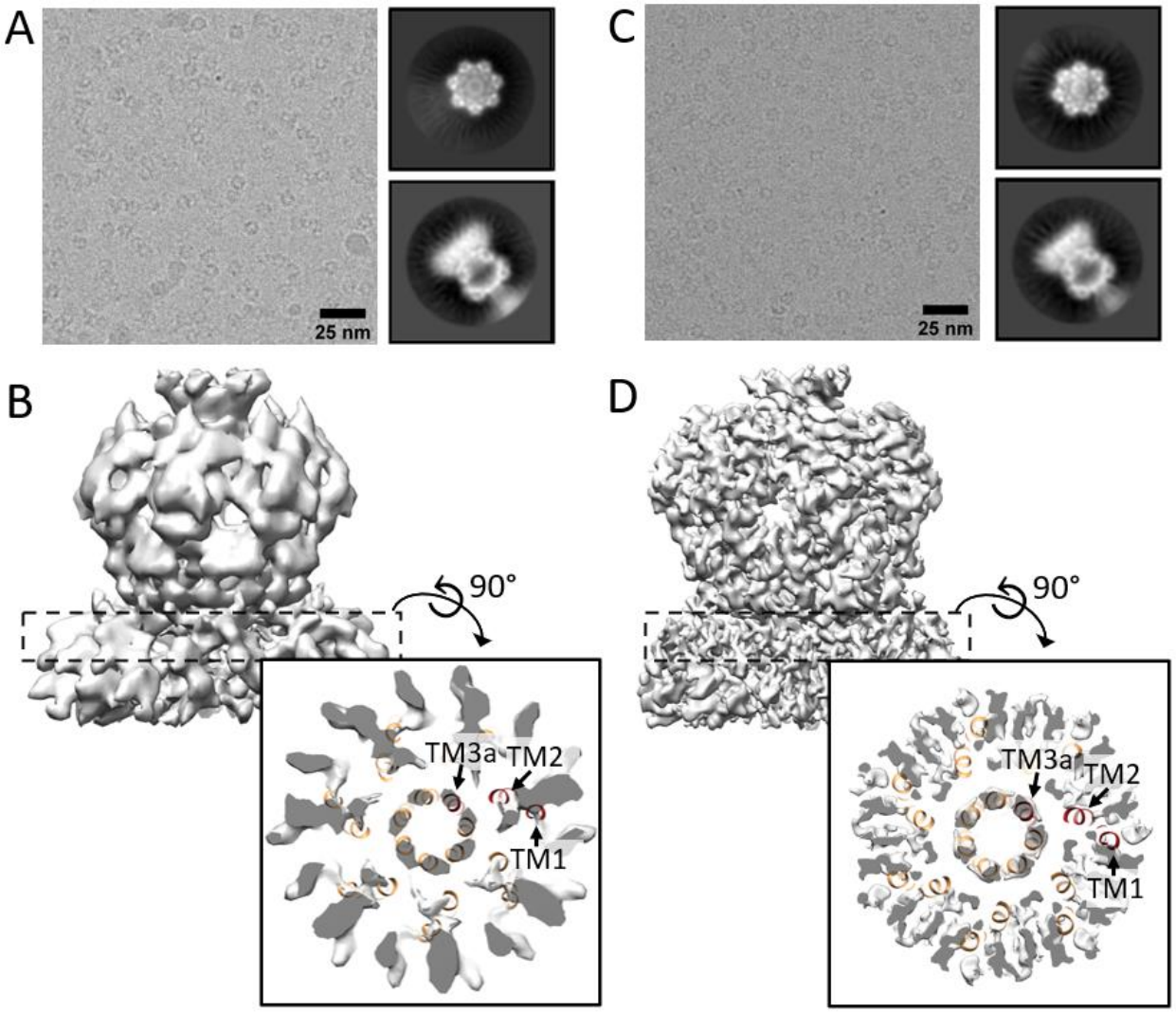


**Figure 3.20 | Cryo-EM and SPA of MscS in Amphipols A8-35 and in DIBMA-stabilised nanodiscs. (A), (B)** Analysis of MscS in Amphipols A8-35. **(C), (D)** Analysis of MscS-DIBMALPs. (A) and (C) show a part of a micrograph from the respective data collection (left) and representative 2D class averages showing a top view (upper right) and a side view (lower right) class average. The edge of one box corresponds to 24 nm. The final maps are depicted in grey in (B) and (D), and the slices highlighted by the dashed boxes are viewed from the periplasmic side together with the fitted model of closed MscS (orange; PDB 6RLD (Rasmussen et al., 2019a). One subunit is coloured red, and the helices TM3a, TM2 and TM1 are marked.

**Table 3.4 | Data acquisition and map parameters of MscS in Amphipols A8-35 and MscS-DIBMALPs.**

| | MscS in Amphipols A8-35 | MscS-DIBMALPs |
|---|---|---|
| **Data collection** | | |
| Microscope | Titan Krios G3 | |
| Voltage (kV) | 300 | |
| Camera | Falcon III EC | |
| Data collection mode | linear | counting |
| Electron exposure ($e^-/(Å^2)$) | 83.5 | 56.26 |
| Underfocus (µm) | 1.4 – 2.2 | 1.4 – 2.2 |
| Pixel size (Å) | 1.0635 | 1.0635 |
| Number of movies | 4396 | 2000 |
| **Map parameters** | | |
| Final number of particles | 13396 | 13052 |
| Symmetry imposed | C7 | C7 |
| Map resolution (Å) | 8.5 | 4.1 |
| Processing Software | *Relion* 3.1 | *Relion* 3.1 |

### 3.2.2 Effect of various DDM concentrations on the conformation of MscS

**An increase of DDM in the solubilisation buffer results in closed MscS.** Zhang et al. recently presented MscS in different conformational states, which were linked to the amount of bound lipids (Zhang et al., 2021). This ”lipids-move-first” model was suggested previously (Pliotas et al., 2015), stating that lipid extrusion from the pockets triggers channel gating. The lipids-move-first model was tested in the absence of a membrane by delipidating MscS. Increasing the detergent concentrations increases the degree of delipidation (Gupta et al., 2018), as does the duration of incubating the sample in detergent (Bechara et al., 2015). Therefore, as a first trial, the DDM concentration in the solubilisation buffer was increased to 1.5 % and the incubation time to 1.5 h (“low DDM” / condition 1), compared to 1 % in the standard solubilisation buffer and 1 h incubation (standard purification / condition 0). The remaining purification steps were not altered, so the 0.05 % DDM in the IMAC wash buffer and the 0.03 % DDM in the SEC buffer were maintained. For assessing the conformational state of MscS, a cryo-EM data set was obtained and analysed, resulting in a map with 3.9 Å resolution and showing that MscS is still in a closed conformation (figure 3.21 B, left; figure 3.22). Map and model parameters are listed in table 3.5.

**Table 3.5 | Data acquisition and map parameters (A) and model parameters (B) of the different MscS samples.**

| | Condition<br>Conformation | 1<br>closed | 2a<br>open | 3a<br>closed | 2b<br>open |
|---|---|---|---|---|---|
| **A** | | | | | |
| | **EMDB code** | **EMD-12997** | **EMD-13003** | **EMD-13006** | **EMD-12996** |
| | **Data collection** | | | | |
| | Microscope | | Titan Krios G3 | | |
| | Voltage (kV) | | 300 | | |
| | Camera | | Falcon III | | |
| | Data collection mode | | counting | | |
| | Electron exposure ($e^-/(Å^2)$) | | 80 | | |
| | Pixel size (Å) | | 1.0635 | | |
| | Underfocus (µm) | 1.2 – 2.2 | 1.2 – 2.2 | 1.2 – 2.2 | 1.0 – 2.0 |
| | Number of movies collected | 1859 | 6287 | 2262 | 3292 |
| | **Map parameters** | | | | |
| | Final number of particles | 140826 | 841492 | 399384 | 232197 |
| | Symmetry imposed | C7 | C7 | C7 | C7 |
| | Map resolution (Å) | 3.9 | 3.1 | 3.1 | 2.3 |
| | Sharpening *B*-factor ($Å^2$) | -235 | -138 | -174 | -50 |
| | Processing Software | | *Relion* 3.1 | | |
| **B** | | | | | |
| | **PDB code** | **7ONL** | **7OO0** | **7OO6** | **7ONJ** |
| | **Model composition** | | | | |
| | Non-hydrogen atoms | | 16016 | 14546 | 17717 |
| | Protein residues | | 1834 | 1827 | 1834 |
| | Ligands | | 56 | 14 | 63 |
| | **Validation** | | | | |
| | MolProbity Score | | 1.58 | 1.48 | 1.47 |
| | Clashscore | | 7.27 | 9.05 | 8.68 |
| | Poor rotamers (%) | | 0.00 | 0.00 | 0.47 |
| | *R. m. s. deviations* | | | | |
| | Bond lengths (Å) | | 0.007 | 0.003 | 0.008 |
| | Bond angles (°) | | 0.624 | 0.413 | 0.667 |
| | *Ramachandran plot* | | | | |
| | Favoured (%) | | 96.92 | 98.46 | 99.23 |
| | Allowed (%) | | 3.08 | 1.54 | 0.77 |
| | Outliers (%) | | 0.00 | 0.00 | 0.00 |

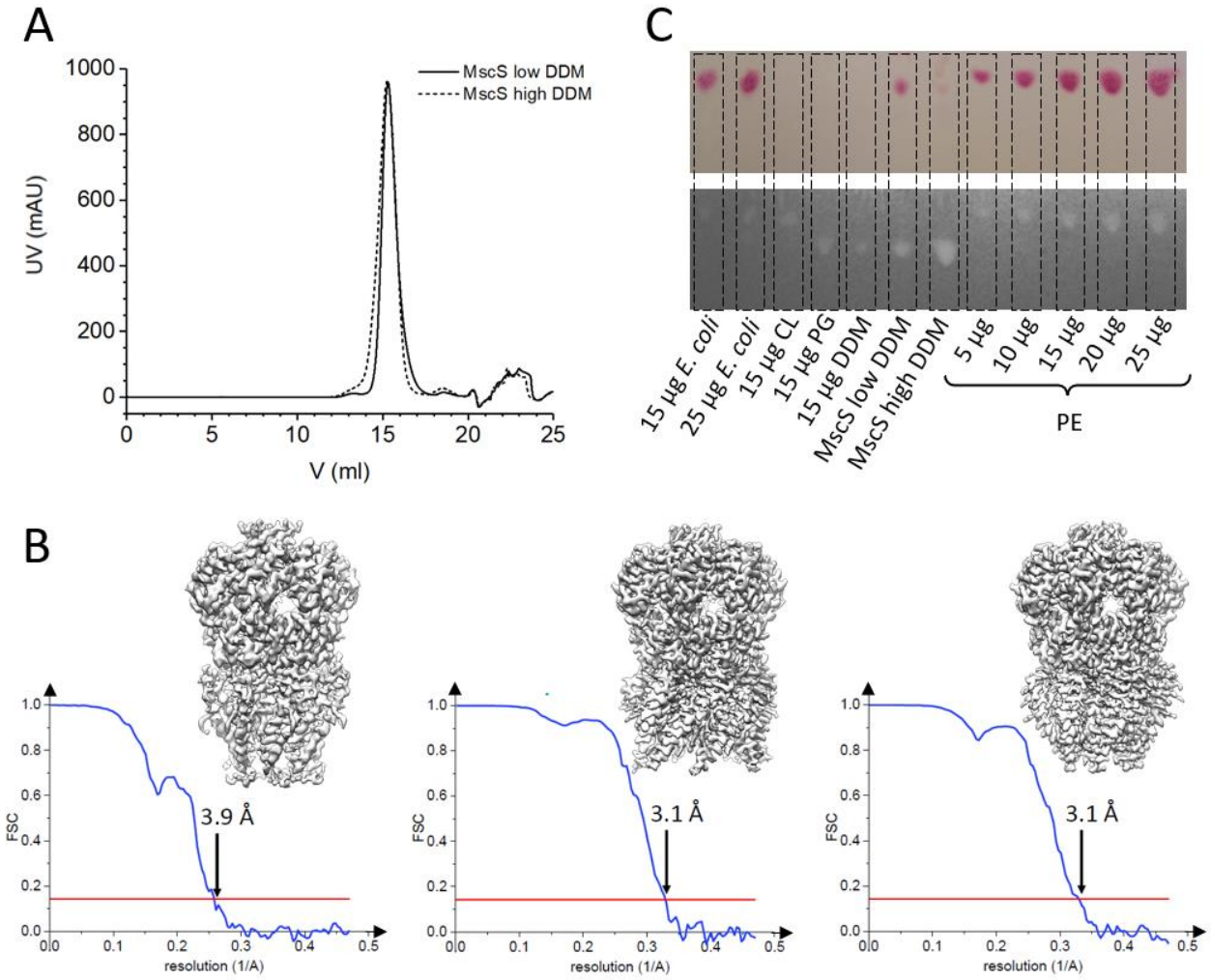


**Figure 3.21 | Purification and analysis of MscS samples solubilised and purified in DDM. (A)** The SEC elution profiles of MscS under condition 1 (solid line, low DDM) and under condition 2a (dashed line, high DDM) show no significant differences. **(B)** Final maps of MscS under the conditions 1, 2a and 3a (from left) with their corresponding FSC curves. The threshold of 0.143 is indicated as a red line. MscS is found in a closed conformation under condition 1 (washed with 0.05 % DDM during IMAC), in an open conformation under condition 2a (washed with 0.5 % DDM during IMAC). The addition of lipids to MscS from condition 2a reverted MscS to the closed state (condition 3a). **(C)** Lipid extracts from MscS purified under conditions 1 (low DDM), and 2a (high DDM) were compared to different lipid standards and DDM in TLC analysis. Visualisation of all lipids and DDM was achieved by primulin and UV lighting first (bottom), followed by visualisation of PE by ninhydrin and heating (top). For open MscS (high DDM), less PE is detected but a higher amount of DDM. Part of the figure adapted from Flegler et al. (2021).

**Increasing the DDM concentration during IMAC produces an open conformation.** Next, the DDM concentration in the wash buffer was increased from 0.05 % to 0.5 % compared to the standard purification, but the DDM concentration in the SEC buffer was kept at 0.03 % DDM ("high DDM" / condition 2a). A cryo-EM map at 3.1 Å resolution was obtained, showing MscS in an open conformation (figure 3.21 B, middle; figure 3.22). The map agrees

well with earlier crystal structures of MscS in its open form (Pliotas et al., 2015; Wang et al., 2008). Comparison of the SEC runs (figure 3.21 A) shows that the peak of open MscS is slightly shifted towards a smaller elution volume, but no discernible shift of the peak maxima between closed and open MscS, highlighting the necessity to use cryo-EM and subsequent image processing for elucidating the conformational state of MscS. TLC of lipid extracts from the different MscS preparations showed that under condition 1 (low DDM), more lipids are co-purified than under condition 2a (high DDM; figure 3.21 C). Only DDM and PE were detected in both samples, and a comparison with defined amounts of PE revealed that approximately 5 µg PE are associated with MscS under condition 1 (low DDM) and significantly less for MscS under condition 2a (high DDM). For both samples, the total lipid amount applied to the TLC plate comes from ~500 µg protein sample. MscS obtained under condition 2a, however, shows a higher amount of PG or DDM. As these two standards run at the same height, it is not possible to distinguish between them in the MscS sample, but the bright spot observed with primulin/UV detection is most likely dominated by DDM due to sample preparation.
These findings agree with previous studies: In an earlier cryo-EM structure of MscS in MSP nanodiscs that was found in a closed state, three lipid molecules per subunit were identified (Rasmussen et al., 2019a), while in a MscS sample that was prepared for crystallisation under more delipidating conditions, five lipids per complex were identified by native MS (Pliotas et al., 2015). This is within experimental error compared to one lipid molecule per subunit resolved in the cryo-EM map under condition 2a.

**Delipidation of MscS is reversible in vitro.** Lipids were added as mixed micelles (0.1 mg/ml azolectin final) to the sample that produced the open conformation and incubated for 30 min at room temperature before grid preparation (condition 3a). Cryo-EM analysis revealed a closed conformation, that shows no significant differences to the conformation obtained under condition 1 but has a higher resolution of 3.1 Å (figure 3.21 B, left; figure 3.22). Conclusively, sufficiently delipidated MscS is in an open conformation and can change back to the closed conformation by re-lipidation in vitro.

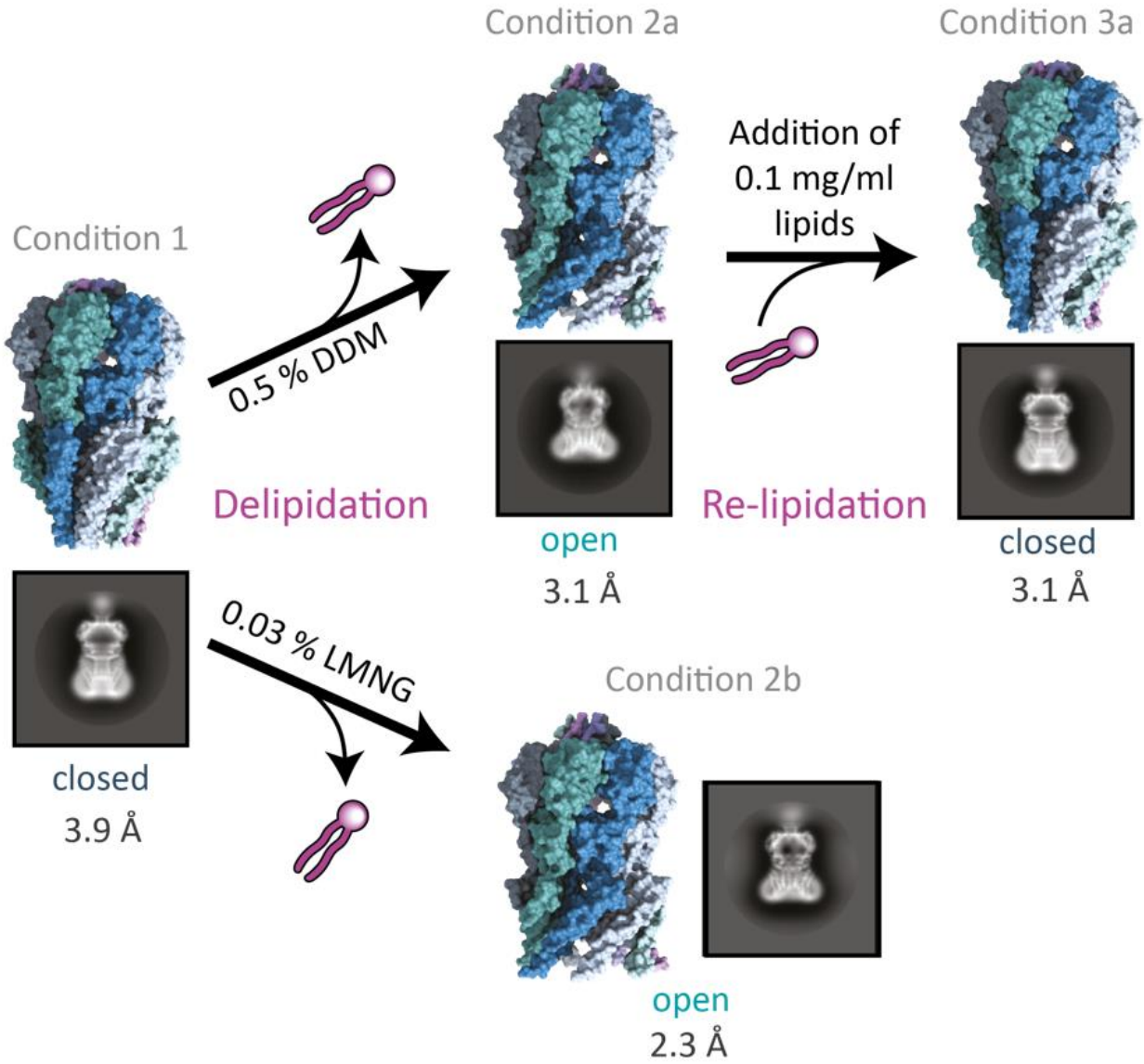


**Figure 3.22 | Experimental approach and final structures to obtain MscS in open and closed conformations.** MscS solubilised in DDM (either 1 % DDM (condition 0, not shown), or 1.5 % DDM) and washed with 0.05 % DDM during IMAC produced a closed conformation (condition 1), while washing with 0.5 % DDM resulted in an open form (condition 2a). Addition of 0.1 mg/ml lipids returned MscS to the closed conformation (condition 3a). Exchanging DDM to 0.03 % LMNG during IMAC also produced an open conformation (condition 2b). The MscS structures are shown as surface representations without ligands with their subunits coloured uniquely. A representative side-view 2D class average from the respective cryo-EM analysis is shown for all conditions. The edge of the box corresponds to 27.2 nm. Figure adapted from Flegler et al. (2021).

### 3.2.3 Open structure of MscS in LMNG at 2.3 Å resolution

Neopentyl glycol detergents have a strong delipidating effect on membrane proteins (Gupta et al., 2018; Ilgü et al., 2014). LMNG belongs to this class of detergents and was tested on MscS. Therefore, MscS was solubilised in 1 % DDM for 1 h (condition 0), and the detergent was exchanged to LMNG during IMAC by using a wash buffer containing 0.03 % LMNG, while the SEC buffer contained 0.02 % LMNG (condition 2b). This condition resulted in an open MscS at 2.3 Å resolution (figure 3.23, figure 3.24), which agrees well with the open conformation obtained under condition 2a and previous open crystal structures. The high resolution is probably explained by the stabilising effect of maltose neopentyl glycols (Chae et al., 2010, 2008).

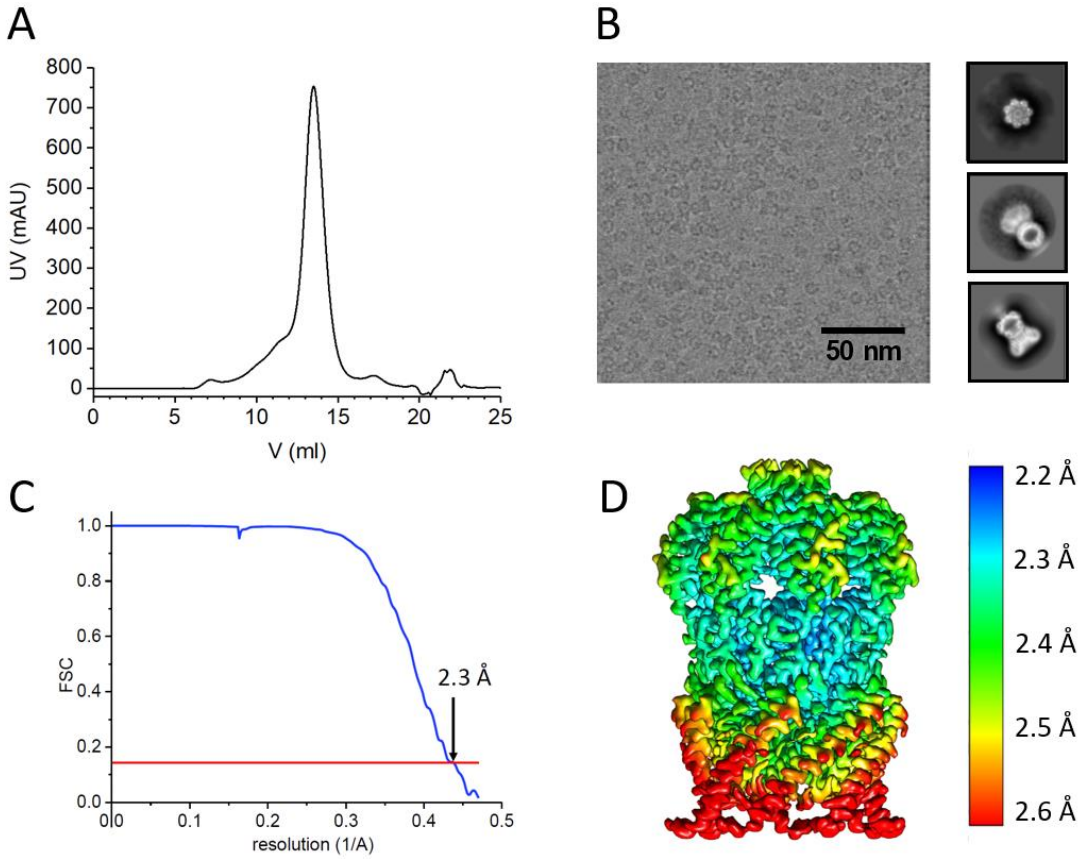


**Figure 3.23 | Purification and cryo-EM analysis of MscS in LMNG. (A)** The SEC profile shows one main peak at 14 ml. **(B)** Representative micrograph from the cryo-EM data collection and selected 2D class averages from the image analysis. Side and top views were approximately present in equal parts. The edge of the box corresponds to 27.2 nm. **(C)** The FSC curve is shown for the final refinement, with the threshold of 0.143 depicted as a red line. **(D)** The map is coloured by its local resolution and shows the resolution distribution across the complex: The resolution in the cytosolic vestibule is highest and diminishes towards the paddle helices. Part of the figure adapted from Flegler et al. (2021).

### 3.2.4 Ligands in the closed and open cryo-EM structures of MscS

**The lipid molecule coordinated by R88 is visible in the map of closed MscS obtained under condition 3a.** Various lipid and detergent molecules were identified in the different MscS maps. The map of closed MscS obtained after re-lipidation under condition 3a has a better resolution than the map produced by condition 1. This might be due to more complete lipidation under condition 3a, but also to the higher particle number in this data set (table 3.5). The map shows density for the lipid molecule at the periplasmic side of the pore, coordinated by R88, which was also in previous EM maps observed as best resolved lipid (Rasmussen et al., 2019a; Reddy et al., 2019). In proximity to this lipid, a DDM molecule is observed with its headgroup probably coordinated by Q92. The hydrophobic pockets of the map of closed MscS contain unassigned densities, but it was not possible to model any ligands. In the map of open MscS obtained under condition 2a, a lipid molecule was modelled in this position, as for the map of MscS in LMNG produced by condition 2b. The cryo-EM structure of MscS in MSP nanodiscs revealed three lipid molecules per subunit in total (Rasmussen et al., 2019a).

**Lipid-, DDM-, and LMNG molecules are identified in the open MscS structure obtained under condition 2b.** Open MscS in LMNG (condition 2b) could theoretically contain co-purified lipids from the membrane, DDM from the solubilisation and LMNG from further purification steps. All three types of ligands were identified, and finally, one lipid, three DDM and five LMNG molecules were modelled per subunit (figure 3.24). The resolved lipid is coordinated by R59 that is located in the loop connecting the paddle helices TM1 and TM2. A DDM molecule per subunit is lying parallel to this lipid (figure 3.24 B, E). One set of DDM molecules is found at the periphery of the pore, with their aliphatic chains intercalating in the spaces between the TM3a helices that emerge upon channel opening (figure 3.24, A, F). Their headgroups are facing towards the cytosolic domain and are likely to be coordinated by Q112 at the cytosolic exit of the pore. A second set of DDM molecules is identified in the pore towards the periplasmic exit, where their headgroups are probably coordinated by Q92 in the loop connecting the helices TM2 and TM3a (figure 3.24 C, F). LMNG molecules are present at the paddle loop close to the lipid molecule as well as in the gaps that arise between the TM1 helices during opening (figure 3.24 A, D, G, H).

**LMNG molecules form stacks in the MscS complex.** Two LMNG molecules are stacked at the loop connecting the TM1 and TM2 helices close to the resolved lipid (figure 3.24 A, G). Three more LMNG molecules form a stack in the grooves between the TM1 helices at the periplasmic side, with their headgroups facing towards the pore axis and their aliphatic chains facing outwards (figure 3.24 D, H). The middle LMNG molecule is anchored between Y27 in the helix TM1 and R88 in the periplasmic loop between the TM2 and TM3a helices. Structures of closed MscS embedded in a lipid bilayer show R88 forming a salt bridge with a lipid headgroup (Rasmussen et al., 2019a; Reddy et al., 2019), so probably lipids would be in similar positions in MscS in a membrane. Upon opening, grooves arise between the TM1 helices, and R88 moves outwards with the potential bound lipid molecule. Comparing the open MscS structures, DDM molecules are seen under condition 2a in regions where LMNG molecules are seen under condition 2b.

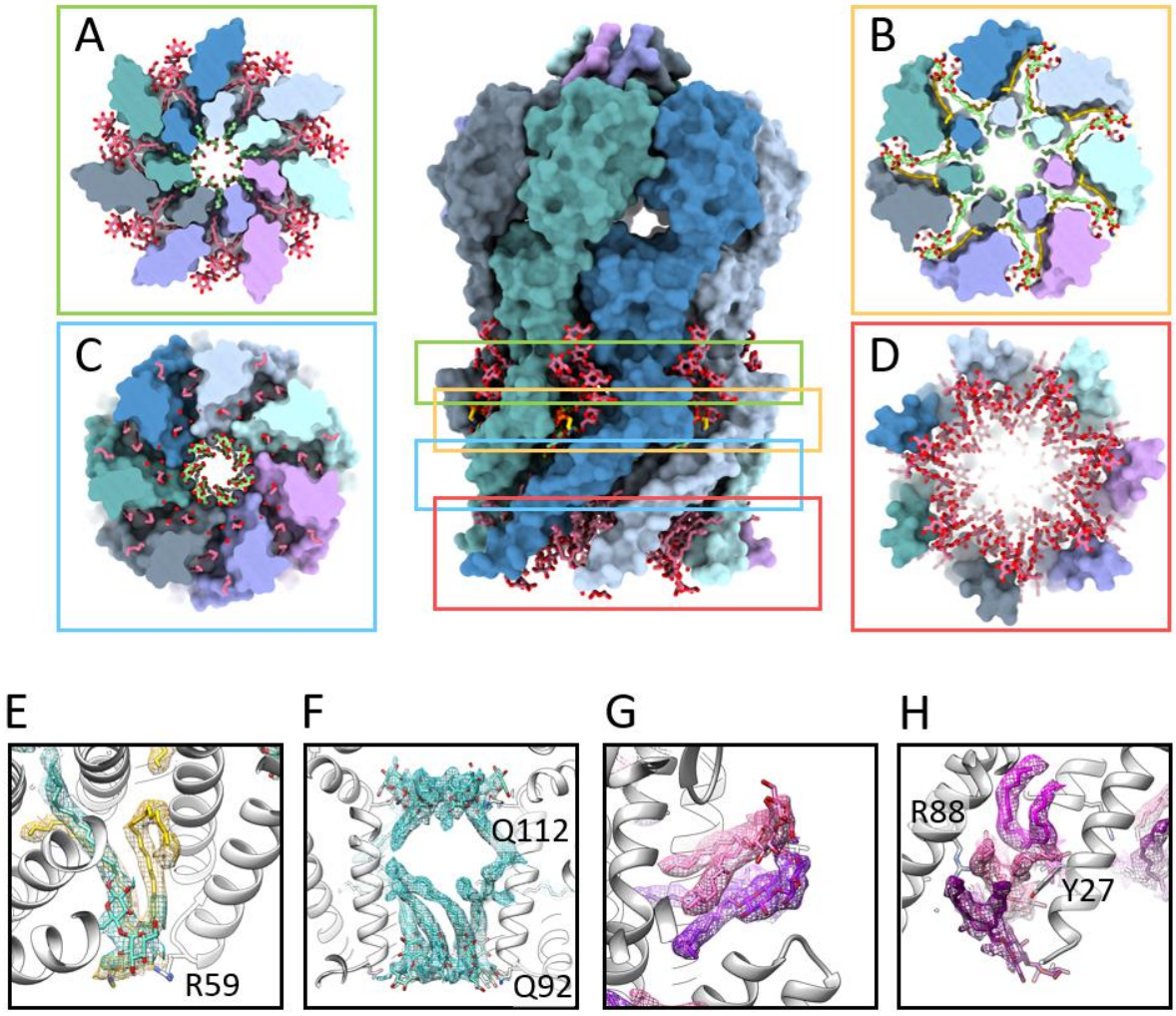


**Figure 3.24 | Ligands identified in the open structure of MscS in LMNG. (A)-(D)** Slices highlighted in the surface representation (coloured by subunits) in the middle viewed along the symmetry axis from the periplasmic side. Lipid molecules are shown in yellow, LMNG molecules in red, and DDM molecules in light green. **(E)-(H)** Close-ups of selected ligands in their respective densities are depicted as mesh. Lipids are coloured yellow, DDM molecules cyan, and LMNG molecules in different shades of purple. The protein backbone is shown as a grey ribbon. **(A)** At the cytosolic side of the transmembrane domain, two LMNG molecules per subunit (close-up in **G**) stack near the paddle loop and one DDM molecule is found in the pore with its headgroup facing towards the cytosolic exit (close-up in **F**). **(B)** Parallel to the lipid molecule coordinated by R59, a DDM molecule is resolved (close-up in **E**). **(C)** At the periplasmic exit of the pore, one set of DDM molecules is present with their headgroups facing towards the periplasmic side (close-up in **F**). **(D)** In the gaps between the TM1 helices, three LMNG molecules per subunit stack. The middle one is clamped between R88 and Y27 (close-up in **H**).

## 3.3 Structural characterisation of a large paralogue

The three large MscS-like channels YbiO, YjeP and MscK are predicted to have 11 TM helices per subunit and an additional N-terminal periplasmic domain. This domain is predicted to be a bundle of helices and has been proposed to form a coiled-coil structure (Pivetti et al., 2003), while the architecture of the remaining channel, particularly the cytosolic domain, is predicted to be conserved to MscS. Having demonstrated the structural features of the small channel MscS (Rasmussen et al., 2019a) and the medium-sized channel YnaI, a structure of a large paralogue remained elusive. Therefore, the established purification methods were applied on the large channels to get structural insights into one large paralogue and to compare it to MscS and YnaI. Because the purification yield of YjeP is reduced only by 70 % compared to MscS, and therefore still higher than that of the smaller YbiO (yield reduced by 95 %) (Edwards et al., 2012), it was tested first whether YjeP can be extracted from plasma membranes with DIBMA copolymer.

### 3.3.1 Purification trials of YjeP

**DIBMA cannot solubilise YjeP from *E. coli* membranes.** YjeP is comprised of 1107 amino acids, corresponding to an MW of 123 kDa for one subunit and 861 kDa for the homoheptamer. As an initial trial, using the same procedure that proved successful for YnaI failed, a solubilisation test was conducted to analyse different conditions. Previously, dynamic light scattering measurements of DIBMA addition to large unilamellar vesicles made from PC have shown that the hydrodynamic diameter of empty DIBMA-stabilised nanodiscs increases with a decreasing DIBMA/PC ratio (Oluwole, 2017; Oluwole et al., 2017). So, it was tested whether the addition of less DIBMA (⅓x compared to standard) would aid solubilisation of YjeP, as well as the supplementation of the sample with a standard amount of DIBMA with 1 mM DDM (figure 3.25). Besides, it was also tested whether increasing the DIBMA concentration (3x compared to standard) would lead to solubilisation of YjeP. Moreover, a combination of DIBMA copolymer and 1 mM DDM was tested for solubilisation.

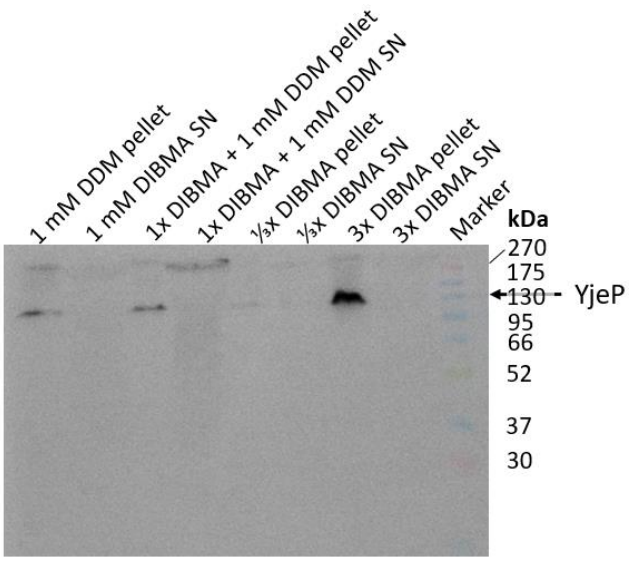


**Figure 3.25 | Western blot analysis of the solubilisation trials of YjeP in DIBMA.** YjeP was solubilised in 1 mM DDM only as a negative control, as well as in the standard amount of DIBMA (1x DIBMA) supplemented with 1 mM DDM, in one-third of DIBMA compared to the standard amount (⅓x DIBMA) and three times more DIBMA compared to the standard amount (3x). For each trial, both the pellet and the supernatant (SN) after solubilisation was analysed. The differences in the pellet intensities arise from the imprecise handling when preparing the pellet sample for SDS-PAGE.

The Western blot shows that neither of the attempts led to satisfying solubilisation of YjeP. Merely YjeP tested with the standard amount of DIBMA and supplemented with 1 mM DDM shows a protein signal for the supernatant, which is not corresponding to the molecular weight expected for YjeP, but rather is stuck in the well at the beginning of the separating gel. This indicates that DIBMA can slightly solubilise YjeP with the addition of DDM but probably leads to aggregates that cannot be separated by SDS PAGE. The control shows that 1 mM DDM alone is not sufficient to solubilise YjeP. On the other hand, YjeP can be solubilised using the standard procedure with 1 % (w/v) DDM (figure 3.26 B).

**YjeP in Amphipols A8-35 is very heterogenous on negative-stain- and cryo micrographs.** YjeP was solubilised and purified in DDM, and the detergent was exchanged by Amphipols A8-35 prior to a SEC. The SEC showed one maximum at an elution volume of 8 ml (P1), which corresponds to the void volume of the column, followed by a shoulder at an elution volume of ~9.5 ml (P2) (figure 3.26 A). The purification was monitored by SDS-PAGE (figure 3.26 B), which showed that the elution fractions of both peaks clearly contained YjeP as a pure product. As the fractions of P1 showed highly aggregated protein, the fractions of P2 were pooled and concentrated to 0.7 mg/ml. Micrographs of negatively stained YjeP showed both single particles and clustering of several particles (figure 3.26 C). The particles did not look homogeneous, which was confirmed by cryo-EM: particles appeared very fuzzy on the micrographs, tending to form aggregates, and were very inhomogeneous in size and shape (figure 3.26 D).

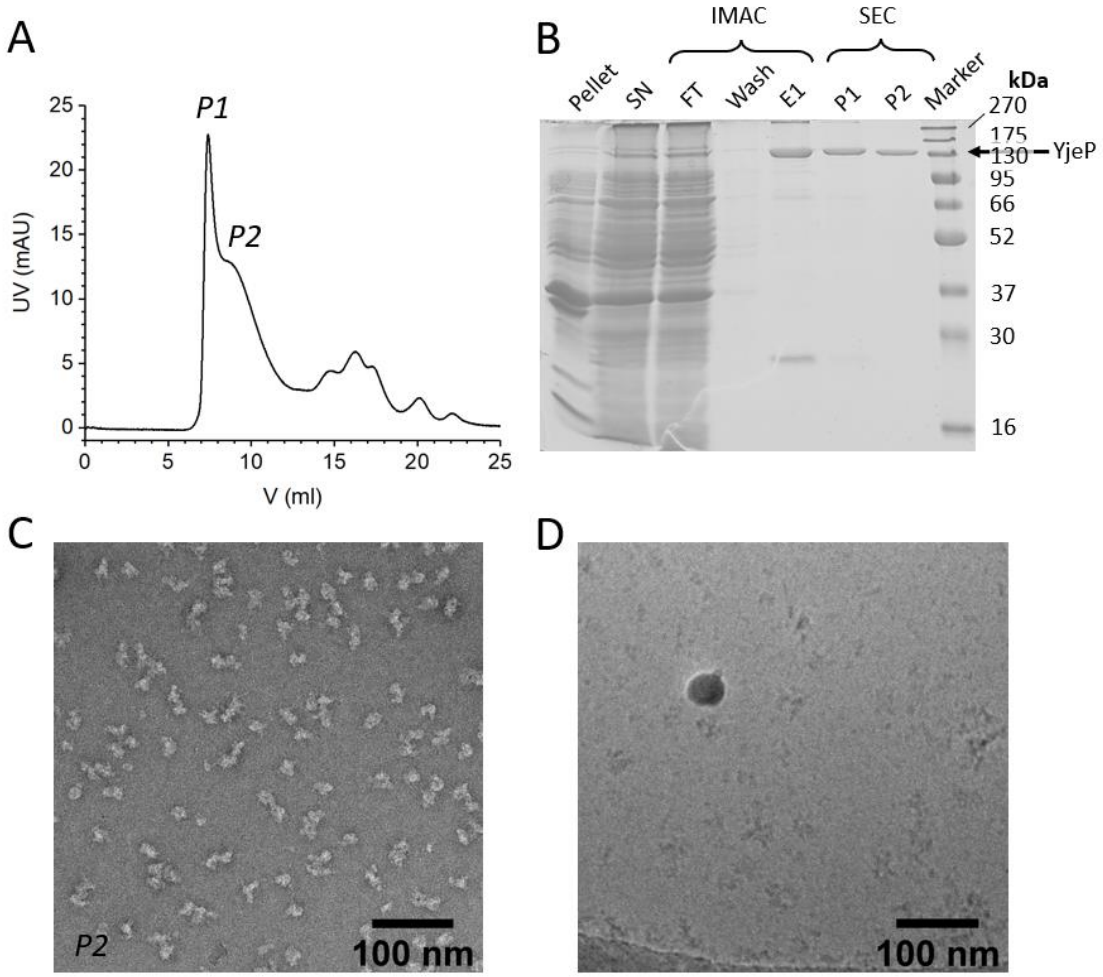


**Figure 3.26 | Purification of YjeP in Amphipols A8-35. (A)** In the SEC profile, P1 with its maximum at an elution volume 8 ml is visible (corresponding to the void volume of the used column), followed by a shoulder at ~9.5 ml (P2). The SEC chromatogram indicates that the used column is unsuitable for the large YjeP complex. **(B)** The purification was analysed by SDS-PAGE. As the detergent was exchanged by Amphipols after the IMAC, the IMAC elution fraction E1 contains YjeP in DDM, while peak 1 and peak 2 of the SEC contain YjeP in Amphipols. **(C)** The micrograph of the negatively stained sample of the pooled and concentrated fractions of peak 2 revealed considerable heterogeneity as well as smaller clusters of particles. **(D)** The micrograph of the vitrified sample showed particles that seem to be aggregated and stick to the rim of the hole.

## 3.3.2 Purification of YbiO in Amphipols A8-35

The purification yield of YbiO is lower than for YjeP (Edwards et al., 2012), but it is smaller in size (566.4 kDa vs 859.6 kDa), which is mainly due to its significantly shorter N-terminal periplasmic domain. This periplasmic domain is predicted by *MEMSAT* (Nugent and Jones, 2009) to be only 138 residues long in YbiO, compared to 477 in YjeP. For both proteins, this domain is predicted by *PSIPRED* (Jones, 1999) to be predominantly helical, but its exact

arrangement is not known. So, it is possible that the large size of this domain in YjeP is the reason for the observed heterogeneity and aggregation and impedes structural studies by cryo-EM. Therefore, the smaller YbiO was purified next and reconstituted into Amphipols A8-35. The SEC showed a maximum at an elution volume of 11 ml (P2) (figure 3.27 A). As observed for YjeP (figure 3.26), Another peak (P1) at an elution volume of 8 ml corresponds to the void volume of the column. SDS-PAGE and Western blot confirmed that the elution fractions of P2 contained YbiO (figure 3.27 B), although its signal is observed at a much lower molecular weight (~66 kDa) than expected (theoretical MW of one subunit: 81 kDa). Though the irregular migration of membrane proteins in SDS gels is well described (Rath et al., 2009; Renthal, 2006), mass spectrometry was applied to corroborate the full-length size of the purified YbiO in Amphipols A8-35 (figure 3.27 C). As for YnaI, YbiO was examined functionally by electrophysiology for adaptation (figure 3.27 D). Under a prolonged stimulus, no spontaneous closings appear, indicating that YbiO, as YnaI, does not adapt.

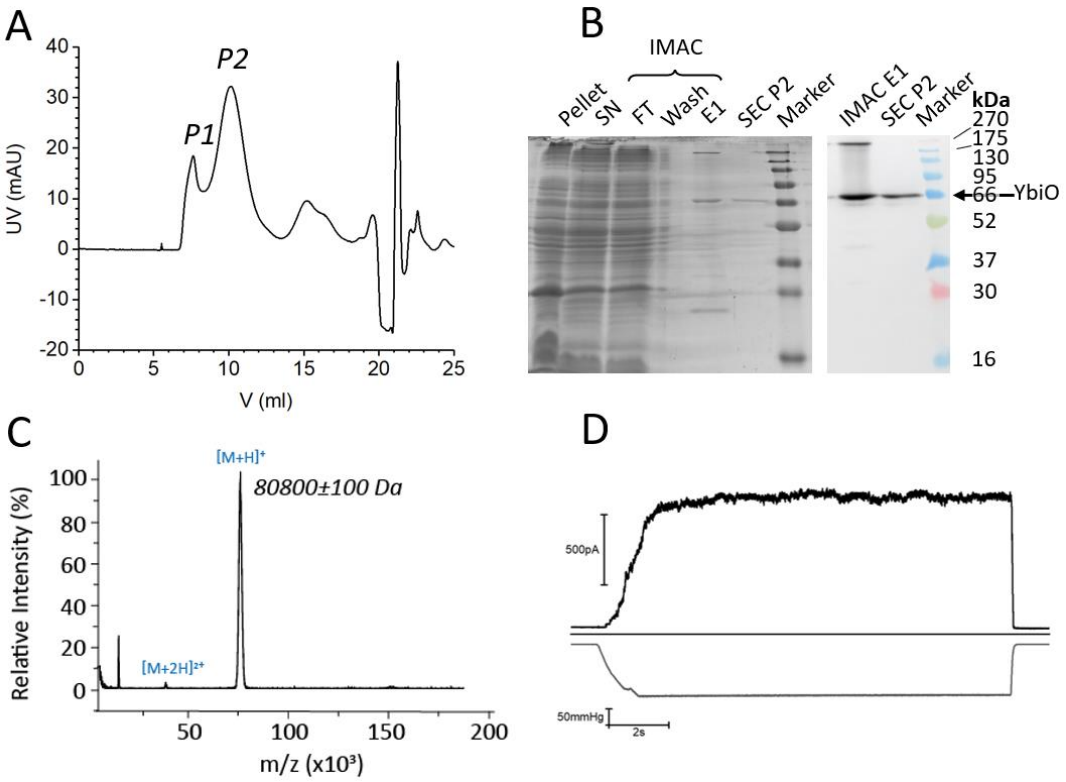


**Figure 3.27 | Purification and analysis of YbiO in Amphipols A8-35. (A)** Besides the peak P1 corresponding to the void volume of the used column (8 ml), the SEC profile shows a peak at an elution volume of ~11 ml (P2). **(B)** SDS-PAGE (left) and Western Blot (right) confirmed that the fractions of P2 contain YbiO. **(C)** The full-length of purified YbiO in Amphipols was confirmed by mass spectrometry: The mass spectrum reveals a size of 80.8 kDa compared to a theoretical mass of 80.9 kDa, considering the C-terminal $His_6$ tag ($LEH_6$) and the cleavage of an 18-residue signal sequence. **(D)** The patch clamping trace of YbiO was recorded under a prolonged stimulus and did not show any spontaneous closings; hence, YbiO does not adapt. Part of the figure adapted from Flegler et al. (2020).

### 3.3.3 Structural analysis of YbiO in Amphipols A8-35

**The predicted additional TM helices are not resolved.** Single particles of YbiO in amphipols A8-35 were visible on the micrographs from cryo-EM data collection, and during image processing, 2D classification demonstrated that the particles do not adopt a preferred orientation as YnaI or MscS (figure 3.28 A). Data acquisition and map parameters are given in table 3.6. 2D class averages showed two domains as seen for MscS and YnaI: One part exhibiting clear secondary structure features, corresponding to the cytosolic vestibule, and a broader, unsharp part, presenting the TMD (figure 3.28 B). The smearing of the transmembrane moiety already points either towards a high degree of flexibility of this domain or indicates denaturation of the outer TMD. Further processing of the data resulted in a 3.0 Å resolution map of vestibule and TM3 together with parts of the innermost paddle, while the rest of the complex remained unresolved (figure 3.28 C, D). The quality of the map, however, varies significantly over different regions of the complex. The cytosolic vestibule is very well resolved, as is the pore helix TM3. Only the helices TM1 and TM2, which correspond to the two paddle helices of MscS, are visible, but none of the predicted eight additional helices. This relates to the smeared-out membrane part observed in the 2D class averages in is also reflected by the *B*-factor distribution of the model (figure 3.28 G).

**The structure of YbiO matches the architecture of MscS and YnaI.** For YbiO, only a model from the cytosolic vestibule, the pore helices, the TM2 helices and a fragment of the backbone of the TM1 helices was built. The overall architecture of the built model, in particular the vestibule, looks very much like MscS in its closed conformation. Compared to MscS, the paddle helices TM1 and TM2 are rotated by ~10° clockwise (viewed from the periplasmic side) and are slightly tilted relative to the TM1 helix of MscS (figure 3.28 E, F). This clockwise rotation of the paddle, though to a much smaller degree, is also observed for the open conformation of MscS, raising the assumption that YbiO in Amphipols is not fully closed. Like in YnaI, the pore of YbiO seems to be partially lifted out of the membrane plane on the cytosolic side, and an indentation on the periplasmic side is visible, which is even larger as in YnaI (figure 3.28 D). One striking difference between YbiO and MscS and YnaI is the presence of a strong density ring around the TM3b helices in YbiO (figure 3.28 D). Although it could not be modelled, it is likely that it derives from the loop connecting the helices TM1 and TM2,

which is predicted by *MEMSAT* (Nugent and Jones, 2009) to be 19 residues long in YbiO instead of only 6 in MscS.

**Table 3.6 | Data acquisition and map parameters of YbiO in Amphipols A8-35.**

| | |
|---|---|
| **A** | |
| **EMDB code** | **EMD-11629** |
| **Data collection** | |
| Microscope | Titan Krios G3 |
| Voltage (kV) | 300 |
| Camera | Falcon III |
| Data collection mode | linear |
| Electron exposure ($e^-/(Å^2)$) | 80 |
| Underfocus (µm) | 1.4 – 2.6 |
| Pixel size (Å) | 1.0635 |
| Number of movies collected | 41113 |
| **Map parameters** | |
| Final number of particles | 212613 |
| Symmetry imposed | C7 |
| Map resolution (Å) | 2.9 |
| Sharpening *B*-factor ($Å^2$) | -138 |
| Processing Software | *Relion* 3.0 |
| **B** | |
| **PDB code** | **7A46** |
| **Model composition** | |
| Non-hydrogen atoms | 10647 |
| Protein residues | 1407 |
| Ligands | 0 |
| **Validation** | |
| MolProbity Score | 1.82 |
| Clashscore | 7.12 |
| Poor rotamers (%) | 1.84 |
| **R. m. s. deviations** | |
| Bond lengths (Å) | 0.009 |
| Bond angles (°) | 0.671 |
| **Ramachandran plot** | |
| Favoured (%) | 96.48 |
| Allowed (%) | 3.52 |
| Outliers (%) | 0.00 |

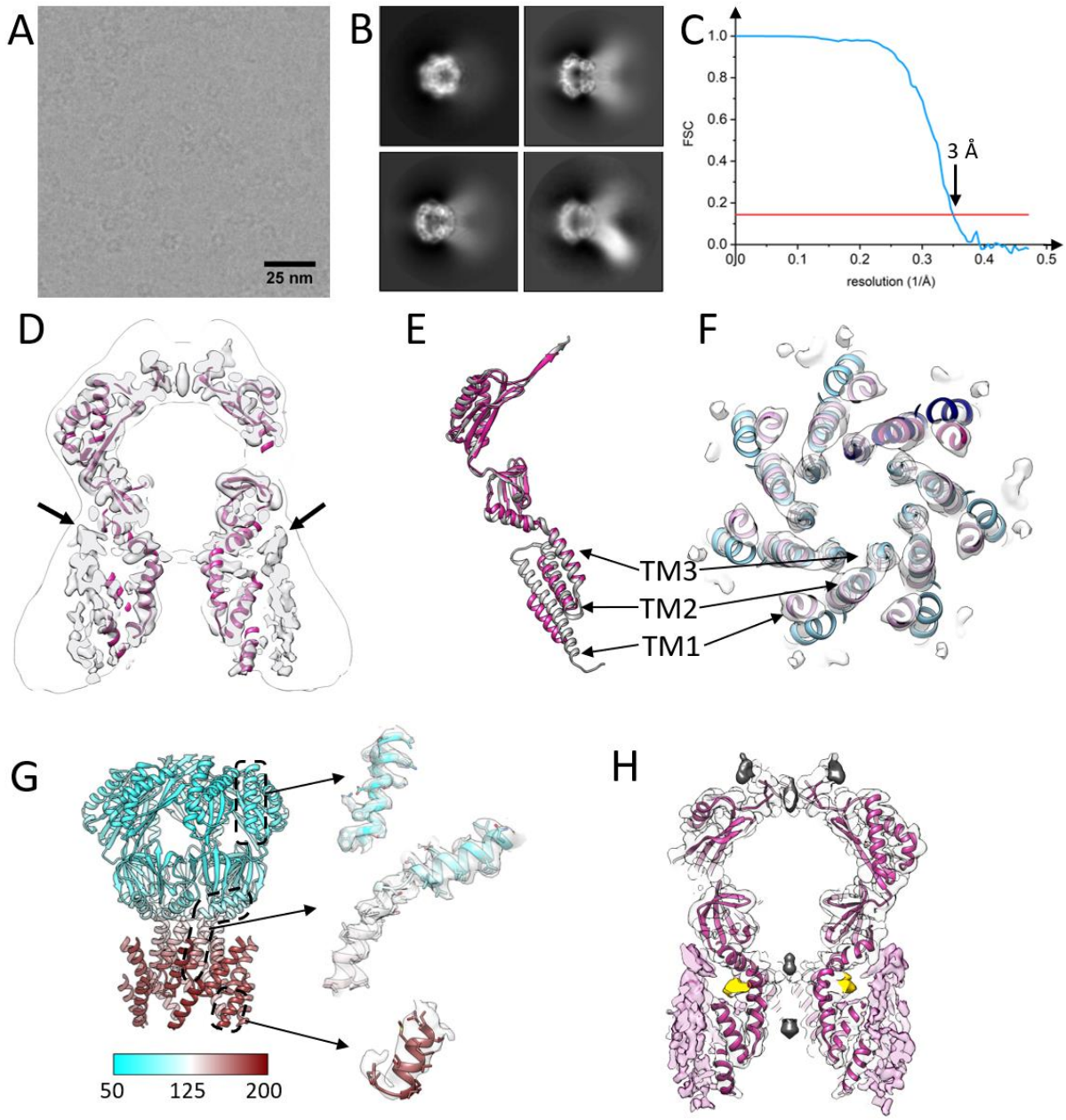


**Figure 3.28 | The cryo-EM structure of YbiO reveals a conserved architecture of the cytosolic domain and a flexible transmembrane part. (A)** Cut-out of a micrograph from the data collection. **(B)** Representative 2D class averages show differently tilted side views. The moiety deriving from the membrane domain is smeared. **(C)** The FSC curve of the final map. The threshold of 0.143 is represented by the red line. **(D)** In this 10 Å thick central slice through the map and model of YbiO viewed from the side, the model of YbiO is depicted in purple. The *LocScale* (Jakobi et al., 2017) map is shown in grey at a lower contour level, and as an outline, the lowpass-filtered map is displayed at a higher contour level to visualise the indentation on the periplasmic side. The additional density ring is highlighted by the two arrows. **(E)** The comparison of one subunit of YbiO (purple) with MscS (blue) viewed from the side shows that the TM3a helix is moved away from the pore axis by 2 Å and that the TM1 helix is differently tilted reminiscent of the opening transition of MscS. **(F)** The comparison of YbiO (purple, one subunit coloured darker) and MscS (blue, one subunit coloured darker) viewed along the symmetry axis from the periplasmic side. The TM1 helices of YbiO are rotated clockwise around

◀ the symmetry axis compared to MscS. **(G)** The model of YbiO is coloured by its local *B*-factor determined with *Phenix* ADP-refine for the model using the sharpened map. The close-ups of the regions highlighted in dashed boxes are shown in their corresponding EM density. **(H)** Unassigned densities in YbiO might derive from aggregation/noise accumulation (dark grey), part of the unmodelled protein (pink) or lipids (yellow). Part of the figure adapted from Flegler et al. (2020).

**YbiO is stabilised by lipids during purification.** As only a minor part of the transmembrane domain of YbiO could be modelled, it is challenging to look for unassigned densities that might correspond to eventually bound lipid molecules as observed in MscS and YnaI. In the pockets between the helices TM2, TM3a and TM3b, however, a density fragment is visible that does not correspond to a protein residue (figure 3.28 H) and could originate from a bound lipid. This is, nonetheless, speculative and needs further validations. Purification of YbiO in a lipid-enriched buffer allowed concentrating to some degree (~5 mg/ml) without aggregation, indicating a supporting effect of lipids on the stability of the complex (figure 3.29 A). 2D class averages of negatively stained YbiO, reveal on one hand the triangular or Y-shaped form that is expected for the channel, and on the other hand, a huge conformational heterogeneity of the complex (figure 3.29 B).

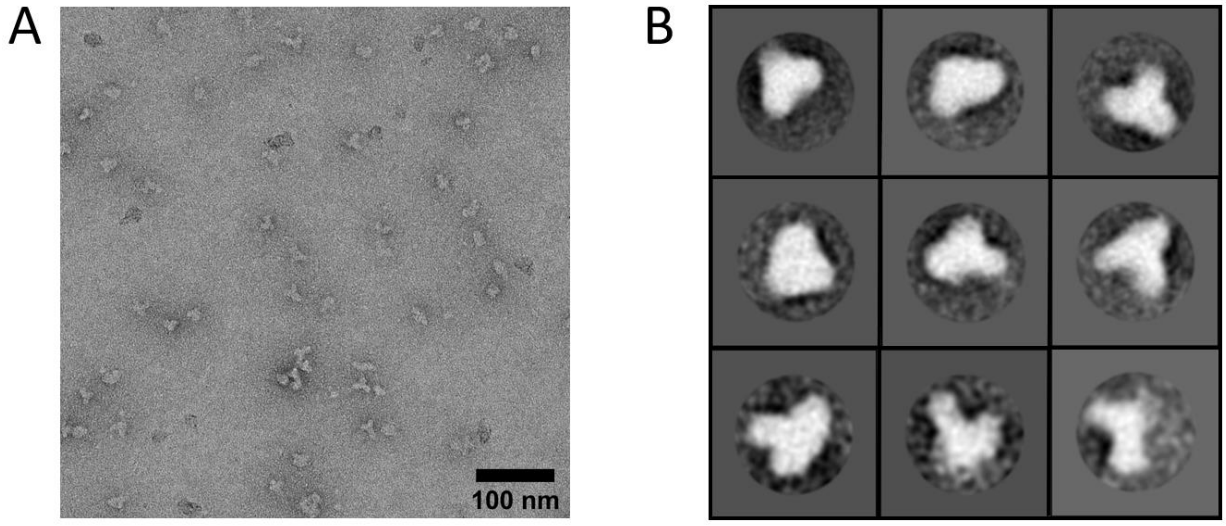


**Figure 3.29 | Analysis of negatively stained YbiO. (A)** Representative micrograph of a 1:250 dilution of a 5 mg/ml sample showing that predominantly single particles are present. **(B)** Selected class averages of a small data collection (60 micrographs) of negatively stained YbiO reveal conformational heterogeneity of the complex. The edge of the box corresponds to 44 nm.

## 3.4 Comparison of MscS, YnaI and YbiO

Having established structures of MscS (Rasmussen et al., 2019a), YnaI and YbiO, it was possible to compare structural features of a small, medium, and large channel and relate them to functional properties of the different channels. As the cytosolic vestibule and the pore helices were well resolved in all channels, the focus was set to these regions. The resolutions in these regions allowed examination of the structures in detail, as well as the application of simulations regarding the pore hydrophobicity and computational electrophysiology.

### 3.4.1 Inter-subunit interactions

Hydrogen bonds and salt bridges between different subunits were found in the cytosolic vestibules of MscS, YnaI and YbiO, but not in the TMDs (figure 3.30 A). The interactions are found in analogous regions in the three channels but are not confined to specific residues. The locations of H bonds are more preserved than those of salt bridges and were predominantly found in the β barrels and β domains. H bonds were identified using the function *Find HBonds* embedded in *UCSF Chimera* (Pettersen et al., 2004), and salt bridges were analysed using the *Salt Bridges* function of *VMD* (Humphrey et al., 1996).

The extended β sheet between two adjacent subunits observed in YnaI is also present in MscS and in YbiO, as are the intermolecular H bonds in the β barrel. Salt bridges were found in the αβ domains of the three channels, but while the salt bridges in MscS are located between the portals and the β barrel, the salt bridges in YnaI are more restricted to the portal regions and the β domains. Only one salt bridge was detected in YbiO, also located in the β domain (figure 3.30 A, B).

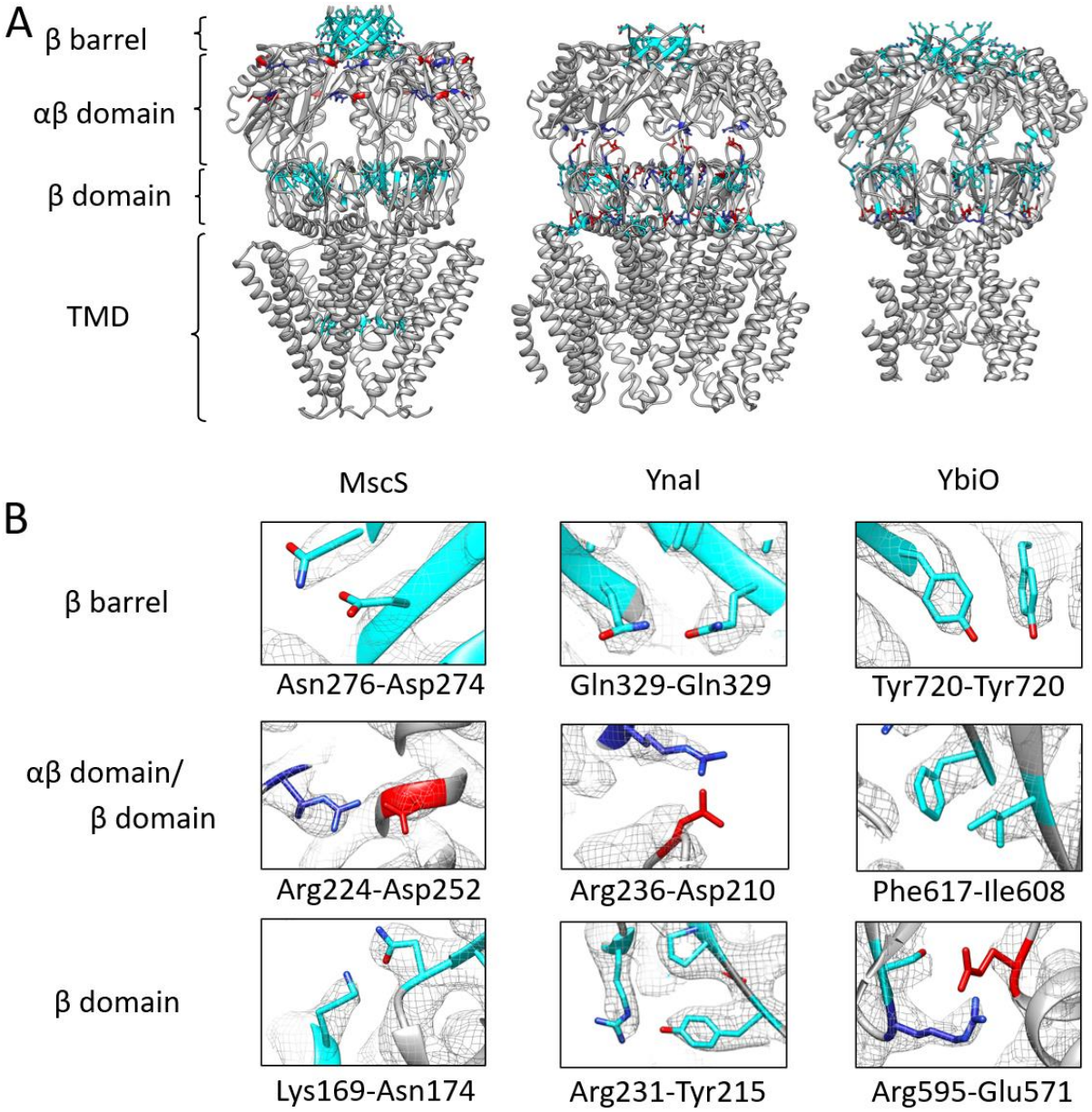


**Figure 3.30 | Inter-subunit H bonds and salt bridges in MscS, YnaI and YbiO. (A)** The models of MscS (PDB ID: 6RLD (Rasmussen et al., 2019a)), YnaI, and YbiO (from left) are shown as grey ribbons. Residues involved in hydrogen bonding are shown in cyan, residues forming salt bridges are coloured in red (negatively charged) and blue (positively charged), respectively. **(B)** For selected interactions in the β barrel, the αβ- and/ or β domain, the involved residues are shown in their respective densities, depicted as grey mesh (MscS EMDB-ID: 4919 (Rasmussen et al., 2019a)). The interactions are not conserved in specific residues but are found in similar positions. Figure adapted and modified from Flegler et al. (2020).

### 3.4.2 Constricting residues of the pores and portals

**Each channel has two rings of sealing residues in the pore.** All three channels display two sealing rings in the pore, where side chains point towards the sevenfold symmetry axis and mark the narrowest parts of the pores**.** Located at the cytosolic end of the pore helices TM3a, MscS has L105 and L109, which forms a vapour lock in the closed conformation (Anishkin et al., 2010; Anishkin and Sukharev, 2004) (figure 3.31 A, B). The pore of MscS is narrow and hydrophobic. Although it does not completely block the path, it causes dewetting (i.e., local desolvation), inhibiting the passage of water and solutes, which is shown by the 13 kJ/mol energetic barrier to water (figure 3.32 B). The N-terminally located sealing (L105) defines the narrowest part of the pore (6.2 Å), while the L109 ring has a diameter of 8.0 Å. All diameters were determined using the program CHAP (Klesse et al., 2019; Rao et al., 2019). In analogous positions, YnaI has L154 and M158 (figure A, B). Mutation of M158 to alanine led to a significantly higher conductance of the channel and also showed that this methionine is responsible for the $Na^+/K^+$ selectivity of the channel (Yu et al., 2018). The diameter profile observed in MscS is reverted in YnaI: The diameter of the cytosol-facing methionine ring (4.7 Å) is not only considerably smaller than the L109 in the homologous position in MscS but also smaller than the N-terminally located sealing ring of L154 (6.0 Å) (figure 3.31 A, B). The sealing ring residues in YbiO are L549 and F553 and resemble the diameter profile of YnaI: The cytosol facing F553 sealing ring creates with 6.9 Å a narrower constriction than the N-terminally L549 sealing ring (7.4 Å) (figure 3.31 A, B). Although the TM3a helices are spaced 2 Å further away from the pore axis, the larger phenylalanine side chain leads to constriction similar to MscS. The phenylalanine residue is conserved among the three large paralogues (figure 3.31 A). In their cytosolic domains, all channels have two different access gates into the vestibule: the C-terminal β barrel and the side portals, that are located at the interface of the β and αβ domains. A further constriction ring of residues is found along the symmetry axis in the β barrel: with 4.9 Å (M273 in MscS and Y720 in YbiO) and 4.5 Å (L331 in YnaI) these regions exhibit a very similar constricting diameter (figure 3.31 D).

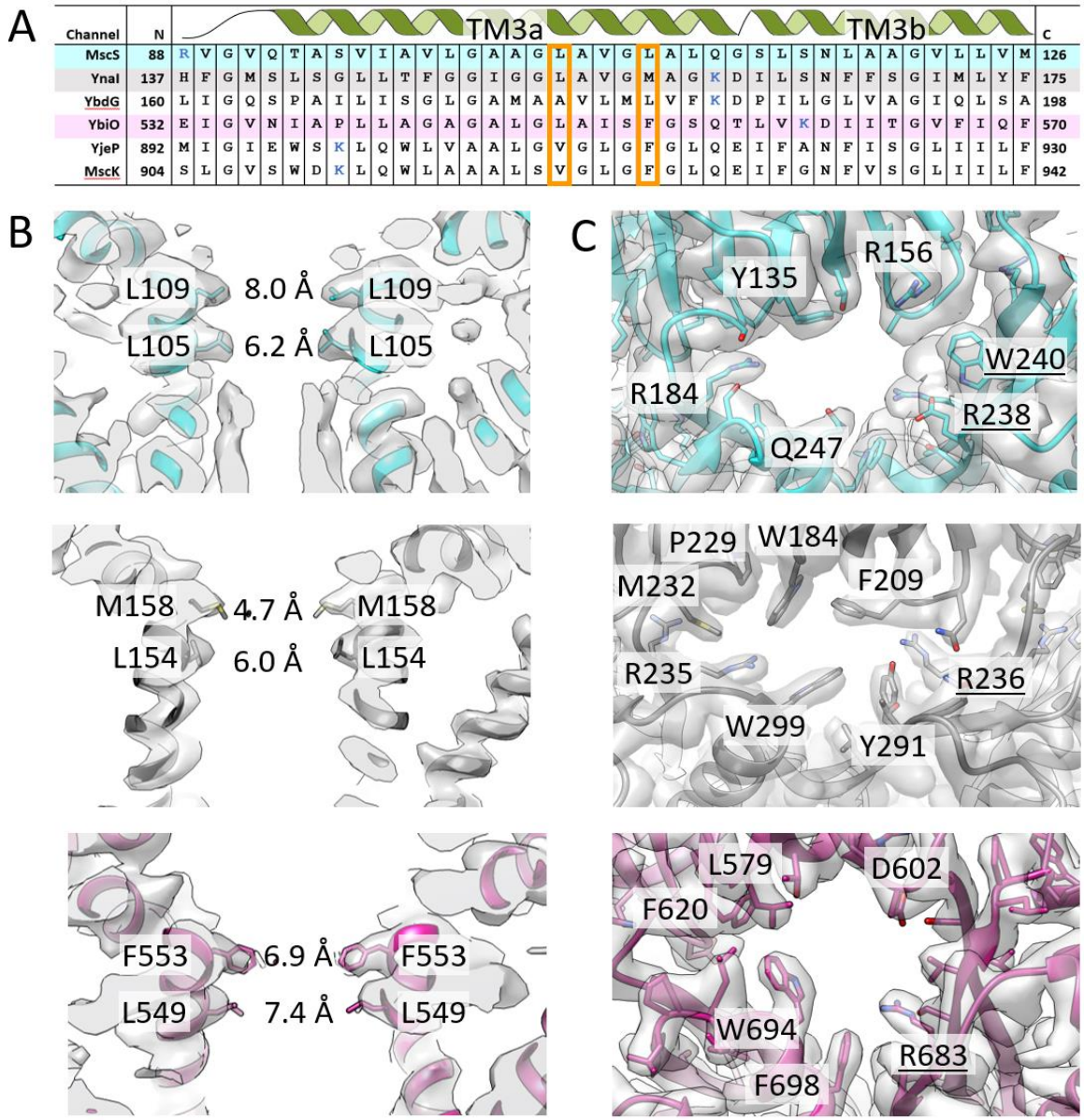


D

| | MscS | YnaI | YbiO |
|---|---|---|---|
| Conductance (nS) | 1.25 | 0.1 | 1.0 |
| Constricting pore residues (Ø Å) | L105 (6.2), L109 (8.0) | L154 (6.0), M158 (4.7) | L549 (7.4), F553 (6.9) |
| Minimal portal diameter (Ø Å) | 6.1 | 3.4 | 6.2 |
| Constricting β-barrel residue (Ø Å) | M273 (4.9) | L331 (4.5) | Y720 (4.9) |

**Figure 3.31 | Comparison of the pores and portals of MscS, YnaI and YbiO. (A)** Multiple sequence alignment of the TM3 helices of the MS paralogues in *E. coli*. The two sealing ring residues are framed in orange, and positively charged residues are depicted in blue. **(B)** Detailed view on the pores of MscS (cyan), YnaI (dark grey), and YbiO (purple) in their respective densities (grey). In the side view slices of the pores, the side chains of the constricting sealing ring residues are labelled, and the diameter of the pore at these positions is marked. **(C)** Detailed view on the portals of MscS (cyan), YnaI (dark grey) and YbiO (purple) in their respective densities (grey). Selected constricting residues are shown and labelled, and residues from the adjacent subunit are underlined. **(D)** Selected channel properties are listed for MscS, YnaI and YbiO, as well as different constricting residues. The values of the conductance are taken from literature (Edwards et al., 2012; Sukharev, 2002). Part of the figure adapted from Flegler et al. (2020).

**The lateral portals of MscS, YnaI and YbiO are structurally finetuned.** Based on early structures of *E. coli* MscS (Bass et al., 2002; Wang et al., 2008), the side portals were proposed to be the entrance into the vestibule, which was supported by a study that compared *E. coli* MscS to MscS from *Thermoanaerobacter tengcongensis*. These portals are also present within YnaI and YbiO, and all channels have in common that they are framed by many bulky side chains that are mainly aromatic and charged (figure 3.31 C). The position of these residues, however, is not conserved. In MscS, W240 is important for the stability and assembly of the complex (Rasmussen et al., 2007), and other residues close to the portals, E187 and E227, determine MscS anion selectivity (Cox et al., 2013). W184 in the portal region of YnaI is required for channel function (Böttcher et al., 2015). The portals of MscS and YbiO are similarly large with diameters of 6.1 Å and 6.2 Å, respectively, but are much smaller in YnaI. Because aromatic moieties like W184, F209, Y291 and W299 largely occlude the portals in YnaI, the minimal diameter is only 3.4 Å (figure 3.31 D). Their narrowness might be one cause for the low conductance of YnaI (0.1 nS) compared to MscS (1.25 nS) and YbiO (1.0 nS).

### 3.4.3 Comparison of the hydrophobicity of the pores

**The transmembrane parts of the pores of MscS, YnaI and YbiO differ in hydrophobicity.** The program CHAP (Klesse et al., 2019; Rao et al., 2019) was used to compare the pores of the three channels in more detail. The analysis is shown only for the closed(-like) conformations. The transmembrane gate and the cytosolic constriction site (the β barrel) were investigated separately (figure 3.32). The pore of YnaI is more hydrophilic than in MscS, and it is less locally dehydrated, as the energetic barrier to water is only 1.5 kJ/mol compared to 13 kJ/mol in MscS. Hence, the conformation of the closed-like YnaI probably rather reflects a "partially closed" state. This agrees with computational electrophysiology simulations (3 × 200 ns): no ions passed the TM gate. The pore of YbiO, in contrast to YnaI, is hydrophobic as in MscS. However, as the helical axes of the pore helices are farther spaced in YbiO, the pore has, apart from the constricting residue F553, a larger diameter than the pore in MscS. Therefore, the pore is predicted to be hydrated and remains hydrated during MD simulations. Computational electrophysiology simulations indicate a conductance of ~30 pS and $Cl^-$ selectivity.

**The cytosolic domain of YbiO is more hydrophilic than in MscS and YnaI.** The β barrels of MscS and YnaI are predicted by CHAP to be closed, while the one of YbiO is open and could conduct. As the 18 C-terminal residues were not modelled, it is nonetheless possible that the β barrel is blocked in this region. Computational electrophysiological simulations suggest that $Cl^-$ ions enter YbiO via the side portals. The side portals of YnaI are also predicted to be open, despite being narrow in both the closed-like and the open-like conformation. Although in computational electrophysiological simulations, no conductance was observed, they remain hydrated during MD simulations.

A

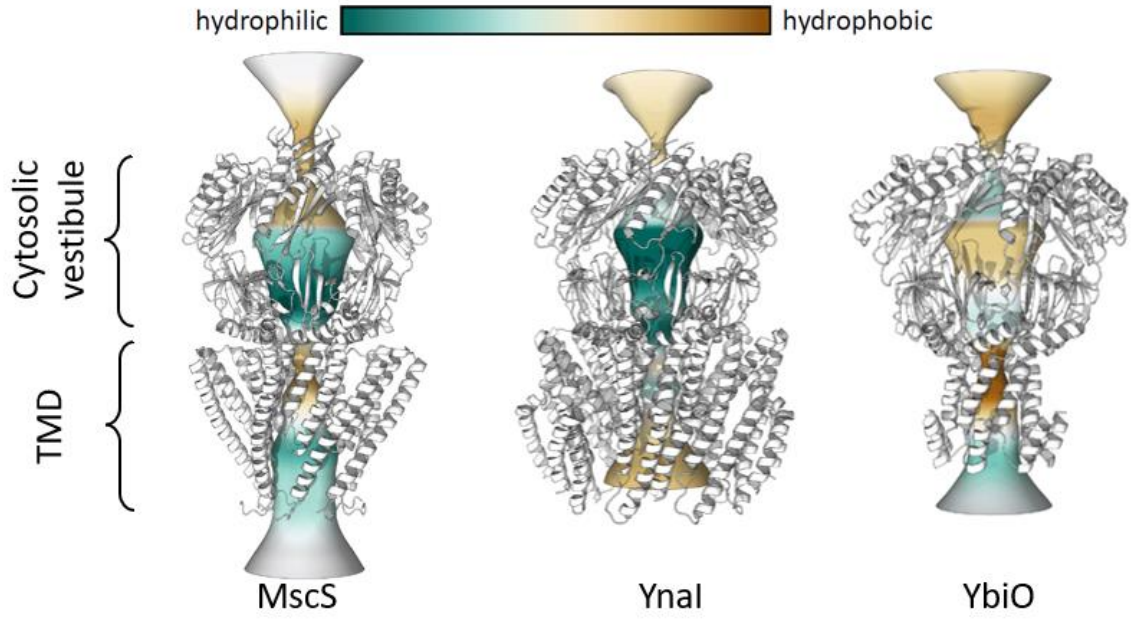


B

| Channel structure | Transmembrane gate | | Cytosolic constriction | |
|---|---|---|---|---|
| | Prediction | $G_{water}$ (kJ mol$^{-1}$) | Prediction | $G_{water}$ (kJ mol$^{-1}$) |
| **MscS** | Dehydrated/closed | 13.0 | Dehydrated/closed | 32.5 |
| **YnaI** | Partially deh. at M158 | 1.5 | Dehydrated/closed | 5.3 |
| **YbiO** | Hydrated | 0.0 | Hydrated | 0.1 |

**Figure 3.32 | Visualisation of the hydrophobicity of the pores of MscS, YnaI and YbiO. (A)** The models of MscS (PDB 6RLD (Rasmussen et al., 2019a)), YnaI, and YbiO (from left) are shown as white ribbons. Hydrophobicity of the transmembrane (sealing ring residues in the pore) and cytosolic constrictions (β barrel) was determined with CHAP (Klesse et al., 2019) and is colour-coded. **(B)** Summary of the wetting/dewetting simulations along the pore axis for the transmembrane and cytosolic constrictions. Figure adapted and modified from Flegler et al. (2020).

# 4 DISCUSSION

The key findings of this work are evaluated in this section. Many results are also discussed in Flegler et al. (2020) and Flegler et al. (2021). Furthermore, the results are assessed here under consideration of the most recent internal and external findings that are relevant in this field and for this work and were not yet integrated into the publications.

## 4.1 Structural analyses of MscS-like channels

### 4.1.1 Advantages and limitations of different reconstitution systems

**YnaI can be solubilised into DIBMA-stabilised nanodiscs.** The SMA and DIBMA copolymers can generate lipid bilayer nanodiscs directly from plasma membranes and extract integral membrane proteins into these nanodiscs without the need to use classic detergents. This method was declared to provide a native-like environment, and the resulting particles were referred to as "native nanodiscs" (Dörr et al., 2014). DIBMA is expected to form larger nanodiscs than the more established SMA that forms nanodiscs with a diameter of 9-11 nm (Oluwole et al., 2017). Solubilisation of membrane proteins with SMA copolymer successfully led to different cryo-EM structures (Johnson et al., 2020; Parmar et al., 2018; Qiu et al., 2018; Tascón et al., 2020; Yoder and Gouaux, 2020; Yu et al., 2021), even for a protein complex with a membrane cross-section of approximately 9 nm x 13 nm (Sun et al., 2018). Although it was shown that SMA could extract the transporter AcrB with 36 TM helices (Postis et al., 2015), it failed to extract YnaI (35 TM helices). The AcrB trimer has a very compact arrangement of the TM domain, which has a diameter of only 80 Å (Murakami et al., 2002), so possibly the tapered shape of the TMD of YnaI increases the membrane cross-section to the degree that prevents the incorporation of YnaI into SMA-stabilised nanodiscs. Solubilisation of large unilamellar vesicles with DIBMA resulted in nanodiscs with diameters of 18-35 nm, depending on the DIBMA/lipid ratio (Oluwole et al., 2017). However, the suitability of DIBMA for cryo-

EM structural studies has not been demonstrated so far. In the present work, DIBMA was added directly to lysed *E. coli* cells that overexpressed YnaI, without a separate membrane purification step. YnaI was extracted and purified in DIBMA-stabilised nanodiscs; yet its solubilisation efficiency is only ~30 % compared to solubilisation of YnaI with DDM. This is noteworthy less than reported for DIBMA regarding total membrane protein mass, where DIBMA was shown to solubilise 70 % from *E. coli* BL21 compared to solubilisation with DDM (Oluwole et al., 2017). As no classic detergent is used throughout the extraction, and it is claimed that the protein is kept in its immediate lipid environment, this approach is considered to provide the most native-like environment for membrane proteins. However, it should be mentioned that besides the main lipid components of *E. coli* membranes – PE, PG and CL – also trace lipids like phosphatidylserine (PS) and phosphatic acid (PA) are present (Oliver et al., 2014). While in the TLC analysis of a lipid extract from DDM-purified YnaI, PE was identified as the main co-purified lipid, overexpression of YnaI could lead to depletion of the trace lipids from the membrane, resulting in a non-native membrane composition for the overexpressed protein. Indeed, Hu et al. (2021) recently observed a potential enrichment of PS and CL in their preparation of YnaI with LMNG, which could not be confirmed by our TLC analysis, perhaps due to the sample size used for TLC.

Limitations of DIBMA copolymer are not only its decreased solubilisation efficiency but also the size of the integral membrane protein. The large paralogue YjeP that comprises 77 TM helices in total was not extracted by DIBMA from native *E. coli* membranes following the procedure that led to the successful purification of YnaI. Even alteration of the polymer amount or supplementation with DDM did not result in solubilised YjeP, as shown by Western blot analysis. On the other hand, YjeP could be sufficiently solubilised in DDM (see figure 3.26 B).

**MscS and YnaI in Amphipols or nanodiscs adopt a preferred orientation on cryo-EM grids.** The first map of YnaI in Amphipols A8-35 at 3.3 Å resolution showed that YnaI adopted a preferred orientation with the sevenfold symmetry axis oriented perpendicular to the plane of the ice, which resulted in less than 2 % side views. The resulting map did not resolve the additional two TM helices compared to MscS, and this finding agrees with an earlier incomplete cryo-EM structure of YnaI in Amphipols A8-35, where the protein only could be modelled from helix TM2 (see figure 1.8) (Yu et al., 2018). Preferential orientation of the particles on the grid is often caused by the adsorption to the air-water interface (figure 4.1). While this leads to an enrichment of the sample and therefore decreases the needed concentration to obtain the desired grid coverage, it can also denature proteins (Taylor and

Glaeser, 2008). The uneven distribution of projections leads to resolution anisotropy of the map that appears in a loss of resolution parallel to the axis of the preferred orientation (Barth et al., 1989). Furthermore, much more data is required, as only a few particles are in side-view orientation, needed for image processing.

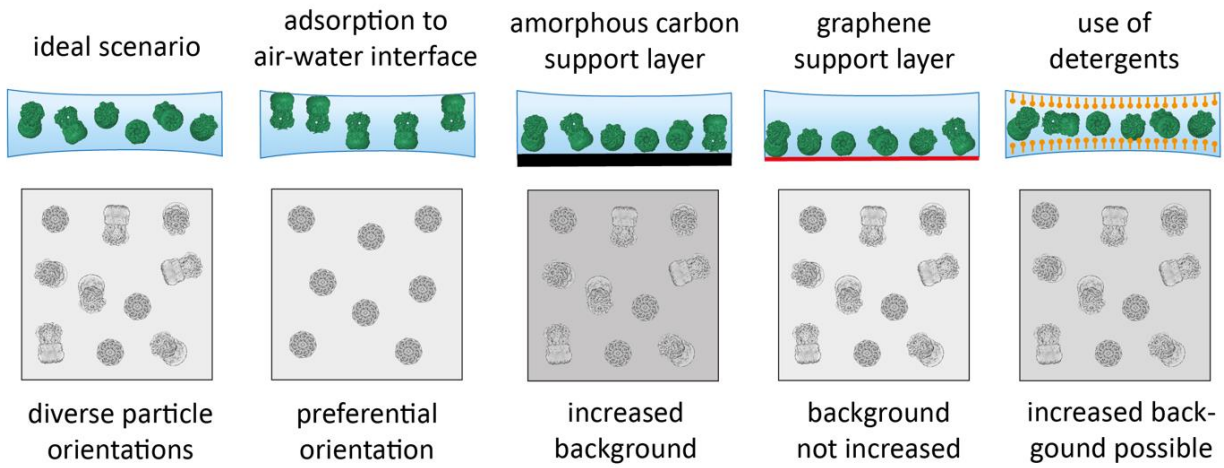


**Figure 4.1 | Preferential particle orientation and solutions.** The upper row depicts the particle organisation in a hole of a vitrified grid, and the lower row shows exemplarily the outcome as 2D projections. Ideally, particles (green) are vitrified in random orientations, resulting in various projections of the sample. Adsorption to the air-water interface can induce a preferred particle orientation, resulting in missing projection views. Strategies to prevent adsorption to the air-water interface include grid support layers like amorphous carbon or graphene and the use of detergents. While commercial carbon layers on grids (black line) are at least ~2 nm thick and thus contribute to the background (which is especially hampering for small particles), graphene can be added as a monolayer on the grids (0.35 nm) (red line) and does not increase the background. The presence of detergents also impedes adsorption to the air-water interface, either when the membrane protein sample is in a detergent-containing buffer or by the addition of a secondary detergent below its CMC (orange). Detergent molecules can add to the background, as well as micelles deriving from the primary detergent. The sample concentrates on support layers, leading to a much smaller required particle concentration than in the presence of detergents. As not all depicted approaches were tested, the shown particle behaviour is hypothetical and only based on results described in the literature. Particle representations were prepared using the cryo-EM map of MscS in MSP nanodiscs (EMDB 4919 (Rasmussen et al., 2019a)).

Support layers like carbon (Bai et al., 2013; Nguyen et al., 2015), graphene (Pantelic et al., 2012), or graphene oxide (Pantelic et al., 2010) can be used to ameliorate the particle orientation distribution. However, they either add background to the images or are difficult to handle in terms of glow-discharging. Unless the grids with a support layer are freshly prepared and therefore exhibit a hydrophilic surface, they need to be glow-discharged, because they will become hydrophobic due to adsorption of contaminants within a short time, and a hydrophobic

surface impedes proper wetting and adsorption of the sample. The chosen plasma gas determines the result of glow-discharging a surface: In-air glow-discharge systems make surfaces hydrophilic by introducing negative charges; however, the created plasma has enough energy to destroy support layers. Graphene monolayers can be made hydrophilic without damage by partial hydrogenation using a low-energy $H_2$ plasma (Russo and Passmore, 2014), or they can be functionalised them using helium plasma as a carrier (Naydenova et al., 2019). If support layers should be avoided, an alternative reconstitution system might promote different particle orientations.

Blob-based autopicking and 2D classification of YnaI-DIBMALPs revealed that approximately 33 % of the particles are present as side views. Thus, YnaI in DIBMA showed a reduced preferential orientation, resulting in a map with finally 327161 particles compared to 67740 particles in the final Amphipol map. However, as many particles in the data set were present as dimers-/trimers-of heptamers, the formation of those small aggregates likely contributed to the increase in side-views rather than the properties of the polymer (see figure 3.4 A). Other DIBMALPs data sets – LPC-treated YnaI (see figure 3.12 E) and MscS in Amphipols and DIBMA (see figures 3.20 A and C) support this observation. Not only polymer-stabilised nanodiscs but also MSP nanodiscs can lead to preferential particle orientation, as described for MscS (Rasmussen et al., 2019a). For MscS in MSP nanodiscs, particle side-views were induced by "controlled aggregation" upon $Ni^{2+}$ addition utilising the C-terminal $His_6$ tag. The large paralogue YbiO in Amphipols A8-35 did not show preferential orientation on cryo-EM grids. One explanation could be that YbiO is more aggregated than MscS and YnaI, resulting in fewer top views. It is also possible that the N-terminal periplasmic domain of YbiO alters particle orientations or further promotes aggregation, decreasing preferential orientation. Particle orientation diversity, while maintaining single particles, is best provided by the use of detergents, as shown for the MscS data sets. Without further additives or auxiliary equipment, a sufficient number of particles for high-resolution structure determination was obtained from data sets of moderate sizes (see table 3.5). The sample must not necessarily be stabilised by a primary detergent but can also be reconstituted in Amphipols or nanodiscs because also the addition of a mild secondary detergent, e.g. CHAPSO, below its CMC can reduce preferential orientation (Chen et al., 2019). This approach is also helpful when the primary detergent has a low CMC like LMNG. Such a combination allowed Hu et al. to purify YnaI successfully: Preferred orientation of YnaI in LMNG was counteracted by the addition of fluorinated Fos-choline-8 (Hu et al., 2021). However, the significantly higher sample concentration required in the presence of detergent is often a hurdle (Kampjut et al., 2021). In the case of MscS, a 10-fold

higher concentration was needed for MscS in LMNG and DDM compared to MscS in Amphipols, DIBMA-, or MSP nanodiscs (~5 mg/ml vs ~0.5 mg/ml) to achieve a comparable particle coverage of the grid. Moreover, in this work, it was not possible to sufficiently concentrate any of the paralogues apart from MscS in DDM, which, so far, underpins the dependency on a suitable detergent-free system, another final detergent, or a modified expression construct.

**Amphipols A8-35 have an impairing effect on MscS-like channels.** Amphipols have proven to successfully stabilise different membrane proteins in their native state (Tribet et al., 1996), and several structures of membrane proteins in Amphipols were elucidated by cryo-EM (Famelis et al., 2019; Saponaro et al., 2021; Sauer et al., 2020; Weaver et al., 2020; S. Zhang et al., 2017; Zubcevic et al., 2016). In this study, maps of MscS, YnaI, and YbiO reconstituted into Amphipols A8-35 were obtained. The map of YnaI only resolved the pore helix TM3 and the paddle helices TM2 and TM1, but nothing of the additional helices TM-N1 and TM-N2. Unresolved outer TM helices of YnaI were also observed in an earlier study and might be due to the high flexibility of the outer TM helices (Yu et al., 2018) or, additionally, the smaller particle number in the final map compared to YnaI-DIBMALPs. In the map of MscS in Amphipols A8-35, the pore helices were resolved and matched those of the closed conformation of MscS. The TMD observed in 2D class averages, however, was flatter, reminiscent of the inactivated conformation described by Zhang et al. (Zhang et al., 2021) (figure 4.2 A, middle), which would also be in agreement with the closed pore that was observed for this state. However, 3D reconstruction showed the conserved architecture of the cytosolic vestibule and revealed that apart from the pore helices, no defined density is present for the TMD (figure 4.2 A and B, left). So, even if the inactivated conformation were captured in Amphipols, it would be most likely denatured.

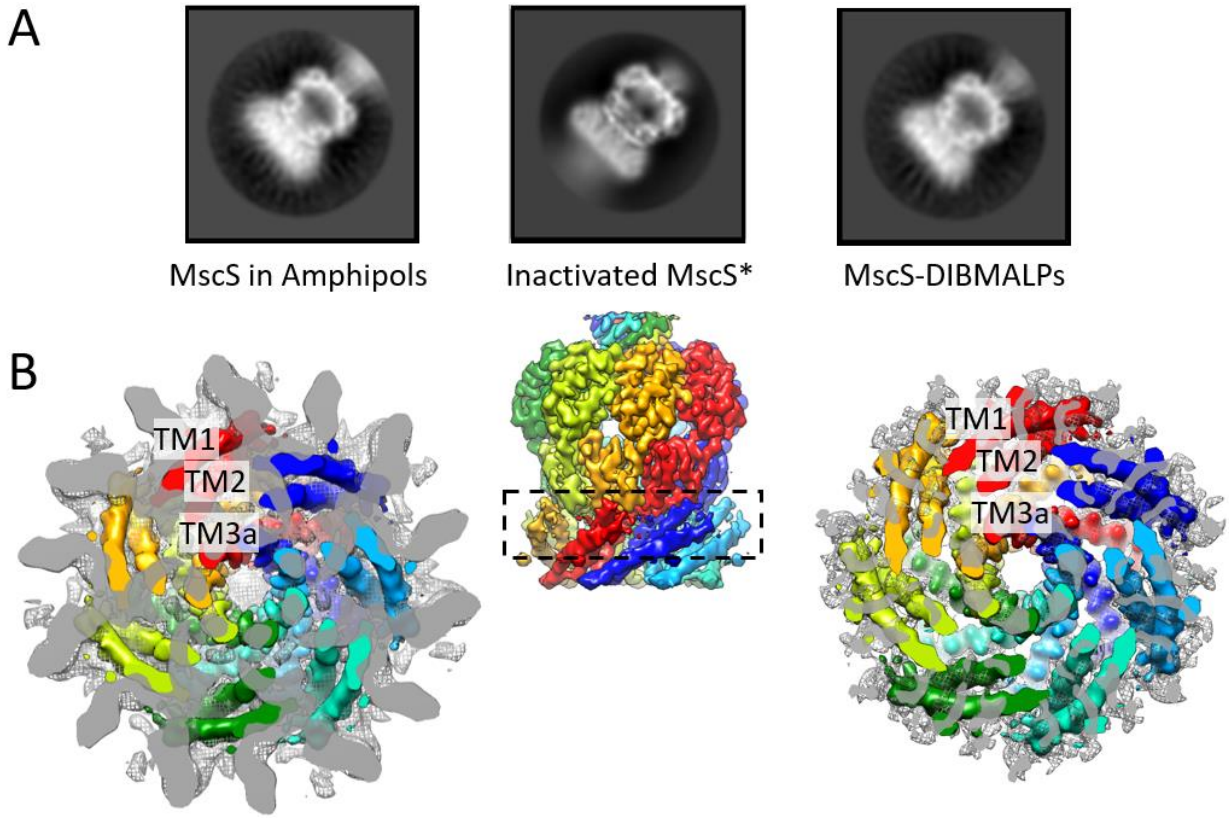


**Figure 4.2 | MscS in Amphipols A8-35 and in DIBMA-stabilised nanodiscs. (A)** Side-view class averages of both MscS in Amphipols (left) and of MscS-DIBMALPs (right) show a flatter TMD reminiscent of inactivated MscS (middle). The edge of the box of MscS in Amphipols and MscS-DIBMALPs corresponds to 24 nm, and the edge of the box of inactivated MscS corresponds to 21.6 nm. **(B)** The protein density of inactivated MscS (middle; EMDB 21464 (Zhang et al., 2021)) is coloured by its subunits and fitted into the maps (grey) of MscS in Amphipols (left) and MscS-DIBMALPs (right). The slice highlighted in the dashed box in the middle is depicted viewed from the periplasmic side. While the density of the pore helices fits the density of inactivated MscS, the remaining TMD is distorted. The helices of the red subunit are marked. The 2D class average of inactivated MscS (denoted as ”desensitised” in the original paper) is reprinted by permission from Yixiao Zhang et al.: ”Visualization of the mechanosensitive ion channel MscS under membrane tension”, Springer *Nature* (Zhang et al. (2021)).

Other studies showed that cryo-EM maps of TRPV1 and NOMPC in MSP nanodiscs were of superior quality compared to those in Amphipols (Gao et al., 2016; Jin et al., 2017b; Liao et al., 2013). This already hints that Amphipols somehow might impair the structure or stability of some membrane proteins; however, no effect has been reported that is comparable to the alteration of the TMD observed for MscS. The extremely high affinity of Amphipols for hydrophobic particles is considered one main advantage of this system (Popot, 2010), yet it is also possible that this strong interaction leads to the distortion of the contacting TM helices or that it exerts pressure on the channel, which could result in a conformational change of MscS,

and additionally perturbs the TMD. A study on the ion channel TRPV2 in nanodiscs and Amphipols revealed that Amphipols constricted the channel and abolished the C2 symmetry in regions that are bound by the Amphipol polymer (Zubcevic et al., 2019). This effect could also explain the unresolved outer sensor paddle of YnaI in Amphipols and could contribute to the understanding of why the majority of the TMD in YbiO is not resolved.

**DIBMA copolymer is detrimental to the contacting protein regions.** Similar to MscS in Amphipols, MscS in DIBMA-stabilised nanodiscs exhibited a flatter and disturbed TMD (figure 4.2 A and B, right). The resolved pore helices resemble a closed pore, but no defined density is present that could account for the sensor paddles. For YnaI in DIBMA-stabilised nanodiscs, the pore helices and the paddle helices TM2 and TM1 could be reliably assigned and the helix TM-N1 located. The outermost paddle-helix TM-N2 and the cytosolic loop connecting this helix to TM-N1 are embedded in the polymer-/lipid belt and are most likely in direct contact with the polymer. Together with the effect of DIBMA seen for MscS, this affirms that the density fragments observed in the putative region of the helix TM-N2 and the loop do not represent the true structure and location but are heavily perturbed through interactions with DIBMA copolymer. This finding is confirmed by the cryo-EM structure of YnaI presented by Hu et al. They prepared the protein with the detergent LMNG, and the resulting cryo-EM map showed a micellar belt that does not impair the outermost helix TM-N2 as observed for our YnaI-DIBMALPs structure (figure 4.3 A). A closer look at the models reveals an overall very good agreement for the vestibule and the helices TM3 to TM-N1, but helix TM-N2 diverges substantially, as both its location and its orientation is different in the two models (figure 4.3 B).

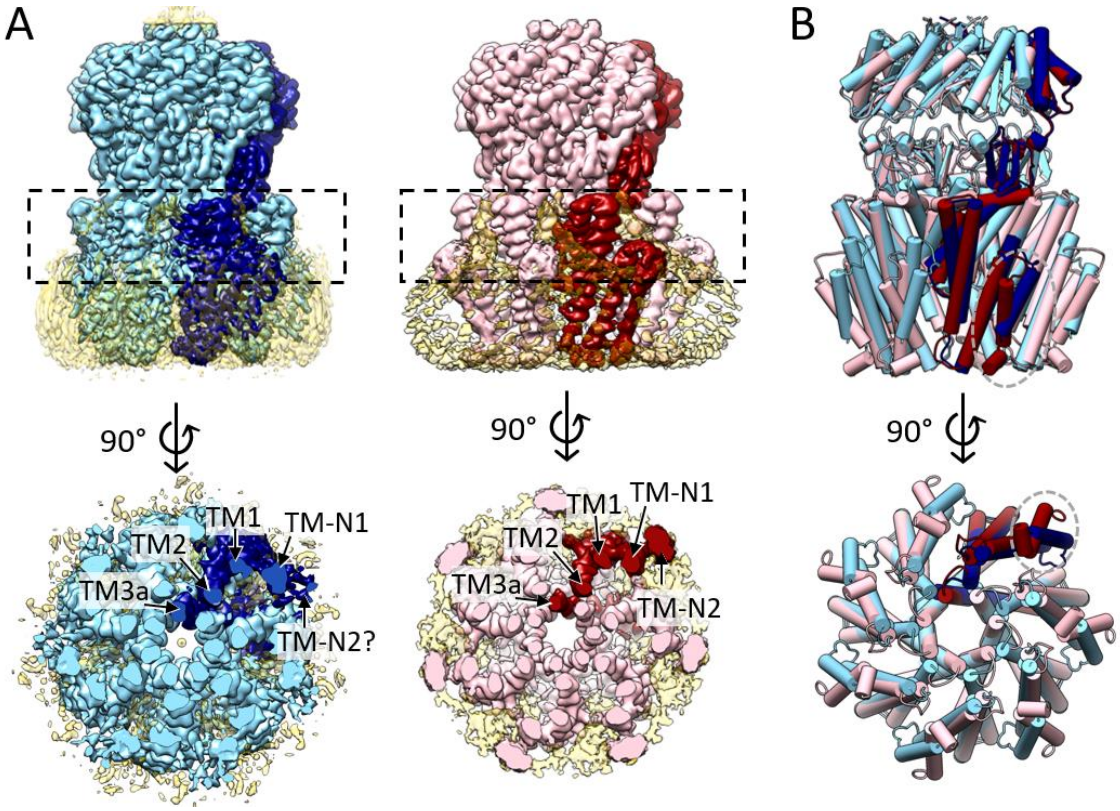


**Figure 4.3 | Comparison of YnaI-DIBMALPs and YnaI in the detergent LMNG. (A)** The cryo-EM maps of YnaI-DIBMALPs (left) and YnaI in LMNG (right; PDB 6URT and EMDB 20862 (Hu et al., 2021)) are coloured by protein model density (blue and pink/ red, respectively, and micellar density (pale yellow). One subunit is coloured darker. Already in the side views (upper), the better density for the outer sensor paddle of YnaI in LMNG is visible. The views from the periplasmic side (lower) show the slice of the TMD highlighted in the dashed box and depict a region where all five helices are expected to be cut. The helices are indicated for the dark subunit. Where YnaI in DIBMA only shows fragments of the putative TM-N2, the helix is clearly distinguishable from the micellar density in YnaI in LMNG. **(B)** The models of the two YnaI structures using the same colour code as in (A) are aligned. Apart from the helix TM-N2 and the loop between the helices TM-N1 and TM-N2 (highlighted in grey dashed ovals), they agree well.

**Amphipols A8-35 and DIBMA copolymer probably affect MscS-like channels differently.** Although DIMBA copolymer and Amphipols A8-35 perturb TM helices of both MscS and YnaI, the effect on the structures is different: In MscS, the complete sensor paddle is affected and deformed or denatured, respectively, while in YnaI only TM-N2 and the loop to helix TM-N1 are impaired, while the integrity of the remaining TMD is maintained. Thus, it seems that DIBMA copolymer and Amphipols A8-35 destroy contacting protein regions in both channels but additionally lead to a complete alteration, excluding the pore helices, of the TMD in MscS. Maybe because MscS is more susceptible to pressure than YnaI (Edwards et al., 2012; Sukharev, 2002), the specific properties of a reconstitution system have a more profound effect on it.

### 4.1.2 The overall architecture is conserved among *E. coli* MS channels

**YnaI in DIBMA-stabilised nanodiscs is perhaps not captured in its ultimately closed state.** The cryo-EM map of YnaI in DIBMA-stabilised nanodiscs had a final overall resolution of 3 Å. The resolution is not uniform over the complex and worsens towards the outer N-terminal TM helices, but the map revealed protein density beyond the two sensor paddle helices of MscS. The overall organisation of the complex is highly similar to closed MscS, as underpinned by the r.m.s.d. of 1.8 Å for the α carbons for both models. Therefore, it was assumed that YnaI is also in a closed-like form. MD simulations, however, showed that the pore in closed-like YnaI is only partially dehydrated but not conductive to ions. The pore in YnaI is more hydrophilic than in MscS, and possibly M158, which is in the equivalent position to L109 in MscS, does not create a strong hydrophobic seal as in MscS, despite having a narrower pore diameter (4.7 Å in YnaI vs 8.0 Å in MscS). The second sealing ring has a similar diameter in YnaI (6.0 Å) and MscS (6.2 Å). The "vapour lock" in MscS, formed by the two sealing ring residues L105 and L109 (Anishkin et al., 2010; Anishkin and Sukharev, 2004), exhibits an energetic barrier to water of 13 kJ/mol compared to only 1.5 kJ/mol in YnaI at the position of M158. Concluding from these MD simulations, it seems possible that the conformation of YnaI captured in DIBMA-stabilised nanodiscs does not represent the fully closed channel. However, the recent structure of YnaI in LMNG (Hu et al., 2021) that was interpreted as closed form shows an r.m.s.d of the α carbons of the helices TM3a and TM3b (residues 140-176) of the two YnaI models of only 1.0 Å, supporting our interpretation of the closed conformation of YnaI in DIBMA nanodiscs. On the other hand, Hu et al. also did not show any other evidence that the conformation of YnaI they captured represents the ultimately closed state. Another possible explanation for the partially wetted pore might be that lipid molecules are present in the pore that ultimately occlude the permeation pathway, that were not considered for the simulation and are neither resolved in the map of YnaI-DIBMALPs nor in the map of YnaI in LMNG (Hu et al., 2021). Such pore lipids were resolved in several MscS cryo-EM structures (figure 4.4 A) (Rasmussen et al., 2019a; Reddy et al., 2019) and were assumed to gradually move to the periphery of the pore and leave the channel during gating (Zhang et al., 2021). Spectroscopic data indicated a contrary situation: While the pore-facing residue L105W in MscS did show only weak quenching in tryptophan fluorescence quenching experiments (Pliotas et al., 2015), the equivalent residue L154W in YnaI was highly quenched (Böttcher et al., 2015). The behaviour in these quenching experiments coincides again two

residues away for G152W (YnaI) and A103W (MscS), which face towards the hydrophobic pocket, and are similarly quenched (figure 4.4 A). Reddy et al. (2019) observed lipid densities in MscS in the periplasmic half in the pore, which means they could be too far away from L105W to be quenched. Nonetheless, concluding from the structural data, the presence of pore lipids in YnaI is unlikely, as the preparation of YnaI with DIBMA copolymer is carried out without classic detergents and should therefore theoretically provide the gentlest way to purify YnaI regarding bound lipids.

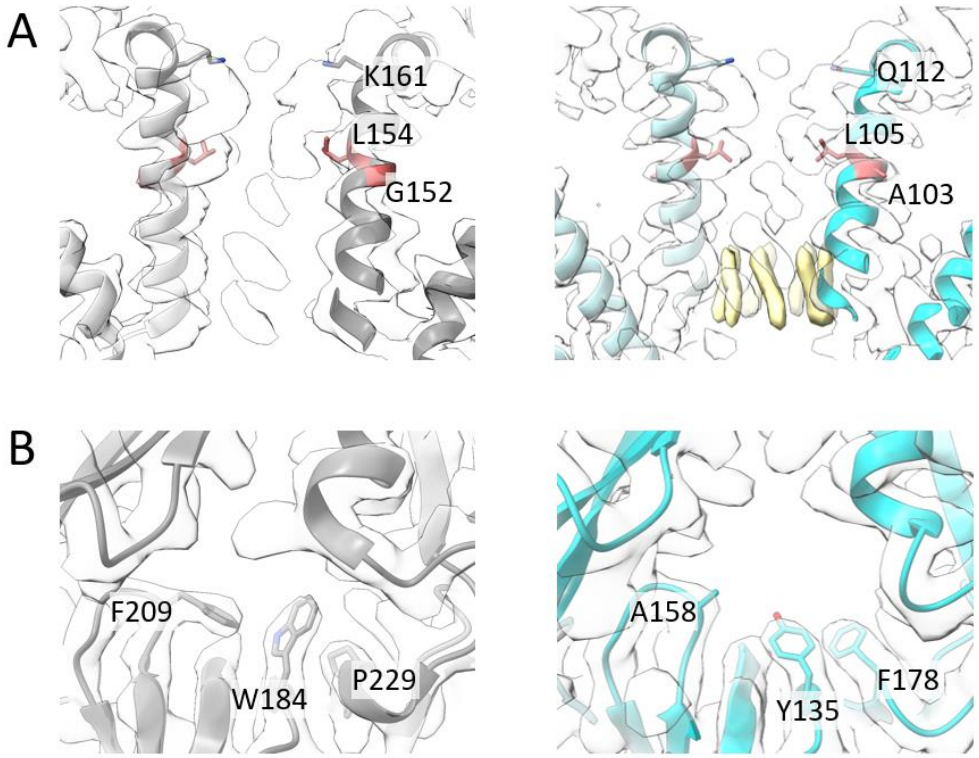


**Figure 4.4 | Selected residues in the pores and portals of YnaI and MscS. (A)** Residues in the pore that were investigated by tryptophan fluorescence quenching are shown in red for YnaI (grey) and MscS (cyan; PDB 6RLD and EMDB 4919 (Rasmussen et al., 2019a)) in their corresponding densities (white). For clarity, only two subunits of the models are shown, and one is coloured in lighter colours. L154 and G152 in YnaI, and A103 in MscS were shown to be highly accessible to lipids, L105W in MscS exhibited only weak quenching (Böttcher et al., 2015; Pliotas et al., 2015), although density fragments within the pore (pale yellow) were attributed to lipid tails (Rasmussen et al., 2019a; Reddy et al., 2019). The additional pore-lining residues K161 in YnaI and G113 in MscS, respectively, are also shown and marked. **(B)** In the portal of YnaI (grey), according to Hu et al. (2021), P229 interacts with W184, which in turn also interacts with F209 via T-shaped aromatic interaction. The equivalent residues are shown for MscS (cyan), highlighting that only two putative interaction partners are present.

**The occluded portals in YnaI can explain the low conductance of the channel.** The closed β barrel already suggested by the closed and open crystal structures for MscS (Bass et al., 2002; Wang et al., 2008), and instead, it was assumed that the seven lateral portals in the cytosolic vestibule that arise between two adjacent subunits constitute the access pathway into the vestibule. These portals are also present in YnaI and YbiO but have a significantly smaller diameter in YnaI. As MD simulations showed that the β barrel of YnaI is not hydrated, it is anticipated that the side portals also represent the entrance into the vestibule in YnaI. Experimentally, the conductance of YnaI is remarkably lower than for MscS or YbiO (Edwards et al., 2012; Sukharev, 2002), which is reflected by the portal diameters of the three channels. MD simulations predict the portals in YnaI to be hydrated, but with an open cross-section of 3.4 Å, they possibly only allow the passage of hydrated sodium, potassium, or chloride ions. The portals in YnaI are mainly occluded by aromatic residues like W184, F209, Y291 and W299 (see figure 3.31 B). W184 is strictly required for channel function (Böttcher et al., 2015), which is not observed for the analogous residue Y135 in MscS. Hu et al. (2021) suggested that W184 interacts with P229 (also in the portal region) by hydrophobic effect and CH-π interaction and that W184 and F209 stack against each other by aromatic T-shape interaction (figure 4.4 B). As the CH-π interaction is very strong between tryptophane and proline (Brandl et al., 2001), even a conservative mutation of W184 to a tyrosine (Böttcher et al., 2015) would weaken this interaction, introducing flexibility to W184 and therefore also to F209 and thus possibly leading to full occlusion of the portal. In MscS, only interaction partners Y135 and F178, at the equivalent positions of W184 and P229 of YnaI, are present (figure 4.4 B). Another indication that the portals highly influence ion conductance is that the mutation F209A in YnaI almost quadruples the conductance (Yu et al., 2018). The idea that the sizes of the entrances into the vestibule determine conductance was promoted previously for potassium channels (Naranjo et al., 2016).

However, there are, of course, other reasons for the low conductance of YnaI. E.g. the mutation of K161, which is located on the helix TM3b close to the joint to helix TM3a and faces towards the pore axis, to alanine was also shown to increase the ion conductance (Yu et al., 2018). This lysine represents an additional constriction along the conduction pathway in YnaI and is also present in YbdG, while all other paralogues in *E. coli* have a shorter side chain – a glutamine – in this position (see figure 3.31 A). Furthermore, upon opening, the pore of YnaI widens less than, e.g. in MscS. The influence of the open pore diameter on the conductance is discussed in section 4.3.2.

**YbiO in Amphipols also likely represents a partly open form.** The large paralogue YbiO was purified in Amphipols A8-35, and judging from its pore helices, it also seems to be in a closed conformation. Compared to MscS, its pore is similarly hydrophobic. MD simulations predicted that the pore of YbiO is hydrated and can conduct. The pore of YbiO is overall wider, as the TM3a helices are spaced farther apart, while the constricting residue F553 establishes a similar pore diameter as in MscS. Additionally, the paddle helices, especially helix TM1, are slightly rotated clockwise (viewed from the periplasmic side), which is also observed for the open conformation of MscS (Wang et al., 2008). Hence, the structure of YbiO in Amphipols probably represents a partly open form of YbiO, perhaps an effect of the Amphipols. Not only the transmembrane pore of YbiO is predicted to conduct, but also the β barrel, though it is still possible that it is sterically occluded as the ultimate C-terminal residues were not modelled. For MscS and YnaI, MD simulations indicated a non-conductive β barrel.

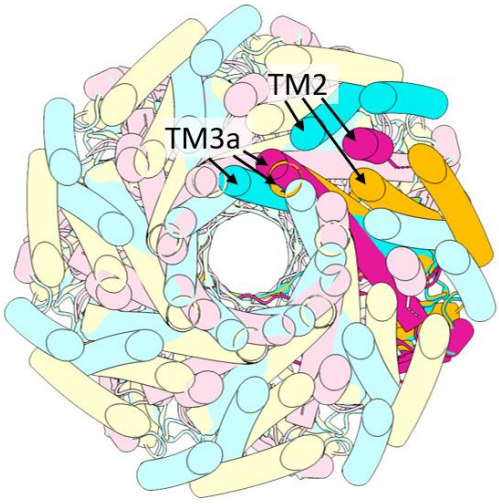


**Figure 4.5 | Alignment of YbiO with closed and open MscS.** The slice of the TMD viewed from the periplasmic side shows that the helix TM2 of YbiO (pink) does not align with helix TM2 of closed MscS (cyan; PDB 6RLD, EMDB 4919 (Rasmussen et al., 2019a)) and is rotated clockwise, reminiscent of the transition towards open MscS (yellow/orange). The pore helices TM3a of YbiO are spaced farther apart than in closed MscS. One subunit of each model is highlighted in darker colours.

### 4.1.3 The extended membrane domain of YnaI is highly flexible

**Flexibility aggravates the resolution of the outer sensor paddle.** The most significant structural difference between YnaI and MscS is the presence of the additional sensor paddle in YnaI. Owing to the weak density in this region, only the helical backbones of these two additional helices with alanines as side chains were placed in the map, highlighting the propeller-shaped organisation of this domain. Although the comparison to the YnaI model by Hu et al. (2021) revealed that the helix TM-N2 of YnaI in DIBMA-stabilised nanodiscs is modelled in an incorrect position and orientation, the propeller-shaped arrangement of the TM helices is nonetheless maintained. The weaker density observed in the TMD compared to the vestibule is consistent with other cryo-EM maps of MscS-like channels (Deng et al., 2020; Hu

et al., 2021; Li et al., 2020; Rasmussen et al., 2019a; Reddy et al., 2019; Yu et al., 2018). The absence of interactions between adjacent blades undoubtedly contributes to the poor quality of the map in this region, as it renders the domain more flexible. Sample flexibility leads to heterogeneity in the data set, which results in blurred regions in the maps (Scheres, 2016). During image processing, such regions are incorrectly averaged, leading to loss of the coherent signal. The flexibility of the membrane domain of YnaI is reflected by the *B*-factors of the model and is further corroborated by the asymmetric analysis of the complex. While the C7 symmetry is largely maintained for the cytosolic vestibule, the membrane part shows vast variations between the different subunits (see figure 3.9 C). As the cryo-EM map of YnaI in LMNG from Hu et al. (2021) resolves the additional sensor paddle better, the weak density in this region cannot only be contributed to the flexibility of this region. As discussed in section 4.1.1, the deleterious effect of DIBMA on the contacting helices surely constitutes the biggest contribution to the weak density in the outer TMD. Furthermore, the weak density for the outer helix bundle made the estimation of a suitable density threshold for a mask more difficult. The discrepancy of the density distribution across the complex possibly led to the generation of too tight masks, which in turn affected the outcomes of 3D classifications and 3D refinements.

**The flexibility of the TMD is probably a prerequisite for opening.** The open forms of MscS (Wang et al., 2008) and the eukaryotic YnaI-like channel AtMSL1 (Deng et al., 2020) (discussed in section 4.3.2) indicate that upon opening, the paddle helices of one subunit move as a rigid body and slide against the neighbouring paddle. Hence, it seems that the single paddles need to move independently for this rearrangement and that inter-subunit interactions would restrict this flexibility. Intra-subunit interactions are observed as density bridges that connect the paddle helices TM1 and TM-N1 (see figure 3.8 B). Likely candidates for H bond formation are residues T83 and T91 of helix TM1 that face towards helix TM-N1. Hu et al. (2021) investigated the interface between helices TM1 and TM-N1 by alanine substitutions and suggested charged residues (e.g. TM1-K93 and TM-N1-H43) as interaction candidates. Besides, the abundance of hydrophobic amino acids in TM-N1 and TM1 would also add to the tight packing of these helices through hydrophobic interactions.

### 4.1.4 The TMDs of YnaI and YbiO constitute a dome-like architecture

**The size of the periplasmic indentation varies between differently sized channels.** The second helix bundle of YnaI is shifted against the inner helix bundle towards the periplasm, creating a large indentation on the periplasmic side. This indentation is also present in MscS and in YbiO – although, for this channel, the eight additional helices could not be resolved – hinting at similarities in their sensing mechanism. The indentation in YnaI is larger than in MscS but putatively smaller than in YbiO (figure 4.6), so the size of the indentation is likely associated with the number of transmembrane helices. However, as the majority of the TMD of YbiO was not resolved, this is speculative and can only be suggested from the obtained incomplete map and the side-view 2D class averages (see figure 3.28 B). Furthermore, the condition of YbiO is still unknown, as Amphipols presumably perturb contacting TM helices of MscS-like channels (see section 4.1.1).

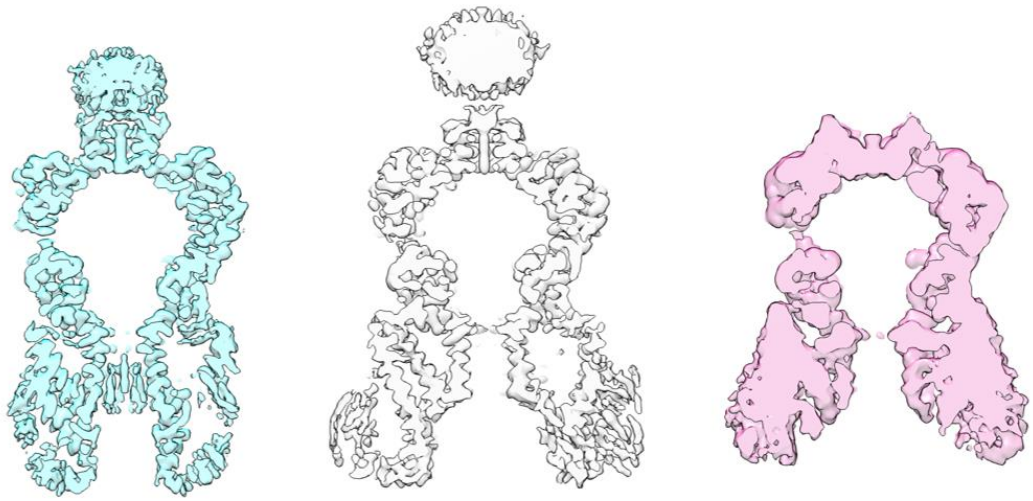

**Figure 4.6 | The periplasmic indentations of MscS, YnaI and YbiO.** The same central slice is shown for MscS (cyan; EMDB 4919 (Rasmussen et al., 2019a)), YnaI (grey) and YbiO (purple), showing an increased indentation for YnaI and YbiO compared to MscS.

**The membrane around YnaI is slightly locally curved.** The tapered membrane domain of YnaI hints that the membrane around the channel is locally curved (Böttcher et al., 2015), as the wedged shape of the channel would not be well compatible with a flat membrane. The dome-like arrangement of the paddle helices accompanied by local membrane curvature is reminiscent of the PIEZO 1 and 2 channels (Guo and MacKinnon, 2017; Saotome et al., 2017; Wang et al., 2019; Zhao et al., 2018), suggesting it might have a similar function. PIEZO channels are large trimers with the TM helices of the subunits being arranged tentacle-like

around the central pore. PIEZO 1 was found to curve the membrane locally when closed, resulting in a dome-like structure. The authors hypothesised that this dome gets flattened when the membrane is submitted to tension, which could provide the energy for channel opening (Guo and MacKinnon, 2017). A similar sensing model was indicated for MscS by idealised models (Phillips et al., 2009) and MD simulations (Pliotas et al., 2015), where the membrane was less locally curved in the open state. In our open-like conformation of YnaI, we also observe a flattening of the dome-like structure, which is, however, smaller than for PIEZO channels. 2D class averages of YnaI-containing proteoliposomes showed the curvature of the liposome as well as a subtle local bending of the membrane (see figure 3.19), though to a much smaller degree than expected considering the membrane curvature proposed for MscS by MD simulations (Pliotas et al., 2015). Other MD simulations, however, had suggested a notably smaller degree of local curvature for MscS (Sotomayor and Schulten, 2004). One should note that, from a single channel perspective, global membrane curvature is essentially flat and thus is neglectable for channel activity (O. Bavi et al., 2016). The addition of LPC to the proteoliposomes prior to freezing resulted in 2D class averages that are barely distinguishable from those without LPC treatment. Only some class averages showed a flatter TMD, which would be compatible with the single particle data set for LPC-treated YnaI-DIBMALPs, where also many particles represented the closed-like conformation. However, as similar class averages are also present in the data set of the proteoliposomes that were not doped with LPC, it can rather be attributed to the fact that some particles were picked in a slightly tilted orientation instead of a pure side view. Also, no change in membrane curvature is visible. Hence, the experiment was inconclusive and should be redone, probably with longer incubation times with LPC: While the proteoliposomes were vitrified immediately after 40 min of incubation with LPC, the proteoliposomes used for subsequent protein extraction with DIBMA were incubated with LPC (and DIBMA) overnight, which can explain the different outcome of the experiments.

## 4.2 Lipids in the context of mechanosensation

### 4.2.1 Delipidation as an alternative for channel gating

**State-of-the-art model for the lipids-move-first gating paradigm.** Models other than local membrane curvature exist that describe the sensing of membrane tension (Rasmussen, 2016). One of these models is based on lipids that were detected in the pockets between pore and paddle helices of MscS (Pliotas et al., 2015). This model suggests that lipid extrusion from the pockets upon tension drives MscS into the open conformation. MS channels sense the tension in the membrane upon hypoosmotic shock and not the pressure in the cell that causes this tension (Moe and Blount, 2005; Sokabe et al., 1991). Furthermore, no additional proteins or cofactors are involved in sensing, as MscS and MscL purified and reconstituted into artificial bilayers retain their mechanosensitivity (Rasmussen, 2016; Sukharev, 2002; Sukharev et al., 1993). The force-from-lipids principle states that anisotropic forces defined by the pressure profile of biological lipid bilayers and their changes trigger the structural reorganisation of embedded membrane proteins (Anishkin et al., 2014; Martinac et al., 1990). How exactly do these forces lead to channel opening? A few earlier gating paradigms were suggested that rest on membrane properties, but more recently, Pliotas et al. (2015) observed in a crystal structure aliphatic chains in the pockets of open MscS, far away from the membrane plane, and presented a model where the amount of phospholipids in these pockets drives gating. Fluorescence quenching experiments to investigate protein-lipid interactions showed quenching for residues on helix TM3b, but also for residues in the adjacent β domain, suggesting that those lipids must lie perpendicular to the bilayer lipids (Rasmussen et al., 2019b). The role of associated lipids in MscS gating was further supported by cryo-EM structures of MscS in a bilayer environment that resolved several lipid molecules in the pockets and even the pore that are not in direct contact with the membrane (Rasmussen et al., 2019a; Reddy et al., 2019). The most recent gating model presented by Zhang et al. (2021) displays the extrusion of coordinated lipids in MscS as the driving force for conformational changes (lipids-move-first model, figure 1.6). The authors employed a novel approach to imitate membrane tension within MSP nanodiscs. Lipid removal from the nanodiscs by βCD creates a tension that enabled the observation of not only the open but also an adapted state (denoted as desensitised in Zhang et al.) by cryo-EM analysis. The open conformation was obtained from a G113A mutant, which is known to prevent adaptation (Edwards et al., 2008), and thus, the channel was supposed to be trapped in

the open state. The 2D class averages and the 3D reconstruction exhibited a smeared-out density of TMD, leading to the interpretation of a dynamic TMD in the open conformation. They argued that the dynamic nature of the TMD in the open conformation facilitates leaving of the pore lipids. Another explanation for the smeared-out TMD might be insufficient removal of lipids from MscS-G113A by βCD, resulting in an unstable open state. Moreover, inhomogeneous lipid removal by βCD might lead to particle subsets that are non-uniformly delipidated, resulting in the smeared-out TMD observed in cryo-EM.
Furthermore, the use of short-chain lipids gave rise to a sub-conducting state, that MscS enters under sustained tension after having opened fully and before finally adopting the adapted conformation. The gating model presented by Zhang et al. highlights the interaction of MscS with lipids and their role in initiating gating and driving MscS into the different conformations.

**Delipidation explains the conformational states of previous MscS structures.** To investigate the interaction of MscS with coordinated lipids independently from the direct contact of MscS with the membrane, MscS was subjected to different detergent conditions, which revealed that MscS, even in the absence of a membrane environment, can be switched between its closed and open states. Which conformation MscS adopts is dependent on the number of bound lipids: in the closed conformation, more lipids are associated with MscS than in the open conformation. Reversibility of the delipidation by the addition of lipids further corroborates the finding that lipid molecules drive gating independently of a membrane environment. These findings explain why some past structures of MscS were obtained in a closed (Bass et al., 2002; Lai et al., 2013; Rasmussen et al., 2019a; Reddy et al., 2019; Zhang et al., 2012) or an open (Lai et al., 2013; Pliotas et al., 2015, 2012; Wang et al., 2008) conformation: Different detergents and conditions were used, and the degree of detergent-mediated delipidation determines the conformational state of MscS.

**Changing of the cross-sectional area upon opening of MscS.** As the structures of MscS obtained in this work were solubilised and purified in detergents, it must be carefully evaluated which molecules are indeed detergent molecules and which might be replaced by lipids in a native membrane environment. Lipid molecules were identified in the pockets of detergent-solubilised MscS, indicating that the effect of the membrane and the effect of the pocket lipids on the conformation of MscS can indeed be separated. The findings agree with the earlier model (Pliotas et al., 2015) in so far as it underpins the importance of the pocket lipids, yet the model needs to be updated. According to the anisotropic transbilayer pressure profile (figure 4.7 A),

tension is highest at the onset of the fatty acid chains. Upon opening, not only does the volume of the pockets decrease, but also – even more notable – the covered membrane cross-section on the periplasmic side increases from about 30 Å to 65 Å because the periplasmic ends of the TM1 helices move outwards (figure 4.7 A, B). This is not only an expansion that would also be a possible force for tension sensing, as indicated for MscL (Perozo et al., 2002a; Sukharev et al., 2001). The situation in MscS is more complex. While on the cytosolic side, the volume in the grooves and pockets between adjacent sensor paddles decreases and lipids leave, gaps arise on the periplasmic side between neighbouring TM1 helices (figure 4.7 B), establishing a new interface between the membrane and the bulk water phase in the funnel. Thus, in a membrane environment, lipids from the periplasmic leaflet likely enter the gaps between the TM1 helices to avoid the exposure of the hydrophobic core because if the lipids take similar positions as the LMNG molecules observed in the structure, the lipid headgroups would be facing the hydrophilic surface between the N-terminal end of helix TM1 and the loop connecting helices TM2 and TM3a.

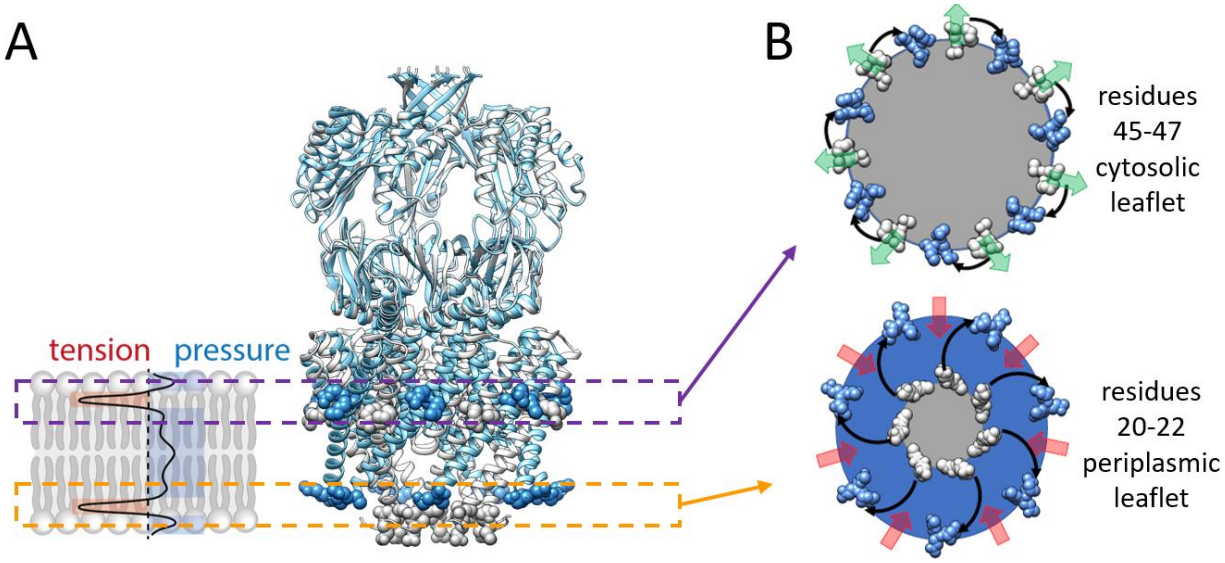


**Figure 4.7 | Gating transition of MscS in the regions of highest tension. (A)** The overlay of the closed and open models of MscS highlights residues at the onsets of fatty acid chains, where the highest tension is according to the transbilayer pressure profile (middle). Residues of the closed conformation are shown as grey spheres (residues 45-47) and of the open conformation as blue spheres (residues 20-22) for the cytosolic leaflet (purple dashed box) and the periplasmic leaflet (orange dashed box). **(B)** The cross-sectional areas (grey circle for the closed and blue circle for the open conformation) are viewed from the periplasmic side and reveal that upon opening, no increase of the area is observed on the cytosolic side (top), but a huge expansion of the area at the periplasmic side (bottom). This leads to gaps arising between adjacent TM1 helices at the periplasmic side, which can be entered by lipids (red arrows), while lipids on the cytosolic side are expelled because the volume of the hydrophobic grooves and pockets decreases (green arrows). Part of the figure adapted from Flegler et al. (2021).

**The delipidation of open MscS in LMNG is incomplete.** The pockets of open MscS in a native membrane environment are predicted to be less occupied by lipids (Pliotas et al., 2015) because the volume of the pockets decreases in the open conformation. However, in the high-resolution structure of open MscS, one lipid molecule and two LMNG molecules per pocket were identified. The observed structure is not dynamic, as demonstrated by the high resolution over the whole complex, which is in contrast to the gating model proposed by Zhang et al. (2021) suggesting that the open conformation is dynamic. However, as discussed above, the observed smeared-out ("dynamic") TMD could also be a result of incomplete or inhomogeneous delipidation of the sample. Nevertheless, it is likely that the two LMNG molecules observed in the pockets of our structure increase the stability of the open conformation and the high resolution of MscS under this condition was probably only accomplished because of the stabilising properties of LMNG (Chae et al., 2010, 2008). Furthermore, it seems unlikely that (several) lipid headgroups shield the openings of the hydrophobic pockets towards the bulk water face and can accommodate their hydrophobic lipid tails in the small pockets of the open form. LMNG molecules, on the other hand, have shorter hydrophobic tails which fit into these smaller pockets. One lipid molecule, coordinated by R59, is resolved in our structure, which adjusts to the limited space by bending of a lipid tail. Due to the purification procedure, this lipid must originate from the *E. coli* plasma membrane, and its presence in the open form is so far surprising, as the mutation R59L resulted in a strong GOF phenotype: as the interaction with the lipid is weakened by impairing salt bridge formation, lipid removal should be easier and thus explain why the channel is easier to gate (Rasmussen et al., 2019b). Nonetheless, it is compatible with the gating model by Zhang et al. (2021), which proposes that MscS, under sustained tension, enters an inactivated state when it loses all coordinated lipids. Hence, the delipidation by LMNG seems to be incomplete, and retaining the lipid that is bound by R59 kept MscS in the open and not the sub-conducting or inactivated state. Whether more thorough delipidation would result in MscS in the adapted state needs to be proved. Unexpectedly, Hu et al. (2021) found their YnaI solubilised and purified in LMNG in a closed (or closed-like) conformation. However, they used even less LMNG during IMAC (0.01 % compared to 0.03 % for MscS). Additionally, under consideration that the pockets in YnaI are slightly bigger than in MscS, and thus more lipids would need to leave for channel opening, YnaI was even less complete delipidated, which can explain its closed conformation in LMNG (Hu et al., 2021). These observations support the interpretation that MscS was not wholly delipidated by LMNG.

**The ligands in closed and open MscS provide the foundation for an updated lipids-move-first model.** Understanding the position of ligands in the closed and open conformations of MscS contributes substantially to the understanding of MscS gating. Putting the pieces together, lipids leaving the grooves between adjacent paddles likely initiate the gating transition because they are in the region of highest tension (figure 4.8). Upon opening, the volume of the hydrophobic pockets decreases, which leads to lipid extrusion from the grooves and pockets. While the cross-sectional area does not increase on the cytosolic side of the channel, it enlarges on the periplasmic side (figure 4.7, figure 4.8). As a result, gaps arise between adjacent TM1 helices, and lipids from the periplasmic leaflet enter these gaps to shield the bulk water phase in the funnel from the surrounding membrane. These lipids can equilibrate with the hook lipid.

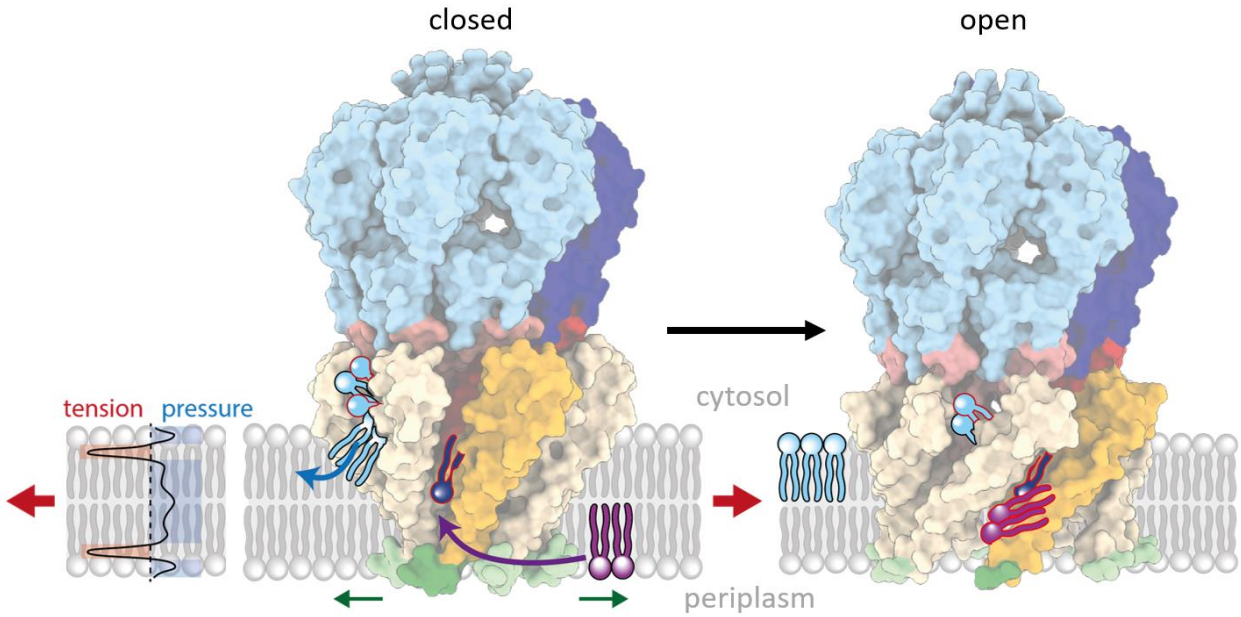


**Figure 4.8 | Gating transition of MscS.** According to the anisotropic pressure profile of the membrane (left), tension is highest at the onset of fatty acid chains. MscS is shown in its closed (PDB 6RLD (Rasmussen et al., 2019a)) and open conformation and coloured by its domains: the vestibule is depicted in blue, the pore helices in pink/red, the sensor paddles in yellow/orange and the anchor domain in green. One subunit is coloured darker. Associated lipids are shown, and lipids that were observed directly or suggested by detergent molecules are outlined in red. Upon opening, the membrane cross-section changes significantly on the periplasmic side as the anchor domains move outwards (green arrows) but not at all at the cytosolic side. Lipids (light blue) are expelled from the grooves at the cytosolic leaflet (blue arrow) because the volume of the pockets decreases upon opening. These lipids probably trigger the gating transition of MscS. As gaps arise at the periplasmic side upon opening, lipids (purple) from the surrounding periplasmic leaflet can enter (purple arrows) with their headgroups facing the bulk water phase in the funnel (red arrows) and equilibrate with the hook lipid (dark blue).

**A possible role for the pore lipids is the participation in adaptation.** The densities observed in the pore of open MscS produced with LMNG are best interpreted as DDM molecules. Seven molecules each were identified on the cytoplasmic and the periplasmic side of the pore. Upon opening, the pore helices move outwards and are consequently farther spaced from the adjacent pore helices. This rearrangement generates gaps that are occupied by hydrophobic chains of the DDM molecules. Lipids on the periplasmic side of the pore are probably also present in the closed structure of MscS in MSP nanodiscs, as represented by elongated densities (Rasmussen et al., 2019a; Reddy et al., 2019). It is, of course, possible that these densities are also DDM molecules, as MscS was solubilised and purified in DDM prior to reconstitution into MSP nanodiscs if it is not removed during reconstitution. However, fluorescence quenching experiments have indicated that residues A94 and G101 (figure 4.9), which line the pore on the periplasmic half, are in contact with lipids (Rasmussen et al., 2019b). The mutant G113W on the cytosolic side of the pore, in contrast, exhibited only very low quenching. As MscS was reconstituted in a lipid bilayer for these fluorescence quenching experiments, it was presumably also in the closed conformation like MscS in MSP nanodiscs. This supports not only the interpretation that the elongated densities in the pore of closed MscS would be lipids in a membrane environment but also that they are present only on the periplasmic side of closed MscS, but on both sides in the open forms, as observed in the LMNG structure. Lipids in the pore were previously suggested to play a role in the mechanism for adaptation (Zhang et al., 2016), by penetrating the pore through inter-subunit clefts that appear between adjacent TM3a helices upon opening. Thus, the obtained open structures could reflect the adapted state. If lipids were indeed responsible for adaptation in MscS, it would explain why there are no pore lipids identified in YnaI and YjeP: Both larger paralogues did not show adaptation when exposed to a sustained pressure stimulus. However, if the open MscS structure obtained with LMNG represented the adapted state, it would not explain why lipid densities are also found in the pore of closed MscS (Reddy et al., 2019), and it is not in accordance with the gating model by Zhang et al. (2021) which proposes that adaptation (in their study, more specifically inactivation) is a consequence of losing all coordinated lipids. Furthermore, it is difficult to imagine how lipids enter the pore without unfavourably exposing their hydrophilic headgroups or their hydrophobic tails. The DDM molecule that is resolved next to the lipid in the pocket and protrudes from outside into the pore, however, could be taken by a lipid molecule in a membrane environment, as it would still be compatible with the space requirements of the pocket (see figure 3.24 E).

### 4.2.2 Coordinated lipids in closed YnaI

**Pocket lipids have a conserved function in YnaI and MscS.** In YnaI, lipids were identified at similar positions and orientations as in MscS. The density of the lipid molecules is less pronounced in YnaI as in MscS, suggesting a higher degree of flexibility, and only one molecule could be modelled instead of two as in MscS (Rasmussen et al., 2019a). The headgroup of the lipid identified in YnaI could be allocated to density near K108 in the inner cytosolic loop, which forms a salt bridge to the phosphate headgroup. Neutralising the charge by the mutation K108L weakens the lipid-binding in YnaI, and the pressure required for opening is decreased. Similarly, a strong GOF phenotype is also observed for R59L in MscS at a comparable position (Rasmussen et al., 2019b) (figure 4.9). There is no strict conservation of specific residues on sequence level among the MscS-like channels, but the cytosolic loops often harbour many positively charged amino acids. This is true for most bacterial inner membrane proteins, as the "positive-inside rule" postulates the precedented occurrence of positively charged amino acids at cytoplasmic ends of TM helices, which determines the topology of membrane proteins (Baker et al., 2017; von Heijne, 2006, 1992). The coordination of lipids by positively charged amino acids located in the cytosolic loops of MscS and YnaI that connect the TM1 and TM2 helices provides a role for the positively charged residues beyond topology determination. The position of the lipid molecule in YnaI, especially its fatty acid tails, is further corroborated by previous fluorescence quenching experiments. F168W and W201, which are almost parallel to the lipid tails and face towards the pocket, showed lipid accessibility (Böttcher et al., 2015). However, G152, which is more towards the periplasmic side of TM3a, also showed strong quenching and is not within proximity of the lipid, which would argue for the presence of another lipid molecule here (figure 4.9). Hu et al. (2021) also observed additional density in their YnaI structure in a different position and modelled a lipid molecule there coordinated by R120 and Q100 (figure 4.9). They could show in downshock experiments that an R120A mutant is more capable of protecting *E. coli* from hypoosmotic shock than WT YnaI, supporting the role of R120 in lipid coordination. The mutation Q100A led to severe growth inhibition, which is a strong indicator for a GOF phenotype. The authors hypothesised that Q100A is toxic because it might trap YnaI in an open state. The lipid is also modelled in a very different orientation, which does not satisfy the results from the previous quenching experiments (Böttcher et al., 2015) or is not investigated with tryptophan fluorescence quenching so far. However, the behaviour of the mutants is in agreement with the

updated lipids-move-first model, where channel opening is induced by lipid extrusion from the grooves and pockets because, in these mutants, lipid removal should be facilitated resulting in gating at a lower tension. As for MscS, there are putatively also several lipid molecules per subunit in YnaI. Hence, it is quite possible that both positions – K108 and R120/Q100 – are involved in lipid coordination. Interestingly, the lipid headgroup coordinated by K108 is in the pocket between the helices TM3 and TM2, while the lipid headgroup coordinated by R120/Q100 is in the grooves between the helices TM2 and TM3 (figure 4.9). Moreover, the lipid headgroup coordinated by R120/Q100 is closer to the cytoplasmic leaflet than the lipid headgroup coordinated by K108.

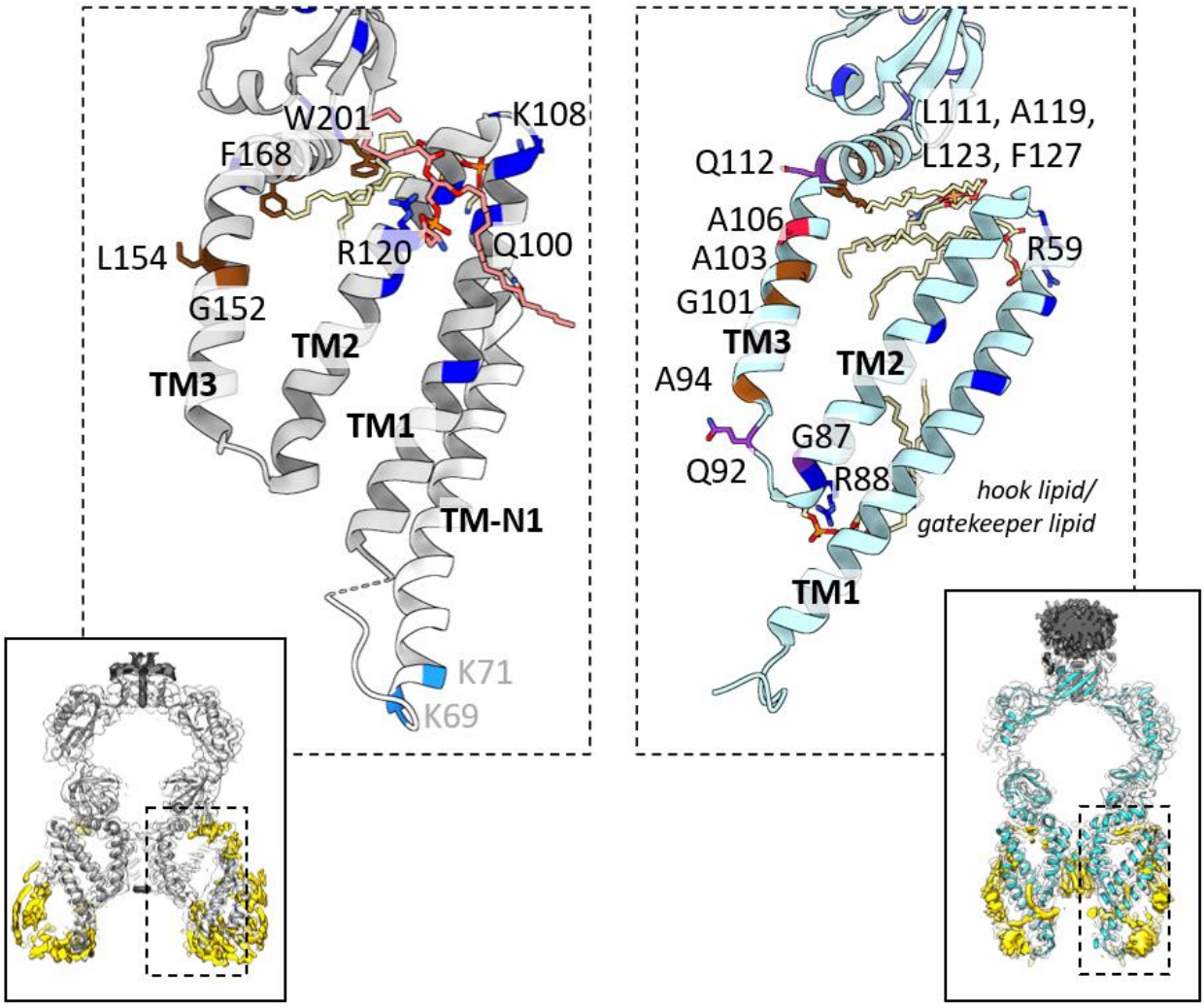


**Figure 4.9 | Residues involved in lipid coordination in MscS and YnaI in their closed conformations.** The inserts at the bottom corners show MscS (cyan, right) and YnaI (grey, left) in the same orientation, and lipid densities are depicted in yellow. One subunit of each channel, highlighted in the dashed boxes, is shown in more detail enlarged in the top middle. Lipids are shown in pale yellow, and the lipid in YnaI presented by Hu et al. is shown in pale pink (PDB 6URT (Hu et al., 2021). Positively charged residues are blue, and only for confirmed lipid coordination partners the side chain is shown and labelled. Residues that are in contact with lipids based on quenching experiments with tryptophan

◄ mutants are coloured brown. Residues in MscS that are involved in ligand binding, as shown in this work, are depicted in purple, and A106, which produces the open conformation upon mutation to valine, is coloured red. The TM helices are labelled in bold. Helices TM-N1 in YnaI, for which no side chains were modelled, is shown in white, and the putative positions for two lysines are depicted in light blue.

**The hook lipid is absent in YnaI.** The common feature of lipid binding in the pockets of MscS-like channels, as well as the GOF phenotype in connection with the lipid coordination, also suggests that sensing the membrane tension is conserved. The best-resolved lipid molecule observed in MscS is the lipid in the height of the cytoplasmic leaflet, coordinated by R88 close to the periplasmic loop (figure 4.9), and not in the height of the cytosolic loop connecting the TM2 and TM1 helices. Because of its shape, this lipid was initially named "hook lipid" (Reddy et al., 2019) and later "gatekeeper lipid" as it was proposed to initiate the gating transition according to the model by Zhang et al. (2021). In the analogous region in YnaI, however, no lipid-shaped densities could be detected, and no positively charged residue is present that could serve as a salt bridging partner. Nevertheless, the outer helix bundle in YnaI probably shields this region from the surrounding membrane, so it is rather unlikely to find a coordinated lipid there. There are two lysines in the sequence of YnaI that are putatively in the region of the outer periplasmic loop that connects helices TM1 and TM-N1 (figure 4.9). The positions of these lysines are affirmed by the YnaI structure by Hu et al. (2021). However, neither of the two maps shows density in this region that could clearly be assigned to lipids. Whether this is due to the density quality in this region or whether there indeed are no lipids remains to be shown. If the sensing mechanism were conserved among the MscS-like channels, the absence of a hook lipid in YnaI would contradict the gating model by Zhang et al. (2021), stating that the hook lipid must leave the channel to enable the opening movement. The putative role of the hook lipid is discussed in the following section 4.2.3.

### 4.2.3 The role of the hook lipid in the gating model of MscS

**The hook lipid is unlikely to initiate the gating transition.** Investigation of MscS under different detergent conditions did not only prove that delipidation leads to the gating of MscS in the absence of a membrane and that the open conformation is stabilised by detergent. It also unveiled a network of several associated ligands that is preserved between differently prepared samples, indicating that MscS provides specific spaces for ligand binding. Among all ligands, the tails of those in the grooves between adjacent sensor paddles where the cytosolic leaflet is

attached are least resolved, suggesting that those lipids are the most dynamic ones. Consequently, they are easiest removed by membrane tension and should therefore trigger gating of MscS. In this height of the onset of the fatty acid chains, tension is highest according to the anisotropic transbilayer pressure profile on both leaflets (figure 4.8), and here an increase in tension is seen upon stretching the membrane (Gullingsrud et al., 2001). Thus, this region must be of most importance for tension sensing (Cantor, 1997; Ridone et al., 2018). The typically best-resolved lipid is the "hook lipid" (Reddy et al., 2019) or "gatekeeper lipid" (Zhang et al., 2021) coordinated by R88 (figure 4.8, figure 4.9). In the closed conformation of MscS, this lipid is in the height of the cytoplasmatic leaflet but flipped by 180° compared to the lipids in the cytoplasmatic leaflet. According to the pressure profile of the membrane, this lipid experiences positive pressure in the centre of the membrane and reaches the high-tension region at the height of the onset of the fatty acid chains with the end of its fatty acid tails. Cryo-EM maps by Zhang et al. (2021)showed that upon lipid extraction with βCD from MSP nanodiscs harbouring MscS, this lipid was the first to disappear, supporting its role as a "gatekeeper" lipid. However, if it were indeed the first to leave the closed MscS, its charged headgroup would have to cross the hydrophobic core of the bilayer, which would energetically be very unfavourable. In the gating model derived from our structures (figure 4.8), the hook lipid is fixed between two neighbouring sensor paddles in the height of the middle of the membrane. Its charged headgroup faces towards the funnel and for energetic reasons it cannot dissociate into the cytoplasmic leaflet, while the periplasmic leaflet is blocked by the TM1 helix. The hydrophobic grooves and pockets are filled with lipids from the cytoplasmic leaflet. The lipids in the grooves in the height of highest tension according to the trasbilayer pressure profile are the first to leave the channel, initiating the gating transition. At the periplasmic side, lipids from the periplasmic leaflet enter the arising gaps between the TM1 helices, preventing the exposure of the bulk water phase in the funnel, and can equilibrate with the hook lipid.

**The role of the hook lipid remains controversial.** The βCD experiments by Zhang et al. (2021) indicate that the hook lipids leave first, but the channel is found in the closed conformation, although it was hypothesised that the hook lipids keep the channel closed by impeding the helices TM1 and TM2 to slide against each other. Removal of the hook lipids whose lipid tails are wedged between these helices should therefore increase the mobility of the helices, triggering the opening transition. The mutation of R88 to serine or tryptophan resulted in LOF phenotypes. The mutants were less able to protect *E. coli* in downshock experiments, less stable than WT MscS, and more difficult to activate (Edwards et al., 2008;

Rasmussen et al., 2010). These observations contradict its role as "gatekeeper" because, without this lipid, MscS should be easier to gate, though implying that it is still vital for functioning. However, the hook lipid could also have a different role in gating. In the eukaryotic K2P channel TRAAK, a lipid accesses the permeation pathway in the closed state through intermembrane fenestrations and thus blocks the pore (see figure 1.2). Opening reorganises a TM helix so that this cavity is closed, preventing the lipid from blocking the pore and triggering further conformational changes to fully open the channel (Brohawn, 2015; Brohawn et al., 2014a). Similarly, in MscS, one could speculate that the gating transition, initiated by lipids leaving the pockets, could lead to destabilisation of the hook lipid, which can exit its position upon equilibration with lipids entering from the periplasmic leaflet and thus enable the channel to open completely. Because of its proximity to the pore, however, the hook lipid could also be involved in adaptation by blocking the pore. However, this is speculative, and further experiments are required to clarify the role of the hook lipid in gating.

## 4.3 Towards a gating model of YnaI

### 4.3.1 The gating mechanism of YnaI is based on flexible pore helices

**The condition of the TMD observed for LPC-treated YnaI is unclear.** The combination of LPC, which can activate MS channels (Perozo et al., 2002a, 2002b; Vásquez et al., 2008a), and DIBMA copolymer, which can extract membrane proteins from their lipid environment (Oluwole et al., 2017), enabled the isolation of LPC-treated YnaI. Single-particle analysis revealed that three different conformational states were present in the data set: The closed-like state that corresponds to the closed form obtained without LPC, an open-like state with a flatter TMD and curved pore helices, and a transition intermediate. Given the structural resemblance between the closed states of MscS and YnaI, the open-like conformation of YnaI is surprisingly different, exhibiting outwards-bending pore helices and a more flattened TMD. The TMD in open-like YnaI, however, is merely resolved, as already indicated by the blurry appearance in the 2D class averages. Zhang et al. (2021) observed a smeared-out TMD in the 2D class averages and in the 3D reconstruction of open MscS obtained upon adding βCD to MSP nanodiscs. They concluded that the open conformation of MscS is dynamic; however, as discussed above, other explanations for this observed blurry TMD of MscS are possible (see

section 4.2.1). Different explanations are also conceivable for the smeared-out TMD in LPC-treated YnaI. The membrane domain could also be dynamic, because no stabilising detergents or mutations are present; but a dynamic behaviour is not backed up by further experiments and is therefore unlikely. Moreover, the treatment with LPC could result in inhomogeneous channel populations, as indicated by the presence of the transition intermediate. However, having demonstrated that DIBMA copolymer not only impairs contacting helices of MscS and YnaI, but also leads to a completely altered, yet denatured TMD of MscS, it must be taken into consideration that the sensor paddles of LPC-treated YnaI-DIBMALPs are perturbed. One explanation, why such a massive effect of DIBMA is observed only for the TMD of YnaI upon treatment with LPC, might be that addition of LPC resulted in the anticipated open form, which exhibits a rearrangement of the paddle helices that exposes all sensor paddle helices– not only the outermost helix – to the copolymer, resulting in their denaturation. The pore helices seem not to be affected by the polymer, which is supported by the experiments with the pore mutants.

**The GGxGG motif is important for the gating of YnaI.** For the first open crystal structure, the A106V mutant – a mutation in the pore helix TM3a – was used (figure 4.9). The introduction of a bulkier residue in this position presumably disturbs the tight helix packing that stabilises the closed conformation (Deng et al., 2020; Wang et al., 2008). This mutant produced a rigid, well-resolved membrane domain, indicating that this mutation not only opens MscS but also stabilises the membrane domain in its open conformation. It showed that during MscS gating, the paddle helices TM1 and TM2 rotate clockwise (viewed from the periplasmic side) as a rigid body, and the TM3a helices move away from the centre (Wang et al., 2008). The pore in YnaI is wider than in the closed(-like) conformation, and MD simulations predicted a hydrated pore for the open-like YnaI state, while the pore for the closed-like state was predicted to be non-conductive to ions. The most striking feature of open-like YnaI, however, is the bending of the pore helix TM3a. This bending occurs at a glycine-rich sequence in the helix, $^{149}$GGIGG$^{153}$, on the periplasmic side of the sealing residues L154 and M158. Only one or two glycines are present in the pore helices of all six MscS-like channels in *E. coli* (figure 4.10). In MscS, they are part of a gear-like interaction of glycines and alanines between neighbouring pore helices that is important for functioning (see figure 1.5 D) (Edwards et al., 2005). Glycines are generally known as helix breakers and have, apart from prolines, the lowest helix propensity among all natural amino acids (Lyu et al., 1990; Pace and Scholtz, 1998). Nevertheless, they are notably common in TM α helices, probably because of the feasible close helix packing (Dong et al., 2012; Eilers et al., 2002; Javadpour et al., 1999). Additionally, their

conformational flexibility might facilitate structural rearrangements that are needed for functioning. Hence, the GGxGG motif in the TM3a helix of YnaI is probably metastable and supports conformational switching, as the bent pore helices of the open-like conformation indicate. As far as the obtained structures from the LPC-treated YnaI data set allow judging, the observed transition intermediate exhibits a similarly altered TMD as the open-like conformation, but the pore helices are less bent, while the constricting diameter of the pore still resembles that of the closed state. The presence of this transition intermediate suggests that during opening, the rearrangement of the paddle helices and the rearrangement of the pore helices are not tightly coupled. However, it is also possible that this intermediate state is a mixture of closed- and open-like substates that could not be separated by classification approaches. The gating model based on the flexibility of the pore helices is supported by the behaviour of the two mutants. The G149A/G152A mutant (AGxAG motif) should stabilise the helix – and thus the closed conformation – and leads to a LOF phenotype, while the G149P mutant (PGxGG motif) that is designed to introduce a kink and therefore to stabilise the open conformation leads to a GOF phenotype. One should note that doping the membrane with LPC provides, like the MscS A106V mutant, only an artificial way to open MS channels. Therefore, it is still possible that the observed open-like conformation represents not the fully open state of YnaI or even an artefact as suggested for the outer TMD. Nevertheless, the obtained different structures, and the mutants, can help to understand the gating transition of YnaI.

### 4.3.2 The open-like YnaI conformation

**The conformation of open-like YnaI is different compared to the open conformation of the plant homologue AtMSL1.** The GGxGG motif is unique to YnaI among the paralogues in *E. coli*, where only one or two glycines are found. It is, however, widely distributed in homologues in other organisms, and exists also in variations (figure 4.10). One of the better-characterised homologues is the plant channel MSL1 from *A. thaliana* (AtMSL1), whose closed structure has first been elucidated using the detergent digitonin (Li et al., 2020), and a gating mechanism has been proposed recently by reconstitution into MSP nanodiscs and the digitonin derivate glycol-diosgenin (GDN) (Deng et al., 2020). The latter study corroborated the closed conformation of the first and further introduced the mutation A320V, which is the equivalent to the A106V mutation that produced the open MscS form (Wang et al., 2008).

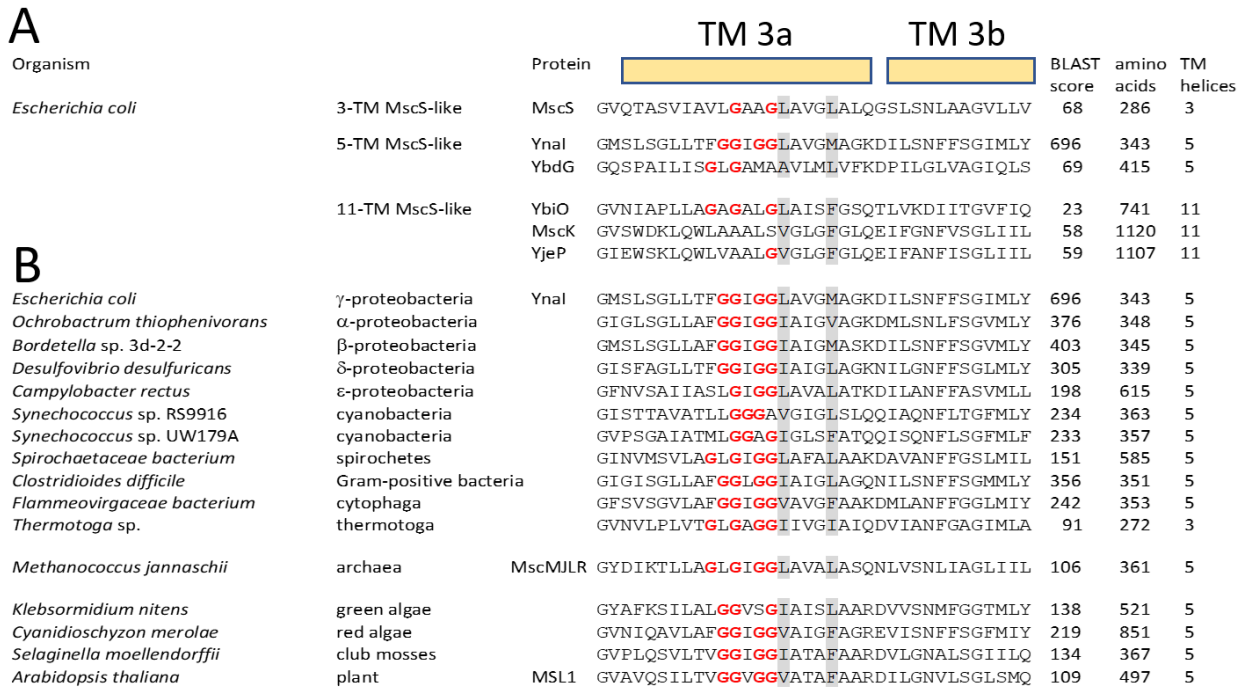


**Figure 4.10 | Alignment of the TM3 helix from *E. coli* YnaI. (A)** The alignment of YnaI with the *E. coli* paralogues highlights the unique glycine pattern of YnaI among these. **(B)** Bacterial, archaeal, and plant homologues were identified in a BLAST search with YnaI as a query. Glycines in the region of the GGIGG motif in YnaI are red, and the sealing residues in grey. Figure adapted from Flegler et al. (2020).

The availability of the closed and open conformations of AtMSL1 allowed a detailed description of the conformational changes occurring upon opening (figure 4.11). The closed form of AtMSL1 is similar to YnaI in its closed state. In the AtMSL1-A320V mutant, the four paddle helices are rotated counterclockwise as a rigid body by ~135° around the pore helix, accompanied by an outward movement of ~30 Å (figure 4.10) (Deng et al., 2020). These structural rearrangements result in a flattened TMD and an area expansion of the channel. TM3a tilts radially within the membrane plane, and the kink connecting to TM3b vanishes, leading to one straight helix, which is concurrent with a widening of the pore. Both open(-like) conformations of YnaI and AtMSL1 have a wider pore than their closed conformations, which is shortened with respect to the membrane plane. The paddles helices must relocate in a way that flattens the TMD and result in a diminished periplasmic indentation. The relocation of the paddles is only directly visible in AtMSL1-A320V but can be suggested from the flat TMD observed for open-like YnaI. The major difference is the behaviour of the pore helices. The shortening of the pore is realised by outward bending of the pore helices in open-like YnaI, while in AtMSL1 it is caused by radially tilting of the pore helices within the membrane plane. Moreover, the kink separating the pore helices into TM3a and TM3b (designated as TM5a and TM5b by Deng et al. (2020)) vanishes in AtMSL1-A320V but is maintained in open-like YnaI.

The pore in AtMSL1-A320V is wider than in open-like YnaI: Based on the constricting residues in the pore, F323 in AtMSL1 (PDBs 6VXM and 6VXN (Deng et al., 2020)) and M158 in YnaI, respectively, the pore diameter increases in AtMSL1 from 11.6 Å to 23.5 Å and from 8.2 Å to 15.7 Å in YnaI. The straightening of the pore helix could also be facilitated by the absence of the β barrel in AtMSL1 (Deng et al., 2020; Li et al., 2020), which is present in YnaI and is important for oligomerisation and stability in MscS (Schumann et al., 2004).

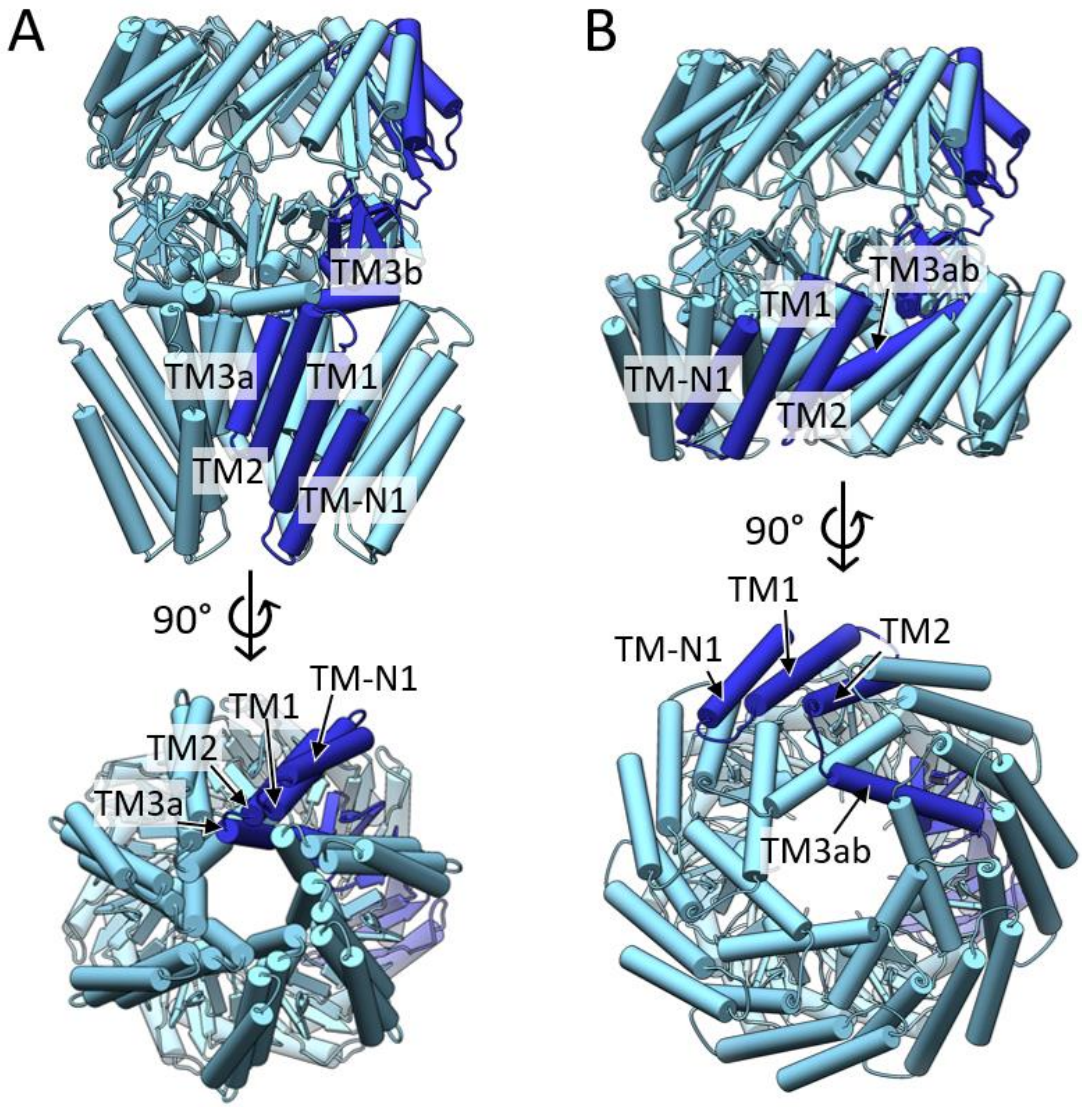


**Figure 4.11 | The closed and open structure of AtMSL1. (A)** AtMSL1 is shown in light blue with one subunit highlighted in dark blue and annotated helices (PDB 6VXM (closed) and 6VXN (open) (Deng et al., 2020)). AtMSL1 is shown in side-view (top) and top view, viewed from the periplasmic side (bottom). The numbering of the helices is adapted to the numbering of MscS/YnaI (see figure 1.3 C). As observed for YnaI and other MscS-like channels, a kink separates the pore helices into TM3a and TM3b **(B)** For the AtMSL1-A320V mutant that produced the open conformation, the same colour code is used as in (A) and it is depicted in the same orientation with the same subunit highlighted. The paddle helices move approximately as a rigid body, and the helices TM3a and TM3b are joined (TM3ab).

**Straightening of the pore helices.** A complete straightening of the pore helix TM3 was already suggested earlier for MscS in MD simulations by Sukharev and coworkers (dashpot model, see figure 1.6) (Akitake et al., 2007; Anishkin et al., 2008b). This model also proposed a different closed state. Cryo-EM structures of MscS in MSP nanodiscs captured in different conformations (Rasmussen et al., 2019a; Reddy et al., 2019; Zhang et al., 2021) contradict the dashpot gating model. The open conformation of MscS based on the A106V mutation was, in turn, backed up by crystal structures of MscS purified in DDM (Lai et al., 2013; Pliotas et al., 2015) or cryo-EM structures of MscS purified in DDM or LMNG in the present work, which are all essentially identical to the first open crystal structure (Wang et al., 2008). Nevertheless, as patch clamp experiments of alanine mutants supported the conformations observed in the MD simulations, their existence cannot be excluded entirely. The observed open conformation for AtMSL1-A320V provided for the first time a structural proof of the hypothesis that the kink separating the helices TM3a and TM3b can indeed vanish in a MscS-like channel. One could speculate that the fully open form of YnaI is similar to the AtMSL1-A320V structure, as they are highly similar regarding their closed structures and their sequences, especially in the pore-forming helices. So, it is possible that the observed open-like conformation is, as the observed intermediate conformation, also a transition intermediate and the ultimate open form, which resembles that of AtMSL1-A320V (figure 4.12 A).

**Relation of the pore diameter to the conductance.** Other explanations are conceivable for the structural differences between the open states of YnaI and AtMSL1. One would simply be that the open structures are indeed just different as YnaI and AtMSL1 are individual proteins from different organisms. The reported single-channel conductance of AtMSL1 in *E. coli* spheroplasts is 1.12 nS (Deng et al., 2020) and 1.2 nS (C. P. Lee et al., 2016), respectively. Both values are in the range of *E. coli* MscS (1.25 nS (Edwards et al., 2005)) and are significantly higher than for YnaI (0.1 nS (Edwards et al., 2012)). The higher conductance of AtMSL1 might justify its different open state regarding the larger pore. Hence, the observed open-like YnaI conformation could also represent the true open state of YnaI because the small pore of this conformation would reflect the comparably small conductance (figure 4.12 B). However, this model is not supported by the computational electrophysiological experiments, that showed for the open-like YnaI conformation a reduced conductance of ~10 pS (V = -200 mV) and ~40 pS (V = +200 mV), respectively, compared to the previously experimentally determined conductance of 0.1 nS (Edwards et al., 2012).

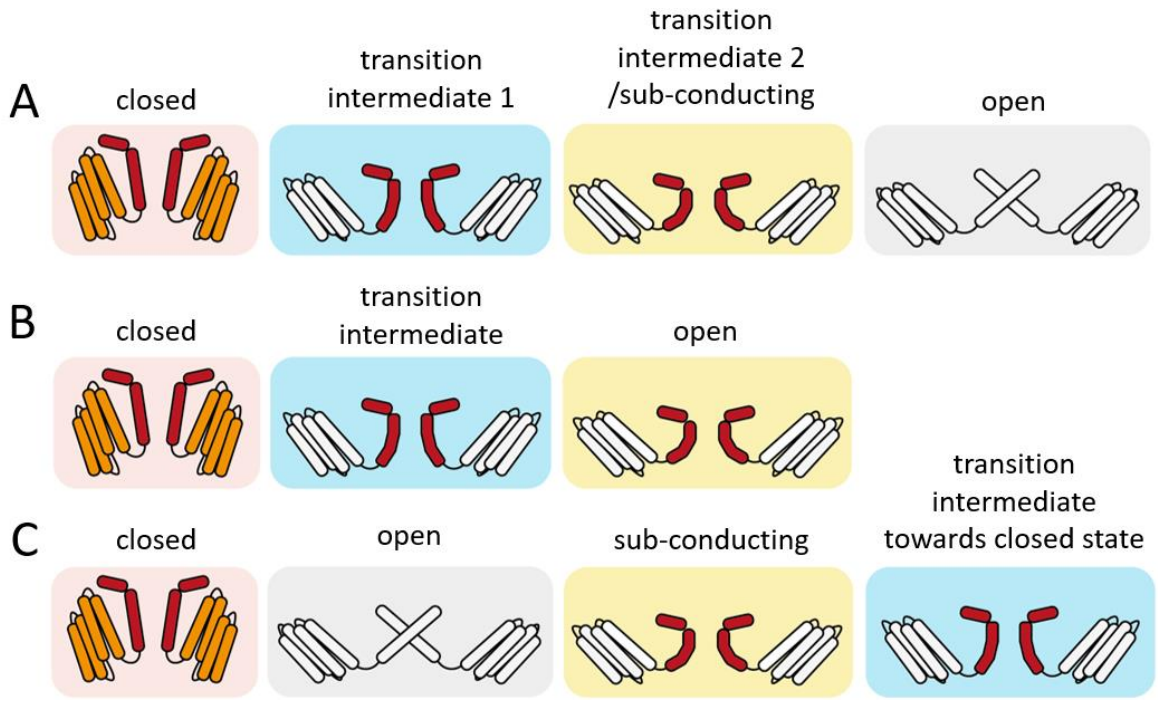


**Figure 4.12 | The role of the open-like YnaI conformation in alternative gating models.** The TMDs of the different YnaI conformations are coloured by their domains: The pore helices TM3a and TM3b are red, and the sensor paddle helices are orange. Helices that could not be assigned but are suggested by the open AtMSL1-A320V mutant are white. The observed closed conformation has a red background, the intermediate state a blue one, the open-like conformation a yellow one, and the open AtMSL1 conformation (Deng et al., 2020) a grey one. **(A)** In this model, the open-like conformation represents a sub-conducting state because LPC is not sufficient to open YnaI completely (open-like conformation). The fully open state would be reminiscent of AtMSL1-A320V. **(B)** The open-like conformation could indeed be the true open state of YnaI, which would agree with the small conductance of YnaI. **(C)** If the open state produced by LPC was unstable, it could collapse into a sub-conducting state, represented by the open-like conformation. In this scenario, the transition intermediate would represent an intermediate between the sub-conducting (open-like) and the closed conformation.

**The open-like YnaI conformation as sub-conducting state.** On the other hand, the open-like YnaI conformation could represent neither the fully open channel nor a transition intermediate but a sub-conducting state. Sub-conducting states have previously been reported for MscS (Anishkin and Sukharev, 2009; Cox et al., 2013; Edwards et al., 2005; Pliotas et al., 2015; Rasmussen et al., 2015; Shapovalov and Lester, 2004), indicating that the channels entered the open state before entering any sub-conducting states. This phenomenon was also observed for AtMSL1, showing that a significant portion of channels in patch clamp experiments was already found in a sub-conducting state or entered one after a full opening (Deng et al., 2020). Interestingly, those numbers were even higher for AtMSL1-A320V: 82 % of all channels switched to a sub-conducting state after opening. Maybe the fully open YnaI channel cannot

be accomplished by applying LPC because the open state obtained by LPC is unstable and thus collapses into a sub-conducting state (figure 4.12 C). In this model, the observed intermediate conformation could be a transition intermediate towards the closed state. However, it must be considered in which states a channel can dwell long enough to be captured in such large numbers as observed in the cryo-EM data set. The captured conformations thus cannot simply be understood as dynamic transition intermediates. This makes this model unlikely, as a channel would rather adopt the closed conformation than an intermediate form.

For MscS, it was shown that LPC added to inside-out patches (which is equivalent to the addition of LPC to the cytosolic leaflet) generated a stable open state *in vitro* when applied to spheroplasts or liposomes in patch clamp experiments, and the single-channel properties did not differ from those opened by pressure (Vásquez et al., 2008a). In contrast, in another study, LPC-activated MscS channels exhibited a reduced conductance, irrespective of which side of the bilayer it was added (Pliotas et al., 2015). In this model, MscS would enter the sub-conducting state from the closed state. As this behaviour was observed by the addition of LPC, it could be adopted to the obtained open-like YnaI conformation. Conclusively, this means that YnaI treated with LPC has never entered the fully open state and is thus trapped in a sub-conducting state, equivalent to the model where it is termed a transition intermediate (figure 4.12 A). This model is supported by a posterior evaluation of the LPC experiments: only ~5.5 LPC molecules per 1 YnaI molecule were theoretically present in the experimental setup, and only ~1 LPC molecule per ~180 lipid molecules. This highlights that the amount of LPC used was probably too low to fully open YnaI, resulting in a sub-conducting conformation, and can explain the coexistence of the different states.

### 4.3.3 A summary for possible functioning of YnaI

For deriving a functional model for YnaI, several observations and facts, as well as comparisons with MscS, must be considered. First, the membrane around YnaI is locally only slightly curved. It is unlikely that local membrane curvature changes are the driving gating forces. Second, lipids fill the pockets of YnaI similar to MscS, which presumably leave the channel for opening. Third, the pore helices are flexible and bend outwards. The bending of the pore occurs gradually. Fourth, relocation of the sensor paddles is decoupled from pore widening and the four paddle helices of one subunit likely move as a rigid body. Finally, the obtained open-like YnaI conformation probably represents a sub-conducting state that the

channel adopts because full opening cannot be accomplished by the chosen conditions (figure 4.12 A).

It remains elusive whether lipids from the periplasmic leaflet enter the arising gaps in the transmembrane domain on the periplasmic side upon opening like proposed for MscS. Considering the location of the paddle helices in open AtMSL1, and assuming a similar arrangement for open YnaI, the bulk water phase in the funnel would probably not be exposed, as the outer helix bundle TM-N1 and TM-N2 shield arising gaps from the lipid environment. However, these questions can only be addressed with the availability of a well-resolved open YnaI conformation, eventually by introducing the equivalent mutation (A155V) to MscS-A106V and AtMSL1-A320V. The structure must resolve the TMD as well as lipids to clarify the open conformation and gating mechanism of YnaI.

## 4.4 Closing remarks

This work showed different purification strategies for structural analyses of MscS-like channels and highlighted the difficulty to choose the most suitable system, as all have their benefits and pitfalls.

The medium-sized MscS paralogue YnaI was purified without the use of classic detergents using DIBMA copolymer. The complete absence of classic detergents was considered beneficial for MscS-like channels because, as shown for MscS, lipids, which can be harshly washed away by the wrong kind or amount of detergent, play a decisive role in the conformational state of the channel (Zhang et al., 2021). However, the obtained map probably does not represent the fully closed state, already indicating that the effects of DIBMA copolymer can affect the conformational state. The obtained cryo-EM map with an overall resolution of 3.0 Å was suitable for model building, underpinning the conserved architecture to MscS and shedding light on the arrangement of the two additional TM helices. Furthermore, the identification of a bound lipid molecule in YnaI in a similar position and orientation as in MscS (Rasmussen et al., 2019a) indicates similarities in their mechanisms. Thus, this work investigated for the first time the applicability of DIBMA for the preparation of a membrane protein for structural studies by cryo-EM, but also revealed further limitations associated with the use of DIBMA copolymer: The studies on MscS revealed that DIBMA is detrimental to contacting TM helices, explaining why the outermost helix TM-N2 of YnaI is probably

denatured. A similar effect is observed for Amphipols A8-35. Nonetheless, DIBMA copolymer allowed the extraction of LPC-treated YnaI, which resulted in cryo-EM maps that provide a glimpse on a possible gating mechanism of YnaI. Although the obtained structures might not represent ultimate conformational states, and their outer TMD is probably also affected by DIBMA copolymer, they are informative. The application of DIBMA to MscS and YnaI described in this work showed that DIBMA can indeed solubilise the channels from native *E. coli* membranes, but it has a detrimental effect on the proteins or on the bilayer, which in turn leads to perturbation of the contacting helices. As no other high-resolution structures of membrane proteins solubilised in DIBMA copolymer are available yet, the effect of DIBMA on the structural integrity of membrane proteins has not been investigated elsewhere. However, a recent study successfully purified a mammalian serotonin transporter using DIBMA copolymer and demonstrated that the transporter retained its activity (Dilworth et al., 2021); but nonetheless it is possible that the function is not affected by a partially perturbed TMD. Further structural studies of membrane proteins in DIBMA-stabilised nanodiscs would be needed to draw a general conclusion regarding the effect of DIBMA copolymer.

MscS was additionally purified in the detergents DDM and LMNG, revealing how and why different purification strategies affect the conformational state and the integrity of the channel. MscS was switched between its closed and open state by deliberately delipidating and re-lipidating the channel. This proved, on the one hand, the sensitivity of the conformational state to detergents and resulted, on the other hand, in a 2.3 Å map of open MscS in LMNG. This map revealed an intricate network of non-protein densities within the open channel, allowing the careful evaluation of bound ligands and deriving an updated lipids-move-first gating model for MscS. Although delipidation provides a novel method to activate MscS, it will be difficult to apply it to the larger paralogues because these tend to aggregate when concentrated in detergent. However, the purification of YbiO in a buffer supplemented with lipids and the improved resolution of closed MscS in DDM obtained after the addition of lipids prove that a more complete lipidation has a stabilising effect on MscS-like channels. Thus, the routine addition of lipids to the purification buffers provides an option for the successful purification of the larger paralogues by detergents. Though not providing a native lipidic environment, detergent molecules offer the advantage over polymer-stabilised- or MSP nanodiscs, that they adapt more flexible to the size of the transmembrane part of a protein. This is also an intrinsic feature of the Salipro system (Frauenfeld et al., 2016) and Peptidiscs (Carlson et al., 2018). Hence, these novel approaches for handling membrane proteins, possibly in combination with lipid addition, offer further alternatives worth trying for the larger paralogues.

# 5 REFERENCES


Abascal JLF, Vega C. 2005. A general purpose model for the condensed phases of water: TIP4P/2005. *J Chem Phys* **123**:234505. doi:10.1063/1.2121687

Abraham MJ, Murtola T, Schulz R, Páll S, Smith JC, Hess B, Lindahl E. 2015. GROMACS: High performance molecular simulations through multi-level parallelism from laptops to supercomputers. *SoftwareX* **1**–**2**:19–25. doi:10.1016/J.SOFTX.2015.06.001

Adams PD, Afonine P V., Bunkóczi G, Chen VB, Davis IW, Echols N, Headd JJ, Hung LW, Kapral GJ, Grosse-Kunstleve RW, McCoy AJ, Moriarty NW, Oeffner R, Read RJ, Richardson DC, Richardson JS, Terwilliger TC, Zwart PH. 2010. PHENIX: A comprehensive Python-based system for macromolecular structure solution. *Acta Crystallogr Sect D Biol Crystallogr* **66**:213–221. doi:10.1107/S0907444909052925

Adrian M, Dubochet J, Lepault J, McDowall AW. 1984. Cryo-electron microscopy of viruses. *Nat 1984 3085954* **308**:32–36. doi:10.1038/308032a0

Ahn VE, Leyko P, Alattia J-R, Chen L, Privé GG. 2006. Crystal structures of saposins A and C. *Protein Sci* **15**:1849–1857. doi:10.1110/PS.062256606

Akitake B, Anishkin A, Liu N, Sukharev S. 2007. Straightening and sequential buckling of the pore-lining helices define the gating cycle of MscS. *Nat Struct Mol Biol* **14**:1141–1149. doi:10.1038/nsmb1341

Akitake B, Anishkin A, Sukharev S. 2005. The "Dashpot" Mechanism of Stretch-dependent Gating in MscS. *J Gen Physiol* **125**:143. doi:10.1085/JGP.200409198

Alberts B. 1998. The cell as a collection of protein machines: preparing the next generation of molecular biologists. *Cell* **92**:291–294. doi:10.1016/S0092-8674(00)80922-8

Alemany R, Perona JS, Sánchez-Dominguez JM, Montero E, Cañizares J, Bressani R, Escribá P V., Ruiz-Gutierrez V. 2007. G protein-coupled receptor systems and their lipid environment in health disorders during aging. *Biochim Biophys Acta - Biomembr* **1768**:964–975. doi:10.1016/J.BBAMEM.2006.09.024

Angiulli G, Dhupar HS, Suzuki H, Wason IS, Van Hoa FD, Walz T. 2020. New approach for membrane protein reconstitution into peptidiscs and basis for their adaptability to different proteins. *Elife* **9**. doi:10.7554/ELIFE.53530

Anishkin A, Akitake B, Kamaraju K, Chiang CS, Sukharev S. 2010. Hydration properties of mechanosensitive channel pores define the energetics of gating. *J Phys Condens Matter* **22**. doi:10.1088/0953-8984/22/45/454120

Anishkin A, Akitake B, Sukharev S. 2008a. Characterization of the resting MscS: Modeling and analysis of the closed bacterial mechanosensitive channel of small conductance. *Biophys J* **94**:1252–1266. doi:10.1529/biophysj.107.110171

Anishkin A, Kamaraju K, Sukharev S. 2008b. Mechanosensitive Channel MscS in the Open State: Modeling of the Transition, Explicit Simulations, and Experimental Measurements of Conductance. *J Gen Physiol* **132**:67. doi:10.1085/JGP.200810000

Anishkin A, Loukin SH, Teng J, Kung C. 2014. Feeling the hidden mechanical forces in lipid bilayer is an original sense. *Proc - Natl Acad Sci USA*. doi:10.1073/pnas.1313364111

Anishkin A, Sukharev S. 2009. State-stabilizing Interactions in Bacterial Mechanosensitive Channel Gating and Adaptation. *J Biol Chem* **284**:19153–19157. doi:10.1074/JBC.R109.009357

Anishkin A, Sukharev S. 2004. Water Dynamics and Dewetting Transitions in the Small Mechanosensitive Channel MscS. *Biophys J* **86**:2883–2895. doi:10.1016/S0006-3495(04)74340-4

Árnadóttir J, Chalfie M. 2010. Eukaryotic Mechanosensitive Channels. *Annu Rev Biophys* **39**:111–137. doi:10.1146/ANNUREV.BIOPHYS.37.032807.125836

Autzen HE, Julius D, Cheng Y. 2019. Membrane mimetic systems in CryoEM: keeping membrane proteins in their native environment. *Curr Opin Struct Biol* **58**:259–268. doi:10.1016/J.SBI.2019.05.022

Bai XC, Fernandez IS, McMullan G, Scheres SHW. 2013. Ribosome structures to near-atomic resolution from thirty thousand cryo-EM particles. *Elife* **2013**. doi:10.7554/ELIFE.00461

Baker JA, Wong W-C, Eisenhaber B, Warwicker J, Eisenhaber F. 2017. Charged residues next to transmembrane regions revisited: "Positive-inside rule" is complemented by the "negative inside depletion/outside

enrichment rule." *BMC Biol 2017 151* **15**:1–29. doi:10.1186/S12915-017-0404-4
Bald WB. 1984. The relative efficiency of cryogenic fluids used in the rapid quench cooling of biological samples. *J Microsc* **134**:261–270. doi:10.1111/J.1365-2818.1984.TB02519.X
Bannwarth M, Schulz GE. 2003. The expression of outer membrane proteins for crystallization. *Biochim Biophys Acta* **1610**:37–45. doi:10.1016/S0005-2736(02)00711-3
Bartesaghi A, Merk A, Banerjee S, Matthies D, Wu X, Milne JLS, Subramaniam S. 2015. 2.2 å resolution cryo-EM structure of β-galactosidase in complex with a cell-permeant inhibitor. *Science (80- )* **348**:1147–1151. doi:10.1126/SCIENCE.AAB1576
Bartesaghi A, Subramaniam S. 2009. Membrane protein structure determination using cryo-electron tomography and 3D image averaging. *Curr Opin Struct Biol* **19**:402–7. doi:10.1016/j.sbi.2009.06.005
Barth M, Bryan RK, Hegerl R. 1989. Approximation of missing-cone data in 3D electron microscopy. *Ultramicroscopy* **31**:365–378. doi:10.1016/0304-3991(89)90335-5
Bass RB, Strop P, Barclay M, Rees DC. 2002. Crystal structure of Escherichia coli MscS, a voltage-modulated and mechanosensitive channel. *Science (80- )* **298**:1582–1587. doi:10.1126/science.1077945
Bavi N, Cortes DM, Cox CD, Rohde PR, Liu W, Deitmer JW, Bavi O, Strop P, Hill AP, Rees D, Corry B, Perozo E, Martinac B. 2016. The role of MscL amphipathic N terminus indicates a blueprint for bilayer-mediated gating of mechanosensitive channels. *Nat Commun 2016 71* **7**:1–13. doi:10.1038/ncomms11984
Bavi N, Cox CD, Perozo E, Martinac B. 2017. Toward a structural blueprint for bilayer-mediated channel mechanosensitivity. *Channels* **11**:91. doi:10.1080/19336950.2016.1224624
Bavi O, Cox CD, Vossoughi M, Naghdabadi R, Jamali Y, Martinac B. 2016. Influence of Global and Local Membrane Curvature on Mechanosensitive Ion Channels: A Finite Element Approach. *Membranes (Basel)* **6**:14. doi:10.3390/MEMBRANES6010014
Bayburt TH, Carlson JW, Sligar SG. 1998. Reconstitution and imaging of a membrane protein in a nanometer-size phospholipid bilayer. *J Struct Biol* **123**:37–44. doi:10.1006/JSBI.1998.4007
Bayburt TH, Grinkova Y V., Sligar SG. 2002. Self-Assembly of Discoidal Phospholipid Bilayer Nanoparticles with Membrane Scaffold Proteins. *Nano Lett* **2**:853–856. doi:10.1021/NL025623K
Bayburt TH, Sligar SG. 2010. Membrane protein assembly into Nanodiscs. *FEBS Lett*. doi:10.1016/j.febslet.2009.10.024
Bechara C, Nöll A, Morgner N, Degiacomi MT, Tampé R, Robinson C V. 2015. A subset of annular lipids is linked to the flippase activity of an ABC transporter. *Nat Chem* **7**:255–262. doi:10.1038/nchem.2172
Bellare JR, Davis HT, Scriven LE, Talmon Y. 1988. Controlled environment vitrification system: An improved sample preparation technique. *J Electron Microsc Tech* **10**:87–111. doi:10.1002/JEMT.1060100111
Berrier C, Coulombe A, Houssin C, Ghazi A. 1989. A patch-clamp study of ion channels of inner and outer membranes and of contact zones of E. coli, fused into giant liposomes. Pressure-activated channels are localized in the inner membrane. *FEBS Lett* **259**:27–32. doi:10.1016/0014-5793(89)81486-3
Bligh EG, Dyer WJ. 1959. A rapid method of lipid extraction and purification. *Can J Biochem Physiol* **37**:911–917. doi:10.1139/o59-099
Blount P, Iscla I. 2020. Life with Bacterial Mechanosensitive Channels, from Discovery to Physiology to Pharmacological Target. *Microbiol Mol Biol Rev* **84**. doi:10.1128/MMBR.00055-19
Blount P, Sukharev SI, Moe PC, Martinac B, Kung C. 1999a. [24] Mechanosensitive channels of bacteria. *Methods Enzymol* **294**:458–482. doi:10.1016/S0076-6879(99)94027-2
Blount P, Sukharev SI, Moe PC, Martinac B, Kung C. 1999b. c. *Methods Enzymol* **294**:458–482. doi:10.1016/S0076-6879(99)94027-2
Blount P, Sukharev SI, Schroeder MJ, Nagle SK, Kung C. 1996. Single residue substitutions that change the gating properties of a mechanosensitive channel in Escherichia coli. *Proc Natl Acad Sci U S A* **93**:11652–11657. doi:10.1073/pnas.93.21.11652
Bogdanov M, Mileykovskaya E, Dowhan W. 2008. Lipids in the Assembly of Membrane Proteins and Organization of Protein Supercomplexes: Implications for Lipid-Linked Disorders. *Subcell Biochem* **49**:197. doi:10.1007/978-1-4020-8831-5_8
Booth IR. 1985. Regulation of cytoplasmic pH in bacteria. *Microbiol Rev* **49**:359.
Booth IR, Edwards MD, Black S, Schumann U, Bartlett W, Rasmussen T, Rasmussen A, Miller S. 2007. Physiological Analysis of Bacterial Mechanosensitive Channels. *Methods Enzymol* **428**:47–61. doi:10.1016/S0076-6879(07)28003-6
Booth IR, Louis P. 1999. Managing hypoosmotic stress: aquaporins and mechanosensitive channels in Escherichia coli. *Curr Opin Microbiol* **2**:166–169. doi:10.1016/S1369-5274(99)80029-0
Böttcher B, Prazak V, Rasmussen A, Black SS, Rasmussen T. 2015. The Structure of YnaI Implies Structural and Mechanistic Conservation in the MscS Family of Mechanosensitive Channels. *Structure* **23**:1705–1714. doi:10.1016/j.str.2015.06.023
Brandl M, Weiss MS, Jabs A, Sühnel J, Hilgenfeld R. 2001. C-h···π-interactions in proteins. *J Mol Biol* **307**:357–377. doi:10.1006/JMBI.2000.4473

Brenner S, Horne RW. 1959. A negative staining method for high resolution electron microscopy of viruses. *Biochim Biophys Acta* **34**:103–110. doi:10.1016/0006-3002(59)90237-9

Briggs JAG, Huiskonen JT, Fernando KV, Gilbert RJC, Scotti P, Butcher SJ, Fuller SD. 2005. Classification and three-dimensional reconstruction of unevenly distributed or symmetry mismatched features of icosahedral particles. *J Struct Biol* **150**:332–339. doi:10.1016/J.JSB.2005.03.009

Brilot AF, Chen JZ, Cheng A, Pan J, Harrison SC, Potter CS, Carragher B, Henderson R, Grigorieff N. 2012. Beam-induced motion of vitrified specimen on holey carbon film. *J Struct Biol* **177**:630–637. doi:10.1016/J.JSB.2012.02.003

Brohawn SG. 2015. How ion channels sense mechanical force: insights from mechanosensitive K2P channels TRAAK, TREK1, and TREK2. *Ann N Y Acad Sci* **1352**:20–32. doi:10.1111/NYAS.12874

Brohawn SG, Campbell MG, MacKinnon R. 2014a. Physical mechanism for gating and mechanosensitivity of the human TRAAK K+ channel. *Nature* **516**:126–130. doi:10.1038/NATURE14013

Brohawn SG, Mármol J del, MacKinnon R. 2012. Crystal structure of the human K2P TRAAK, a lipid- and mechano-sensitive K+ ion channel. *Science* **335**:436. doi:10.1126/SCIENCE.1213808

Brohawn SG, Su Z, MacKinnon R. 2014b. Mechanosensitivity is mediated directly by the lipid membrane in TRAAK and TREK1 K+ channels. *Proc Natl Acad Sci* **111**:3614–3619. doi:10.1073/PNAS.1320768111

Bruhn H. 2005. A short guided tour through functional and structural features of saposin-like proteins. *Biochem J* **389**:249. doi:10.1042/BJ20050051

Buchan DWA, Jones DT. 2019. The PSIPRED Protein Analysis Workbench: 20 years on. *Nucleic Acids Res* **47**:W402–W407. doi:10.1093/nar/gkz297

Bussi G, Donadio D, Parrinello M. 2007. Canonical sampling through velocity rescaling. *J Chem Phys* **126**:014101. doi:10.1063/1.2408420

Campbell MG, Cheng A, Brilot AF, Moeller A, Lyumkis D, Veesler D, Pan J, Harrison SC, Potter CS, Carragher B, Grigorieff N. 2012. Movies of Ice-Embedded Particles Enhance Resolution in Electron Cryo-Microscopy. *Structure* **20**:1823–1828. doi:10.1016/J.STR.2012.08.026

Cantor RS. 1997. Lateral Pressures in Cell Membranes: A Mechanism for Modulation of Protein Function. *J Phys Chem B* **101**:1723–1725. doi:10.1021/JP963911X

Cao E, Liao M, Cheng Y, Julius D. 2013. TRPV1 structures in distinct conformations reveal activation mechanisms. *Nat 2013 5047478* **504**:113–118. doi:10.1038/nature12823

Carlson ML, Stacey RG, Young JW, Wason IS, Zhao Z, Rattray DG, Scott N, Kerr CH, Babu M, Foster LJ, Duong Van Hoa F. 2019. Profiling the Escherichia coli membrane protein interactome captured in Peptidisc libraries. *Elife* **8**. doi:10.7554/ELIFE.46615

Carlson ML, Young JW, Zhao Z, Fabre L, Jun D, Li Jianing, Li Jun, Dhupar HS, Wason I, Mills AT, Beatty JT, Klassen JS, Rouiller I, Duong F. 2018. The peptidisc, a simple method for stabilizing membrane proteins in detergent-free solution. *Elife* **7**. doi:10.7554/eLife.34085

Caterina MJ, Schumacher MA, Tominaga M, Rosen TA, Levine JD, Julius D. 1997. The capsaicin receptor: a heat-activated ion channel in the pain pathway. *Nat 1997 3896653* **389**:816–824. doi:10.1038/39807

Chae PS, Rasmussen SGF, Rana RR, Gotfryd K, Chandra R, Goren MA, Kruse AC, Nurva S, Loland CJ, Pierre Y, Drew D, Popot JL, Picot D, Fox BG, Guan L, Gether U, Byrne B, Kobilka B, Gellman SH. 2010. Maltose-neopentyl glycol (MNG) amphiphiles for solubilization, stabilization and crystallization of membrane proteins. *Nat Methods* **7**:1003–1008. doi:10.1038/nmeth.1526

Chae PS, Wander MJ, Bowling AP, Laible PD, Gellman SH. 2008. Glycotripod amphiphiles for solubilization and stabilization of a membrane-protein superassembly: Importance of branching in the hydrophilic portion. *ChemBioChem* **9**:1706–1709. doi:10.1002/cbic.200800169

Chandler D. 2005. Interfaces and the driving force of hydrophobic assembly. *Nat 2005 4377059* **437**:640–647. doi:10.1038/nature04162

Chang G, Spencer RH, Lee AT, Barclay MT, Rees DC, Bartlett W, Dong C, Naismith JH, Booth IR. 1998. Structure of the MscL Homolog from Mycobacterium tuberculosis: A Gated Mechanosensitive Ion Channel. *Science (80- )* **282**:2220–2226. doi:10.1126/science.282.5397.2220

Chen F, Gerber S, Heuser K, Korkhov VM, Lizak C, Mireku S, Locher KP, Zenobi R. 2013. High-mass matrix-assisted laser desorption ionization-mass spectrometry of integral membrane proteins and their complexes. *Anal Chem* **85**:3483–3488. doi:10.1021/ac4000943

Chen J, Noble AJ, Kang JY, Darst SA. 2019. Eliminating effects of particle adsorption to the air/water interface in single-particle cryo-electron microscopy: Bacterial RNA polymerase and CHAPSO. *J Struct Biol X* **1**:100005. doi:10.1016/J.YJSBX.2019.100005

Chen S, McMullan G, Faruqi AR, Murshudov GN, Short JM, Scheres SHW, Henderson R. 2013. High-resolution noise substitution to measure overfitting and validate resolution in 3D structure determination by single particle electron cryomicroscopy. *Ultramicroscopy* **135**:24–35. doi:10.1016/J.ULTRAMIC.2013.06.004

Chen VB, Arendall WB, Headd JJ, Keedy DA, Immormino RM, Kapral GJ, Murray LW, Richardson JS, Richardson DC. 2010. *MolProbity* : all-atom structure validation for macromolecular crystallography. *Acta*

*Crystallogr Sect D Biol Crystallogr* **66**:12–21. doi:10.1107/S0907444909042073

Cheng LE, Song W, Looger LL, Jan LY, Jan YN. 2010. The role of the TRP channel NompC in Drosophila larval and adult locomotion. *Neuron* **67**:373–380. doi:10.1016/J.NEURON.2010.07.004

Cheng Y, Wolf E, Larvie M, Zak O, Aisen P, Grigorieff N, Harrison SC, Walz T. 2006. Single Particle Reconstructions of the Transferrin–Transferrin Receptor Complex Obtained with Different Specimen Preparation Techniques. *J Mol Biol* **355**:1048–1065. doi:10.1016/J.JMB.2005.11.021

Chesler AT, Szczot M. 2018. Portraits of a pressure sensor. *Elife* **7**. doi:10.7554/eLife.34396

Chipot C, Dehez F, Schnell JR, Zitzmann N, Pebay-Peyroula E, Catoire LJ, Miroux B, Kunji ERS, Veglia G, Cross TA, Schanda P. 2018. Perturbations of Native Membrane Protein Structure in Alkyl Phosphocholine Detergents: A Critical Assessment of NMR and Biophysical Studies. *Chem Rev* **118**:3559–3607. doi:10.1021/ACS.CHEMREV.7B00570

Chung HJ, Bang W, Drake MA. 2006. Stress Response of Escherichia coli. *Compr Rev Food Sci Food Saf* **5**:52–64. doi:10.1111/J.1541-4337.2006.00002.X

Coste B, Mathur J, Schmidt M, Earley TJ, Ranade S, Petrus MJ, Dubin AE, Patapoutian A. 2010. Piezo1 and Piezo2 Are Essential Components of Distinct Mechanically Activated Cation Channels. *Science (80- )* **330**:55–60. doi:10.1126/science.1193270

Cox CD, Nomura T, Ziegler CS, Campbell AK, Wann KT, Martinac B. 2013. Selectivity mechanism of the mechanosensitive channel MscS revealed by probing channel subconducting states. *Nat Commun* **4**:2137. doi:10.1038/ncomms3137

Craig AF, Clark EE, Sahu ID, Zhang R, Frantz ND, Al-Abdul-Wahid MS, Dabney-Smith C, Konkolewicz D, Lorigan GA. 2016. Tuning the size of styrene-maleic acid copolymer-lipid nanoparticles (SMALPs) using RAFT polymerization for biophysical studies. *Biochim Biophys Acta - Biomembr* **1858**:2931–2939. doi:10.1016/J.BBAMEM.2016.08.004

Crowther RA, DeRosier DJ, Klug A. 1970. Reconstruction of a three-dimensional strcuture from projection and its application to electron microscopy **317**:319–340. doi:10.1098/RSPA.1970.0119

Cuéllar J, Perales-Calvo J, Muga A, Valpuesta JM, Moro F. 2013. Structural Insights into the Chaperone Activity of the 40-kDa Heat Shock Protein DnaJ: Binding and remodeling of a native substrate. *J Biol Chem* **288**:15065. doi:10.1074/JBC.M112.430595

Cuevas Arenas R, Klingler J, Vargas C, Keller S. 2016. Influence of lipid bilayer properties on nanodisc formation mediated by styrene/maleic acid copolymers. *Nanoscale* **8**:15016–15026. doi:10.1039/C6NR02089E

Cui C, Smith DO, Adler J. 1995. Characterization of mechanosensitive channels in Escherichia coli cytoplasmic membrane by whole-cell patch clamp recording. *J Membr Biol* **144**:31–42. doi:10.1007/BF00238414

Darden T, York D, Pedersen L. 1993. Particle mesh Ewald: An $N \cdot \log(N)$ method for Ewald sums in large systems. *J Chem Phys* **98**:10089–10092. doi:10.1063/1.464397

De Zorzi R, Mi W, Liao M, Walz T. 2016. Single-particle electron microscopy in the study of membrane protein structure. *Microscopy* **65**:81–96. doi:10.1093/jmicro/dfv058

Deng Z, Maksaev G, Schlegel AM, Zhang J, Rau M, Fitzpatrick JAJ, Haswell ES, Yuan P. 2020. Structural mechanism for gating of a eukaryotic mechanosensitive channel of small conductance. *Nat Commun* **11**:1–9. doi:10.1038/s41467-020-17538-1

Denisov IG, Sligar SG. 2016. Nanodiscs for structural and functional studies of membrane proteins. *Nat Struct Mol Biol* **23**:481–486. doi:10.1038/nsmb.3195

Dilworth M V., Findlay HE, Booth PJ. 2021. Detergent-free purification and reconstitution of functional human serotonin transporter (SERT) using diisobutylene maleic acid (DIBMA) copolymer. *Biochim Biophys Acta Biomembr* **1863**. doi:10.1016/J.BBAMEM.2021.183602

Doerner JF, Febvay S, Clapham DE. 2012. Controlled delivery of bioactive molecules into live cells using the bacterial mechanosensitive channel MscL. *Nat Commun 2012 31* **3**:1–8. doi:10.1038/ncomms1999

Dong H, Sharma M, Zhou H-X, Cross TA. 2012. Glycines: Role in α-Helical Membrane Protein Structures and a Potential Indicator for Native Conformation. *Biochemistry* **51**:4779. doi:10.1021/BI300090X

Dong YY, Pike ACW, Mackenzie A, McClenaghan C, Prafulla A, Dong L, Quigley A, Grieben M, Goubin S, Mukhopadhyay S, Ruda GF, Clausen M V., Cao L, Brennan PE, Burgess-Brown NA, Sansom MSP, Tucker SJ, Carpenter EP. 2015. K2P channel gating mechanisms revealed by structures of TREK-2 and a complex with Prozac. *Science* **347**:1256–1259. doi:10.1126/SCIENCE.1261512

Dörr JM, Koorengevel MC, Schäfer M, Prokofyev A V, Scheidelaar S, van der Cruijsen EAW, Dafforn TR, Baldus M, Killian JA. 2014. Detergent-free isolation, characterization, and functional reconstitution of a tetrameric K+ channel: the power of native nanodiscs. *Proc Natl Acad Sci U S A* **111**:18607–12. doi:10.1073/pnas.1416205112

Dörr JM, Scheidelaar S, Koorengevel MC, Dominguez JJ, Schäfer M, van Walree CA, Killian JA. 2016. The styrene-maleic acid copolymer: a versatile tool in membrane research. *Eur Biophys J* **45**:3–21. doi:10.1007/s00249-015-1093-y

Dowhan W, Bogdanov M. 2002. Chapter 1 Functional roles of lipids in membranes. *New Compr Biochem* **36**:1–

35. doi:10.1016/S0167-7306(02)36003-4
Dowhan W, Mileykovskaya E, Bogdanov M. 2004. Diversity and versatility of lipid–protein interactions revealed by molecular genetic approaches. *Biochim Biophys Acta - Biomembr* **1666**:19–39. doi:10.1016/J.BBAMEM.2004.04.010
Drew D, Fröderberg L, Baars L, de Gier J-WL. 2003. Assembly and overexpression of membrane proteins in Escherichia coli. *Biochim Biophys Acta* **1610**:3–10. doi:10.1016/S0005-2736(02)00707-1
Dubochet J, Adrian M, Chang JJ, Homo JC, Lepault J, McDowall AW, Schultz P. 1988. Cryo-electron microscopy of vitrified specimens. *Q Rev Biophys* **21**:129–228. doi:10.1017/S0033583500004297
Dubochet J, Chang J-J, Freeman R, Lepault J, McDowall AW. 1982. Frozen aqueous suspensions. *Ultramicroscopy* **10**:55–61. doi:10.1016/0304-3991(82)90187-5
Dunker AK, Brown CJ, Lawson JD, Iakoucheva LM, Obradovic´ Z. 2002. Current Topics Intrinsic Disorder and Protein Function †. doi:10.1021/BI012159
Dürr KL, Chen Le, Stein RA, De Zorzi R, Folea IM, Walz T, Mchaourab HS, Gouaux E. 2014. Structure and dynamics of AMPA receptor GluA2 in resting, pre-open, and desensitized states. *Cell* **158**:778–792. doi:10.1016/J.CELL.2014.07.023
Dürr UHN, Gildenberg M, Ramamoorthy A. 2012. The magic of bicelles lights up membrane protein structure. *Chem Rev* **112**:6054–6074. doi:10.1021/cr300061w
Edwards K, Johnsson M, Karlsson G, Silvander M. 1997. Preparations of Small Unilamellar Liposomes. *Biophys J* **73**:258–266. doi:10.1016/S0006-3495(97)78066-4
Edwards MD, Bartlett W, Booth IR. 2008. Pore mutations of the Escherichia coli MscS channel affect desensitization but not ionic preference. *Biophys J* **94**:3003–3013. doi:10.1529/biophysj.107.123448
Edwards MD, Black S, Rasmussen T, Rasmussen A, Stokes NR, Stephen T-L, Miller S, Booth IR. 2012. Characterization of three novel mechanosensitive channel activities in *Escherichia coli*. *Channels* **6**:272–281. doi:10.4161/chan.20998
Edwards MD, Li Y, Kim S, Miller S, Bartlett W, Black S, Dennison S, Iscla I, Blount P, Bowie JU, Booth IR. 2005. Pivotal role of the glycine-rich TM3 helix in gating the MscS mechanosensitive channel. *Nat Struct Mol Biol* **12**:113–119. doi:10.1038/nsmb895
Efremov RG, Leitner A, Aebersold R, Raunser S. 2014. Architecture and conformational switch mechanism of the ryanodine receptor. *Nat 2014 5177532* **517**:39–43. doi:10.1038/nature13916
Eilers M, Patel AB, Liu W, Smith SO. 2002. Comparison of Helix Interactions in Membrane and Soluble α-Bundle Proteins. *Biophys J* **82**:2720–2736. doi:10.1016/S0006-3495(02)75613-0
Emsley P, Lohkamp B, Scott WG, Cowtan K. 2010. Features and development of Coot. *Acta Crystallogr Sect D Biol Crystallogr* **66**:486–501. doi:10.1107/S0907444910007493
ExPASy - ProtParam tool. n.d. https://web.expasy.org/protparam/
Famelis N, Rivera-Calzada A, Degliesposti G, Wingender M, Mietrach N, Skehel JM, Fernandez-Leiro R, Böttcher B, Schlosser A, Llorca O, Geibel S. 2019. Architecture of the mycobacterial type VII secretion system. *Nat 2019 5767786* **576**:321–325. doi:10.1038/s41586-019-1633-1
Faruqi AR, Henderson R. 2007. Electronic detectors for electron microscopy. *Curr Opin Struct Biol* **17**:549–555. doi:10.1016/J.SBI.2007.08.014
Fiedorczuk K, Letts JA, Degliesposti G, Kaszuba K, Skehel M, Sazanov LA. 2016. Atomic structure of the entire mammalian mitochondrial complex I. *Nature* **538**:406–410. doi:10.1038/NATURE19794
Flegler VJ, Rasmussen A, Borbil K, Boten L, Chen H-A, Deinlein H, Halang J, Hellmanzik K, Löffler J, Schmidt V, Makbul C, Kraft C, Hedrich R, Rasmussen T, Böttcher B. 2021. Mechanosensitive channel gating by delipidation. *Proc Natl Acad Sci U S A* **118**:e2107095118. doi:10.1073/PNAS.2107095118
Flegler VJ, Rasmussen A, Rao S, Wu N, Zenobi R, Sansom MSP, Hedrich R, Rasmussen T, Böttcher B. 2020. The MscS-like channel YnaI has a gating mechanism based on flexible pore helices. *Proc Natl Acad Sci* **117**.
Frauenfeld J, Löving R, Armache J-P, Sonnen AF-P, Guettou F, Moberg P, Zhu L, Jegerschöld C, Flayhan A, Briggs JAG, Garoff H, Löw C, Cheng Y, Nordlund P. 2016. A saposin-lipoprotein nanoparticle system for membrane proteins. *Nat Methods 2016 134* **13**:345–351. doi:10.1038/nmeth.3801
Fujiyoshi Y. 2013. Low Dose Techniques and Cryo-Electron Microscopy. *Methods Mol Biol* **955**:103–118. doi:10.1007/978-1-62703-176-9_6
Gao Y, Cao E, Julius D, Cheng Y. 2016. TRPV1 structures in nanodiscs reveal mechanisms of ligand and lipid action. *Nat 2016 5347607* **534**:347–351. doi:10.1038/nature17964
Ge J, Li W, Zhao Q, Li N, Chen M, Zhi P, Li R, Gao N, Xiao B, Yang M. 2015. Architecture of the mammalian mechanosensitive Piezo1 channel. *Nature* **527**:64–69. doi:10.1038/nature15247
Geertsma ER, Nik Mahmood NAB, Schuurman-Wolters GK, Poolman B. 2008. Membrane reconstitution of ABC transporters and assays of translocator function. *Nat Protoc* **3**:256–266. doi:10.1038/NPROT.2007.519
Glaeser RM. 2008. Retrospective: radiation damage and its associated "information limitations." *Elsevier*. doi:10.1016/j.jsb.2008.06.001

Goddard TD, Huang CC, Meng EC, Pettersen EF, Couch GS, Morris JH, Ferrin TE. 2018. UCSF ChimeraX: Meeting modern challenges in visualization and analysis. *Protein Sci* **27**:14–25. doi:10.1002/pro.3235

Gohon Y, Giusti F, Prata C, Delphine Charvolin, Timmins P, Ebel C, Tribet C, Popot J-L. 2006. Well-Defined Nanoparticles Formed by Hydrophobic Assembly of a Short and Polydisperse Random Terpolymer, Amphipol A8-35. *Langmuir* **22**:1281–1290. doi:10.1021/LA052243G

Gohon Y, Pavlov G, Timmins P, Tribet C, Popot JL, Ebel C. 2004. Partial specific volume and solvent interactions of amphipol A8-35. *Anal Biochem* **334**:318–334. doi:10.1016/J.AB.2004.07.033

Gohon Y, Popot JL. 2003. Membrane protein–surfactant complexes. *Curr Opin Colloid Interface Sci* **8**:15–22. doi:10.1016/S1359-0294(03)00013-X

Gonen T, Sliz P, Kistler J, Cheng Y, Walz T. 2004. Aquaporin-0 membrane junctions reveal the structure of a closed water pore. *Nat 2004 4296988* **429**:193–197. doi:10.1038/nature02503

González W, Valdebenito B, Caballero J, Riadi G, Riedelsberger J, Martínez G, Ramírez D, Zúñiga L, Sepúlveda F V., Dreyer I, Janta M, Becker D. 2014. K2P channels in plants and animals. *Pflügers Arch - Eur J Physiol 2014 4675* **467**:1091–1104. doi:10.1007/S00424-014-1638-4

Grant T, Grigorieff N. 2015. Measuring the optimal exposure for single particle cryo-EM using a 2.6 Å reconstruction of rotavirus VP6. *Elife* **4**. doi:10.7554/eLife.06980

Grant T, Rohou A, Grigorieff N. 2018. CisTEM, user-friendly software for single-particle image processing. *Elife* **7**. doi:10.7554/eLife.35383

Grethen A, Oluwole AO, Danielczak B, Vargas C, Keller S. 2017. Thermodynamics of nanodisc formation mediated by styrene/maleic acid (2:1) copolymer. *Sci Rep* **7**:11517. doi:10.1038/s41598-017-11616-z

Grinkova Y V., Denisov IG, Sligar SG. 2010. Engineering extended membrane scaffold proteins for self-assembly of soluble nanoscale lipid bilayers. *Protein Eng Des Sel* **23**:843–848. doi:10.1093/PROTEIN/GZQ060

Gulati S, Jamshad M, Knowles TJ, Morrison KA, Downing R, Cant N, Collins R, Koenderink JB, Ford RC, Overduin M, Kerr ID, Dafforn TR, Rothnie AJ. 2014. Detergent-free purification of ABC (ATP-binding-cassette) transporters. *Biochem J* **461**:269–278. doi:10.1042/BJ20131477

Gullingsrud J, Kosztin D, Schulten K. 2001. Structural Determinants of MscL Gating Studied by Molecular Dynamics Simulations. *Biophys J* **80**:2074–2081. doi:10.1016/S0006-3495(01)76181-4

Guo YR, MacKinnon R. 2017. Structure-based membrane dome mechanism for piezo mechanosensitivity. *Elife* **6**. doi:10.7554/eLife.33660

Gupta K, Li J, Liko I, Gault J, Bechara C, Wu D, Hopper JTS, Giles K, Benesch JLP, Robinson C V. 2018. Identifying key membrane protein lipid interactions using mass spectrometry. *Nat Protoc* **13**:1106–1120. doi:10.1038/nprot.2018.014

Hagn F, Etzkorn M, Raschle T, Wagner G. 2013. Optimized Phospholipid Bilayer Nanodiscs Facilitate High-Resolution Structure Determination of Membrane Proteins. *J Am Chem Soc* **135**:1919–1925. doi:10.1021/JA310901F

Hamilton ES, Jensen GS, Maksaev G, Katims A, Sherp AM, Haswell ES. 2015. Mechanosensitive channel MSL8 regulates osmotic forces during pollen hydration and germination. *Science (80- )* **350**:438–441. doi:10.1126/SCIENCE.AAC6014

Hanahan D. 1983. Studies on transformation of Escherichia coli with plasmids. *J Mol Biol* **166**:557–580. doi:10.1016/S0022-2836(83)80284-8

Haswell ES. 2007. MscS-Like Proteins in Plants. *Curr Top Membr* **58**:329–359. doi:10.1016/S1063-5823(06)58013-5

Henderson R, Chen S, Chen JZ, Grigorieff N, Passmore LA, Ciccarelli L, Rubinstein JL, Crowther RA, Stewart PL, Rosenthal PB. 2011. Tilt-pair analysis of images from a range of different specimens in single-particle electron cryomicroscopy. *J Mol Biol* **413**:1028–1046. doi:10.1016/j.jmb.2011.09.008

Henderson R, Sali A, Baker M. 2012. Outcome of the first electron microscopy validation task force meeting. *Structure* **20**:205–214.

Henderson R, Unwin PNT. 1975. Three-dimensional model of purple membrane obtained by electron microscopy. *Nat 1975 2575521* **257**:28–32. doi:10.1038/257028a0

Hengge-Aronis R. 2002. Recent insights into the general stress response regulatory network in Escherichia coli. *J Mol Microbiol Biotechnol* **4**:341–346.

Henrich E, Peetz O, Hein C, Laguerre A, Hoffmann B, Hoffmann J, Dötsch V, Bernhard F, Morgner N. 2017. Analyzing native membrane protein assembly in nanodiscs by combined non-covalent mass spectrometry and synthetic biology. *Elife* **6**. doi:10.7554/ELIFE.20954

Herzik MA, Wu M, Lander GC. 2019. High-resolution structure determination of sub-100 kDa complexes using conventional cryo-EM. *Nat Commun* **10**. doi:10.1038/S41467-019-08991-8

Hess B, Bekker H, Berendsen HJC, Fraaije JGEM. 1997. LINCS: A linear constraint solver for molecular simulations. *J Comput Chem* **18**:1463–1472. doi:10.1002/(SICI)1096-987X(199709)18:12<1463::AID-JCC4>3.0.CO;2-H

Holm PJ, Bhakat P, Jegerschöld C, Gyobu N, Mitsuoka K, Fujiyoshi Y, Morgenstern R, Hebert H. 2006. Structural

basis for detoxification and oxidative stress protection in membranes. *J Mol Biol* **360**:934–945. doi:10.1016/J.JMB.2006.05.056

Hu W, Wang Z, Zheng H. 2021. Mechanosensitive channel YnaI has lipid-bound extended sensor paddles. *Commun Biol* **4**:602. doi:10.1038/s42003-021-02122-0

Humphrey W, Dalke A, Schulten K. 1996. VMD: Visual molecular dynamics. *J Mol Graph* **14**:33–38. doi:10.1016/0263-7855(96)00018-5

Huynh KW, Cohen MR, Jiang J, Samanta A, Lodowski DT, Zhou ZH, Moiseenkova-Bell VY. 2016. Structure of the full-length TRPV2 channel by cryo-EM. *Nat Commun 2016 71* **7**:1–8. doi:10.1038/ncomms11130

Ident and Sim. n.d. https://www.bioinformatics.org/sms2/ident_sim.html

Ilca SL, Kotecha A, Sun X, Poranen MM, Stuart DI, Huiskonen JT. 2015. Localized reconstruction of subunits from electron cryomicroscopy images of macromolecular complexes. *Nat Commun* **6**:8843. doi:10.1038/ncomms9843

Ilgü H, Jeckelmann JM, Gachet MS, Boggavarapu R, Ucurum Z, Gertsch J, Fotiadis D. 2014. Variation of the detergent-binding capacity and phospholipid content of membrane proteins when purified in different detergents. *Biophys J* **106**:1660–1670. doi:10.1016/j.bpj.2014.02.024

Inagaki S, Ghirlando R, Grisshammer R. 2013. Biophysical characterization of membrane proteins in nanodiscs. *Methods* **59**:287–300. doi:10.1016/J.YMETH.2012.11.006

Iosip AL, Böhm J, Scherzer S, Al-Rasheid KAS, Dreyer I, Schultz J, Becker D, Kreuzer I, Hedrich R. 2020. The Venus flytrap trigger hair–specific potassium channel KDM1 can reestablish the K+ gradient required for hapto-electric signaling. *PLOS Biol* **18**:e3000964. doi:10.1371/JOURNAL.PBIO.3000964

Iscla I, Wray R, Blount P. 2008. On the Structure of the N-Terminal Domain of the MscL Channel: Helical Bundle or Membrane Interface. *Biophys J* **95**:2283–2291. doi:10.1529/BIOPHYSJ.107.127423

Jakobi AJ, Wilmanns M, Sachse C. 2017. Model-based local density sharpening of cryo-EM maps. *Elife* **6**. doi:10.7554/ELIFE.27131

Javadpour MM, Eilers M, Groesbeek M, Smith SO. 1999. Helix Packing in Polytopic Membrane Proteins: Role of Glycine in Transmembrane Helix Association. *Biophys J* **77**:1609–1618. doi:10.1016/S0006-3495(99)77009-8

Jin P, Bulkley D, Guo Y, Zhang W, Guo Z, Huynh W, Wu S, Meltzer S, Cheng T, Jan LY, Jan Y-N, Cheng Y. 2017a. Electron cryo-microscopy structure of the mechanotransduction channel NOMPC. *Nat 2017 5477661* **547**:118–122. doi:10.1038/nature22981

Jin P, Bulkley D, Guo Y, Zhang W, Guo Z, Huynh W, Wu S, Meltzer S, Cheng T, Jan LY, Jan YN, Cheng Y. 2017b. Electron cryo-microscopy structure of the mechanotransduction channel NOMPC. *Nature* **547**:118–122. doi:10.1038/nature22981

Johnson RM, Fais C, Parmar M, Cheruvara H, Marshall RL, Hesketh SJ, Feasey MC, Ruggerone P, Vargiu A V., Postis VLG, Muench SP, Bavro VN. 2020. Cryo-EM structure and molecular dynamics analysis of the fluoroquinolone resistant mutant of the acrb transporter from salmonella. *Microorganisms* **8**:1–21. doi:10.3390/microorganisms8060943

Johnson ZL, Lee S-Y. 2015. Liposome reconstitution and transport assay for recombinant transporters. *Methods Enzymol* **556**:373–383. doi:10.1016/BS.MIE.2014.11.048

Jojoa-Cruz S, Saotome K, Murthy SE, Tsui CCA, Sansom MSP, Patapoutian A, Ward AB. 2018. Cryo-EM structure of the mechanically activated ion channel OSCA1.2. *Elife* **7**. doi:10.7554/ELIFE.41845

Jones DT. 1999. Protein secondary structure prediction based on position-specific scoring matrices. *J Mol Biol* **292**:195–202. doi:10.1006/jmbi.1999.3091

Jorgensen WL, Maxwell DS, Tirado-Rives J. 1996. Development and Testing of the OPLS All-Atom Force Field on Conformational Energetics and Properties of Organic Liquids. doi:10.1021/JA9621760

Julius D. 2013. TRP Channels and Pain. *Annu Rev Cell Dev Biol* **29**:355–384. doi:10.1146/ANNUREV-CELLBIO-101011-155833

Kampjut D, Steiner J, Sazanov LA. 2021. Cryo-EM grid optimization for membrane proteins. *iScience* **24**:102139. doi:10.1016/J.ISCI.2021.102139

Ke Z, Oton J, Qu K, Cortese M, Zila V, McKeane L, Nakane T, Zivanov J, Neufeldt CJ, Cerikan B, Lu JM, Peukes J, Xiong X, Kräusslich H-G, Scheres SHW, Bartenschlager R, Briggs JAG. 2020. Structures and distributions of SARS-CoV-2 spike proteins on intact virions. *Nat 2020 5887838* **588**:498–502. doi:10.1038/s41586-020-2665-2

Kefauver JM, Ward AB, Patapoutian A. 2020. Discoveries in structure and physiology of mechanically activated ion channels. *Nat 2020 5877835* **587**:567–576. doi:10.1038/s41586-020-2933-1

Kiefer H. 2003. In vitro folding of alpha-helical membrane proteins. *Biochim Biophys Acta* **1610**:57–62. doi:10.1016/S0005-2736(02)00717-4

Killian JA, Von Heijne G. 2000. How proteins adapt to a membrane–water interface. *Trends Biochem Sci* **25**:429–434. doi:10.1016/S0968-0004(00)01626-1

Kimanius D, Forsberg BO, Scheres SH, Lindahl E. 2016. Accelerated cryo-EM structure determination with

parallelisation using GPUs in RELION-2. *Elife* **5**. doi:10.7554/eLife.18722
Klesse G, Rao S, Sansom MSP, Tucker SJ. 2019. CHAP: A Versatile Tool for the Structural and Functional Annotation of Ion Channel Pores. *J Mol Biol* **431**:3353–3365. doi:10.1016/J.JMB.2019.06.003
Knol J, Veenhoff L, Liang WJ, Henderson PJF, Leblanc G, Poolman B. 1996. Unidirectional reconstitution into detergent-destabilized liposomes of the purified lactose transport system of Streptococcus thermophilus. *J Biol Chem* **271**:15358–15366. doi:10.1074/jbc.271.26.15358
Knowles TJ, Finka R, Smith C, Lin YP, Dafforn T, Overduin M. 2009. Membrane proteins solubilized intact in lipid containing nanoparticles bounded by styrene maleic acid copolymer. *J Am Chem Soc* **131**:7484–7485. doi:10.1021/ja810046q
Koçer A. 2015. Mechanisms of mechanosensing — mechanosensitive channels, function and re-engineering. *Curr Opin Chem Biol* **29**:120–127. doi:10.1016/J.CBPA.2015.10.006
Koçer A, Walko M, Bultern E, Halza E, Feringa BL, Meijberg W. 2006. Rationally designed chemical modulators convert a bacterial channel protein into a pH-sensory valve. *Angew Chem Int Ed Engl* **45**:3126–3130. doi:10.1002/ANIE.200503403
Koçer A, Walko M, Meijberg W, Feringa BL. 2005. A light-actuated nanovalve derived from a channel protein. *Science* **309**:755–758. doi:10.1126/SCIENCE.1114760
Koprowski P, Kubalski A. 1998. Voltage-independent adaptation of mechanosensitive channels in Escherichia coli protoplasts. *J Membr Biol* **164**:253–262. doi:10.1007/s002329900410
Kotov V, Bartels K, Veith K, Josts I, Subhramanyam UKT, Günther C, Labahn J, Marlovits TC, Moraes I, Tidow H, Löw C, Garcia-Alai MM. 2019. High-throughput stability screening for detergent-solubilized membrane proteins. *Sci Reports 2019 91* **9**:1–19. doi:10.1038/s41598-019-46686-8
Kucukelbir A, Sigworth FJ, Tagare HD. 2014. Quantifying the local resolution of cryo-EM density maps. *Nat Methods* **11**:63–65. doi:10.1038/nmeth.2727
Kühlbrandt W. 2014. The resolution revolution. *Science (80- )* **343**:1443–1444. doi:10.1126/science.1251652
Kühlbrandt W, Wang DN, Fujiyoshi Y. 1994. Atomic model of plant light-harvesting complex by electron crystallography. *Nat 1994 3676464* **367**:614–621. doi:10.1038/367614a0
Laemmli UK. 1970. Cleavage of structural proteins during the assembly of the head of bacteriophage T4. *Nature* **227**:680–685. doi:10.1038/227680a0
Lai JY, Poon YS, Kaiser JT, Rees DC. 2013. Open and shut: Crystal structures of the dodecylmaltoside solubilized mechanosensitive channel of small conductance from Escherichia coli and Helicobacter pylori at 4.4 Å and 4.1 Å resolutions. *Protein Sci* **22**:502–509. doi:10.1002/pro.2222
Le Maire M, Champeil P, Møller J V. 2000. Interaction of membrane proteins and lipids with solubilizing detergents. *Biochim Biophys Acta - Biomembr* **1508**:86–111. doi:10.1016/S0304-4157(00)00010-1
Lee AG. 2005. How lipids and proteins interact in a membrane: a molecular approach. *Mol Biosyst* **1**:203–212. doi:10.1039/B504527D
Lee CP, Maksaev G, Jensen GS, Murcha MW, Wilson ME, Fricker M, Hell R, Haswell ES, Millar AH, Sweetlove LJ. 2016. MSL1 is a mechanosensitive ion channel that dissipates mitochondrial membrane potential and maintains redox homeostasis in mitochondria during abiotic stress. *Plant J* **88**:809–825. doi:10.1111/TPJ.13301
Lee SC, Knowles TJ, Postis VLG, Jamshad M, Parslow RA, Lin YP, Goldman A, Sridhar P, Overduin M, Muench SP, Dafforn TR. 2016. A method for detergent-free isolation of membrane proteins in their local lipid environment. *Nat Protoc* **11**:1149–1162. doi:10.1038/nprot.2016.070
Levina N, Tötemeyer S, Stokes NR, Louis P, Jones MA, Booth IR. 1999. Protection of Escherichia coli cells against extreme turgor by activation of MscS and MscL mechanosensitive channels: Identification of genes required for MscS activity. *EMBO J* **18**:1730–1737. doi:10.1093/emboj/18.7.1730
Li C, Edwards MD, Jeong H, Roth J, Booth IR. 2007. Identification of mutations that alter the gating of the Escherichia coli mechanosensitive channel protein, MscK. *Mol Microbiol* **64**:560–574. doi:10.1111/j.1365-2958.2007.05672.x
Li Y, Hu Y, Wang J, Liu X, Zhang W, Sun L. 2020. Structural Insights into a Plant Mechanosensitive Ion Channel MSL1. *Cell Rep* **30**:4518-4527.e3. doi:10.1016/j.celrep.2020.03.026
Li Y, Moe PC, Chandrasekaran S, Booth IR, Blount P. 2002. Ionic regulation of MscK, a mechanosensitive channel from Escherichia coli **21**:5323–5330.
Liao M, Cao E, Julius D, Cheng Y. 2013. Structure of the TRPV1 ion channel determined by electron cryo-microscopy. *Nature* **504**:107–112. doi:10.1038/nature12822
Liu X, Wang J, Sun L. 2018. Structure of the hyperosmolality-gated calcium-permeable channel OSCA1.2. *Nat Commun 2018 91* **9**:1–9. doi:10.1038/s41467-018-07564-5
Lolicato M, Arrigoni C, Mori T, Sekioka Y, Bryant C, Clark KA, Minor DL. 2017. K2P2.1 (TREK-1)–activator complexes reveal a cryptic selectivity filter binding site. *Nat 2017 5477663* **547**:364–368. doi:10.1038/nature22988
Lolicato M, Riegelhaupt PM, Arrigoni C, Clark KA, Minor Jr. DL. 2014. Transmembrane helix straightening and

buckling underlies activation of mechanosensitive and thermosensitive K(2P) channels. *Neuron* **84**:1198–1212. doi:10.1016/J.NEURON.2014.11.017

Long AR, O'Brien CC, Malhotra K, Schwall CT, Albert AD, Watts A, Alder NN. 2013. A detergent-free strategy for the reconstitution of active enzyme complexes from native biological membranes into nanoscale discs. *BMC Biotechnol 2013 131* **13**:1–10. doi:10.1186/1472-6750-13-41

Loveland AB, Demo G, Grigorieff N, Korostelev AA. 2017. Ensemble cryo-EM elucidates the mechanism of translation fidelity. *Nat 2017 5467656* **546**:113–117. doi:10.1038/nature22397

Lyu P, Liff M, Marky L, Kallenbach N. 1990. Side chain contributions to the stability of alpha-helical structure in peptides. *Science (80- )* **250**:669–673. doi:10.1126/SCIENCE.2237416

Lyumkis D, Brilot AF, Theobald DL, Grigorieff N. 2013. Likelihood-based classification of cryo-EM images using FREALIGN. *J Struct Biol* **183**:377–388. doi:10.1016/J.JSB.2013.07.005

Madeira F, Park YM, Lee J, Buso N, Gur T, Madhusoodanan N, Basutkar P, Tivey ARN, Potter SC, Finn RD, Lopez R. 2019. The EMBL-EBI search and sequence analysis tools APIs in 2019. *Nucleic Acids Res* **47**:W636–W641. doi:10.1093/nar/gkz268

Maingret F, Patel AJ, Lesage F, Lazdunski M, Honoré E. 2000. Lysophospholipids open the two-pore domain mechano-gated K(+) channels TREK-1 and TRAAK. *J Biol Chem* **275**:10128–10133. doi:10.1074/JBC.275.14.10128

Maity K, Heumann JM, McGrath AP, Kopcho NJ, Hsu P-K, Lee C-W, Mapes JH, Garza D, Krishnan S, Morgan GP, Hendargo KJ, Klose T, Rees SD, Medrano-Soto A, Saier MH, Piñeros M, Komives EA, Schroeder JI, Chang G, Stowell MHB. 2019. Cryo-EM structure of OSCA1.2 from Oryza sativa elucidates the mechanical basis of potential membrane hyperosmolality gating. *Proc Natl Acad Sci* **116**:14309–14318. doi:10.1073/PNAS.1900774116

Malcolm HR, Blount P, Maurer JA. 2015. The mechanosensitive channel of small conductance (MscS) functions as a Jack-in-the box. *Biochim Biophys Acta* **1848**:159–166. doi:10.1016/J.BBAMEM.2014.10.022

Malcolm HR, Heo YY, Elmore DE, Maurer JA. 2011. Defining the role of the tension sensor in the mechanosensitive channel of small conductance. *Biophys J* **101**:345–352. doi:10.1016/j.bpj.2011.05.058

Malcolm HR, Maurer JA. 2012. The Mechanosensitive Channel of Small Conductance (MscS) Superfamily: Not Just Mechanosensitive Channels Anymore. *ChemBioChem* **13**:2037–2043. doi:10.1002/cbic.201200410

Malhotra K, Alder NN. 2014. Advances in the use of nanoscale bilayers to study membrane protein structure and function. *Biotechnol Genet Eng Rev* **30**:79–93. doi:10.1080/02648725.2014.921502

Martinac B. 2011. Bacterial Mechanosensitive Channels as a Paradigm for Mechanosensory Transduction. *Cell Physiol Biochem* **28**:1051–1060. doi:10.1159/000335842

Martinac B, Adler J, Kung C. 1990. Mechanosensitive ion channels of E. coli activated by amphipaths. *Nature* **348**:261–263. doi:10.1038/348261a0

Martinac B, Bavi N, Ridone P, Nikolaev YA, Martinac AD, Nakayama Y, Rohde PR, Bavi O. 2018. Tuning ion channel mechanosensitivity by asymmetry of the transbilayer pressure profile. *Biophys Rev* **10**:1377–1384. doi:10.1007/s12551-018-0450-3

Martinac B, Buechner M, Delcour AH, Adler J, Kung C. 1987. Pressure-sensitive ion channel in Escherichia coli. *Proc Natl Acad Sci U S A* **84**:2297–2301. doi:10.1073/pnas.84.8.2297

Martinac B, Cox CD. 2017. Mechanosensory Transduction: Focus on Ion Channels. *Ref Modul Life Sci*. doi:10.1016/B978-0-12-809633-8.08094-8

Martinac B, Nomura T, Chi G, Petrov E, Rohde PR, Battle AR, Foo A, Constantine M, Rothnagel R, Carne S, Deplazes E, Cornell B, Cranfield CG, Hankamer B, Landsberg MJ. 2013. Bacterial Mechanosensitive Channels: Models for Studying Mechanosensory Transduction. *Antioxid Redox Signal*. doi:10.1089/ars.2013.5471

Mastronarde DN. 2005. Automated electron microscope tomography using robust prediction of specimen movements. *J Struct Biol* **152**:36–51. doi:10.1016/j.jsb.2005.07.007

McMullan G, Chen S, Henderson R, Faruqi AR. 2009a. Detective quantum efficiency of electron area detectors in electron microscopy. *Ultramicroscopy* **109**:1126–43. doi:10.1016/j.ultramic.2009.04.002

McMullan G, Clark AT, Turchetta R, Faruqi AR. 2009b. Enhanced imaging in low dose electron microscopy using electron counting. *Ultramicroscopy* **109**:1411–6. doi:10.1016/j.ultramic.2009.07.004

McMullan G, Faruqi AR, Henderson R. 2016. Direct Electron Detectors. *Methods Enzymol* **579**:1–17. doi:10.1016/BS.MIE.2016.05.056

Merk A, Bartesaghi A, Banerjee S, Falconieri V, Rao P, Davis MI, Pragani R, Boxer MB, Earl LA, Milne JLS, Subramaniam S. 2016. Breaking Cryo-EM Resolution Barriers to Facilitate Drug Discovery. *Cell* **165**:1698–1707. doi:10.1016/j.cell.2016.05.040

Meyerson JR, Chittori S, Merk A, Rao P, Han TH, Serpe M, Mayer ML, Subramaniam S. 2016. Structural basis of kainate subtype glutamate receptor desensitization. *Nat 2016 5377621* **537**:567–571. doi:10.1038/nature19352

Miller S, Bartlett W, Chandrasekaran S, Simpson S, Edwards M, Booth IR. 2003a. Domain organization of the

MscS mechanosensitive channel of Escherichia coli. *EMBO J* **22**:36–46. doi:10.1093/emboj/cdg011
Miller S, Edwards MD, Ozdemir C, Booth IR. 2003b. The closed structure of the MscS mechanosensitive channel. Cross-linking of single cysteine mutants. *J Biol Chem* **278**:32246–50. doi:10.1074/jbc.M303188200
Moe P, Blount P. 2005. Assessment of Potential Stimuli for Mechano-Dependent Gating of MscL: Effects of Pressure, Tension, and Lipid Headgroups. *Biochemistry* **44**:12239–12244. doi:10.1021/bi0509649
Montell C. 2005. The TRP superfamily of cation channels. *Sci STKE* **2005**. doi:10.1126/STKE.2722005RE3
Morein S, Andersson AS, Rilfors L, Lindblom G. 1996. Wild-type Escherichia coli cells regulate the membrane lipid composition in a "window" between gel and non-lamellar structures. *J Biol Chem* **271**:6801–6809. doi:10.1074/jbc.271.12.6801
Morrison KA, Akram A, Mathews A, Khan ZA, Patel JH, Zhou C, Hardy DJ, Moore-Kelly C, Patel R, Odiba V, Knowles TJ, Javed M-U-H, Chmel NP, Dafforn TR, Rothnie AJ. 2016. Membrane protein extraction and purification using styrene-maleic acid (SMA) copolymer: effect of variations in polymer structure. *Biochem J* **473**:4349–4360. doi:10.1042/BCJ20160723
Murakami S, Nakashima R, Yamashita E, Yamaguchi A. 2002. Crystal structure of bacterial multidrug efflux transporter AcrB. *Nat 2002 4196907* **419**:587–593. doi:10.1038/nature01050
Murata K, Mitsuoka K, Hirai T, Walz T, Agre P, Heymann JB, Engel A, Fujiyoshi Y. 2000. Structural determinants of water permeation through aquaporin-1. *Nat 2000 4076804* **407**:599–605. doi:10.1038/35036519
Murthy SE, Dubin AE, Patapoutian A. 2017. Piezos thrive under pressure: mechanically activated ion channels in health and disease. *Nat Rev Mol Cell Biol 2017 1812* **18**:771–783. doi:10.1038/nrm.2017.92
Murthy SE, Dubin AE, Whitwam T, Jojoa-Cruz S, Cahalan SM, Mousavi SAR, Ward AB, Patapoutian A. 2018. OSCA/TMEM63 are an evolutionarily conserved family of mechanically activated ion channels. *Elife* **7**. doi:10.7554/ELIFE.41844
Naismith JH, Booth IR. 2012. Bacterial Mechanosensitive Channels—MscS: Evolution's Solution to Creating Sensitivity in Function. *Annu Rev Biophys* **41**:157–177. doi:10.1146/annurev-biophys-101211-113227
Nakane T, Kimanius D, Lindahl E, Scheres SHW. 2018. Characterisation of molecular motions in cryo-EM single-particle data by multi-body refinement in RELION. *Elife* **7**. doi:10.7554/ELIFE.36861
Nakane T, Scheres SHW. 2021. Multi-body Refinement of Cryo-EM Images in RELION. *Methods Mol Biol* **2215**:145–160. doi:10.1007/978-1-0716-0966-8_7
Naranjo D, Moldenhauer H, Pincuntureo M, Díaz-Franulic I. 2016. Pore size matters for potassium channel conductance. *J Gen Physiol* **148**:277. doi:10.1085/JGP.201611625
Naydenova K, Peet MJ, Russo CJ. 2019. Multifunctional graphene supports for electron cryomicroscopy. *Proc Natl Acad Sci* **116**:11718–11724. doi:10.1073/PNAS.1904766116
NEB Tm Calculator. n.d. https://tmcalculator.neb.com/#!/main
Nguyen THD, Galej WP, Bai X, Savva CG, Newman AJ, Scheres SHW, Nagai K. 2015. The architecture of the spliceosomal U4/U6.U5 tri-snRNP. *Nat 2015 5237558* **523**:47–52. doi:10.1038/nature14548
Nietlispach D, Gautier A. 2011. Solution NMR studies of polytopic α-helical membrane proteins. *Curr Opin Struct Biol* **21**:497–508. doi:10.1016/J.SBI.2011.06.009
Nogales E, Wolf SG, Downing KH. 1998. Structure of the αβ tubulin dimer by electron crystallography. *Nat 1998 3916663* **391**:199–203. doi:10.1038/34465
Nomura T, Cranfield CG, Deplazes E, Owen DM, Macmillan A, Battle AR, Constantine M, Sokabe M, Martinac B. 2012. Differential effects of lipids and lyso-lipids on the mechanosensitivity of the mechanosensitive channels MscL and MscS. *Proc Natl Acad Sci* **109**:8770–8775. doi:10.1073/pnas.1200051109
Nugent T, Jones DT. 2009. Transmembrane protein topology prediction using support vector machines. *BMC Bioinformatics* **10**. doi:10.1186/1471-2105-10-159
Oliver PM, Crooks JA, Leidl M, Yoon EJ, Saghatelian A, Weibel DB. 2014. Localization of anionic phospholipids in Escherichia coli cells. *J Bacteriol* **196**:3386–3398. doi:10.1128/JB.01877-14
Oluwole AO. 2017. Formation of lipid-bilayer nanodiscs by diisobutylene/maleic acid (DIBMA) copolymer. *Langmuir* **33**:14378–14388.
Oluwole AO, Danielczak B, Meister A, Babalola JO, Vargas C, Keller S. 2017. Solubilization of Membrane Proteins into Functional Lipid-Bilayer Nanodiscs Using a Diisobutylene/Maleic Acid Copolymer. *Angew Chemie Int Ed* **56**:1919–1924. doi:10.1002/anie.201610778
Orlova E V., Saibil HR. 2011. Structural Analysis of Macromolecular Assemblies by Electron Microscopy. *Chem Rev* **111**:7710–7748. doi:10.1021/cr100353t
Pace CN, Scholtz JM. 1998. A Helix Propensity Scale Based on Experimental Studies of Peptides and Proteins. *Biophys J* **75**:422–427. doi:10.1016/S0006-3495(98)77529-0
Pantelic RS, Meyer JC, Kaiser U, Baumeister W, Plitzko JM. 2010. Graphene oxide: A substrate for optimizing preparations of frozen-hydrated samples. *J Struct Biol* **170**:152–156. doi:10.1016/j.jsb.2009.12.020
Pantelic RS, Meyer JC, Kaiser U, Stahlberg H. 2012. The application of graphene as a sample support in transmission electron microscopy. *Solid State Commun* **152**:1375–1382. doi:10.1016/J.SSC.2012.04.038

Papadopoulos JS, Agarwala R. 2007. COBALT: Constraint-based alignment tool for multiple protein sequences. *Bioinformatics* **23**:1073–1079. doi:10.1093/bioinformatics/btm076

Parmar M, Rawson S, Scarff CA, Goldman A, Dafforn TR, Muench SP, Postis VLG. 2018. Using a SMALP platform to determine a sub-nm single particle cryo-EM membrane protein structure. *Biochim Biophys Acta - Biomembr* **1860**:378–383. doi:10.1016/J.BBAMEM.2017.10.005

Parrinello M, Rahman A. 1981. Polymorphic transitions in single crystals: A new molecular dynamics method. *J Appl Phys* **52**:7182–7190. doi:10.1063/1.328693

Perozo E, Cortes DM, Sompornpisut P, Kloda A, Martinac B. 2002a. Open channel structure of MscL and the gating mechanism of mechanosensitive channels. *Nature* **418**:942–948. doi:10.1038/nature00992

Perozo E, Kloda A, Cortes DM, Martinac B. 2002b. Physical principles underlying the transduction of bilayer deformation forces during mechanosensitive channel gating. *Nat Struct Biol* **9**:696–703. doi:10.1038/nsb827

Perozo E, Kloda A, Cortes DM, Martinac B. 2001. Site-Directed Spin-Labeling Analysis of Reconstituted Mscl in the Closed State. *J Gen Physiol* **118**:193–206. doi:10.1085/JGP.118.2.193

Perozo E, Marien Cortes D, Cuello LG. 1998. Three-dimensional architecture and gating mechanism of a K+ channel studied by EPR spectroscopy. *Nat Struct Biol*. doi:10.1038/nsb0698-459

Pettersen EF, Goddard TD, Huang CC, Couch GS, Greenblatt DM, Meng EC, Ferrin TE. 2004. UCSF Chimera - A visualization system for exploratory research and analysis. *J Comput Chem* **25**:1605–1612. doi:10.1002/jcc.20084

Pettersen EF, Goddard TD, Huang CC, Meng EC, Couch GS, Croll TI, Morris JH, Ferrin TE. 2021. UCSF ChimeraX: Structure visualization for researchers, educators, and developers. *Protein Sci* **30**:70–82. doi:10.1002/pro.3943

Peyronnet R, Tran D, Girault T, Frachisse J-M. 2014. Mechanosensitive channels: feeling tension in a world under pressure. *Front Plant Sci* **5**:558. doi:10.3389/fpls.2014.00558

Phillips R, Ursell T, Wiggins P, Sens P. 2009. Emerging roles for lipids in shaping membrane-protein function. *Nature*. doi:10.1038/nature08147

Pivetti CD, Yen M-R, Miller S, Busch W, Tseng Y-H, Booth IR, Saier MH, Jr. 2003. Two families of mechanosensitive channel proteins. *Microbiol Mol Biol Rev* **67**:66–85, table of contents. doi:10.1128/MMBR.67.1.66-85.2003

Pliotas C, Dahl ACE, Rasmussen T, Mahendran KR, Smith TK, Marius P, Gault J, Banda T, Rasmussen A, Miller S, Robinson C V, Bayley H, Sansom MSP, Booth IR, Naismith JH. 2015. The role of lipids in mechanosensation. *Nat Struct Mol Biol* **22**:991–8. doi:10.1038/nsmb.3120

Pliotas C, Ward R, Branigan E, Rasmussen A, Hagelueken G, Huang H, Black SS, Booth IR, Schiemann O, Naismith JH. 2012. Conformational state of the MscS mechanosensitive channel in solution revealed by pulsed electron-electron double resonance (PELDOR) spectroscopy. *Proc Natl Acad Sci* **109**:E2675–E2682. doi:10.1073/pnas.1202286109

Poget SF, Girvin ME. 2007. Solution NMR of membrane proteins in bilayer mimics: small is beautiful, but sometimes bigger is better. *Biochim Biophys Acta* **1768**:3098–3106. doi:10.1016/J.BBAMEM.2007.09.006

Pollock NL, Lee SC, Patel JH, Gulamhussein AA, Rothnie AJ. 2018. Structure and function of membrane proteins encapsulated in a polymer-bound lipid bilayer. *Biochim Biophys Acta - Biomembr* **1860**:809–817. doi:10.1016/J.BBAMEM.2017.08.012

Popot J-L. 2010. Amphipols, Nanodiscs, and Fluorinated Surfactants: Three Nonconventional Approaches to Studying Membrane Proteins in Aqueous Solutions. *Annu Rev Biochem* **79**:737–775. doi:10.1146/annurev.biochem.052208.114057

Popovic K, Holyoake J, Pomès R, Privé GG. 2012. Structure of saposin A lipoprotein discs. *Proc Natl Acad Sci* **109**:2908–2912. doi:10.1073/PNAS.1115743109

Postis V, Rawson S, Mitchell JK, Lee SC, Parslow RA, Dafforn TR, Baldwin SA, Muench SP. 2015. The use of SMALPs as a novel membrane protein scaffold for structure study by negative stain electron microscopy. *Biochim Biophys Acta - Biomembr* **1848**:496–501. doi:10.1016/j.bbamem.2014.10.018

Prabudiansyah I, Kusters I, Caforio A, Driessen AJM. 2015. Characterization of the annular lipid shell of the Sec translocon. *Biochim Biophys Acta - Biomembr* **1848**:2050–2056. doi:10.1016/J.BBAMEM.2015.06.024

Proverbio D, Roos C, Beyermann M, Orbán E, Dötsch V, Bernhard F. 2013. Functional properties of cell-free expressed human endothelin A and endothelin B receptors in artificial membrane environments. *Biochim Biophys Acta* **1828**:2182–2192. doi:10.1016/J.BBAMEM.2013.05.031

Qiu W, Fu Z, Xu GG, Grassucci RA, Zhang Y, Frank J, Hendrickson WA, Guo Y. 2018. Structure and activity of lipid bilayer within a membrane-protein transporter. *Proc Natl Acad Sci U S A* **115**:12985–12990. doi:10.1073/pnas.1812526115

Raetz CRH, Dowhan W. 1990. Biosynthesis and function of phospholipids in Escherichia coli. *J Biol Chem*. doi:10.1016/s0021-9258(19)40001-x

Rao S, Klesse G, Stansfeld PJ, Tucker SJ, Sansom MSP. 2019. A heuristic derived from analysis of the ion channel

structural proteome permits the rapid identification of hydrophobic gates. *Proc Natl Acad Sci U S A* **116**:13989–13995. doi:10.1073/pnas.1902702116

Rasmussen A, Rasmussen T, Edwards MD, Schauer D, Schumann U, Miller S, Booth IR. 2007. The role of tryptophan residues in the function and stability of the mechanosensitive channel MscS from Escherichia coli. *Biochemistry* **46**:10899–10908. doi:10.1021/bi701056k

Rasmussen T. 2016. How do mechanosensitive channels sense membrane tension? *Biochem Soc Trans* **44**:1019–1025. doi:10.1042/BST20160018

Rasmussen T, Edwards MD, Black SS, Rasmussen A, Miller S, Booth IR. 2010. Tryptophan in the pore of the mechanosensitive channel MscS: Assessment of pore conformations by fluorescence spectroscopy. *J Biol Chem* **285**:5377–5384. doi:10.1074/jbc.M109.071472

Rasmussen T, Flegler VJ, Rasmussen A, Böttcher B. 2019a. Structure of the Mechanosensitive Channel MscS Embedded in the Membrane Bilayer. *J Mol Biol* **431**:3081–3090. doi:10.1016/j.jmb.2019.07.006

Rasmussen T, Rasmussen A. 2018. Bacterial mechanosensitive channels, Subcellular Biochemistry. doi:10.1007/978-981-10-7757-9_4

Rasmussen T, Rasmussen A, Singh S, Galbiati H, Edwards MD, Miller S, Booth IR. 2015. Properties of the Mechanosensitive Channel MscS Pore Revealed by Tryptophan Scanning Mutagenesis. *Biochemistry* **54**:4519–30. doi:10.1021/acs.biochem.5b00294

Rasmussen T, Rasmussen A, Yang L, Kaul C, Black S, Galbiati H, Conway SJ, Miller S, Blount P, Booth IR. 2019b. Interaction of the Mechanosensitive Channel, MscS, with the Membrane Bilayer through Lipid Intercalation into Grooves and Pockets. *J Mol Biol* **431**:3339–3352. doi:10.1016/j.jmb.2019.05.043

Rath A, Glibowicka M, Nadeau VG, Chen G, Deber CM. 2009. Detergent binding explains anomalous SDS-PAGE migration of membrane proteins. *Proc Natl Acad Sci U S A* **106**:1760–1765. doi:10.1073/pnas.0813167106

Reddy B, Bavi N, Lu A, Park Y, Perozo E. 2019. Molecular basis of force-from-lipids gating in the mechanosensitive channel mscs. *Elife* **8**. doi:10.7554/eLife.50486

Renthal R. 2006. An unfolding story of helical transmembrane proteins. *Biochemistry* **45**:14559–14566. doi:10.1021/bi0620454

Ridone P, Grage SL, Patkunarajah A, Battle AR, Ulrich AS, Martinac B. 2018. "Force-from-lipids" gating of mechanosensitive channels modulated by PUFAs. *J Mech Behav Biomed Mater* **79**:158–167. doi:10.1016/J.JMBBM.2017.12.026

Rigaud JL, Pitard B, Levy D. 1995. Reconstitution of membrane proteins into liposomes: application to energy-transducing membrane proteins. *Biochim Biophys Acta - Bioenerg* **1231**:223–246. doi:10.1016/0005-2728(95)00091-V

Rohou A, Grigorieff N. 2015. CTFFIND4: Fast and accurate defocus estimation from electron micrographs. *J Struct Biol* **192**:216–221. doi:10.1016/j.jsb.2015.08.008

Ruskin RS, Yu Z, Grigorieff N. 2013. Quantitative characterization of electron detectors for transmission electron microscopy. *J Struct Biol* **184**:385–393. doi:10.1016/J.JSB.2013.10.016

Russo CJ, Passmore LA. 2014. Controlling protein adsorption on graphene for cryo-EM using low-energy hydrogen plasmas. *Nat Methods* **11**:649–652. doi:10.1038/nmeth.2931

Sanders CR, Hare BJ, Howard KP, Prestegard JH. 1994. Magnetically-oriented phospholipid micelles as a tool for the study of membrane-associated molecules. *Prog Nucl Magn Reson Spectrosc* **26**:421–444. doi:10.1016/0079-6565(94)80012-X

Sanders CR, Prosser RS. 1998. Bicelles: a model membrane system for all seasons? *Structure* **6**:1227–1234. doi:10.1016/S0969-2126(98)00123-3

Sanders CR, Sönnichsen F. 2006. Solution NMR of membrane proteins: practice and challenges. *Magn Reson Chem* **44 Spec No**. doi:10.1002/MRC.1816

Saotome K, Murthy SE, Kefauver JM, Whitwam T, Patapoutian A, Ward AB. 2017. Structure of the mechanically activated ion channel Piezo1. *Nat 2018 5547693* **554**:481–486. doi:10.1038/nature25453

Saponaro A, Bauer D, Giese MH, Swuec P, Porro A, Gasparri F, Sharifzadeh AS, Chaves-Sanjuan A, Alberio L, Parisi G, Cerutti G, Clarke OB, Hamacher K, Colecraft HM, Mancia F, Hendrickson WA, Siegelbaum SA, DiFrancesco D, Bolognesi M, Thiel G, Santoro B, Moroni A. 2021. Gating movements and ion permeation in HCN4 pacemaker channels. *Mol Cell* **81**:2929-2943.e6. doi:10.1016/J.MOLCEL.2021.05.033

Sauer DB, Trebesch N, Marden JJ, Cocco N, Song J, Koide A, Koide S, Tajkhorshid E, Wang DN. 2020. Structural basis for the reaction cycle of dass dicarboxylate transporters. *Elife* **9**:1–74. doi:10.7554/ELIFE.61350

Scheres SHW. 2016. Processing of Structurally Heterogeneous Cryo-EM Data in RELION. *Methods Enzymol*. doi:10.1016/bs.mie.2016.04.012

Scheres SHW. 2014. Beam-induced motion correction for sub-megadalton cryo-EM particles. *Elife* **3**:e03665. doi:10.7554/eLife.03665

Scheres SHW. 2012. RELION: Implementation of a Bayesian approach to cryo-EM structure determination. *J Struct Biol* **180**:519–530. doi:10.1016/j.jsb.2012.09.006

Scheres SHW, Chen S. 2012. Prevention of overfitting in cryo-EM structure determination. *Nat Methods* **9**:853–854. doi:10.1038/nmeth.2115

Scheres SHW, Gao H, Valle M, Herman GT, Eggermont PPB, Frank J, Carazo J-M. 2006. Disentangling conformational states of macromolecules in 3D-EM through likelihood optimization. *Nat Methods 2007 41* **4**:27–29. doi:10.1038/nmeth992

Scheres SHW, Valle M, Nuñez R, Sorzano COS, Marabini R, Herman GT, Carazo JM. 2005. Maximum-likelihood Multi-reference Refinement for Electron Microscopy Images. *J Mol Biol* **348**:139–149. doi:10.1016/J.JMB.2005.02.031

Schumann U, Edwards MD, Li C, Booth IR. 2004. The conserved carboxy-terminus of the MscS mechanosensitive channel is not essential but increases stability and activity. *FEBS Lett* **572**:233–237. doi:10.1016/j.febslet.2004.07.045

Schumann U, Edwards MD, Rasmussen T, Bartlett W, Van West P, Booth IR. 2010. YbdG in Escherichia coli is a threshold-setting mechanosensitive channel with MscM activity. *Proc Natl Acad Sci U S A* **107**:12664–12669. doi:10.1073/pnas.1001405107

Schur FKM, Dick RA, Hagen WJH, Vogt VM, Briggs JAG. 2015. The Structure of Immature Virus-Like Rous Sarcoma Virus Gag Particles Reveals a Structural Role for the p10 Domain in Assembly. *J Virol* **89**:10294–302. doi:10.1128/JVI.01502-15

Schur FKM, Obr M, Hagen WJH, Wan W, Jakobi AJ, Kirkpatrick JM, Sachse C, Kräusslich H-G, Briggs JAG. 2016. An atomic model of HIV-1 capsid-SP1 reveals structures regulating assembly and maturation. *Science* **353**:506–8. doi:10.1126/science.aaf9620

Schwendener RA. 2014. Liposomes as vaccine delivery systems: a review of the recent advances. *Ther Adv vaccines* **2**:159–182. doi:10.1177/2051013614541440

Seddon AM, Curnow P, Booth PJ. 2004. Membrane proteins, lipids and detergents: not just a soap opera. *Biochim Biophys Acta - Biomembr* **1666**:105–117. doi:10.1016/J.BBAMEM.2004.04.011

Serna M. 2019. Hands on Methods for High Resolution Cryo-Electron Microscopy Structures of Heterogeneous Macromolecular Complexes. *Front Mol Biosci* **0**:33. doi:10.3389/FMOLB.2019.00033

Shapovalov G, Lester HA. 2004. Gating transitions in bacterial ion channels measured at 3 μs resolution. *J Gen Physiol* **124**:151–161. doi:10.1085/jgp.200409087

Shortle D, DiMaio D, Nathans D. 1981. Directed Mutagenesis. *Annu Rev Genet* **15**:265–294. doi:10.1146/annurev.ge.15.120181.001405

Sigworth FJ. 1998. A Maximum-Likelihood Approach to Single-Particle Image Refinement. *J Struct Biol* **122**:328–339. doi:10.1006/JSBI.1998.4014

Skipski VP. 1975. Thin-Layer Chromatography of Neutral Glycosphingolipids. *Methods Enzymol*. doi:10.1016/0076-6879(75)35178-1

Skipski VP, Peterson RF, Barclay M. 1964. Quantitative analysis of phospholipids by thin-layer chromatography. *Biochem J* **90**:374–378. doi:10.1042/bj0900374

Skrzypek R, Iqbal S, Callaghan R. 2018. Methods of reconstitution to investigate membrane protein function. *Methods* **147**:126–141. doi:10.1016/j.ymeth.2018.02.012

Slotboom DJ, Duurkens RH, Olieman K, Erkens GB. 2008. Static light scattering to characterize membrane proteins in detergent solution. *Methods* **46**:73–82. doi:10.1016/J.YMETH.2008.06.012

Sokabe M, Sachs F, Jing ZQ. 1991. Quantitative video microscopy of patch clamped membranes stress, strain, capacitance, and stretch channel activation. *Biophys J* **59**:722–728. doi:10.1016/S0006-3495(91)82285-8

Song B, Lenhart J, Flegler VJ, Makbul C, Rasmussen T, Böttcher B. 2019. Capabilities of the Falcon III detector for single-particle structure determination. *Ultramicroscopy* **203**:145–154. doi:10.1016/J.ULTRAMIC.2019.01.002

Song Y, Zhang B, Guo F, Yang M, Li Y, Liu Z-Q. 2017. Identification of Intracellular β-Barrel Residues Involved in Ion Selectivity in the Mechanosensitive Channel of Thermoanaerobacter tengcongensis. *Front Physiol* **0**:832. doi:10.3389/FPHYS.2017.00832

Sotomayor M, Schulten K. 2004. Molecular dynamics study of gating in the mechanosensitive channel of small conductance MscS. *Biophys J* **87**:3050–3065. doi:10.1529/biophysj.104.046045

Sotomayor M, Straaten TA van der, Ravaioli U, Schulten K. 2006. Electrostatic Properties of the Mechanosensitive Channel of Small Conductance MscS. *Biophys J* **90**:3496–3510. doi:10.1529/BIOPHYSJ.105.080069

Spencer RH, Chang G, Rees DC. 1999. 'Feeling the pressure': structural insights into a gated mechanosensitive channel. *Curr Opin Struct Biol* **9**:448–454. doi:10.1016/S0959-440X(99)80063-3

Stansfeld PJ, Goose JE, Caffrey M, Carpenter EP, Parker JL, Newstead S, Sansom MSP. 2015. MemProtMD: Automated Insertion of Membrane Protein Structures into Explicit Lipid Membranes. *Structure* **23**:1350–1361. doi:10.1016/J.STR.2015.05.006

Stark H, Chari A. 2016. Sample preparation of biological macromolecular assemblies for the determination of high-resolution structures by cryo-electron microscopy. *Microscopy* **65**:23–34. doi:10.1093/jmicro/dfv367

Stark H, Zemlin F, Boettcher C. 1996. Electron radiation damage to protein crystals of bacteriorhodopsin at different temperatures. *Ultramicroscopy* **63**:75–79. doi:10.1016/0304-3991(96)00045-9

Startek JB, Boonen B, Talavera K, Meseguer V. 2019. TRP Channels as Sensors of Chemically-Induced Changes in Cell Membrane Mechanical Properties. *Int J Mol Sci* **20**. doi:10.3390/IJMS20020371

Steinbacher S, Bass R, Strop P, Rees DC. 2007. Structures of the Prokaryotic Mechanosensitive Channels MscL and MscS. *Curr Top Membr* **58**:1–24. doi:10.1016/S1063-5823(06)58001-9

Stetsenko A, Guskov A. 2017. An Overview of the Top Ten Detergents Used for Membrane Protein Crystallization. *Cryst 2017, Vol 7, Page 197* **7**:197. doi:10.3390/CRYST7070197

Sukharev S. 2002. Purification of the small mechanosensitive channel of Escherichia coli (MscS): The subunit structure, conduction, and gating characteristics in liposomes. *Biophys J* **83**:290–298. doi:10.1016/S0006-3495(02)75169-2

Sukharev S, Durell SR, Guy HR. 2001. Structural Models of the MscL Gating Mechanism. *Biophys J* **81**:917–936. doi:10.1016/S0006-3495(01)75751-7

Sukharev SI, Blount P, Martinac B, Kung C. 1997. Mechanosensitive channels of Escherichia coli: The MscL gene, protein, and activities. *Annu Rev Physiol*. doi:10.1146/annurev.physiol.59.1.633

Sukharev SI, Martinac B, Arshavsky VY, Kung C. 1993. Two types of mechanosensitive channels in the Escherichia coli cell envelope: solubilization and functional reconstitution. *Biophys J* **65**:177–183. doi:10.1016/S0006-3495(93)81044-0

Sukharev SI, Sigurdson WJ, Kung C, Sachs F. 1999. Energetic and spatial parameters for gating of the bacterial large conductance mechanosensitive channel, MscL. *J Gen Physiol* **113**:525–539. doi:10.1085/JGP.113.4.525

Sun C, Benlekbir S, Venkatakrishnan P, Wang Y, Hong S, Hosler J, Tajkhorshid E, Rubinstein JL, Gennis RB. 2018. Structure of the alternative complex III in a supercomplex with cytochrome oxidase. *Nature* **557**:123–126. doi:10.1038/s41586-018-0061-y

Sun L, Zhao L, Yang G, Yan C, Zhou R, Zhou X, Xie T, Zhao Y, Wu S, Li X, Shi Y. 2015. Structural basis of human γ-secretase assembly. *Proc Natl Acad Sci* **112**:6003–6008. doi:10.1073/PNAS.1506242112

Swainsbury DJK, Scheidelaar S, Foster N, van Grondelle R, Killian JA, Jones MR. 2017. The effectiveness of styrene-maleic acid (SMA) copolymers for solubilisation of integral membrane proteins from SMA-accessible and SMA-resistant membranes. *Biochim Biophys Acta - Biomembr* **1859**:2133–2143. doi:10.1016/j.bbamem.2017.07.011

Tascón I, Sousa JS, Corey RA, Mills DJ, Griwatz D, Aumüller N, Mikusevic V, Stansfeld PJ, Vonck J, Hänelt I. 2020. Structural basis of proton-coupled potassium transport in the KUP family. *Nat Commun* **11**:1–10. doi:10.1038/s41467-020-14441-7

Taylor KA, Glaeser RM. 2008. Retrospective on the early development of cryoelectron microscopy of macromolecules and a prospective on opportunities for the future. *J Struct Biol* **163**:214–223. doi:10.1016/j.jsb.2008.06.004

Taylor KA, Glaeser RM. 1974. cc. *Science* **186**:1036–1037. doi:10.1126/SCIENCE.186.4168.1036

Teng J, Loukin S, Anishkin A, Kung C. 2015. The force-from-lipid (FFL) principle of mechanosensitivity, at large and in elements. *Pflugers Arch - Eur J Physiol* **467**:27–37. doi:10.1007/s00424-014-1530-2

Thor K, Jiang S, Michard E, George J, Scherzer S, Huang S, Dindas J, Derbyshire P, Leitão N, DeFalco TA, Köster P, Hunter K, Kimura S, Gronnier J, Stransfeld L, Kadota Y, Bücherl CA, Charpentier M, Wrzaczek M, MacLean D, Oldroyd GED, Menke FLH, Roelfsema MRG, Hedrich R, Feijó J, Zipfel C. 2020. The calcium-permeable channel OSCA1.3 regulates plant stomatal immunity. *Nat 2020 5857826* **585**:569–573. doi:10.1038/s41586-020-2702-1

Tivol WF, Briegel A, Jensen GJ. 2008. An Improved Cryogen for Plunge Freezing. *Microsc Microanal* **14**:375. doi:10.1017/S1431927608080781

Tonge SR, Tighe BJ. 2001. Responsive hydrophobically associating polymers: a review of structure and properties. *Adv Drug Deliv Rev* **53**:109–122. doi:10.1016/S0169-409X(01)00223-X

Towbin H, Staehelin T, Gordon J. 1979. Electrophoretic transfer of proteins from polyacrylamide gels to nitrocellulose sheets: Procedure and some applications. *Proc Natl Acad Sci U S A* **76**:4350–4354. doi:10.1073/pnas.76.9.4350

Tribet C, Audebert R, Popot JL. 1996. Amphipols: Polymers that keep membrane proteins soluble in aqueous solutions. *Proc Natl Acad Sci U S A* **93**:15047–15050. doi:10.1073/pnas.93.26.15047

UniProtKB. n.d. https://www.uniprot.org/uniprot/

Unwin PNT, Henderson R. 1975. Molecular structure determination by electron microscopy of unstained crystalline specimens. *J Mol Biol* **94**:425–440. doi:10.1016/0022-2836(75)90212-0

van Bruggen EFJ, Wiebenga EH, Gruber M. 1960. Negative-staining electron microscopy of proteins at pH values below their isoelectric points. Its application to hemocyanin. *BBA - Biochim Biophys Acta* **42**:171–172. doi:10.1016/0006-3002(60)90771-X

Van Heel M. 1987. Angular reconstitution: a posteriori assignment of projection directions for 3D reconstruction.

*Ultramicroscopy* **21**:111–123.

Vargas C, Arenas RC, Frotscher E, Keller S. 2015. Nanoparticle self-assembly in mixtures of phospholipids with styrene/maleic acid copolymers or fluorinated surfactants. *Nanoscale* **7**:20685–20696. doi:10.1039/C5NR06353A

Vásquez V, Sotomayor M, Cordero-Morales J, Schulten K, Perozo E. 2008a. A structural mechanism for MscS gating in lipid bilayers. *Science (80- )* **321**:1210–1214. doi:10.1126/science.1159674

Vásquez V, Sotomayor M, Cortes DM, Roux B, Schulten K, Perozo E. 2008b. Three-dimensional architecture of membrane-embedded MscS in the closed conformation. *J Mol Biol* **378**:55–70. doi:10.1016/J.JMB.2007.10.086

Veley KM, Maksaev G, Frick EM, January E, Kloepper SC, Haswell ES. 2014. Arabidopsis MSL10 Has a Regulated Cell Death Signaling Activity That Is Separable from Its Mechanosensitive Ion Channel Activity. *Plant Cell* **26**:3115–3131. doi:10.1105/TPC.114.128082

Vestergaard M, Kraft JF, Vosegaard T, Thøgersen L, Schiøtt B. 2015. Bicelles and Other Membrane Mimics: Comparison of Structure, Properties, and Dynamics from MD Simulations. *J Phys Chem B* **119**:15831–15843. doi:10.1021/ACS.JPCB.5B08463

Vinothkumar KR. 2015. Membrane protein structures without crystals, by single particle electron cryomicroscopy. *Curr Opin Struct Biol* **33**:103–114. doi:10.1016/J.SBI.2015.07.009

von Heijne G. 2006. Membrane-protein topology. *Nat Rev Mol Cell Biol 2006 712* **7**:909–918. doi:10.1038/nrm2063

von Heijne G. 1999. Recent advances in the understanding of membrane protein assembly and structure. *Q Rev Biophys* **32**:285–307. doi:10.1017/S0033583500003541

von Heijne G. 1992. Membrane protein structure prediction: Hydrophobicity analysis and the positive-inside rule. *J Mol Biol* **225**:487–494. doi:10.1016/0022-2836(92)90934-C

Wagner T, Merino F, Stabrin M, Moriya T, Antoni C, Apelbaum A, Hagel P, Sitsel O, Raisch T, Prumbaum D, Quentin D, Roderer D, Tacke S, Siebolds B, Schubert E, Shaikh TR, Lill P, Gatsogiannis C, Raunser S. 2019. SPHIRE-crYOLO is a fast and accurate fully automated particle picker for cryo-EM. *Commun Biol* **2**:218. doi:10.1038/s42003-019-0437-z

Walker RG, Willingham AT, Zuker CS. 2000. A Drosophila mechanosensory transduction channel. *Science* **287**:2229–2234. doi:10.1126/SCIENCE.287.5461.2229

Wallin E, von Heijne G. 1998. Genome-wide analysis of integral membrane proteins from eubacterial, archaean, and eukaryotic organisms. *Protein Sci* **7**:1029–1038. doi:10.1002/PRO.5560070420

Wang L, Heng Z, Mingmin Z, Wenhao L, Tuan D, Qiancheng Z, Yiran L, Jianlin L, Xueming L, Bailong X. 2019. Structure and mechanogating of the mammalian tactile channel PIEZO2. *Nature* **573**:225–229. doi:10.1038/s41586-019-1505-8

Wang W, Black SS, Edwards MD, Miller S, Morrison EL, Bartlett W, Dong C, Naismith JH, Booth IR. 2008. The structure of an open form of an E. coli mechanosensitive channel at 3.45 å resolution. *Science (80- )* **321**:1179–1183. doi:10.1126/science.1159262

Wang X, Mu Z, Li Y, Bi Y, Wang Y. 2015. Smaller Nanodiscs are Suitable for Studying Protein Lipid Interactions by Solution NMR. *Protein J* **34**:205–211. doi:10.1007/S10930-015-9613-2

Wang Y, Liu Y, DeBerg HA, Nomura T, Hoffman MT, Rohde PR, Schulten K, Martinac B, Selvin PR. 2014. Single molecule FRET reveals pore size and opening mechanism of a mechano-sensitive ion channel. *Elife* **3**. doi:10.7554/ELIFE.01834

Wang ZL, Heerden D van, Josell D, Shapiro AJ. 1997. Energy-Filtered High-Resolution Electron Microscopy for Quantitative Solid State Structure Determination. *J Res Natl Inst Stand Technol* **102**:1. doi:10.6028/JRES.102.002

Ward R, Pliotas C, Branigan E, Hacker C, Rasmussen A, Hagelueken G, Booth IR, Miller S, Lucocq J, Naismith JH, Schiemann O. 2014. Probing the structure of the mechanosensitive channel of small conductance in lipid bilayers with pulsed electron-electron double resonance. *Biophys J* **106**:834–842. doi:10.1016/j.bpj.2014.01.008

Weaver SJ, Ortega DR, Sazinsky MH, Dalia TN, Dalia AB, Jensen GJ. 2020. CryoEM structure of the type IVa pilus secretin required for natural competence in Vibrio cholerae. *Nat Commun 2020 111* **11**:1–13. doi:10.1038/s41467-020-18866-y

Wiggins P, Phillips R. 2005. Membrane-Protein Interactions in Mechanosensitive Channels. *Biophys J* **88**:880–902. doi:10.1529/BIOPHYSJ.104.047431

Wilson ME, Maksaev G, Haswell ES. 2013. MscS-Like Mechanosensitive Channels in Plants and Microbes. *Biochemistry* **52**:5708. doi:10.1021/BI400804Z

Winardhi RS, Tang Q, You H, Sheetz M, Yan J. 2018. The holdase function of Escherichia coli Hsp70 (DnaK) chaperone. *bioRxiv* 305854. doi:10.1101/305854

Wu J, Yan Z, Li Z, Qian X, Lu S, Dong M, Zhou Q, Yan N. 2016. Structure of the voltage-gated calcium channel Cav1.1 at 3.6 Å resolution. *Nat 2016 5377619* **537**:191–196. doi:10.1038/nature19321

Xue F, Cox CD, Bavi N, Rohde PR, Nakayama Y, Martinac B. 2020. Membrane stiffness is one of the key determinants of E. coli MscS channel mechanosensitivity. *Biochim Biophys Acta - Biomembr* **1862**:183203. doi:10.1016/J.BBAMEM.2020.183203

Yan Z, Bai X, Yan C, Wu J, Li Z, Xie T, Peng W, Yin C, Li X, Scheres SHW, Shi Y, Yan N. 2014. Structure of the rabbit ryanodine receptor RyR1 at near-atomic resolution. *Nat 2014 5177532* **517**:50–55. doi:10.1038/nature14063

Yang Z, Wang C, Zhou Q, An J, Hildebrandt E, Aleksandrov LA, Kappes JC, DeLucas LJ, Riordan JR, Urbatsch IL, Hunt JF, Brouillette CG. 2014. Membrane protein stability can be compromised by detergent interactions with the extramembranous soluble domains. *Protein Sci* **23**:769–789. doi:10.1002/PRO.2460

Yip KM, Fischer N, Paknia E, Chari A, Stark H. 2020. Atomic-resolution protein structure determination by cryo-EM. *Nat 2020 5877832* **587**:157–161. doi:10.1038/s41586-020-2833-4

Yoder N, Gouaux E. 2020. The his-gly motif of acid-sensing ion channels resides in a reentrant 'loop' implicated in gating and ion selectivity. *Elife* **9**:1–18. doi:10.7554/eLife.56527

Yoo J, Cui Q. 2009. Curvature Generation and Pressure Profile Modulation in Membrane by Lysolipids: Insights from Coarse-Grained Simulations. *Biophys J* **97**:2267–2276. doi:10.1016/J.BPJ.2009.07.051

Yu J, Zhang B, Zhang Y, Xu C qiao, Zhuo W, Ge J, Li J, Gao N, Li Y, Yang M. 2018. A binding-block ion selective mechanism revealed by a Na/K selective channel. *Protein Cell* **9**:629–639. doi:10.1007/s13238-017-0465-8

Yu J, Zhu H, Lape R, Greiner T, Du J, Lü W, Sivilotti L, Gouaux E. 2021. Mechanism of gating and partial agonist action in the glycine receptor. *Cell* **184**:957-968.e21. doi:10.1016/j.cell.2021.01.026

Yuan F, Yang H, Xue Y, Kong D, Ye R, Li C, Zhang J, Theprungsirikul Ly, Shrift T, Krichilsky B, Johnson DM, Swift GB, He Y, Siedow JN, Pei Z-M. 2014. OSCA1 mediates osmotic-stress-evoked Ca2+ increases vital for osmosensing in Arabidopsis. *Nature* **514**:367–371. doi:10.1038/NATURE13593

Zalk R, Clarke OB, des Georges A, Grassucci RA, Reiken S, Mancia F, Hendrickson WA, Frank J, Marks AR. 2014. Structure of a mammalian ryanodine receptor. *Nat 2014 5177532* **517**:44–49. doi:10.1038/nature13950

Zhang M, Wang D, Kang Y, Wu J-X, Yao F, Pan C, Yan Z, Song C, Chen L. 2018. Structure of the mechanosensitive OSCA channels. *Nat Struct Mol Biol* **25**:850–858. doi:10.1038/S41594-018-0117-6

Zhang S, Li N, Zeng W, Gao N, Yang M. 2017. Cryo-EM structures of the mammalian endo-lysosomal TRPML1 channel elucidate the combined regulation mechanism. *Protein Cell 2017 811* **8**:834–847. doi:10.1007/S13238-017-0476-5

Zhang W, Cheng LE, Kittelmann M, Li J, Petkovic M, Cheng T, Jin P, Guo Z, Göpfert MC, Jan LY, Jan YN. 2015. Ankyrin Repeats Convey Force to Gate the NOMPC Mechanotransduction Channel. *Cell* **162**:1391. doi:10.1016/J.CELL.2015.08.024

Zhang X, Jin L, Fang Q, Hui WH, Zhou ZH. 2010. 3.3 Å Cryo-EM Structure of a Nonenveloped Virus Reveals a Priming Mechanism for Cell Entry. *Cell* **141**:472–482. doi:10.1016/J.CELL.2010.03.041

Zhang X, Wang J, Feng Y, Ge J. 2012. Structure and molecular mechanism of an anion-selective mechanosensitive channel of small conductance. *Proc Natl Acad Sci U S A*.

Zhang XC, Liu Z, Li J. 2016. From membrane tension to channel gating: A principal energy transfer mechanism for mechanosensitive channels. *Protein Sci* **25**:1954. doi:10.1002/PRO.3017

Zhang Y, Daday C, Gu R-X, Cox CD, Martinac B, de Groot BL, Walz T. 2021. Visualization of the mechanosensitive ion channel MscS under membrane tension. *Nature* 1–6. doi:10.1038/s41586-021-03196-w

Zhang Z, Tateda C, Jiang S-C, Shrestha J, Jelenska J, Speed DJ, Greenberg JT. 2017. A Suite of Receptor-Like Kinases and a Putative Mechano-Sensitive Channel Are Involved in Autoimmunity and Plasma Membrane–Based Defenses in Arabidopsis. *http://dx.doi.org/101094/MPMI-09-16-0184-R* **30**:150–160. doi:10.1094/MPMI-09-16-0184-R

Zhao J, Benlekbir S, Rubinstein JL. 2015. Electron cryomicroscopy observation of rotational states in a eukaryotic V-ATPase. *Nat 2015 5217551* **521**:241–245. doi:10.1038/nature14365

Zhao Q, Zhou H, Chi S, Wang Y, Wang Jianhua, Geng J, Wu K, Liu W, Zhang T, Dong MQ, Wang Jiawei, Li X, Xiao B. 2018. Structure and mechanogating mechanism of the Piezo1 channel. *Nature* **554**:487–492. doi:10.1038/nature25743

Zheng SQ, Palovcak E, Armache J-P, Verba KA, Cheng Y, Agard DA. 2017. MotionCor2: anisotropic correction of beam-induced motion for improved cryo-electron microscopy. *Nat Methods* **14**:331–332. doi:10.1038/nmeth.4193

Zivanov J, Nakane T, Forsberg BO, Kimanius D, Hagen WJ, Lindahl E, Scheres SH. 2018. New tools for automated high-resolution cryo-EM structure determination in RELION-3. *Elife* **7**. doi:10.7554/eLife.42166

Zoonens M, Popot JL. 2014. Amphipols for Each Season. *J Membr Biol* **247**:759–796. doi:10.1007/s00232-014-9666-8

Zubcevic L, Herzik MA, Chung BC, Liu Z, Lander GC, Lee S-Y. 2016. Cryo-electron microscopy structure of the TRPV2 ion channel. *Nat Struct Mol Biol 2015 232* **23**:180–186. doi:10.1038/nsmb.3159

Zubcevic L, Hsu AL, Borgnia MJ, Lee SY. 2019. Symmetry transitions during gating of the trpv2 ion channel in lipid membranes. *Elife* **8**. doi:10.7554/ELIFE.45779

# 6 LIST OF ABBREVIATIONS

| | |
|---|---|
| **2D** | two-dimensional |
| **3D** | three-dimensional |
| **aa** | amino acid(s) |
| **$A_{280}$** | absorbance at 280 nm |
| **AmpR** | ampicillin resistance |
| **APS** | ammonium persulfate |
| ***A. thaliana*** | *Arabidopsis thaliana* |
| **βCD** | β-cyclodextrin |
| **bp** | base pair |
| **BLAST** | basic local alignment search tool |
| **CCD** | charge-coupled device |
| **CHAPSO** | 3-(cholamidopropyl)dimethylammonio-2-hydroxy-1-propane- sulfonate |
| **CL** | cardiolipin |
| **CMC** | critical micellar concentration |
| **CMOS** | complementary metal-oxide-semiconductor |
| **cryo-EM** | electron cryomicroscopy |
| **CTF** | contrast transfer function |
| **DAG** | diacylglycerol |
| **DDM** | n-dodecyl-β-D-maltopyranoside |
| **DED** | direct electron detector |
| **DHPC** | dihexanoylphosphatidylcholine |
| **DIBMA** | poly(diisobutylene-*alt*-maleic acid) |
| **DIBMALPs** | DIBMA lipid particles |
| **DMPC** | dimyristoylphosphatidylcholine |
| **DNA** | deoxyribonucleic acid |
| **DNase** | deoxyribonuclease |
| **DOPC** | 1,2-dioleoyl-*sn*-glycero-3-phosphocholine |
| **DOPE** | 1,2-dioleoyl-*sn*-glycero-3-phosphoethanolamine |
| **DQE** | Detective quantum efficiency |
| **$e^-$** | electron(s) |
| ***E. coli*** | *Escherichia coli* |
| **EM** | electron microscopy |

| | |
|---|---|
| **EMDB** | electron microscopy data bank |
| **EPR** | electron paramagnetic resonance |
| **FSC** | Fourier shell correlation |
| **GOF** | gain-of-function |
| **HEPES** | 4-(2-hydroxyethyl)-1-piperazineethanesulfonic acid |
| **HRP** | horseradish peroxidase |
| **IMAC** | immobilised metal affinity chromatography |
| **IPTG** | isopropyl β-D-thiogalactopyranoside |
| **K2P** | two-pore potassium channel |
| **LacI** | Lac repressor |
| **LB** | Luria Bertani |
| **LMNG** | lauryl maltose neopentyl glycol |
| **LOF** | loss-of-function |
| **LPC** | lysophosphatidylcholine |
| **MALDI-TOF** | matrix-assisted laser desorption ionisation with time-of-flight analysator |
| **MD** | molecular dynamics |
| **MS** | mechanosensitive |
| **MscL** | mechanosensitive channel of large conductance |
| **MscS** | mechanosensitive channel of small conductance |
| **MSL** | MscS-like channel |
| **MSP** | membrane scaffold protein |
| **MW** | molecular weight |
| **NMR** | nuclear magnetic resonance |
| **Ni-NTA** | Nickel nitrilotriacetic acid |
| **$OD_{600}$** | optical density at 600 nm |
| **PA** | phosphatic acid |
| **PBS** | phosphate-buffered saline |
| **PCR** | polymerase chain reaction |
| **PC** | phosphatidylcholine |
| **PE** | phosphatidylethanolamine |
| **PELDOR** | Pulsed electron-electron double resonance |
| **PG** | phosphatidylglycerol |
| **PMSF** | phenylmethylsulfonyl fluoride |
| **POPG** | 1-palmitoyl-2-oleoyl-*sn*-glycero-3-phospho-(1'-rac-glycerol) |

| | |
|---|---|
| **PS** | Phosphatidylserine |
| **r.m.s.d.** | root mean square deviation |
| **RyR1** | ryanodine receptor 1 |
| **Salipro** | saposinlipoprotein |
| **SDS** | sodium-dodecyl sulfate |
| **SDS-PAGE** | SDS polyacrylamide gel electrophoresis |
| **SEC** | size exclusion chromatography |
| **SGD** | stochastic gradient descent |
| **SMA** | poly(styrene-*co*-maleic acid) |
| **SMALPs** | SMA lipid particles |
| **SNR** | signal-to-noise ratio |
| **SPA** | single-particle analysis |
| **TBS** | Tris-buffered saline |
| **TBST** | Tris-buffered saline with Tween |
| **TEM** | transmission electron microscope |
| **TEMED** | tetramethylethylendiamine |
| **TLC** | thin layer chromatography |
| **TM** | transmembrane |
| **TMD** | transmembrane domain |
| **TRP** | transient receptor potential |
| **TRPV1** | TRP cation channel V1 |
| **UV** | ultraviolet |
| **v/v** | volume per volume |
| **WT** | wildtype |
| **w/v** | weight per volume |

Furthermore, the common one-letter and three-letter codes for amino acids according to IUPAC regulations were used.

# CURRICULUM VITAE

# ACKNOWLEDGEMENTS

First of all, I want to thank my primary supervisor, Bettina Böttcher, for giving me the opportunity to work on such an exciting project and opening the fascinating world of electron microscopy and image processing. I really enjoyed being part of her group, and I felt consistently supported and encouraged. Bettina's ideas and creativity, advice and discussions, contributed to the success of this work. Furthermore, I thank her for her patience in dealing with my many How?s and Why?s.

I want to thank the additional members of my thesis committee, Christian Stigloher and Rainer Hedrich, for their time and interest. Their input, suggestions, and questions were very valuable to me and helped me see my project from a different perspective.

I am very grateful to Tim Rasmussen, who worked on this project together with me. He shared not only his experience and enthusiasm for mechanosensitive channels with me but also the lab bench and the chocolate plate between our office places. Tim analysed some of the data sets presented in this thesis, carefully read this thesis, and contributed to my work in so many more ways. Without all the discussions, ideas, knowledge and support, this work would look different from now. I really appreciate all the work-related and non-work-related conversations we had.

Thanks to my further (present and previous) colleagues Christian Kraft, Cihan Makbul, Matthias Grießmann, Samuel Song and Julian Lenhart for the enjoyable atmosphere in lab and office, the chats and discussions, for the purchase of a proper coffee machine, their open ears, and the time together. Especially thanks to Christian, who spent a lot of time introducing us to all the EM equipment in the RVZ and collected many of the data sets at Berta.

I want to say a huge thank you to Akiko Rasmussen, who is also part of the mechanosensitive-channels-team. Her experience in functional analyses of mechanosensitive channels, and especially the electrophysiological experiments she conducted, were very important for understanding our channels. Akiko always found the time to explain things, and her knowledge was very valuable to me.

I further want to express my gratitude to our collaboration partners Mark Sansom and Shanlin Rao from Oxford University and Renato Zenobi and Na Wu from ETH Zurich, for complementing our studies with their methods.

Thank you to my master student Fabian Töppke, and to Lukas Hahn, Stefan Forster, and Malik Salman Haider from Robert Luxenhofer's group for the uncomplicated and interesting collaborations and their efforts in teaching me about polymer chemistry.
I further thank the people of the structural biology unit at the Rudolf Virchow Center, Würzburg, for a nice, inspiring, and helpful working environment.
I would like to thank the students participating in our EM master practical in 2020, for doing a good job in carefully screening and initially analysing the data sets of MscS prepared under different conditions.
I also want to acknowledge Wim Hagen from EMBL Heidelberg for helping me with his straightforward emails to finalise the automatic tilt-series collection setup on Berta.

Looking back on the way I have come, I want to thank my family for their unconditional love and support. I especially thank my parents, who encouraged and supported me throughout. Their interest in me and my work, despite "not understanding what you are doing", and their always open ears and open arms mean a lot to me. Thank you to my twin brother Pascal for mutual motivation, for his numerous calls and visits, and for always finding a way to make me laugh. My uncle Gerhard is a scientist himself, and I would like to thank him for his consistent curiosity and interest in my project. I am sure the always enthusiastically told stories about his work contributed substantially to my own decision to become a scientist. I further want to thank my wonderful Oma Regina, who supported me in so many possible ways and taught me countless things. She was – and always will be – a huge inspiration to me. Also, thank you to my parents-in-law for being always interested in my work.
I thank my best friend and husband Alex from the bottom of my heart for covering my back throughout all these years, for his love and patience and understanding, for sharing all happy and sad moments with me, and for his belief in me. Because of his unlimited support, I could both work on this fascinating project and start a family of my own. Finally, I want to thank my children Emilia and Julian for adding so much joy to my life.